



Bournemouth University

Ulterius Corrosion Health Monitoring (UCHM) using wireless sensor technologies

Jawwad Latif

A thesis is submitted in partial fulfilment of the requirements of
Faculty of Science and Technology, Department of Design and Engineering,
Bournemouth University for the degree of Doctor of Philosophy

26 April 2019

Faculty of Science and Technology, Bournemouth University

In Collaboration with

Defence Science and Technology Laboratory (DSTL) and Ministry of Defence, UK

Copyright Statement

This copy of the thesis has been supplied on condition that anyone who consults it is understood to recognise that its copyright rests according to the Bournemouth University and Defence Science and Technology Laboratory agreement and that no quotation from the thesis and no information derived from it may be published without the written permission from BU legal team.

Abstract

Complex metal structures operating in harsh environmental conditions are prone to various forms of coating failures and corrosion damage. The costly Scheduled-based-Maintenance (SBM) strategies are practiced for metal structures that result in huge financial overhead for industries. The current research work is aim to provide the solutions to anticipate the condition of a metal structure in terms of corrosion damage and coating failure for proactive and optimal Condition-base-Maintenance (CBM) decisions.

The experimental investigation has shown that the adhesion loss between coating and substrate system in the form of blisters is driven by complex electrochemical and mechanical parameters. The propagation criteria can be defined through threshold levels of bending moment incorporating residual and diffusion-induced stresses. The current work also investigated the environmental impact on structures which are operating at remote locations. It has been observed that the accumulation of salt particles from atmosphere resulting in corrosion under the coating is primarily controlled by the speed of the wind. An algorithm has been proposed that incorporates the effect of wind speed to estimate the accumulation of salt particles and the amount of salt diffusivity. Experimental and simulation analysis has further shown that the low wind speed and low temperature are considered the most appropriate environmental conditions for structures operating at remote locations. Meanwhile, the high temperature and high wind speed can result in high corrosion damage beneath the coating. The prognostic algorithms resulted in the development of a comprehensive Condition-based-Maintenance framework to determine the cost-effective maintenance strategy among Patch recoat, Part recoat and Complete recoat. The CBM framework suggests that the Part recoating strategy is cost-effective as compared to Patch recoating strategy if the area of the part to be recoated is '2x' times larger than the area of patch and number of path failure per year is more than '2'. Meanwhile, the Patch recoating strategy results in low cost if the annual patch failures are less than '7' and area of the part to be recoated is '10x' times larger than the area of the patch.

Real time monitoring of the impact of significantly varying operating condition for mobile structures is very challenging for condition assessment. The combination of μ -

Linear Polarisation Resistance (LPR) and μ -strain gauge sensors have been investigated to monitor the development of residual stresses and corrosion reaction beneath the coating. The measurements from μ -strain gauge sensor in response to small temperature gradients can provide instant information regarding the development of tensile or compressive stresses within the coating of structures as observed in experiments. The combination of μ -LPR and μ -strain gauge sensors has been found an effective solution for proactive corrosion detection in real time for the structures operating mobile and at remote locations.

Publications

(resulted from this research project)

Journal Publications

- Latif, J., Khan, Z., Nazir, H., Stokes, K. and Plummer, J., 2018. Condition monitoring and predictive modelling of coating delamination applied to remote stationary and mobile assets. Structural Health Monitoring. (Q1)
- J Latif, ZA Khan, MH Nazir, K Stokes, J Plummer, “Life assessment prognostic modelling for multi-layered coating systems using a multidisciplinary approach”, Materials Science and Technology, 2017. (Q1)
- Jawwad Latif, Zulfiqar A. Khan, Mian H. Nazir, Keith Stokes & Richard Smith (2019) An optimal condition based maintenance scheduling for metal structures based on a multidisciplinary research approach, Structure and Infrastructure Engineering (Q1)
- Khan, Z. A., Latif, J., Nazir, H., Saeed, A. and Stokes, K., “Predictive and prognostic modelling and simulation of coating failures due to corrosion and mechanical failures” , International Journal of Computational Methods and Experimental Measurements, 2017.

Journal article (Submitted)

- Structural Monitoring System for proactive detection of corrosion and coating failure

Conference Publications

- Khan, Z. A., Latif, J., Nazir, H., Saeed, A. and Stokes, K., “Sensor based corrosion condition monitoring of coating substrate system informed by fracture mechanics, electrochemistry and heat transfer concepts”, Department of Defense - Allied Nations Technical Corrosion Conference, 2017.
- Latif, J. and Khan, Z., 2018. Corrosion prediction algorithm and condition monitoring system for efficient diagnosis and prognosis of high value mobile and stationary assets. In: Fifteenth International Conference on Condition Monitoring

and Machine Failure Prevention Technologies (CM 2018/MFPT 2018) 10-12 September 2018 Nottingham, UK. <http://www.bindt.org/events/NDT-2018/>.

- M.H. Nazir, Z.A. Khan, J. Latif, “Development of a Mechano-Electrochemical Model for Prognostics of Nano-Composite Coatings Subject to Corrosion Failures”, STLE 73rd Annual Meeting & Exhibition, 2018.

Conferences/Workshops Presentations

- 73rd STLE annual meeting and exhibition, Minneapolis convention center Minneapolis, Minnesota, USA
- One day international research workshop NanoCorr, Energy & Modelling-Tsinghua University Beijing China
- Second Annual SciTech Conference, Bournemouth University, 18 May 2016

Poster award

- Best Poster award, Second Annual SciTech Conference, Bournemouth University, May, 2016

Table of Contents

Copyright Statement	II
Abstract	III
Publications	V
List of Figures	XI
List of Tables	XV
Acknowledgements	XVI
Author's Declaration	XVII
Nomenclature	XVIII
Abbreviations	XXI
Chapter 1: Introduction.....	1
1.1 Research outline	1
1.2 Scope of the project.....	4
1.2.1 Museums	4
1.2.2 Academia	4
1.2.3 Defence industry	4
1.2.4 General industry.....	4
1.3 Research question.....	6
1.4 Objectives	6
1.5 Methodology	7
1.5.1 Experimental analysis	7
1.5.2 Prognostic modelling	7
1.5.3 Wireless Condition Monitoring System	7
1.6 Research novelty	8
1.7 Structure of the thesis	10
Chapter 2: Literature Review	13

2.1 Corrosion theory	13
2.1.1 Reasons for corrosion	15
2.1.2 Atmospheric effect on corrosion prediction	16
2.1.3 Weather conditions at Dorset.....	17
2.1.4 Corrosion monitoring techniques	20
2.2 Protective coatings	22
2.2.1 Blistering failure	23
2.2.2 Micro-cracks and stress factor	31
2.3 Maintenance of structures	34
2.3.1 Cost of corrosion and maintenance.....	34
2.3.2 Maintenance strategies.....	35
2.4 Conclusion.....	37
Chapter 3: Blistering Failure	39
3.1 Experimental methodology	40
3.1.1 Sample preparation	40
3.1.2 Pre-Experimental analysis	41
3.1.3 Immersion Test	44
3.1.4 Post-Experimental Analysis.....	46
3.2 Prognostic modelling.....	47
3.2.1 Integration of diffusion and bending model	51
3.2.2 Fracture mechanics concept.....	52
3.2.3 Blister growth rate model	55
3.3 Coating life assessment algorithm.....	57
3.3.1 Algorithm implementation.....	58
3.4 Results and discussions	61
3.5 Conclusion.....	65
Chapter 4: Micro-cracks and Diffusion.....	66

4.1 Experimental methodology	67
4.2 Experimental results	70
4.3 Prognostic modelling.....	73
4.3.1 Salinity Model.....	74
4.3.2 Temperature model	76
4.3.3 Relative humidity model.....	77
4.3.4 Exposure time	77
4.4 Proposed algorithm.....	77
4.5 Results and discussions	78
4.6 Conclusion.....	82
Chapter 5: Condition-based-Maintenance	84
5.1 Maintenance Strategy Evaluation Algorithm	84
5.1.1 Input parameters	86
5.2 Prognostic modelling.....	89
5.2.1 Coating failure modelling	89
5.2.2 Maintenance cost modelling	91
5.3 Maintenance history database.....	97
5.4 Algorithm implementation	99
5.5 Results and discussion.....	103
5.6 Conclusion.....	105
Chapter 6: Wireless Condition Monitoring System.....	107
6.1 Wireless Condition Monitoring System	107
6.2 Remote Terminal Units (RTUs).....	109
6.2.1 HP_RTU	109
6.2.2 NCEM_Smartv1.0 RTU	117
6.3 Base Station.....	121
6.4 Proactive Corrosion Detection System.....	125

6.5 Experimental methodology	126
6.6 Results and discussions	129
6.7 Conclusion.....	134
Chapter 7: Conclusion and Future work.....	136
7.1 Inclusive Condition Monitoring System	138
7.2 Recommendations	139
7.3 Summary	141
References	142
Appendix A: Paper I	149
Appendix B: Paper II.....	164
Appendix C: Paper: III	176
Appendix D: Paper IV	194
Appendix E: Paper V	224
Appendix F: Simulation code	233
Appendix G: Data sheet.....	238
Appendix H: Data sheet	245
Appendix I: Data sheet.....	250
Appendix J: Data sheet.....	258
Appendix K: Data sheet	260
Appendix L: LabVIEW Program	262
Appendix M: Data sheet.....	265
Appendix N: Arduino code.....	266
Appendix O: LabVIEW Program.....	294

List of Figures

Figure 1.1 Basic architecture of the project	5
Figure 1.2 Milestones achieved in the project	11
Figure 1.3 Structure of the thesis	12
Figure 2.1: Contents of chapter	13
Figure 2.2: Corrosion reaction (Latif, J. et al., 2018a).....	14
Figure 2.3: Rainy days at Dorset for 3 years (Latif, J. et al., 2018a)	18
Figure 2.4: Relative humidity at Dorset for 3 years (Latif, J. et al., 2018a)	18
Figure 2.5: Wind speed at Dorset for 3 years (Latif, J. et al., 2018a)	19
Figure 2.6: The Valentine tank at the tank Museum before maintenance	20
Figure 2.7: Various corrosion monitoring techniques	21
Figure 2.8: Parameters in blister failure	25
Figure 2.9: Modes of fracture {, #181;Roylance, 2001 #191}	26
Figure 2.10: Direction of stresses and crack	26
Figure 2.11: Straight-sided blister.....	28
Figure 2.12: Diffusion of salt particles and corrosion reaction.....	32
Figure 2.13: Methods involved in Condition-based-Maintenance.....	36
Figure 3.1: Contents of the chapter	39
Figure 3.2: Coating layers applied to samples	41
Figure 3.3: White Light Interferometry	42
Figure 3.4: Scanning Electron Microscopy.....	43
Figure 3.5: The cross-sectional SEM images for coating thickness (Latif, J. et al., 2018b)	44
Figure 3.6: Coated samples inside aqueous salt solution.....	45
Figure 3.7: Environmental chamber.....	45
Figure 3.8: Surface profiles of samples after the experiment (Latif, J. et al., 2018b)....	47
Figure 3.9: Multidisciplinary research approach for prognostic modelling (Latif, J. et al., 2018b)	50
Figure 3.10: Coating life assessment algorithm (Latif, J. et al., 2018b)	58
Figure 3.11: Blister height of each sample (Latif, J. et al., 2018b).....	61
Figure 3.12: Blister propagation of each sample (Latif, J. et al., 2018b).....	62
Figure 3.13: Simulation results for de-bonding driving force (Latif, J. et al., 2018b)....	63

Figure 3.14: Simulation results for Velocity of blister vs Elastic modulus of the coating (Latif, J. et al., 2018b)	64
Figure 3.15: Simulation results for Velocity of blister vs bending moment (Latif, J. et al., 2018b)	64
Figure 4.1: Contents of the chapter	66
Figure 4.2: Three electrode system (Latif, J. et al., 2018a).....	68
Figure 4.3: Architecture of μ LPR sensor [31]	68
Figure 4.4: Corrosion monitoring system installed on Valentine Tank (Latif, J. et al., 2018a).....	69
Figure 4.5: Corrosion monitoring system (Khan, Z. A. et al., 2017).....	70
Figure 4.6: Corrosion monitoring at Turret top of Valentine tank during stationary and remote activities (Latif, J. et al., 2018a).....	71
Figure 4.7: Corrosion rate and Salinity measurements during remote activity A1 (Latif, J. et al., 2018a)	71
Figure 4.8: Corrosion rate and Salinity measurements during remote activity A2 (Latif, J. et al., 2018a)	72
Figure 4.9: Corrosion rate and Salinity measurements during remote activity A3 (Latif, J. et al., 2018a)	72
Figure 4.10: Algorithm for estimation of salinity transport rate depending on various geographical locations (Latif, J. et al., 2018a)	78
Figure 4.11: Salinity transport rate for increasing wind speed during the summer season (Latif, J. et al., 2018a)	80
Figure 4.12: Salinity transport rate for decreasing wind speed during the summer season (Latif, J. et al., 2018a)	80
Figure 4.13: Salinity transport rate for increasing wind speed during the winter season (Latif, J. et al., 2018a)	81
Figure 4.14: Salinity transport rate for decreasing wind speed during the winter season (Latif, J. et al., 2018a)	82
Figure 4.15: Salinity transport rate depending on the distance from the sea (Latif, J. et al., 2018a).....	83
Figure 5.1: Contents of the chapter	85
Figure 5.2: Basic Architecture of Maintenance Strategy Evaluation Algorithm	86
Figure 5.3: Recoating Maintenance Strategy Evaluation Algorithm	87
Figure 5.4: Input parameters	88

Figure 5.5: Profiles for de-bonding driving force and maintenance strategies	97
Figure 5.6: Recoating Maintenance Strategy Evaluation Simulation	102
Figure 5.7: Simulation results for de-bonding driving force vs de-bonding index.....	104
Figure 5.8: Annual cost of maintenance for coating-substrate system with different coating thickness	105
Figure 5.9: Simulation results for recoating maintenance strategy for metal structures	106
Figure 6.1: Contents of the chapter	107
Figure 6.2: Wireless Condition Monitoring System	108
Figure 6.3: Flowchart for Remote terminal unit	110
Figure 6.4: cRIO-9063 controller (Appendix G)	111
Figure 6.5: NI-9207 module.....	112
Figure 6.6: NI-9017 module.....	112
Figure 6.7: SEA-9741 module (Appendix J)	113
Figure 6.8: Components in LabVIEW software	114
Figure.6.9: Accessories used for strain gauge installation.....	114
Figure 6.10: Several steps involved in the installation of the strain gauge sensor on the coated sample	115
Figure 6.11: Experimental results acquired from strain gauge monitoring system from sample	116
Figure 6.12: Applying protective coating on the sensor	116
Figure 6.13: Sample after immersion test	117
Figure 6.14: High-Performance Remote Terminal Unit	117
Figure 6.15: Flowchart for NCEM_Smartv1.0	118
Figure 6.16: Arduino Mega 2560 Rev3	119
Figure 6.17: Real Time Clock.....	119
Figure 6.18: Electronic circuit for μ LPR sensor	119
Figure 6.19: Electronic circuit for μ -strain gauge sensor.....	120
Figure 6.20: Electronic circuit for DHT22 sensor	120
Figure 6.21: Electronic circuit for battery life	120
Figure 6.22: GSM module.....	121
Figure 6.23: NCEM_Smartv1.0 RTU	121
Figure 6.24 Flow chart for Base Station	122

Figure 6.25: Base Station system	123
Figure 6.26: Graphical user interface of software at the base station	123
Figure 6.27: Inserting a corrosion sensor in an aqueous salt solution to verify the corrosion detection	124
Figure 6.28: The RTU's connected with sensors.....	124
Figure 6.29: Sensors are kept inside the salt spray chamber.....	124
Figure 6.30: The base station system displaying measurements from RTUs	124
Figure 6.31: The base station system displaying measurements from RTUs	125
Figure 6.32: Proactive corrosion detection system	126
Figure 6.33 Polished samples.....	127
Figure 6.34 Sample with μ LPR sensor	128
Figure 6.35 Sample with μ LPR sensor	128
Figure 6.36 Accessories for installation of μ -strain gauge sensor	129
Figure 6.37 Sample with μ -strain gauge sensor	129
Figure 6.38 Sample inside environmental chamber	129
Figure 6.39 Measurements of μ -strain gauge sensor during 1st experiment	131
Figure 6.40 Measurements of μ LPR sensor during 1st experiment.....	132
Figure 6.41 Measurements of μ -strain gauge sensor during 2nd experiment.....	132
Figure 6.42 Measurements of μ LPR sensor during 2nd experiment	133
Figure 6.43 Measurements of μ -strain gauge sensor during 3rd experiment.....	133
Figure 6.44 Measurements of μ LPR sensor during 3rd experiment	134
Figure 7.1: Basic architecture of an Inclusive Condition Monitoring System.....	138
Figure 7.2: Inclusive Condition Monitoring System	139
Figure 7.3: Application of machine learning algorithms	141

List of Tables

Table 2-1: Prognostic models for coating failure in the recent years	30
Table 2-2: Factors considered for estimating the cost of corrosion	35
Table 3-1: Composition of Structural steel S275	40
Table 3-2: Coating thickness and roughness of samples (Latif, J. et al., 2018b).....	44
Table 3-3: De-bonding index for the coating-substrate system	55
Table 3-4: Blister propagation criteria	57
Table 3-5: De-bonding driving force to define the state of the coating-substrate system	57
Table 4-1: ISO classification of deposition rate of sodium chloride depending on different environmental conditions (Standardization, I. O. F.)	73
Table 5-1: Conditions for patch failure	90
Table 5-2: Blister propagation criteria	91
Table 5-3: Uniform Database for Maintenance of metal structures.....	97
Table 6-1 Surface roughness of each sample	127

Acknowledgements

I will take this opportunity to express my heartiest gratitude to Prof. Zulfiqar Khan, my supervisor. His continuous support, help, and guidance were a strong source of inspiration, encouragement and confidence. He also provided an excellent opportunity for me to meet experts in the research area. I would also like to thank Richard Smith, Mike Hayton, The Tank Museum Bovington for providing the facility for our experimental and simulation study. I am also thankful to Prof. Dr. Keith Stokes, Mr. Joseph Plummer and Dr Hammad Nazir for his professional advice and timely discussions. My appreciation goes to all the staff I have worked with so closely at Bournemouth University, especially laboratory staff.

I should also mention my parents, wife, brothers and sisters who contributed continuous support and encouragement. Last but not least I appreciate help and support of colleagues and friends.

This research is jointly funded by the Defence Science & Technology Laboratory (DSTL) and Bournemouth University UK, the authors acknowledge their support & contributions.

Author's Declaration

This thesis contains the original work of the author except otherwise indicated. All contents of this thesis except materials from external sources are subject to confidentiality as set out in the contractual legal agreement between Bournemouth University UK and Defence Science and Technology Laboratory, Ministry of Defence (MoD), UK.

Nomenclature

σ_{d_s}	Diffusion induced stress of substrate material
$\sigma_{d_{ci}}$	Diffusion induced stress for i^{th} coating material
$\sigma_{r_{ci}}$	Residual stress for i^{th} coating material
σ_{r_s}	Residual stress of substrate material
$\overline{V}_{p\ k}$	Partial molar volume
c'_k	Concentration gradient
s	Thickness of substrate
ε_{u_d}	Uniform bending strain due to diffusion-induced stress
ε_{u_r}	Uniform bending strain due to residual stress
ρ_d	Bending curvature due to diffusion-induced stress
ρ_r	Bending curvature due to residual induced stress
μ_k^Q	Chemical potential for isotropic material
r	Radius of blister
E_i	Elastic modulus of i^{th} coating material
h_i	Thickness of i^{th} layer of coating
ν_i	Poisson's ratio of i^{th} material
σ_{cr}	Critical stress of single layer coating
$\sigma_{cr'}$	Critical stress of multi-layered coating
G_o	Resultant strain energy release rate
T_{th}	Total thickness of coating
σ_T	Total unbuckled stress
\cap	De-bonding index
Γ_{IC}	Interface toughness

j	Mode mixity ratio
F_{cr}	Critical de-bonding driving force
F	De-bonding driving force
M_{Th}	Threshold bending moment
M_{ini}	Initiation bending moment
a	Blister diameter
w	Blister amplitude
$\overline{V}_{p\ k}$	Partial molar volume
σ_r	Residual stress
ε	Strain
α	Coefficient of thermal expansion mismatch
M	Bending moment
λ	Roughness
N	Pre-buckling stress
F_c	Future cost
ir	Interest rate
Ar_p	Patch area to be recoat
Sp_p	Surface preparation cost
C_p	Patch coating cost
A_e	Total are of vehicle to recoat
Sp_e	Surface preparation cost
C_e	Coating cost
Ar_c	Component area to be recoat
Sp_c	Part surface preparation cost

C_c	Cost of Part coating
t_n	Time duration for patch failure
t_c	Time duration for Part failure
T_e	Time duration for complete failure
σ_c	Compressive stress
S_n	Salinity at different regions
S_0	Salinity at non-coastal region
S_1	Salinity at coastal region
S_2	Salinity at coastal region
S_3	Salinity near sea region

Abbreviations

NCEM	NanoCorr, Energy Modelling
DSTL	Defence Science and Technology Laboratories
SEM	Scanning Electron Microscopy
LPR	Linear Polarisation Resistance
SBM	Scheduled-based-Maintenance
CBM	Condition-based-Maintenance
DAQ	Data acquisition unit
NaCl	Sodium Chloride
RTU	Remote terminal Unit
HP_RTU	High performance remote terminal unit
GPS	Global positioning system
GSM	Global System for Mobile communication
NI	National Instruments
RTC	Real time clock
PID	Proportional–integral–derivative
LMI	Logistics Management Institute
FPGA	Field Programmable Gate Arrays

Chapter 1: Introduction

The NanoCorr, Energy Modelling (NCEM) research group is providing high-quality research outcomes in detection, prevention and prognostic solutions for condition monitoring of large and complex metal structures. The current research work is the continuation of successful completion of research projects carried out from 2011 to 2015 by NCEM research group at Bournemouth University in collaboration with Defence Science and Technology Laboratories (DSTL), Ministry of Defence UK and The Tank Museum Bovington, UK (Nazir, M. H., 2015; Saeed, A., 2013). In previous projects, the structural degradation factors in large military tanks which were operated in World War I and World War II have been investigated. The research findings have resulted in the development of the Vehicle Conservation Centre at The Tank Museum. These investigations further lead to the development of mathematical models to define the behaviour of various forms of structural deterioration modes.

The current project is aim to build the prognostic solutions for large vehicles operating in remote locations. These prognostic solutions lead to the development of a comprehensive condition based maintenance algorithm and wireless structural health monitoring system. This project is also match funded by Defence Science and Technology Laboratories (DSTL), Ministry of Defence (MoD), UK and Bournemouth University (BU), UK. This chapter explains the abstract view of the project, research question, objectives, the novelty in the project and structure of the overall thesis.

1.1 Research outline

Corrosion is an electrochemical process which involves oxidation-reduction reactions resulting in deterioration of metal and formation of rust. The corrosion of metals depends on various factors including the chemical composition of metal, surface condition, grain boundary composition, crystal structures, the creation of galvanic potentials due to the geometry of the structure, variation in temperature at the metal surface exposed to the environment, heat transfer, humidity, wetting, salinity in the atmosphere, wear and undesired stresses (Corrosion, 2012). A large number of factors involved in the corrosion phenomena make it difficult and complex for accurate prognosis. Corrosion affects a large number of industries such as Infrastructure,

Chapter 1: Introduction

Transportation, Utilities, production and manufacturing industry. In Infrastructure industry where highway bridges, airports, and railroads are prone to corrosion damage resulting in loss of strength causing major health and safety issues. In the transportation industry, the corrosion in motor vehicles, ships and aircraft causes a major threat to durability and safety issues. The drinking water, telecommunications, production and manufacturing industries are also greatly affected by corrosion damage. Corrosion has huge economic consequences on industries resulting in direct and indirect cost. The NACE international has utilised various methods to estimate the financial impact of cost. It has been found that corrosion and its maintenance strategies are costing almost 3.4% of global Gross Domestic Product (GDP) (Inspectioneering, 2016; Koch, G. E. A., 2016).

Organic coatings are applied to metal structures acting as a barrier to protect them from the surrounding environment. Although coatings play a vital role in the protection of metal structures, they also result in adhesion loss or breakdown exposing metal to the environment. Researchers have analysed the complex parameters involved in corrosion and coating failure mechanisms to propose predictive and prognostic models for condition assessment of metal structures. Efficient prognostic models can help the organisations to make accurate life assessment and maintenance scheduling of their structures.

Scheduled-based-Maintenance (SBM) and Condition-based-Maintenance (CBM) strategies are commonly practised by industries. These strategies have their own advantages and disadvantages but CBM is considered as an efficient and cost-effective maintenance strategy as compared to SBM (Prajapati, A. et al., 2012). A large number of organisations including the Airforce, Army, navy, marine and automotive companies are adopting CBM strategies. The inclusion of advanced technologies by enabling sensors, data acquisition units, data processing, data analysis and data transmission capabilities can enhance the efficiency of CBM strategy. The real-time data monitored from a metal structure such as vehicles or any other high-value structure can give deeper insight on condition and performance to apply predictive models to help in sustaining mission-critical equipment's or structures used in automotive, manufacturing, maritime, aerospace and other industrial domain. Although very comprehensive literature is available on predictive models, the solutions for complex behaviour of corrosion and

Chapter 1: Introduction

coating failure in real time environment are still scarce. The implementation of prognostic models to predict the deterioration of structure based on real-time data and selection of suitable repairing maintenance strategy are still challenging issues in the CBM strategy.

The NCEM research group has been working with ‘The Tank Museum’, UK and DSTL to propose solutions for the sustainability of the large military vehicles stationed at ‘The Tank Museum’. The large military vehicles are assembled of complex and numerous metal parts. They often operate in diverse and extreme weather conditions such as coastal regions and the marine environment. The exposure of large military vehicles to such environmental conditions results in corrosion damage, wear, loss of coating adhesion from the metal structure, undesired stresses and fatigue cracks in the surface and sub-surface (Saeed, A. et al., 2017). The comprehensive experimental study has been conducted from 2011 to 2013 on large military vehicles at ‘The Tank Museum’, UK (Saeed, A., 2013). These large military vehicles had performed during World War I and II. During their service life, these military vehicles were operated in extreme weather and operating conditions in the battlefield. Now they are commonly stationed for display under a shed in controlled environmental conditions and a few of them outside in uncontrolled environmental conditions. Sometimes vehicles are moved for various outside activities. The inside and outside environmental conditions of the museum were investigated within the context of corrosion damage. The presence of surface contaminations, corrosive pits, the inclusion of sulphide and slags resulted in corrosion damage causes major concerns about the durability of large military vehicles. The research findings resulted in the formation of the Vehicle Conversation Centre in order to provide suitable environmental conditions in large military vehicles to extend durability by preventing structural ageing. Based on observations and experimental investigations, the multidisciplinary and state-of-the-art prognostic solutions have been proposed in the research work from 2013 to 2015 (Nazir, M. H., 2015). The adhesion loss and corrosion damage resulting from diffusion of corrosive products, undesired stresses due to a temperature gradient, surface roughness and coating thickness have been investigated and modelled (Nazir, M. and Khan, Z. A., 2017). The basic architecture for condition monitoring is shown in Figure 1.1. It contains prognostic models, real-time condition monitoring and proactive decision-making mechanisms for

Chapter 1: Introduction

maintenance. The current research project was aimed to provide solutions for Condition-based-Maintenance scheduling through Multidisciplinary and Transdisciplinary research approaches.

1.2 Scope of the project

The current research work will contribute to academia, general industry, museums and defence industry. The scope of the project is:

1.2.1 Museums

The prognostics solutions from current research will provide a framework for making adequate decisions regarding conservation of the large military vehicles. The general public visiting the museum will enjoy the historical military vehicles for an extended time.

1.2.2 Academia

The solution in the current project based on multidisciplinary and transdisciplinary research approach will provide a platform for the development of more complex and accurate prognostic models for future researchers.

1.2.3 Defence industry

Air and ground military vehicles are complex objects and subjected to numerous structural breakdown mechanisms. The solutions proposed in current work will provide a framework to the defence industry to preserve their sensitive equipment for a long period of time with optimised maintenance cost.

1.2.4 General industry

The proposed solutions will also help the civil infrastructure, aerospace industry and food production industries to prolong the functional life of metal equipment's/structures.

Chapter 1: Introduction

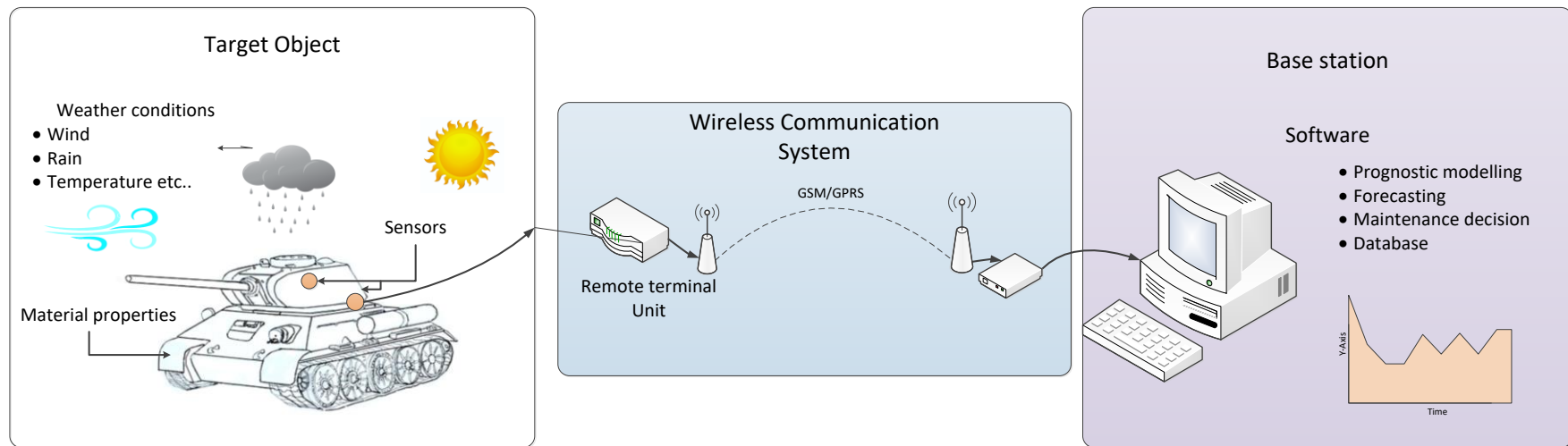


Figure 1.1 Basic architecture of the project

1.3 Research questions

The ambiguous nature of environmental conditions for structures operating stationary at remote locations makes damage assessment more challenging. The rate of deterioration for metal structure can be computed more accurately by considering the effect of significantly varying environmental factors. The primary aim of the project is to reduce the maintenance cost based on modern prognostic solutions which consider multidisciplinary parameters for assessment of structural deterioration. The main research questions for the current project can be written as follows:

- What are the factors that drive the structural deterioration for the metal structures operating mobile and at remote locations?
- How the cost associated with maintenance can be reduced based on the impact of complex mechanical and electromechanical parameters?
- How to acquire critical parameters such as residual stresses in real time from structures operating mobile and at remote locations to schedule condition based maintenance?

1.4 Objectives

1. To analyse the behaviour of debonding driving force by performing accelerated corrosion experiments on coating-substrate systems that contain metal and corrosion resistant coating material commonly used in large structures.
2. To investigate the environmental impact on vehicles that are operating inside and outside the Museum environment to identify the significantly varying factor that drives the corrosion phenomena beneath the coating.
3. To design a Condition-based-Maintenance framework for low-cost maintenance decisions for large and complex metal structures without compromising the structural integrity.
4. To investigate the corrosion and strain gauge sensors through experimental methods that can provide real-time information for corrosion initiation and development of residual stresses within coating for structures operating at remote locations.

1.5 Methodology

The project covers a variety of aspects including prognostic modelling leading to cost-effective maintenance strategies and the development of a wireless condition monitoring system. Multiple methodologies have been adopted to achieve the desired objectives. The prognostic modelling involves experimental investigation, mathematical modelling and simulation. The development of a wireless monitoring system involves communication hardware, microcontroller board, software and sensors. The performance of the developed system is also analysed through experimental techniques.

1.5.1 Experimental analysis

The experimental methods for accelerated corrosion testing have been performed to analyse the corrosion and coating failure behaviour of coated samples. The experimental procedure involves the following steps:

- Sample preparation
- Pre-experimental analysis
- Accelerated corrosion testing
- Post-experimental analysis
- Results and discussions

1.5.2 Prognostic modelling

The behaviour of corrosion and coating failure observed through experimental methodology has been formulated in the form of mathematical models and simulation analysis carried out using time iterative approaches on the MATLAB platform and Microsoft Excel.

1.5.3 Wireless Condition Monitoring System

The system contains remote terminal units and the base station. The high performance and low-cost remote terminal units have been built. The high-performance remote terminal unit (RTU) was built on a commercially available data acquisition unit. The system is programmable through software called LabVIEW and can work as a standalone processor based on the desired application. The low-cost system has been

Chapter 1: Introduction

built on commercially available Arduino boards. They can also be programmed through software called Arduino IDE. The sensors are attached to RTU's and linked to General Packet Radio Services (GPRS) module for wireless data transmission. The software at a base station connected with GPRS module was programmed on LabVIEW.

1.6 Research novelty

Corrosion within the high-value structure is affecting a large number of organisations resulting in a huge financial loss. The implementation of time and cost-effective maintenance scheduling is evident. The condition assessment of high-value structures with complex metal structure operating in a harsh environment and at various geographical locations becomes challenging. The inclusion of all critical parameters in prognostic modelling can provide more accurate information for efficient maintenance decisions. The current project aimed to provide state-of-the-art condition monitoring solutions based on multidisciplinary and transdisciplinary research approach. The milestones achieved in the current project have been mentioned compressively in Figure 1.2.

The structures that operate at remote locations deteriorate due to blistering and micro-cracks. These are considered two most common modes of coating failures that have been addressed. A comprehensive prognostic algorithm based on multi-disciplinary research has been proposed to predict the formation and propagation speed of circular blistering failure (Latif, J. et al., 2018b) (Appendix A). It also provides criteria for the propagation or stoppage of the blistering effect. This also led to the development of the mathematical equations of de-bonding driving forces for straight-sided blister (Khan, Z. A. et al., 2018) (Appendix B).

The opening of cracks within a coating allows salt particles to diffuse into the coating-substrate system resulting in corrosion damage under the coating. The damage rate is driven by the concentration of salt particles. The deposition of salt particles over the metal structure depends on the atmosphere at operating conditions. The speed of the wind and the geographical locations are the controlling factors for a deposition rate of salt particles. An algorithm is proposed to estimate the diffusion of salt particles depending on wind speed and geographical locations (Latif, J. et al., 2018a) (Appendix C).

Chapter 1: Introduction

The cost-effective recoating maintenance strategy for metal structures is very challenging due to numerous influential factors. The transdisciplinary research approach has been used to integrate a multidisciplinary prognostic algorithm to the cost of maintenance to provide a framework for the evaluation of optimal recoating maintenance strategy discussed in Chapter 5 (Appendix D).

The real-time condition monitoring requires a wireless remote terminal unit with sensors and software at the base station to store and analyse real-time data. The corrosion sensor has already been investigated and experimented in the previous projects within NCEM. In the current project, the μ -strain gauge sensor is investigated to monitor the tensile and compressive stresses within coating (Khan, Z. A. et al., 2017) (Appendix E).. The corrosion monitoring sensor based on linear polarisation resistance method to monitor electrochemical changes and micro-strain gauge sensors used to monitor mechanical changes within a coating are embedded with Global System for Mobile (GSM) communication system to develop the wireless remote terminal unit. The remote terminal unit is able to provide the measurements of critical parameters from metal structures operating stationary in a controlled environment or a remote location or mobile. Two remote terminal units are developed as one is developed with commercially available high-performance data acquisition units (National Instruments).

The second remote terminal unit is low-cost named as NCEM_Smart v1.0 developed using commercially available microcontroller boards to install on a number of target vehicles to be monitored. The performance of NCEM_Smart v1.0 is evaluated with the high-performance remote terminal unit in laboratory experimentation. The software for the base station is also programmed to acquire and store real-time data for analysis. The developed condition monitoring system will also help in future research findings in corrosion and coating failure for the remote and mobile structure and in extending the research work for civil, aerospace and marine applications within NCEM research group. The development of the condition monitoring system has been discussed in detail in Chapter 6.

1.7 Structure of the thesis

The chapters in the report have been organised as shown in Figure 1.3. There is a total of seven chapters in the report. The abstract view of the overall project including research outline, the desired objectives and the methodology has been explained in this chapter. The comprehensive literature review is elaborated in Chapter 2. It includes the basic concepts of corrosion and common modes of coating failure. The latest research findings leading to the development of prognostic models are also mentioned in detail. The cost associated with maintenance in the defence industry and the maintenance strategies are also given in the chapter.

The blistering and micro-cracks are the two most common modes of coating failure found on large vehicles at “The Tank Museum” have been addressed. Chapter 3 explains the formation and propagation speed of blistering failure through experimental methods leading to the development of the prognostic algorithm.

Chapter 4 includes the condition monitoring of a large vehicle at “The Tank Museum” to investigate the environmental impact on the structure. The prognostic model for deposition rate and diffusion rate of salinity for structures operating at various geographical locations has been proposed and simulation results have been discussed in detail.

A comprehensive multidisciplinary algorithmic approach has been proposed in Chapter 5 to provide optimal maintenance solutions for metal structures. The prognostic models elaborated in previous chapters have been linked with maintenance cost to evaluate optimal recoating strategy among Part recoat, Patch recoat and Complete Recoat. The algorithm estimates the optimal recoating strategy based on specifications of coating material, structural material and operating conditions.

The accurate life assessment and the selection of an optimal maintenance strategy for metal structures based on real-time parameters are evident for critical structures. Therefore, Wireless Condition Monitoring System has been developed in the current project. It includes the development of remote terminal units along with base station system explained in Chapter 6. Chapter 7 includes the conclusions resulting from objectives achieved in current project leading to future recommendations.

Chapter 1: Introduction

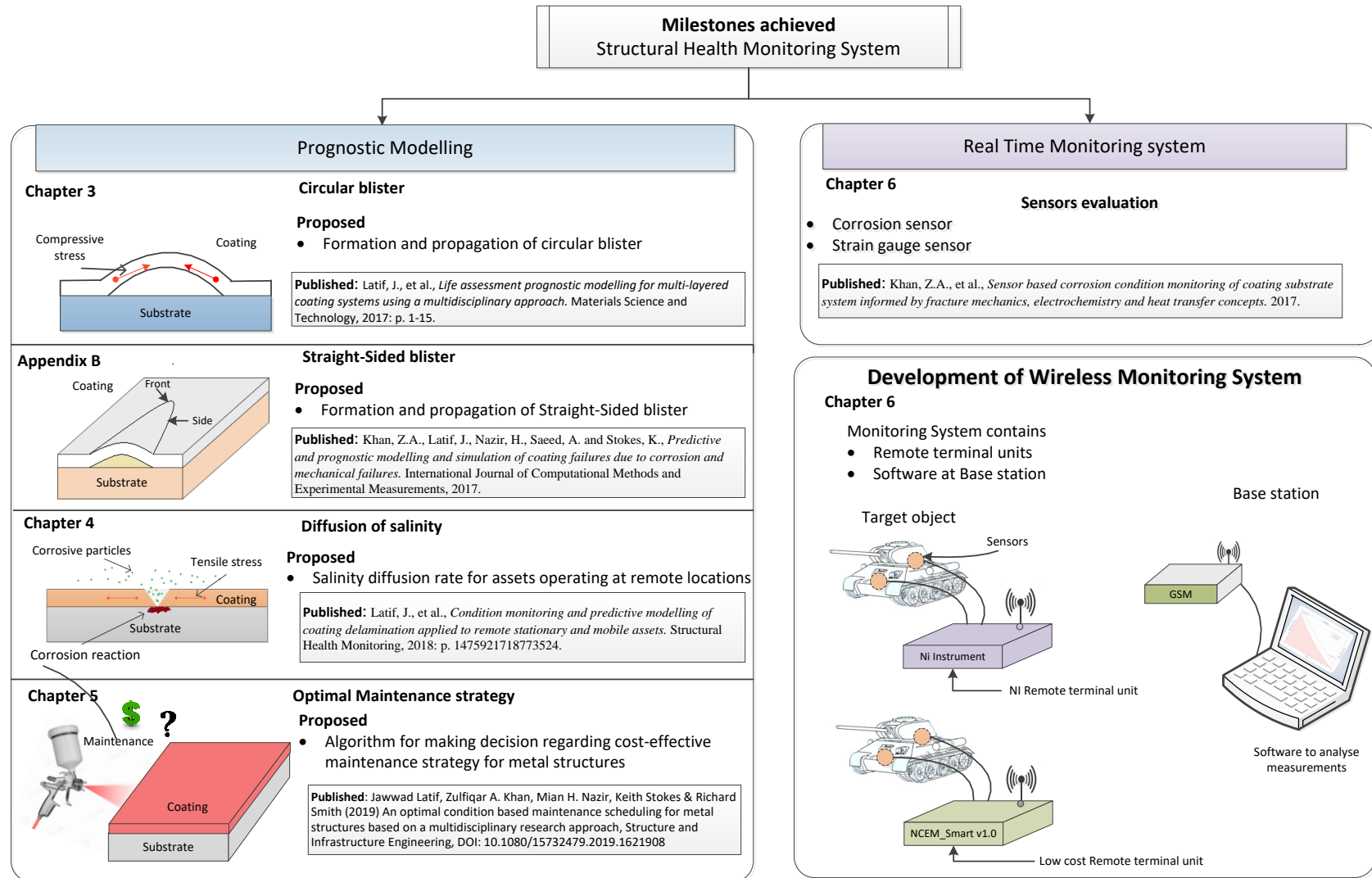


Figure 1.2 Milestones achieved in the project

Chapter 1: Introduction

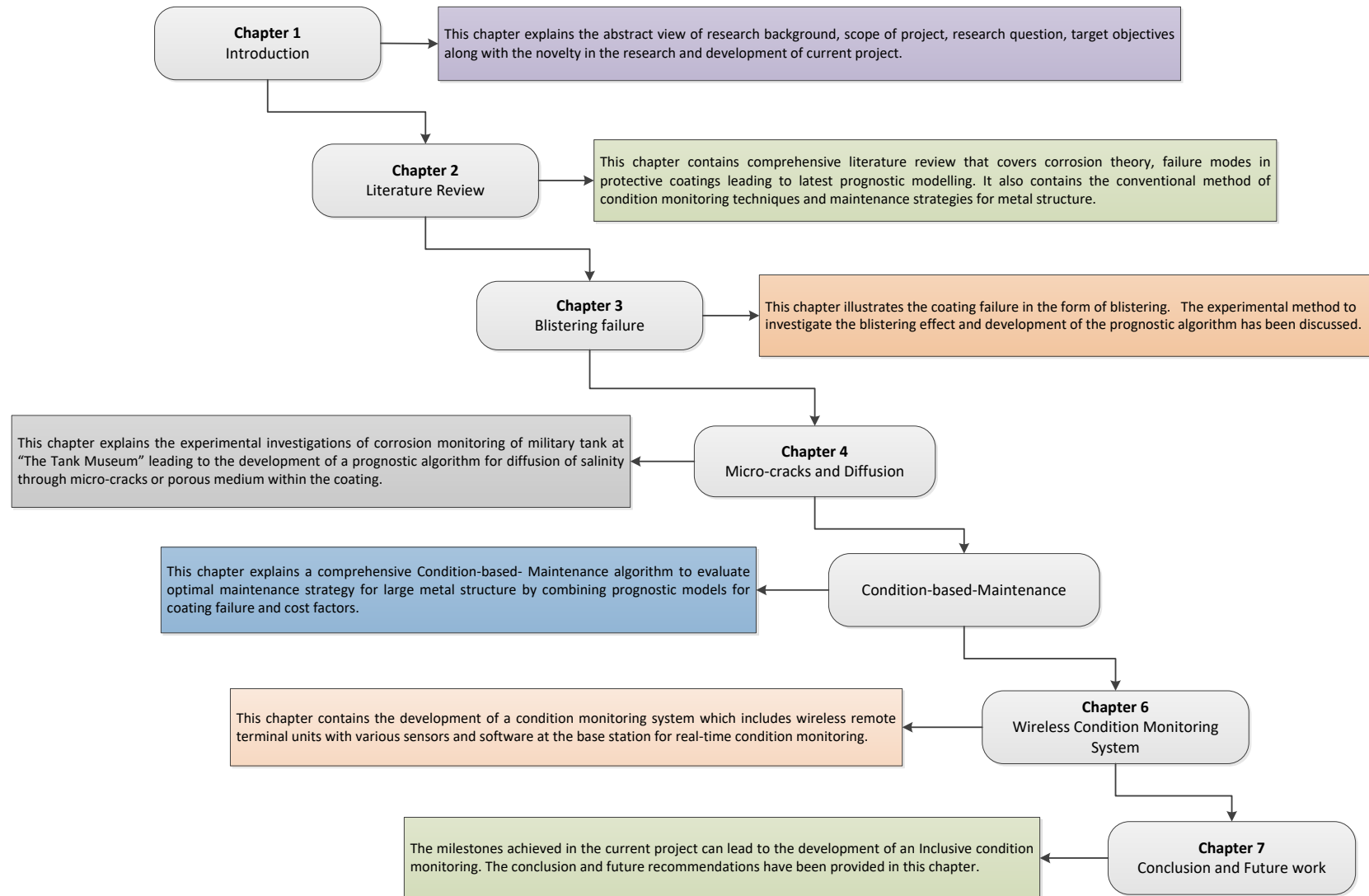


Figure 1.3 Structure of the thesis

Chapter 2: Literature Review

The aim of the current research project is the development of a condition monitoring system to provide efficient maintenance framework for large structures such as military vehicles. The project covers various aspects of the research and development of condition monitoring application and it requires in-depth understanding of failure mechanism, modern prognostic solutions and condition monitoring techniques. Therefore, this chapter provides comprehensive literature regarding these key elements and the chapter has been divided into four sections as shown in Figure 2.1. These four sections include corrosion theory, protective coatings, maintenance strategies and the conclusion resulting from the literature. The basic concepts of corrosion, the complexity in modelling corrosion phenomena and corrosion monitoring techniques have been mentioned in corrosion theory. The complex parameters involved in coating failure mechanism and modern prognostic models for the assessment of coatings are elaborated in Protective coatings section. The cost of maintenance, implications and the strategies practised by organisations are explained in Maintenance strategies. In the end, the research gaps identified in literature in developing condition monitoring system has been summarised in Conclusion.

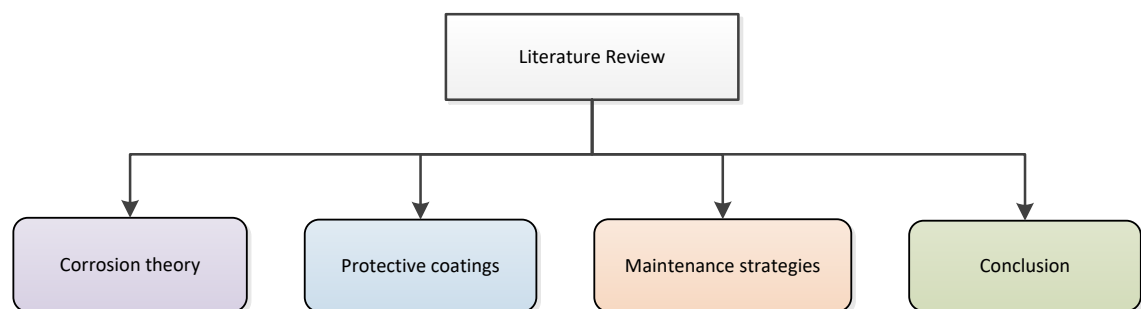


Figure 2.1: Contents of chapter

2.1 Corrosion theory

The corrosion phenomenon is referred to as an electrochemical process that results due to the formation of oxidation-reduction reactions within the metal (Corrosion, 2012). The oxidation and reduction sites appear randomly within metal depending on the crystalline structure of the metal. The presence of electrolyte (usually water), oxygen

Chapter 2: Literature Review

and metal are necessary for the formation of the electrochemical reaction. The loss of electrons at oxidation site results in deterioration of metal strength. The corrosion reaction in iron is shown in Figure 2.2.

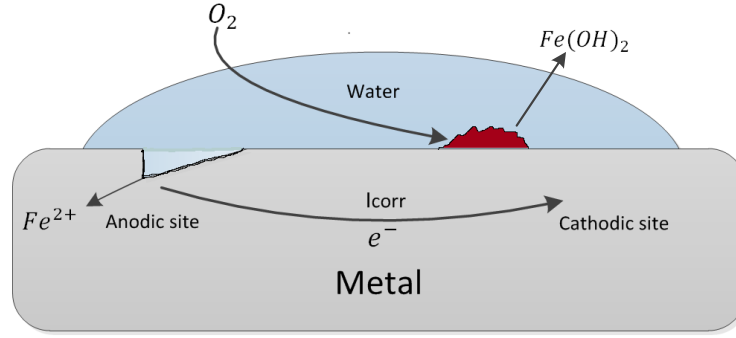
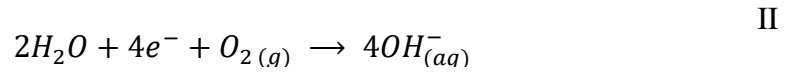


Figure 2.2: Corrosion reaction (Latif, J. et al., 2018a)

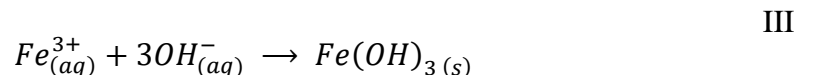
The anodic site produces ferrous (Fe^{+2}) ions by losing electrons as:



The water and oxygen combines with electrons to produce hydroxide OH^{-} ions as:



The reaction of Fe^{+2} ions with OH^{-} ions produces porous rust $Fe(OH)_2_{(s)}$ as follows:



The $Fe(OH)_3$ crystallises into $Fe_2O_3 \cdot H_2O$ which is red brown rust known as rusting. The anodic and cathodic sites can be or cannot be near to each other. The deviation in acidity (pH) will also affect the corrosion process. The release of electron increases at low acidity (pH) which accelerates the corrosion reaction. The presence of pollutants/corrosive elements in electrolyte also results in an increase in the rate of corrosion (Perez, N., 2004; Revie, R. W., 2008). The corrosion phenomena is one of the main factor of deterioration in metal structures including military vehicles which can occur in various modes depending on operating environmental conditions, properties of material, geometry of structures and time of exposure to harsh atmospheric conditions (Saeed, A. et al., 2015). The corrosion in critical components can results in loss of

Chapter 2: Literature Review

strength leading to the destruction of complete structural failure resulting in financial loss and safety hazards. The large numbers of organisations are affected by corrosion including transportation, civil infrastructures, utilities, production and manufacturing (Javaherdashti, R., 2000).

2.1.1 *Reasons for corrosion*

The contact of metal with meteorological factors results in corrosion which can be a small pit or it could escalate over the metal structure leading to partial or complete failure. There could be numerous reasons for corrosion including operating conditions, material of structure, presence of corrosive elements and bio-organism, metal-to-metal contact and temperature. Few of them are explained below:

2.1.1.1 Structure material

The selection of material is based on cost, physical and mechanical properties, so it can be welded, designed into desired shapes conveniently. Therefore, the corrosion resistant property of the material is given secondary priority. Carbon steel is most commonly used material for the manufacturing of metal structures (Keytometals). The use of Aluminium military vehicles has greatly increased in past few decades because of its reduced weight and corrosion resistant properties in order to improve the vehicle mobility, less prone to corrosion in marine applications and convenience in maintenance (Totalmateria, Jul-2004). The cost of steel and aluminium fluctuates depending on demand and global supply but generally, steel is cheaper than aluminium (Hornbacher, A.).

2.1.1.2 Operating conditions

Once the metal structure is installed for service, the operating environmental conditions play a major role in determining the durability of the metal structure. The critical threshold level for relative humidity was found to be 80% (Latif, J. et al., 2018a). Therefore, the corrosion reaction can even occur when the relative humidity is higher than the critical threshold level and the temperature is above than 0°C. The corrosive elements such as the presence of salinity in the atmosphere, pH factor, temperature gradient and other biological organisms influence the corrosion reaction (Corvo, F. et al., 2008). The intrusion of water into the structure and its confinement within the areas

Chapter 2: Literature Review

of structure which are difficult to access to monitor or within components makes the structure susceptible to corrosion damage.

2.1.1.3 Metal-to-Metal contact

The formation of an electrochemical cell for corrosion reaction requires an anodic site to release electrons which are consumed by the cathodic site in the presence of electrolyte that could be the wetness with corrosive elements. This phenomenon can be established through metal-to-metal contact within the structure (Corrosion, 2012; Javaherdashti, R., 2000; Revie, R. W., 2008).

2.1.2 Atmospheric effect on corrosion prediction

Several methodologies have been applied to predict the corrosion damage including mathematical models, probabilistic approaches and neural networks. In the past, the environmental impact on corrosion has been investigated at various geographical locations to propose prognostic solutions. The relation between meteorological factors and corrosion damage was proposed using an exponent of power-law (Feliu, S. et al., 1993a; Feliu, S. et al., 1993b). The researchers attempted to propose a general equation for complex corrosion phenomena that could be applicable to any geographical region. The regression models were proposed after monitoring the corrosion rate of carbon steel at 43 different locations (Revie, R. W., 2008). The corrosion of carbon steel has been investigated in indoor and outdoor environmental conditions of Cuba (Mendoza, A. R. and Corvo, F., 2000). There is no corrosion damage in the absence of water and mathematical models described earlier do not result in zero in the absence of water. Therefore, an appropriate term for time-of-wetness is added in the model along with parameters including sulphur dioxide, salinity and temperature (Klinesmith, D. E. et al., 2007).

The proposed mathematical solutions for prediction of corrosion damage which are mentioned in previous section have not shown significant accuracy. The experimental finding has shown a significant difference in estimation of corrosion damage in diverse environmental conditions. The meteorological factors vary significantly over different geographical locations, therefore the power law function is not an appropriate solution for corrosion prediction in real time scenario especially for structures which are operating remotely and mobile.

2.1.3 *Weather conditions at Dorset*

The large military vehicles at The Tank Museum operate under severe and harsh environmental conditions of Dorset, UK. More than 300 large military vehicles are operating stationary at Museum or remote locations. The military vehicles were subjected to harsh atmospheric conditions during service life in past, therefore various modes of deterioration have been identified. The atmospheric conditions of Dorset, UK where these military operating was analysed through world weather online (Worldweatheronline). The rain is a source of water which is an essential element for corrosion reaction. The number of rainy days per month for three years from 2014 to 2016 at Dorset, UK is shown in Figure 2.3. It can be seen that the Dorset has frequent rain throughout the calendar year. The critical threshold level for humidity to initiate corrosion is 80%. The data for relative humidity recorded for three years shows that most of the time during the calendar year, the level of relative humidity remains greater than the threshold level as presented in Figure 2.4. The entrainment of salt particles begins at wind speed equal to 3 m/s. The average wind speed in Dorset always remained greater than 3 m/s as shown in Figure 2.5. The high deposition of salt particles can be expected over the surface of large military vehicles. The diffusion of salt particles is also one of the major factors that resulted in various modes of corrosion damages in large military vehicles. The Valentine Tank stationed at The Tank Museum is operated for indoor and outdoor activities. The environmental impact of Dorset has resulted in deterioration of Valentine Tank as shown in Figure 2.6.

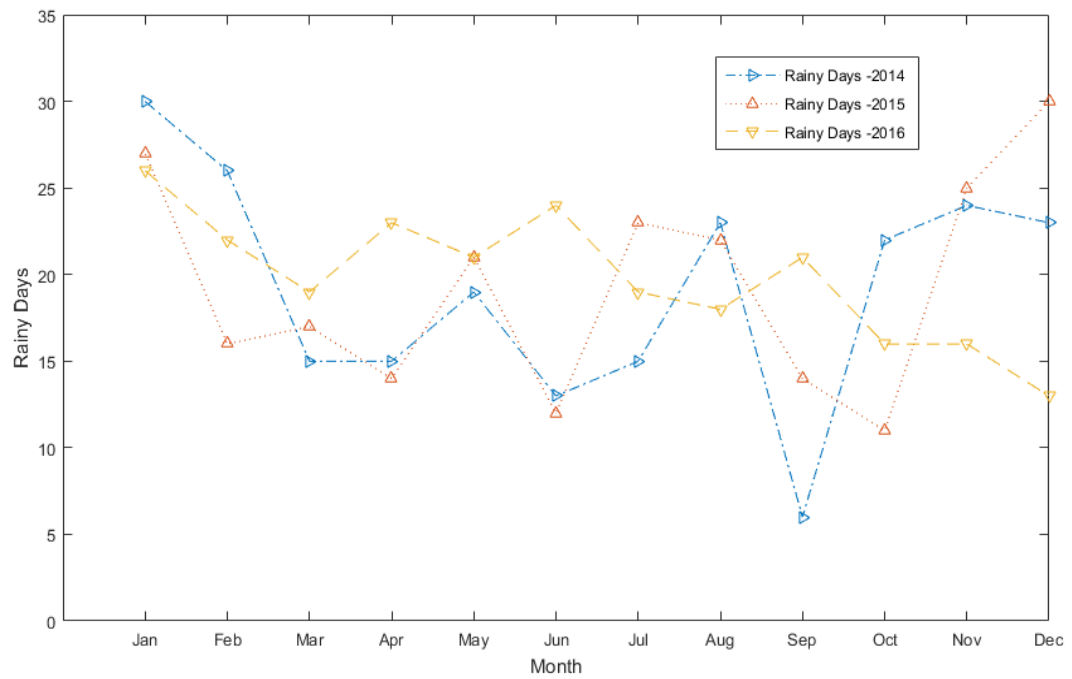


Figure 2.3: Rainy days at Dorset for 3 years (Latif, J. et al., 2018a)

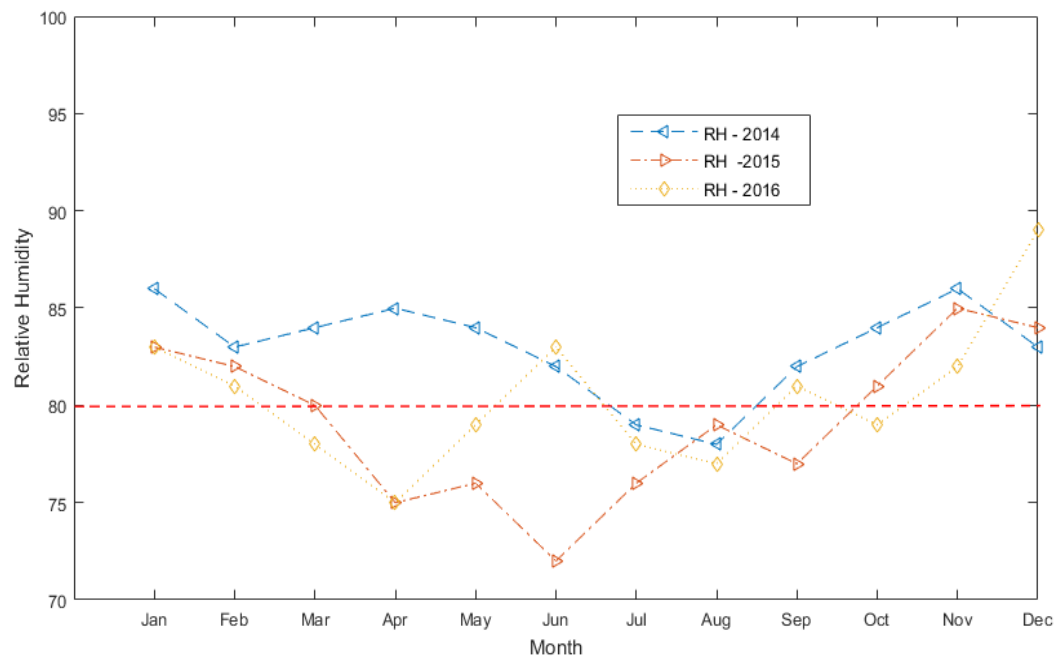


Figure 2.4: Relative humidity at Dorset for 3 years (Latif, J. et al., 2018a)

Chapter 2: Literature Review

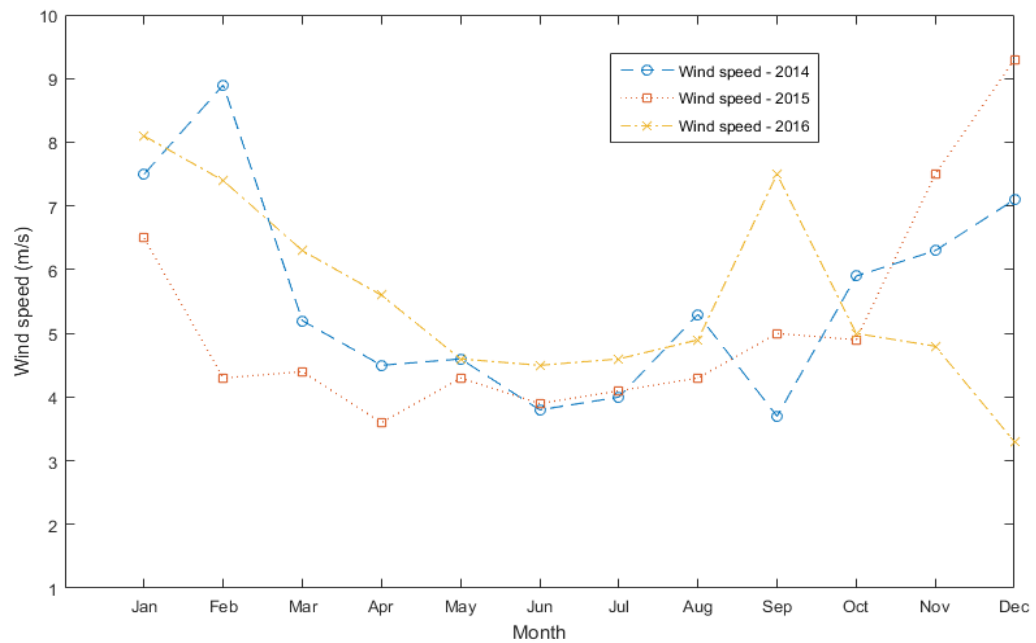


Figure 2.5: Wind speed at Dorset for 3 years (Latif, J. et al., 2018a)



(a) Valentine tank stationed at “The Tank Museum”



(b) Inside condition of Valentine Tank



(c) Inside condition of Valentine Tank



(d) Coating failure at edges of the vehicle structure

Figure 2.6: The Valentine tank at the tank Museum before maintenance

2.1.4 Corrosion monitoring techniques

Corrosion monitoring techniques are generally characterised as direct or indirect techniques. The direct corrosion monitoring techniques measure the change in potential or current resulting from corrosion reaction. While the indirect corrosion monitoring techniques estimate the outcome of corrosion reaction that corrosive elements may exist (Roberge, P. R.). Some of the most commonly used corrosion monitoring techniques are listed in Figure 2.7.

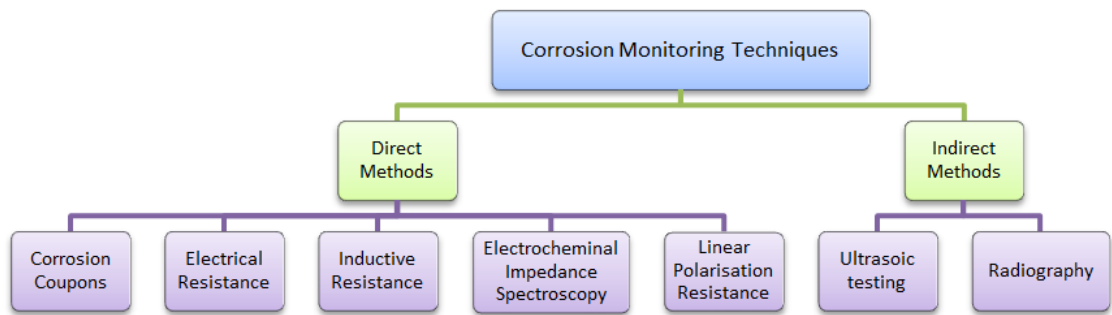


Figure 2.7: Various corrosion monitoring techniques

The corrosion monitoring techniques can be intrusive or non-intrusive. The intrusive method requires access to the structure. The Corrosion Coupons, Electrical Resistance, Inductive Resistance Probe and Linear polarisation resistance techniques are Intrusive, while corrosion potential and chemical analysis techniques are non-intrusive. Every technique has its own advantages and disadvantages. The Corrosion is estimated by measuring weight loss of sample due to corrosion reaction in Corrosion Coupons method. This method is reliable but it requires significant time and it cannot be used for online or real-time corrosion monitoring. The Electrical Resistance method measures the corrosion rate by measuring the change in resistance of the material. The resistance of material changes due to metal loss resulting from corrosion reaction. Although, it can be used to take frequent measurements at any time but it requires calibration with the properties of structural material. The Inductive Resistance technique also works as an Electrical Resistance technique but it measures weight loss through a change in inductive resistance and offers high sensitivity as compared to Electrical Resistance. The Electrochemical Impedance Spectroscopy is a powerful technique for accurate corrosion monitoring by applying signals of low amplitude. Although, it provides very accurate measurement in a controlled environment but it is highly prone to noise in fielded environmental conditions. The Linear Polarisation Resistance technique also provides one of the efficient and powerful methods for direct and on-line corrosion monitoring based on the three-electrode system. It requires relatively clean electrolytic environment for successful measurements. In the current project, the Linear Polarisation Resistance sensors are used for the experimental study of corrosion monitoring and development of condition monitoring system.

The Ultrasonic and Radiography techniques are indirect, non-intrusive and non-destructive corrosion monitoring methods. They can also provide accurate detection and measurement of corrosion rate but these techniques require significant time like Corrosion Coupons method and they cannot be utilised for the online or real-time corrosion monitoring system.

2.2 Protective coatings

Protective coatings are applied to preserve the high-value metal structures from factors causing corrosion damage. They act as a barrier between metal structure and environmental factors to sustain and prolong their functional life for a long period of time. The metal structures without protective coatings are highly receptive towards corrosion which results in minimum functional life. While protective coatings provide an adequate solution to increase the durability of functional life. Coatings play a key role in many applications including thermal sensing instruments, optical filters, electronic semiconductor devices, magnetic recording media, transportation, defence organisations and many other applications. Although, various distinct coatings are utilised for numerous applications but they are generally characterised as Organic and Inorganic Coatings. While the current project is primarily focused on high-value metal structures as military vehicles which are operating at The Tank Museum, Bovington, UK. The organic coatings are applied to a military vehicle to preserve them from harmful factors causing a threat to their structural integrity. The organic coatings are applied to metal structures in liquid form with the help of a brush or spray gun. The protective coatings are also prone to various modes of failure exposing the metal structure to a corrosive atmosphere. The inappropriate pre-treatment and preparation of the metal surface, unsuitable selection of coating material, inappropriate drying process, mechanical damage and lack of protection from corrosive environmental conditions are considered primary reasons for various coating failure modes. These factors individually or in combination results in loss of adhesion between coating and metal substrate (Saeed, A. et al., 2017; Saeed, A. et al., 2015; Saeed, A. et al., 2016). There are several coating failure modes including blistering, micro-cracks, stress corrosion cracking, microbial corrosion and several other failure modes. The interfacial adhesion of coating of military vehicles at The Tank Museum is highly influenced by corrosive

Chapter 2: Literature Review

atmosphere while operating outside in uncontrolled and diverse environmental conditions in Dorset which resulting in coating failure leading to corrosion damage under the coating. In predictive modelling, the current project focussed on developing algorithms based on critical parameters to predict the failure mechanism for proactive maintenance decisions. The blistering effect and corrosion under the coating due to the presence of micro-cracks has been addressed in the current project. The coating failure modes have been elaborated in the following section.

The coating failure at the interface of coating and metal substrate appears in several forms depending on influential parameters. The blistering and micro-cracks are very common coating failure phenomenon that involves a large number of complex parameters. The blistering effect leading to complete disbandment of the coating from the metal substrate, micro-cracks causing corrosion beneath the coating has been found to be one of the major factors in the deterioration of large military vehicles at The Tank Museum (Saeed, A. et al., 2017).

2.2.1 Blistering failure

The blistering defects appear at the interface of coating and metal substrate due to properties are driven by external environmental conditions or the pressure generated from the concentration of impurity ion concentration or spots with loose bonding between coating and metal substrate (Chuang, T. et al., 1997; Hutchinson, J. et al., 1992; Hutchinson, J. W., 1996). The formation of blister depends on various reasons mainly characterised as Osmotic blistering and Non-Osmotic blistering. In Osmotic blistering the coating buckles away because of molecules of moisture which are transferred through a semi-permeable membrane. The coating and metal substrate system operating in an environment with high humidity level are highly susceptible and affected by Osmotic blistering. The contamination of aqueous solution within coating or change in temperature across the coating and metal substrate system plays a major role as driving forces for the propagation of osmotic blisters. The relative humidity level around The Tank Museum always remains high throughout the calendar year, therefore, causing a serious threat to the structural integrity of large military vehicles (Latif, J. et al., 2018a). The blister that occurs due to inappropriate environmental conditions during the application of a coating or due to the properties of the metal substrate is called Non-

Chapter 2: Literature Review

Osmotic blistering. These blisters are also called bubbles which often occur due to an inappropriate thickness of the coating and unsuitable temperature during the drying process. The application of coating over the porous medium of the substrate often traps air or moisture which results in bubbling effect. The non-osmotic blistering (bubbling) effect doesn't always occur over the coating but it can also occur within the coating (Chuang, T. et al., 1997; Machen, J. D., July 12, 2016).

Comprehensive literature is available to explain the complex parameters which are responsible for the formation and propagation of blistering failure. The loss of adhesion in the form of blister at the interface of the coating-substrate system is illustrated in Figure 2.8. Consider the coating buckles away from the substrate due to the pressure 'P' generated by impure ions or compressive stresses within the coating or in a combination of both factors. The thickness of the coating and substrate is shown by 'h' and 's'. The 'δ' is the height of blister and 'R' is the radius of blister. The coating and substrate are isotropic materials. The properties of isotropic materials such as Elastic Modulus and Poisson's ratio show the same behaviour in all directions. The Karman nonlinear plate theory is used to explain the formation of blistering under $R/h \gg 1$ assumption (Ventsel, E. and Krauthammer, T., 2001). The stresses appear within coating when it buckles away from the substrate is known as critical stress (Hutchinson, J. et al., 1992; Hutchinson, J. W., 1996). The threshold value of critical stress at which the blister formation begins is given as:

$$\sigma_c = \left[\frac{h}{R} \right] \left[1.22235 \frac{E}{1 - \nu^2} \right] \quad 2.1$$

According to the relation for critical stress shown above, it depends on the thickness of the coating and also on mechanical properties of coating material including Elastic Modulus 'E' and Poisson's ratio 'ν'. The energy required to produce blister is called as Energy release rate. The relation for energy release rate 'G' is given as following (Hutchinson, J. et al., 1992):

$$G = \left[M^2 + h^2 \Delta N / 12 \right] \left[\frac{6(1 - \nu^2)}{E h^3} \right] \quad 2.2$$

According to Equation 2.1, the energy release rate is also a function of bending moment 'M' and change in resultant stress-force 'ΔN' at the crack tip. The bending

Chapter 2: Literature Review

moment ' M ' describes the bending of the coating layer with respect to the neutral point of axis due to applied moment of force based on the cantilever beam theory concept (Hutchinson, J. W. and Suo, Z., 1991). If the coating has thickness ' h ' and stress or force applied is denoted by σ_f then the resultant bending moment with respect to the neutral point of axis ' x_n ' can be given as:

$$M = \int_0^h \sigma_f (x - x_n) dx \quad 2.3$$

The relation for energy release rate can also be written as following (Nazir, M. et al., 2015d):

$$G = M^2 \left[\frac{6(1 - \nu^2)}{Eh^3} \right] \left[1 + (k\sqrt{\Omega - 1})^2 \right] \quad 2.4$$

The ' Ω ' indicates the de-bonding index which defines the buckling of the coating from the substrate. The de-bonding index is the ratio of stress on the coating and critical stress level as ' $\Omega = \sigma/\sigma_c$ '. If ' $\Omega < 1$ ', it is assumed that there is no blistering and coating-substrate system is in safe condition, If ' $\Omega = 1$ ' then the coating-substrate system is assumed to be in critical situation and ' $\Omega > 1$ ' shows the formation of blister assuming the coating-substrate system in fail state.

The fracture mechanics explains that the growth rate of the blister is driven by mode I and mode II state of stress intensity factor at the crack tip of blister (Irwin, G. R., 1957). The cracks are characterised into three different types of deformation as Opening crack (mode I), Shearing crack (mode II) and tearing crack (mode III) as shown in Figure 2.9 (Maiti, S. K., 2015).

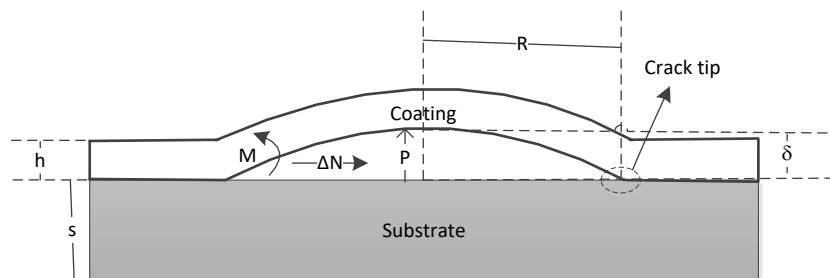


Figure 2.8: Parameters in blister failure

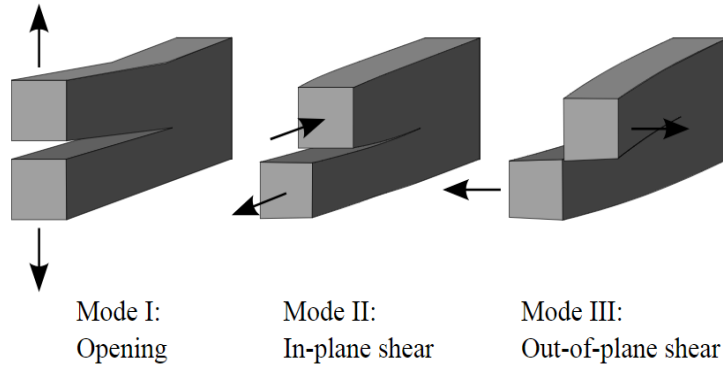


Figure 2.9: Modes of fracture (Roylance, D., 2001)

The coating blister cracks more likely to propagate in opening mode (mode I). Consider stress acting on an object inducing crack as shown in Figure 2.10.

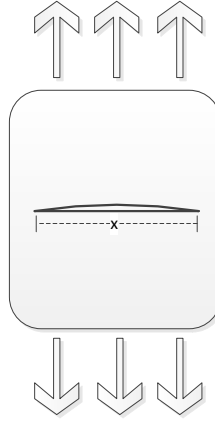


Figure 2.10: Direction of stresses and crack

The stress intensity factor for crack can be defined as (Maiti, S. K., 2015):

$$\sigma = \frac{K}{\sqrt{\pi x}} \quad 2.5(a)$$

$$K = \sigma \sqrt{\pi x} \quad 2.5(b)$$

The intensity of stress at the crack tip is defined by the combination of stress ' σ ' and crack length ' x '. The amount of energy release rate needed to propagate the crack at the interface depends on the ratio of mode II and mode I called as mode mix. The mode mix is defined as:

$$\tan \psi = \frac{K_{II}}{K_I} = \frac{\sqrt{3}(\delta/h) \tan \omega + 4}{\sqrt{3}(\delta/h) - 4 \tan \omega} \quad 2.6$$

Chapter 2: Literature Review

Where ' ψ ' also known as dimensionless phase angle is used to determine the relative proportion of shearing crack (mode II) to opening crack (mode I). The bi-material factor ω depends on Dundur's elastic mismatch parameters ' α ' and ' β ' (Maiti, S. K., 2015; Suo, Z. and Hutchinson, J. W., 1990). The parameters ' α ' and ' β ' denotes the mismatch in extensional stiffness and volumetric stiffness between two bonded materials such as coating and metal-substrate (Hutchinson, J. W. and Suo, Z., 1991; Schmauder, S. and Meyer, M., 1992).

$$\alpha = [\overline{E}_c - \overline{E}_s] / [\overline{E}_c + \overline{E}_s] \quad 2.7$$

$$\beta = \frac{1}{4} \left[\frac{\overline{E}_c(1 - \nu_c)(1 - 2\nu_s) - \overline{E}_s(1 - \nu_s)(1 - 2\nu_c)}{(\overline{E}_c + \overline{E}_s)(1 - \nu_s)(1 - \nu_s)} \right] \quad 2.8$$

The value of ' α ' and ' β ' = 0 if there is no elastic mismatch between coating and substrate and value of bi-material factor ' ω ' is also zero. The parameter ' β ' makes complications in interfacial fracture mechanics application, Hence its value is approximated to zero.

The blister can propagate in the form of a circular shape or it could either propagate as straight-sided shape. The straight-sided blister has two ends labelled as front and side as shown in Figure 2.11. The front and side have different energy release rates which force the blister to propagate in straight-sided shape. The front end has a small energy release rate as compared to side end but the side end experiences very low effective toughness as a result blister crack propagates at the front end. Separate relations for energy release rate have been formulated for the front end and side end as shown in the following equations (Choi, S. R. et al., 1999).

$$G_{side} = G_0 \left(1 - \frac{\sigma_c}{\sigma}\right) \left(1 + 3 \frac{\sigma_c}{\sigma}\right) \quad 2.9(a)$$

$$G_{front} = G_0 \left(1 - \frac{\sigma_c}{\sigma}\right) \quad 2.9(b)$$

The ' G_{side} ' represents the energy release rate at side end and ' G_{front} ' represents the energy release rate at the front end of the straight-sided blister. The ' G_0 ' refers to the steady state energy release rate defined as:

$$G_0 = \sigma^2 h \frac{1 - \nu^2}{2 E} \quad 2.9(C)$$

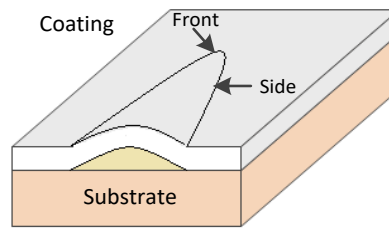


Figure 2.11: Straight-sided blister

The formation and propagation of circular blisters and straight-sided blisters occur due to osmotic or non-osmotic pressure leading to various morphologies including telephone cord such as worm-like and network-like blisters (Chuang, T.-J. et al., 1999). The instability of blisters either circular or straight-sided commonly leads to telephonic cord shape due to high coupling stress greater than critical level. The numerical simulation results show that the propagation of blister in the form of telephonic cord and network-like shapes is highly influenced by stresses within coating and adhesion strength at the interface of the coating-substrate system (Ni, Y. and Soh, A., 2014). According to literature, it can be concluded that the study of the combined effect of diffusion-induced stress and compressive stress can give better understating of blister formation and propagation in the form of different morphologies (Nazir, M. et al., 2015b; Nazir, M. et al., 2015c, 2015e).

The researchers have investigated the complex blistering mechanism to develop a better understanding of the parameters involved in blister formation and propagation in order to propose prognostic models to evaluate the effective performance of protective coatings. The literature review has shown that the blistering mechanism requires incorporation of various complex multidisciplinary parameters for more accurate mathematical modelling. Some of the prognostic models developed for a blistering mechanism in recent years have been shown in Table 2.1. The mathematical models represent the relation for the energy release rate as a function of various parameters. The relation for energy release rate as a function of the height of blister and pressure was developed after investigating the mechanical properties through applied load and shaft displacement (Wan, K.-T. and Liao, K., 1999). The thickness of the coating was incorporated to develop mathematical relations for energy release rate in (Bressers, J. et al., 2000). Another simple relation for energy release rate was derived as a function of blister height, poisson's ratio and pressure (Jahnsen, H., 2001). The mechanical

Chapter 2: Literature Review

property of coating such as Elastic modulus along with blister height and pressure combined to derive a mathematical relation in (Galindo, R. E. et al., 2005; Kappes, M. et al., 2010) for the blistering mechanism. Later on, the fracture mechanics concepts are combined with diffusion parameters to propose a prognostic model in (Prawoto, Y. and Dillon, B., 2012). The configuration of blister along with the strain and stress fields in the outer region of blister has been considered to model adhesion energy for nanomembrane (Ma, Y. et al., 2018). Although numerous mathematical relations were derived but there were still grey areas needs to be addressed.

NCEM research group has investigated various critical parameters through experimental methods to propose comprehensive mathematical models for coating failures. The holistic models are based on electro-chemistry, material science and mechanical parameters. The Khan-Nazir and Khan-Nazir II models are the state-of-the-art inter-disciplinary prognostic models proposed and experimentally validated by NCEM research group. The Khan–Nazir II is the synergistic wear-corrosion model to define delamination of nanocomposite coatings (Nazir, M. H. et al., 2018b). Previously developed synergistic models were valid for only bulk materials. The Khan-Nazir II model can be applied to bulk materials and nanocomposite coatings. It has been formulated on Nano-mechanics, Archard relation and Electro-chemistry concepts to model the combined effects of wear and corrosion.

The Khan-Nazir model proposed in (Nazir, M. and Khan, Z. A., 2017) defines the energy release rate of the coating-substrate system. The formation and propagation of blistering failure is a combined effect of complex parameters. The Khan-Nazir model has been developed by integrating fracture mechanics and diffusion concepts. It formulates the propagation of blister at interfacial crack tip due to the accumulative effect of residual and diffusion-induced stresses. The model is also investigated for various other parameters including coating thickness, thermal mismatch, interfacial toughness and roughness of coating-substrate system. The model also contains mode mix function which is elaborated earlier in this section. The model can be used to estimate the useful life of a part/component of the structure. Therefore, the model is further linked with growth rate in the current project to propose an algorithm that is explained comprehensively in Chapter 3.

Chapter 2: Literature Review

Table 2-1: Prognostic models for coating failure in the recent years

Developer Model	Blistering Model	Reference
Khan-Nazir	$\frac{6(1-v_c^2)}{E_c h^3} \left[M_c^2 + \left(0.2(1+v_c) \sqrt{\frac{1}{0.2(1+v_c) + 0.2(1+v_c^2)} \left(\frac{\rho}{\rho_{cr}} - 1 \right)} \right)^2 \right]$	(Nazir, M. and Khan, Z. A., 2017)
Yong Ma et.al	$1.25 \delta C_1 \left[\frac{\rho_i d_v \alpha_0^2}{d_v \alpha_0^2 + C_1 \alpha^2 \delta} - \rho_e \right]$	(Ma, Y. et al., 2018)
Prawoto et.al	$\frac{\alpha^2 \cdot E^2 \delta}{(1-v_c^2)} (\alpha_{11}^2 \cdot \rho_y^2 + 2 \alpha_{12} \rho_x \rho_y + \alpha_{11}^2 \rho_y^2)$	(Prawoto, Y. and Dillon, B., 2012)
Kappes et.al	$\left(\frac{\rho^4 r^4 E^2}{17.4 h} \right)^{1/6}$	(Kappes, M. et al., 2010)
Galindo et.al	$\sqrt{\rho \cdot C \cdot \delta \cdot E}$	(Galindo, R. E. et al., 2005)
Volinsky et.al	$\frac{\rho \cdot \delta \sqrt{(1-v_c^2)}}{2f}$	(Volinsky, A. et al., 2002)
Jahnsen et.al	$\frac{\rho \sqrt{(1-v_c^2)}}{2\delta}$	(Jahnsen, H., 2001)
Bressers et.al	$\frac{\rho \sqrt{(1-v_c^2)} h}{2}$	(Bressers, J. et al., 2000)
Wan et.al	$\frac{E}{2} \sqrt{5 \cdot C \cdot \rho \cdot \delta}$	(Wan, K.-T. and Liao, K., 1999)
<p>$\rho = \text{blister pressure}$; $\delta = \text{blister height}$; $E = \text{young's modulus}$; $r = \text{blister radius}$; $d_v = \text{depth of cavity}$</p> <p>$\rho_{cr} = \text{critical pressure}$; $\rho_i = \text{Initial pressure}$; $\rho_e = \text{ambient pressure}$; $\alpha_0 = \text{radius of cavity}$</p> <p>$M_c = \text{bending moment of film substrate system due to blistering}$; $C_1 = \text{Volume coefficient}$</p> <p>$h = \text{film thickness}$; C and f depends on the geometry</p>		

2.2.2 *Micro-cracks and stress factor*

Protective coating layer applied on metal structures acting as a barrier from external influential parameters to avoid corrosion also breaks down in the form of micro-cracks within the coating. The corrosion reaction is an electrochemical process but this process is also highly affected by materialistic and mechanical properties of the coating and metal-substrate system (Zhao, X. et al., 2013). The development of micro-cracks within the coating breaks the protective layer. These micro-cracks become the passage for corrosive elements to pass through and react with metal-substrate and initiate corrosion reaction (Holmberg, K. and Mathews, A., 1994). The developments of residual stresses are responsible for the contraction and expansion of micro-cracks. The behaviour of micro-cracks was investigated through experimental findings. The stresses within coating are characterised as intrinsic and extrinsic stress. The intrinsic stresses develop due to the defects or dislocation in the coating and extrinsic stress depends on adhesion of the coating and metal-substrate system. The mismatch in coefficient of thermal expansion between the coating and metal-substrate materials induces compressive or tensile stresses (Hutchinson, J. W., 1996; Totten, G. E., 2002). The relation for stress is given as follows:

$$\sigma = E(\varepsilon - \alpha\Delta T) \quad 2.10$$

Where ' σ ' is the stress resulting from Elastic modulus ' E ', strain ' ε ', coefficient of thermal expansion ' α ' and temperature gradient ' ΔT '. The product of coefficient of thermal expansion ' α ' and temperature gradient ' ΔT ' drives the stress behaviour within the coating. The positive temperature gradient ($\Delta T > 0$) results in compressive residual stress causing contraction within coating micro cracks resulting in decrease in the diffusion of corrosive elements. Although, the decrease in diffusion of corrosive elements also reduces the diffusion induced stress but compressive residual stress tends to increase. When compressive residual stress is higher than a certain level where the coating particles cannot further contract, the coating layer begins to lose adhesion from metal-substrate and buckles away resulting in the formation of a blister. The blistering effect results in an increase in diffusion induced stress by opening contracted micro cracks wider (Hutchinson, J. W., 1996; Liu, X. and Frankel, G., 2006; Nazir, M. et al., 2015b).

On the contrary, the negative temperature gradient ($\Delta T < 0$) results in the development of tensile stress within coating causing expansion of micro-cracks. The expansion of micro-cracks allows corrosive elements to diffuse resulting in increasing diffusion-induced stress. The tensile stress and diffusion-induced stress are driven in the same direction due to the negative temperature gradient exposing metal-substrate. The increase in tensile stress causing widening of micro-cracks and allowing corrosive elements to diffuse into the coating and metal-substrate system to initiate corrosion reaction. The increase in exposure of metal substrate accelerates the corrosion damage at the interface of coating and substrate (Hutchinson, J. W., 1996; Nazir, M. et al., 2015b).

2.2.2.1 Diffusion of Corrosive elements

According to research findings in the past, the development of the porous region or micro-cracks allows corrosive elements to diffuse into the coating and metal-substrate system results in corrosion damage under the coating as shown in Figure 2.12. The corrosion rate is directly proportional to the diffusion of corrosive elements into the coating and metal-substrate system (Riemer, D. P. and Orazem, M. E., 2005; Zhao, X. et al., 2013). The corrosive elements from the surrounding environment accumulate over the coating and metal-substrate system such as the salt particles in the air deposits over metal structure (Meira, G. et al., 2007). These salt particles diffuse through micro cracks or porous medium resulting in corrosion reactions.

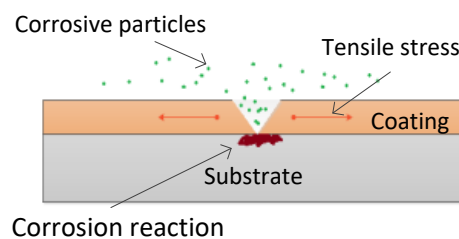


Figure 2.12: Diffusion of salt particles and corrosion reaction

The formation of electrochemical cells at the interface of the coating and metal-substrate system also decreases the strength of bonding between coating and metal (Grundmeier, G. et al., 1998; Grundmeier, G. et al., 2000; Stratmann, M. et al., 1994). The coating starts acting like a jelly medium where the electrochemical cells under the coating are active (Fürbeth, W. and Stratmann, M., 2001; Grundmeier, G. et al., 2000). The diffusion rate of corrosive elements depends on various factors including the

Chapter 2: Literature Review

concentration of corrosive elements, relative humidity, temperature and exposure time of the structure. In the current research, the accumulation of salinity and its diffusion has been addressed. The rate of change of concentration of salt particles over time depends on migration, convection and diffusion (Bastidas-Arteaga, E. et al., 2011).

$$\frac{\partial S}{\partial t} = \text{diffusion} + \text{migration} + \text{convection} \quad 2.11(a)$$

$$\frac{\partial S}{\partial t} = \frac{1}{n} \sum_{S_{en=1}}^n [D_{A_s}(T, RH, t) \nabla S_e + z D_{A_s} S_f \nabla \phi + j_m S_f + R_s + S_s] \quad 2.11(b)$$

The ' $\partial S / \partial t$ ' is the rate of change of salt particles over time depending as a summation of diffusion, migration and convection. The convection and migration factors are neglected in current research. The ' T, RH, t ' represents temperature, relative humidity and time of exposure, respectively. The ' D_{A_s} ' represents the diffusion coefficient which defines the amount of salt particles diffused into the coating and metal substrate system. The diffusion coefficient in a porous medium is lower by a order of two as compared to the diffusion coefficient in aqueous medium (Nazir, M. and Khan, Z. A., 2017).

$$D_{A_s} = \left[\frac{1}{D_{S,STA} f(T) f(RH) f(t)} \right]^2 \quad 2.12$$

In order to predict the corrosion damage under the coating, the accumulation of the concentration of salt elements and the factors driving the diffusion process needs to be addressed. The concentration of salt depends on the speed of wind (Levin, Z. and Cotton, W. R., 2008) and a diffusion phenomenon depends on meteorological parameters including temperature, relative humidity and time of exposure. The speed of wind is a very diverse factor which varies from time to time and from location to location. Furthermore, the quantity of salt particles in the atmosphere also varies from location to location such as the atmosphere of the coastal region contains a high amount of salt particles as compared to the atmosphere in the non-coastal region. The accumulation of hygroscopic particles on the solid surface structures has been described by the concept of aerosol physics. The wind speed can be considered as key parameters to determine the amount of deposition rate on the solid surfaces. The wind speed at

3ms^{-1} is considered a threshold level at which entrainment of marine aerosol initiates (Morcillo, M. et al., 2000).

2.3 Maintenance of structures

The maintenance is characterised as the actions carried out to restore or retain the structural systems to a sustainable condition. The condition of structures depends on operating condition, material, mechanical and physical characteristics (Harris, S. et al., 2006; Nielsen, J. S. and Sørensen, J. D., 2018; Prajapati, A. et al., 2012; Tam, C. and Stiemer, S., 1996a). The component failure or structural breakdown is more likely to take place during operations. The delay or halt in services causes huge financial loss to organisations in the form of direct and indirect cost. The maintenance of structures is necessary in order to ensure their availability and to maintain service life for a long time. The maintenance includes various activities which are also associated with cost. The scheduled recoating maintenance is applied to a large number of military vehicles at The Tank Museum without the consideration of cost implications. The maintenance of critical equipment in the defence industry is an essential and important activity for their availability.

2.3.1 *Cost of corrosion and maintenance*

The maintenance has been daunting and expensive activity in the organisation for maintainability of critical and high-value structures. Various maintenance methodologies are applied to minimise system failures. In the past decades, the financial impact on capital budget resulted from corrosion damage and associated maintenance activities have been estimated. The cost of corrosion and maintenance includes the accumulative cost of inspections, corrosion prevention methods, maintenance activities, research and development for optimising solutions. According to the latest findings, the corrosion results in 3.4% of direct cost to capital budget and indirect cost make this percentage twice (Inspectioneering, 2016). The large numbers of organisations are affected by the consequences of corrosion including automotive, utilities and especially defence sector. The military spends around 23 % of its budget on corrosion and maintenance related activities (Herzberg, E. F. et al., 2006). The efficient implementation of corrosion prevention and maintenance techniques can result in a cost

Chapter 2: Literature Review

saving of around 15% to 35%. The Logistic management Institute (LMI) government consulting organisation estimates the annual cost of corrosion and associated maintenance activities. The applied methodology has been authorised by Corrosion Prevention and Control Integrated Team (CPCIPT). It considers three schemas for cost calculation as mentioned in Table 2.2. Several reports have been issued by LMI organisation on the annual cost of corrosion of ground, marine and air vehicles (Herzberg, E. F. et al., 2006).

In 2016, the LMI has published the latest stat on the annual cost of corrosion for military vehicles. The equipment of army cost around \$3.1 billion of the amount which is about 15% of total expenditure associated with maintenance (Hertzberg, E., 2016; Herzberg, E. F. et al., 2006). The activities related to maintenance including inspections, washing, cleaning, recoating, drying and other surface treatments incur the highest corrosion cost. The research findings have shown the dependency of deterioration of structures on multidiscipline parameters. Therefore, appropriate selection of recoating strategy for individual structure can results in cost reduction through minimising maintenance activities.

Table 2-2: Factors considered for estimating the cost of corrosion

Schema	Description
1.	Depot: The corrosion related cost on maintenance of depot where vehicles are stationed.
	Field: The cost of corrosion maintenance at field level.
	Outside normal reporting: The cost of corrosion related maintenance not considered in conventional maintenance reporting scheme.
2.	Corrective: The cost of maintenance of existing corrosion issues.
	Preventive: The cost of a proactive measure for possible corrosion threats.
3.	Parts: The direct corrosion cost of removable parts.
	Structure: The direct corrosion cost of the structure.

2.3.2 Maintenance strategies

Industrial organisations apply various maintenance strategies to maintain their structures. They are also continuously looking for optimal and efficient strategies to

Chapter 2: Literature Review

improve operational activities. The optimisation framework for maintenance can result in cost savings as the activates associated with recoating maintenance incur most of the corrosion cost according to LMI findings (Herzberg, E. F. et al., 2006). Maintenance strategies are normally classified into following:

- Corrective Maintenance (CM)
- Time-based-Maintenance (TBM)
- Condition-based-Maintenance (CBM)

Corrective Maintenance is considered a most inefficient strategy for critical structures as the failure is rectified after detection. Time-based-maintenance is carried out after fixed time intervals and irrespective of the condition of the structure. The frequent inspections are not required in TBM but this strategy is inefficient for the structures which are subjected to diverse atmospheric and operating conditions (Au-Yong, C. P. et al., 2013). Condition-based-Maintenance strategy is most commonly implemented in organisations for critical and high-value structures. CBM modelling is based on diagnosis, prognostic models, operational activities of structures, data mining of huge measurements collected from sensors, Artificial intelligence and maintenance history as shown in Figure 2.13 (Prajapati, A. et al., 2012). The CBM can be further classified into three categories as Discrete-state deterioration, Proportional hazard model and Continuous-state deterioration (Alaswad, S. and Xiang, Y., 2017). The Markov and Semi-Markov process are types of Discrete-state deterioration models. The Markov process predicts a future event of breakdown based on only the current situation while Semi-Markov process also includes the previous incidents. The common Continuous-state deterioration models include the Gamma process, Inverse Gaussian process and Brownian process are also practised for maintenance in various industrial organisations (Si, X.-S. et al., 2011; Ye, Z. S. and Xie, M., 2015).

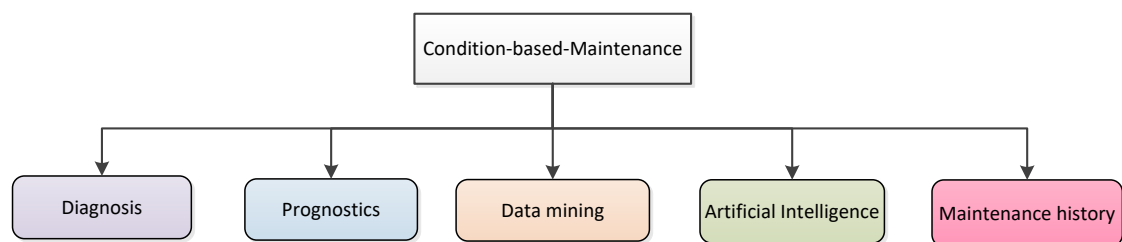


Figure 2.13: Methods involved in Condition-based-Maintenance

The recoating maintenance activities account for the highest cost of corrosion and maintenance. Therefore, the maintenance optimisation framework for recoating of structures can result in significant cost saving. The latest research findings have addressed the effect of multidisciplinary parameters in the deterioration process as discussed in previous sections of this chapter. The conventional stochastic CBM models do not include the multidisciplinary parameters. The appropriate selection and monitoring of these multidisciplinary parameters can result in more accurate and cost-effective prognostics for CBM.

2.4 Conclusion

The Condition-Based-Maintenance is considered the most efficient and accurate method of maintaining the critical and high-value structures. The maintenance decisions within CBM are based on diagnosis, prognostics and data mining. The latest research findings have identified various parameters that have an impact on the service life of structures. The inclusion of those parameters in prognostics can improve the efficiency of CBM. The conventional methods of maintenance do not consider the complex parameters of structural deterioration.

- The coating failure in the form of blisters is very common deterioration mechanism. The formation of blister failure due to the combined effect of diffusion-induced stress and residual stress has been modelled in literature. According to recent experimental investigations, the de-bonding driving at the coating-substrate interface is driven by the development of stresses. The models for the propagation of blister failure is also present in literature but it does not include the effect of diffusion-induced stress and residual stress. Therefore, the algorithm is required to incorporate the effect of stresses for estimation the rate of blister propagation.
- The coating failure in the form of micro-cracks occurs due to poor coating application or mechanical damage. The variation in environmental conditions results in the opening of micro-cracks and also diffusion of corrosive elements through these micro-cracks. The high-value structures such as military vehicles at The Tank Museum operate stationary at remote locations in harsh

environmental conditions of Dorset. The presence of salt particles in atmosphere accumulates over the surface of military vehicles. The diffusion of salt particles through micro-cracks results in corrosion beneath the coating. The deposition rate of salt particles depends on wind speed which makes the prediction of the diffusion rate of salt particles for vehicles operating in diverse conditions more challenging. The model is required to estimate the diffusion of salt particles depending on the speed of wind for the structures operating at remote locations.

- The coating failures in the form of blisters and micro-cracks lead to the breakdown of the protective barrier exposing metal structure to atmospheric conditions. The recoating maintenance is required to retain the condition of the structure. The recoating maintenance includes various activities such as drying, washing, surface treatment and inspections. The recoating maintenance incurs high cost in the defence industry. The research findings have shown that the accurate prediction and appropriate selection of coating-substrate system specifications can improve performance. The increase in performance can result in fewer inspections and recoating maintenance. Another factor is the recoating maintenance strategy depending on size and geometrical configurations of an individual structure. The appropriate selection of recoating maintenance strategies depending on the surface area to be recoated, size of the structure and its part can also result in cost savings. The Condition-Based-Maintenance algorithm is required to incorporate the complex parameters and surface area of the individual structure to be recoated to evaluate optimal recoating maintenance strategy.
- One of the most important aspects of efficient Condition-Based-Maintenance for structures operating at remote locations is the collection of real-time parameters. The wireless condition monitoring system is required to acquire real-time measurements. The developed algorithms are based on temperature, humidity, corrosion reaction and development of stresses in the coating. Therefore, the sensor suite in wireless monitoring system should monitor these critical parameters for efficient prediction and future research objectives.

Chapter 3: Blistering Failure

According to the literature, the effect of multidisciplinary parameters in blistering failure makes the structural prognostics more challenging. The blistering failure results in debonding of the coating from the metal substrate that leads to exposure of the metal structure to the surrounding environment. The blistering is one of the most common modes of coating failure found in large military vehicles at ‘The Tank Museum, UK’. An efficient condition monitoring system for maintenance of structures requires accurate prognostics of coating failures. Although the existing models do incorporate critical factors, the implementation issue of these models in condition monitoring for maintenance of structures in industries still needs to be addressed. The prognostic algorithm for the formation and propagation of blistering failure has been proposed in the chapter and elaborated as shown in Figure 3.1

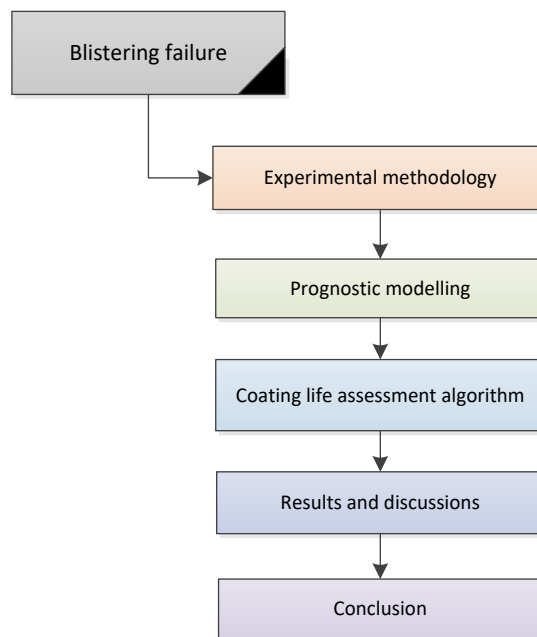


Figure 3.1: Contents of the chapter

An algorithm for the formation of blister and propagation is proposed to evaluate the effective adhesion life of the coating-substrate system. The adhesion depends on complex multidisciplinary parameters including mechanics, material science and fracture mechanics concepts (Hutchinson, J. et al., 1992; Hutchinson, J. W. and Suo, Z., 1991; Jahnsen, H., 2001; Ni, Y. and Soh, A., 2014; Prawoto, Y., 2013; Volinsky, A. et

Chapter 3: Blistering Failure

al., 2002). The de-bonding driving force defines the adhesion between coating and substrate has been formulated. The proposed algorithm indicates the formation of blister by classifying safe, critical and fail states. After the formation of blisters, the algorithm also classifies the conditions for blister growth and estimates the speed of growth rate.

3.1 Experimental methodology

The accelerated corrosion testing has been performed in the laboratory for blistering failure analysis. The experimental methodology includes various steps including sample preparation followed by pre-experimental analysis to analysis the surface roughness and thickness of the coating. After applying accelerated corrosion testing the surface roughness was again measured for blistering analysis.

3.1.1 Sample preparation

The substrate samples of Structural steel were used for experimental investigation. The Structural steel is used in a wide range of applications due to its guaranteed strength and welding properties. It offers various grades with specific chemical and mechanical properties depending on chemical composition. The chemical composition is structural steel S275 is shown in Table 3.1. Three samples of Structural steel S275 were coated using the spray gun method. The Elastic modulus and the coefficient of thermal expansion of S275 are 210 GPa and $12 \times 10^{-6}/^{\circ}\text{C}$, respectively (Gilber, N., May 11 2012).

Table 3-1: Composition of Structural steel S275

Particles	C%	Mn%	P%	S%	Si%
Quantity	0.25 max	1.60 max	0.04 max	0.05 max	0.05max

The red-oxide primer and alkyd coatings which are used in ‘The Tank Museum’ for reacting maintenance of military vehicles were applied on samples. The red-oxide primer coating on the metal surface acting as base coat provides protection from corrosion reactions. The top coat can be applied over re-oxide primer coating which is mostly for decorative purposes. The sample surface was polished with an emery paper of grit size 200 to produce roughness. The 3D Optical Surface Profilometer was used to measure the roughness of surface before coating. The Turco 4215 NC-LT solution was used to clean samples after polishing. The samples were rinsed with de-ionised water

Chapter 3: Blistering Failure

and dried in cold air. The conventional spraying gun method was used to apply red-oxide primer coating over the surface of substrates. The fluid tip of the spray gun and working pressure were 1.4mm and 3.5 bar, respectively. After applying the red-oxide primer coating, the samples were kept to dry for 24 hr at 293.15K before applying the next coat. The Elastic modulus and the coefficient of thermal expansion of red-oxide primer are 6.14 GPa and $21.6 \times 10^{-6}/^{\circ}\text{C}$, respectively (Nazir, M. et al., 2016b). Three samples were prepared as shown in Figure 3.2. The sample 1 was coated with a single layer of red-oxide coating which is labelled as mono-layered sample. The sample 2 was coated with base coat of red-oxide primer and top coat of Alkyd. The sample 3 was coated with two layers of red-oxide and a single layer of alkyd coating. The samples 2 and 3 are labelled as Bi-layered and Tri-layered, respectively.

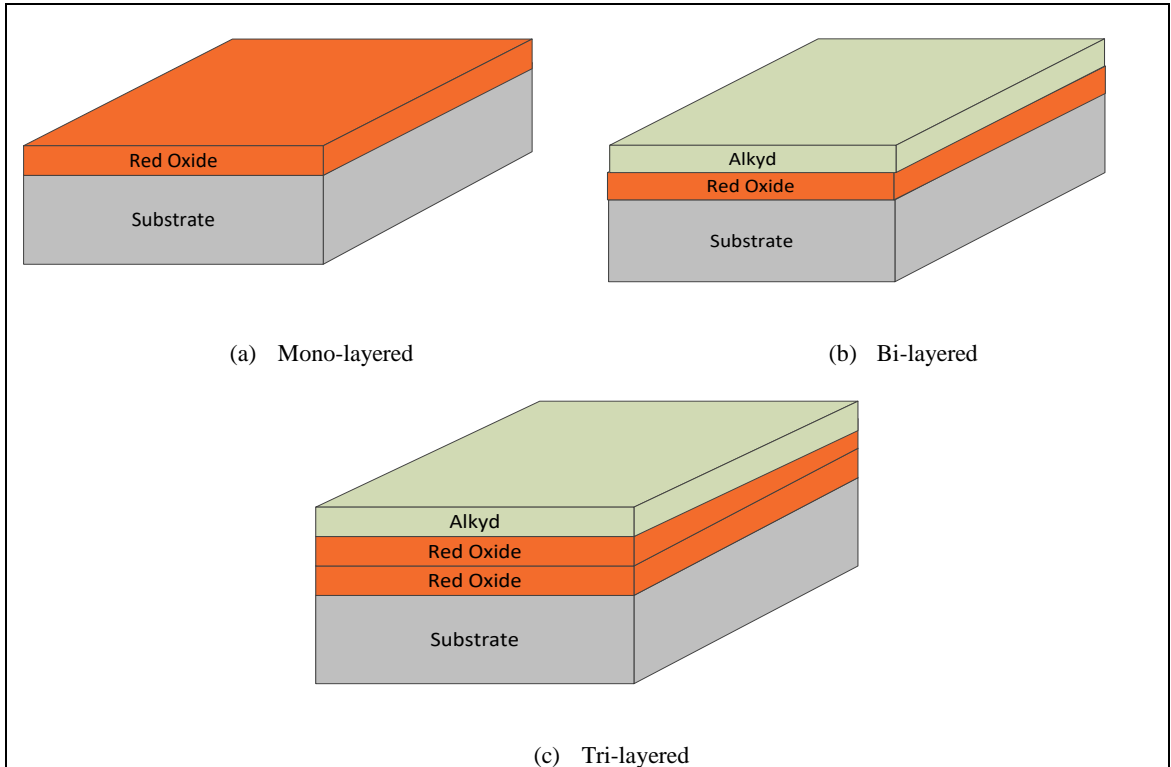


Figure 3.2: Coating layers applied to samples

3.1.2 Pre-Experimental analysis

The roughness of the samples surface was measured before and also after applying the coating. One of the novel non-contact optical methods of measuring surface profile is White Light Interferometry as shown in Figure 3.3. It can measure surface profiles of 3-D structures which vary between tens of nanometres and centimetres. MetroPro 8.3.3

Chapter 3: Blistering Failure

is used to analyse surface profiles. The pits, grooves, volume loss, size and depth of cracks can also be measured using White Light Interferometry. The roughness was measured on multiple locations on each sample. The average value of roughness is given in Table 3.2. The surface roughness of sample Bi-layered before coating was highest and remained highest after the coating also as compare to Mono-layered and Tri-layered.



Figure 3.3: White Light Interferometry

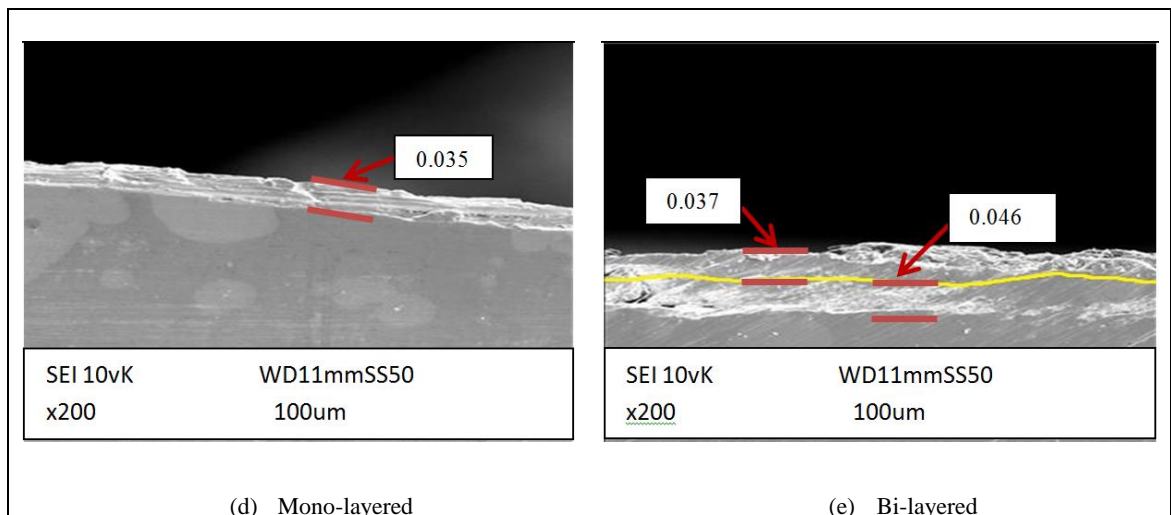
The thickness of the coating-substrate system was measured through Scanning Electron Microscopy (SEM). The microstructural characteristics of the material can be measured using SEM in high resolution. The finely focused beam of electrons scans points by point of the surface of the material which is classified as secondary electrons and back-scattered electrons. The SEM images are produced through secondary electrons that emits from the surface with low energy and grain structures are determined through back-scattered that emits deep from the sample with high energy (Goldstein, J. I. et al., 2017; Hall, C. E., 1953). The state-of-the-art JSM-601 PLUS/LV SEM model as shown in Figure 3.4 was used to measure the thickness of the samples. The cross-sectional SEM images taken to measure the coating thickness of all three

Chapter 3: Blistering Failure

samples are shown in Figure 3.5. The values of the coating thickness of all three samples are listed in Table 3.2. The Mono-layered sample has a minimum thickness of red-oxide primer coating layer of 0.035mm. The top coat was also applied to the Bi-layered sample which has coating thickness of 0.083. In the Bi-layered sample, the thickness of red-oxide primer coating layer and top coat layer are 0.046mm and 0.037mm, respectively. The Tri-layered sample has highest coating thickness of 0.125mm as it contains two layers of red-oxide primer and one layer of top coat. In the Tri-layered sample, the thickness of red-oxide primer coating layers and the top coat layer are 0.086mm and 0.039mm, respectively.



Figure 3.4: Scanning Electron Microscopy



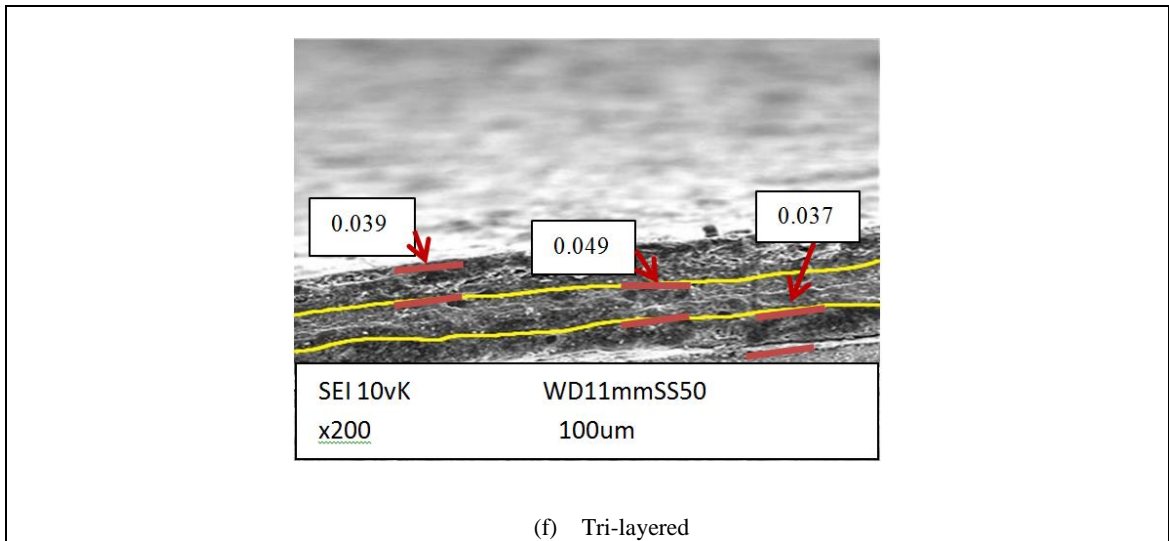


Figure 3.5: The cross-sectional SEM images for coating thickness (Latif, J. et al., 2018b)

Table 3-2: Coating thickness and roughness of samples (Latif, J. et al., 2018b)

Samples	Average roughness (Ra)		Coating Thickness mm
	Pre-coating	Post-coating	
Mono-layered	0.328	1.63	0.035
Bi-layered	0.488	1.72	0.083
Tri-layered	0.384	1.53	0.125

3.1.3 Immersion Test

The accelerated corrosion environment is provided by submerging the test samples in water to evaluate the performance of the material in laboratory experimentation. The degree of acceleration can be increased by increasing temperature, pressure or electrolyte in liquid solution. The presence of salt particles in the atmosphere is the primary source of salinity over the surface structure which is operating at remote locations. The salt particles increase the rate of corrosion reaction and diffusion-induced stresses (Lim, C. et al., 2012; Lin, S. and Hwang, C. C., 1995; Nazir, M. et al., 2016b). The temperature gradients and contamination of water-soluble salt particles are driving forces for Osmotic blistering (Machen, J. D., July 12, 2016).

Chapter 3: Blistering Failure

The corrosive aqueous solution of 5 Molar (M) Sodium chloride (NaCl) was prepared in distilled water. The solution was stirred constantly to completely dissolve the salt particles. The Mono-layered, Bi-layered and Tri-layered samples were degreased with acetone before submerging in an aqueous salt solution as shown in Figure 3.6. The samples in salt solution were kept in an environmental chamber as shown in Figure 3.7 to provide temperature between 320K to 350K. The samples were monitored continuously until circular blisters are visible through magnifying glass.

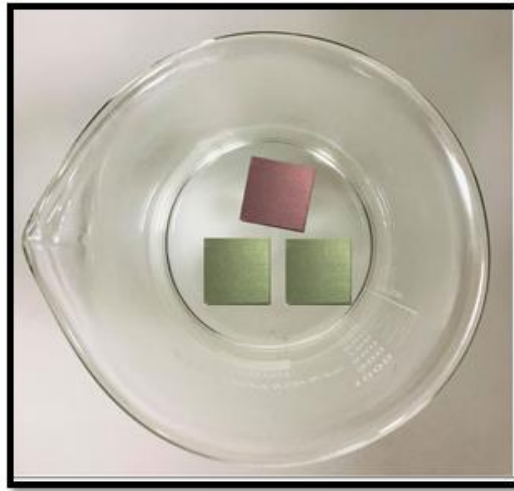


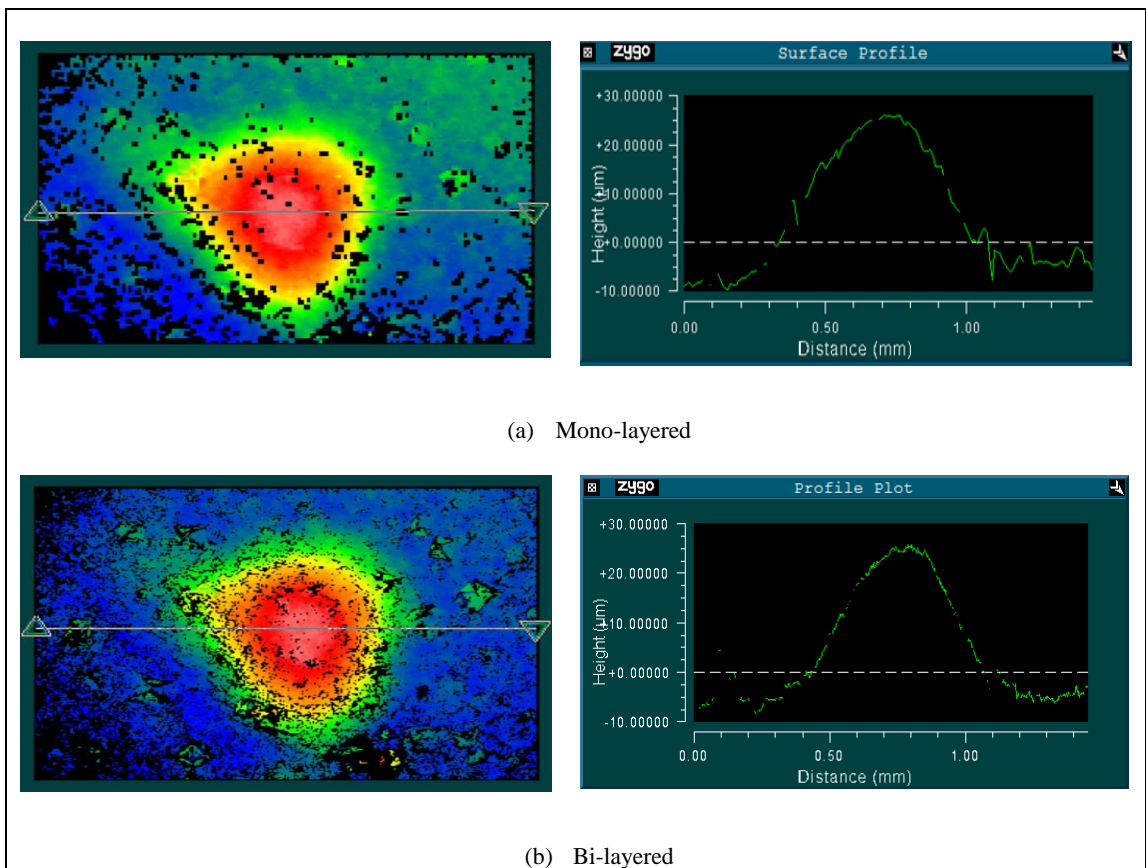
Figure 3.6: Coated samples inside aqueous salt solution



Figure 3.7: Environmental chamber

3.1.4 Post-Experimental Analysis

The samples were carefully taken out from the environmental chamber after visually inspecting the blistering failure on all three samples. The wet samples were dried at very low cold air. The samples were carefully placed on the stage of White Light Interferometry to scan surface profile for all three samples. Multiple blisters have been observed on all three samples at various locations but no significant variations have been found in the size of the average blister. The amplitude of several blisters was measured on several stages during the immersion test and average blister form each sample is shown in Figure 3.8. The highest amplitude of blisters developed on Mono-layered coated sample has been found as compared to the other two samples.



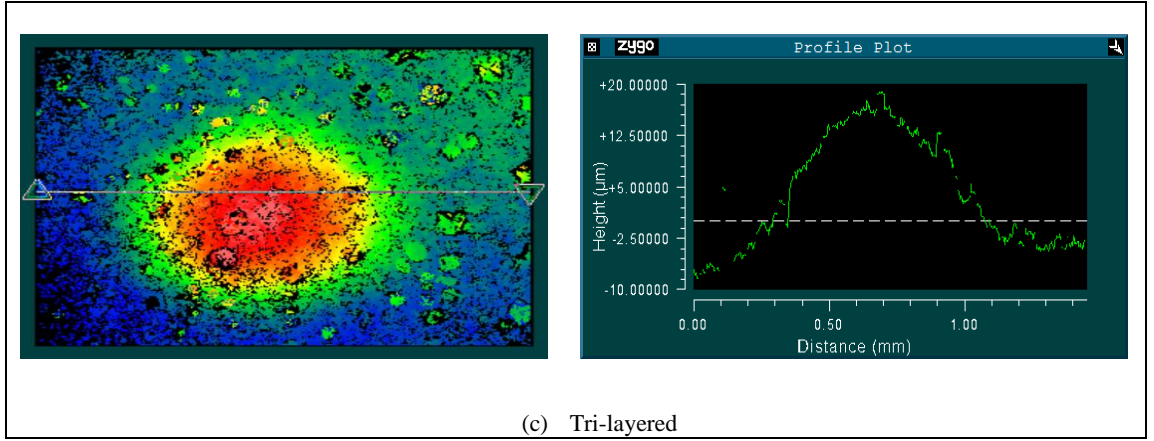


Figure 3.8: Surface profiles of samples after the experiment (Latif, J. et al., 2018b)

3.2 Prognostic modelling

Latest research findings have revealed that the process of coating delamination is driven by the combination of complex multi-disciplinary parameters. The prognostic models have been derived that incorporate the concepts of material science, solid mechanics and fracture mechanics. These prognostic relations predict the circular blister failure of coating substrate-system and estimate the propagation speed of blister. The fusion of multi-disciplinary concepts in the development of prognostic models has been elaborated in the flowchart shown in Figure 3.9. The residual and diffusion-induced stresses are one of the major factors that drive the blistering failure (Lim, C. et al., 2012; Lin, S. and Hwang, C. C., 1995; Nazir, M. et al., 2015b; Nazir, M. et al., 2016b).

The solid mechanics defines the residual stress which depends on temperature gradient ' ΔT ', Elastic modulus ' E ', strain ' ϵ ' and coefficient of thermal expansion ' α ' of the material (Hsueh, C.-H., 2002).

$$\sigma_r = E(\epsilon - \alpha \Delta T) \quad 3.1(a)$$

The temperature gradient ' ΔT ' and coefficient of thermal expansion ' α ' in Equation 3.1(a) can be correlated to the concentration gradient ' c'_k ' and partial molal volume ' \overline{V}_{pk} ' of component 'k', respectively (Zhang, X. et al., 2007). The relation for diffusion-induced stress can be written as:

$$\sigma_d = E \left(\epsilon - \frac{1}{3} c'_k \overline{V}_{pk} \right) \quad 3.1(b)$$

The relation for diffusion-induced stress for the substrate can be written as:

$$\sigma_{ds} = E_s \left(\varepsilon - \frac{1}{3} c_{ks} \overline{V_{pk_s}}' \right) \quad 3.2(a)$$

The relation for diffusion-induced stress for coating materials can be written as:

$$\sigma_{dci} = E_{ci} \left(\varepsilon - \frac{1}{3} c_{kci} \overline{V_{pk_{ci}}} \right) \quad \text{where } i = 1 \dots n \text{ layers} \quad 3.2(b)$$

The diffusion-induced strain ' ε' ' is the combined effect of bending component ' ε_b' ' and uniform bending ' ε_u' ' as ' $\varepsilon = \varepsilon_b + \varepsilon_u'$ '. If the coating thickness, substrate thickness and curvature are represented by ' h' ', ' s' ' and ' ρ' ', then the relation for uniform strain ' ε_u' ' can be written as ' $\varepsilon_b = x - t_b/\rho'$ ' for ($h \geq x \geq -s$). The bending strain is zero when the coating remains undamaged or intact to substrate then ' $x = t_b'$ '. The strain in the coating-substrate system will become equal to uniform strain only as, ' $\varepsilon = \varepsilon_u'$ '. In order to simplify the rest of calculation in modelling, the terms $c'_{kj} = \frac{1}{3} c_{kj}$, $\overline{V_{pk_j}} = \frac{1}{3} \overline{V_{pk_s}}'$ and $j = s, c_i$. The average stress distribution for multi-layered coating-substrate system can be derived by using Equations 3.2(a) and 3.2(b) as:

$$\begin{aligned} & \int_{-s}^0 E_s \left(\varepsilon_{ud} - \frac{1}{3} c'_{ks} \overline{V_{pk_s}} \right) dx_s \\ & + \sum_{i=1}^n \int_{h_{i-1}}^{h_i} E_{ci} \left(\varepsilon_{ud} - \frac{1}{3} c'_{kci} \overline{V_{pk_{ci}}} \right) dx_{ci} = 0 \end{aligned} \quad 3.3$$

The relation for uniform bending strain for the multi-layered coating-substrate system can be derived from Equation 3.3 as:

$$\begin{aligned} \varepsilon_{ud} &= \frac{(E_s s c'_{ks} \overline{V_{pk_s}} + \sum_{i=1}^n E_i t_i c'_{k_i} \overline{V_{pk_i}})}{E_s s + \sum_{i=1}^n E_i t_i} \quad \text{where } i \\ &= 1 \dots n \text{ layers} \end{aligned} \quad 3.4$$

The uniform bending strain can be written in the following form by using the first order approximation method as:

$$\begin{aligned} \varepsilon_{ud} &= \overline{V_{pk_s}} c'_{ks} + \sum_{i=1}^n \frac{E_i t_i (c'_{k_i} \overline{V_{pk_i}} - c'_{ks} \overline{V_{pk_s}})}{E_s s} \quad \text{where } i \\ &= 1 \dots n \text{ layers} \end{aligned} \quad 3.5$$

The applied moment ' M' ' is in equilibrium condition at ' $x = t_b'$ ' then the applied moment per unit width of multi-layered coating-substrate system can be written as:

$$\int_{-s}^0 \sigma_{d_s}(x - t_b)dx + \sum_{i=1}^n \int_{h_{i-1}}^{h_i} \sigma_{d_{c_i}}(x - t_b)dx = M \quad 3.6$$

The incorporation of Equations 3.2(a) and 2(b) in Equation 3.4 results as:

$$\begin{aligned} \int_{-s}^0 E_s \left(\varepsilon_u - \frac{1}{3} c'_{k_s} \overline{V_{p_{k_s}}} \right) (x - t_b) dx_s \\ + \sum_{i=1}^n \int_{h_{i-1}}^{h_i} E_{c_i} \left(\varepsilon_u - \frac{1}{3} c'_{k_{c_i}} \overline{V_{p_{k_{c_i}}}} \right) (x - t_b) dx_{c_i} = M \end{aligned} \quad 3.7$$

The solution of Equation 3.7 can be used to derive Bending curvature which is represented as ' ρ_d '.

$$\begin{aligned} \frac{1}{\rho_d} \\ = \frac{3[E_s(\varepsilon_u - c'_{k_s} \overline{V_{p_{k_s}}})s^2 - \sum_{i=1}^n E_i t_i (\varepsilon_u - c'_{k_i} \overline{V_{p_{k_i}}})(2h_{i-1} + t_i)] + 6M}{E_s s^2(2s + 3t_b) + \sum_{i=1}^n E_i t_i [6h_{i-1}^2 + 6h_{i-1}t_i + 2t_i^2 - 3t_b(2h_{i-1} + t_i)]} \end{aligned} \quad 3.8$$

The resultant force for the multi-layered coating-substrate system can be assumed to be zero due to uniform stress components, and then Equation 3.6 can be written as:

$$\int_{-s}^0 \sigma_{d_s}(x - t_b)dx + \sum_{i=1}^n \int_{h_{i-1}}^{h_i} \sigma_{d_{c_i}}(x - t_b)dx = 0 \quad 3.9$$

The incorporation of Equations 3.2(a) and 3.2(b) in Equation 3.9 results as:

$$\begin{aligned} \int_{-s}^0 E_s \left(\varepsilon_{u_d} - \frac{1}{3} c'_{k_s} \overline{V_{p_{k_s}}} \right) (x - t_b) dx_s \\ + \sum_{i=1}^n \int_{h_{i-1}}^{h_i} E_{c_i} \left(\varepsilon_{u_d} - \frac{1}{3} c'_{k_{c_i}} \overline{V_{p_{k_{c_i}}}} \right) (x - t_b) dx_{c_i} = 0 \end{aligned} \quad 3.10$$

The solution has been simplified as the thickness of the substrate is greater than the thickness of coating layers (Hsueh, C.-H., 2002). The relation for bending curvature can be derived by ignoring applied and using the first approximation method as:

$$\frac{1}{\rho_d} = 6 \sum_{i=1}^n \frac{E_i t_i (c'_{k_i} \overline{V_{p_{k_i}}} - c'_{k_s} \overline{V_{p_{k_s}}})}{E_s s^2} \quad 3.11(a)$$

Chapter 3: Blistering Failure

The bending curvature for each coating in the coating-substrate system can be written as:

$$\frac{1}{\rho_{d_i}} = 6 \frac{E_i t_i (c'_{k_i} \overline{V_{p k_i}} - c'_{k_s} \overline{V_{p k_s}})}{E_s S^2} \quad 3.11(b)$$

Therefore, Equation 3.11 (a) can also be written as:

$$\frac{1}{\rho_d} = \sum_{i=1}^n \rho_{d_i} \quad 3.11(c)$$

The mathematical relation for uniform bending strain ϵ_{u_r} due to residual stress can also be derived as:

$$\epsilon_{u_r} = \alpha_s \Delta T + \sum_{i=1}^n \frac{E_i t_i (\alpha_i - \alpha_s) \Delta T}{E_s S} \quad \text{where } i = 1 \dots n \text{ layers} \quad 3.12$$

Similarly, the relation for bending curvature due to residual stress can be derived as:

$$\frac{1}{\rho_r} = 6 \sum_{i=1}^n \frac{E_i t_i (\alpha_i - \alpha_s) \Delta T}{E_s S^2} \quad 3.13$$

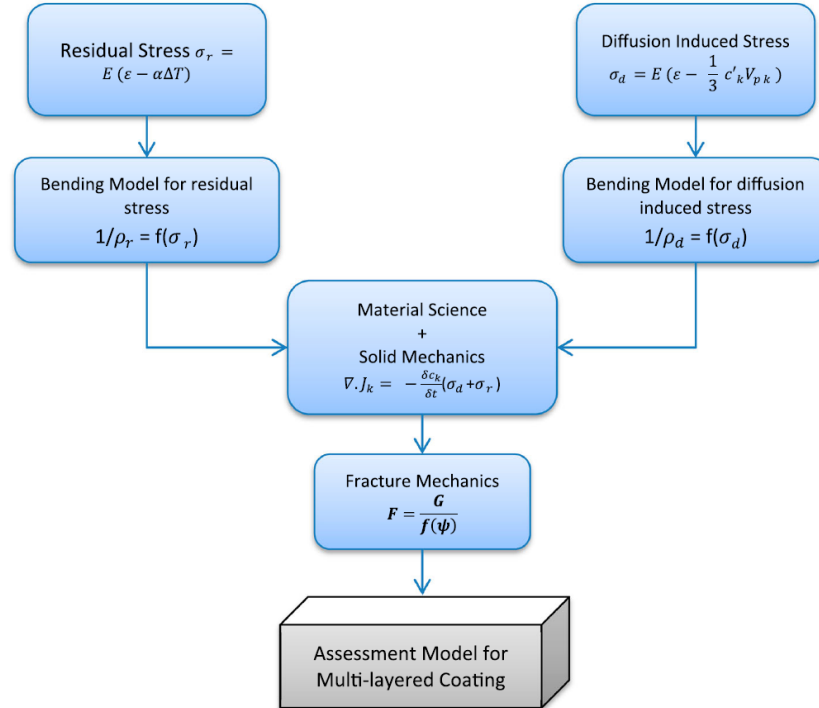


Figure 3.9: Multidisciplinary research approach for prognostic modelling (Latif, J. et al., 2018b)

3.2.1 Integration of diffusion and bending model

Linear beam theory models the deflections of the beam from a neutral point of axis due to stress and strain factors. It has been used to derive the bending models for deflection of thin coatings from a neutral point of axis (Zhang, N.-H. and Xing, J.-J., 2006). The bending models based on residual stress and diffusion-induced stresses are merged to include the combined effect of both factors in blistering failure. The concept of diffusion defined by Fick's Law has been integrated with the bending model. According to the first law of Fick's, the change in chemical potential is directly proportional to diffusion flux (Mejlbro, L., 1996). The relation of chemical potential of isotropic materials given in (Li, J. C.-M., 1978) as:

$$\mu_k^Q = \mu_k^S + RT \ln(c_k) - \overline{V}_{p\ k} \sigma_d \quad 3.14$$

where ' J_k ', ' D_k ', ' c_k ', ' $\nabla\mu_k$ ' and ' R ' represents diffusion flux, diffusion coefficient, concentration of the species, gradient of chemical potential and molar gas constant, respectively. The thermodynamics state is defined by the gradient of chemical potential. The chemical potential in standard state and in stressed state of coating are represented by ' μ_k^S ' and ' μ_k^Q ', respectively.

Fick's second law describes the gradient of concentration of species with respect to time. It can be used to estimate the transport rate of corrosive species in coating layer (Nazir, M. et al., 2016b).

$$\frac{\delta c_k}{\delta t} = D_k \nabla^2 c_k - \frac{\overline{V}_{p\ k} D_k}{RT} \nabla c_k \nabla (\sigma_d + \sigma_r) - \frac{\overline{V}_{p\ k} D_k}{RT} c_k \nabla^2 (\sigma_d + \sigma_r) \quad 3.15$$

Equation 3.15 gives the change in concentration of corrosive species due to diffusion-induced and residual stresses with respect to time which has been derived and experimentally validated (Nazir, M. et al., 2015b). The diffusion model can be written for the substrate as:

$$\begin{aligned} \frac{\delta c_{k_s}}{\delta t} = & D_{k_s} \nabla^2 c_{k_s} - \frac{\overline{V}_{p\ k_s} D_{k_s}}{RT} \nabla c_{k_s} \nabla (\sigma_{r_s} + \sigma_{d_s}) \\ & - \frac{\overline{V}_{p\ k_s} D_{k_s}}{RT} c_{k_s} \nabla^2 (\sigma_{r_s} + \sigma_{d_s}) \end{aligned} \quad 3.16(a)$$

Chapter 3: Blistering Failure

The diffusion model for the multi-layered coating-substrate system can be written as:

$$\frac{\delta c_{k_{c_i}}}{\delta t} = \left\{ \left(D_{k_{c_i}} + \frac{D_{k_{c_i}} E_{c_i} V_{p_{k_{c_i}}}^2}{9RT} c_{k_{c_i}} \right) \frac{\partial^2 c_{k_c}}{\partial^2 x} + \frac{D_{k_{c_i}} E_{c_i} V_{k_{c_i}}^2}{9RT} \left(\frac{\delta c_{k_{c_i}}}{\delta t} \right)^2 - \frac{D_{k_c} E_{c_i} V_{k_c}^2}{9RT} \frac{\delta c_{k_{c_i}}}{\delta t} \left(\frac{1}{\rho_{d_i}} + \frac{1}{\rho_{r_i}} \right) \right\} \quad 3.17$$

Terms can be replaced as: $\frac{E_{c_i}}{\rho_{d_i}} = \frac{\partial \sigma_{d_{c_i}}}{\partial t}$ $\frac{E_{c_i}}{\rho_{r_i}} = \frac{\partial \sigma_{r_{c_i}}}{\partial x}$

$$\sigma_T = \sigma'_d + \sigma'_r = \frac{\partial \sigma_{d_{c_i}}}{\partial t} + \frac{\partial \sigma_{r_{c_i}}}{\partial x} \quad 3.18(a)$$

$$\begin{aligned} & \frac{\partial \sigma_{d_{c_i}}}{\partial t} + \frac{\partial \sigma_{r_{c_i}}}{\partial x} \\ &= \frac{\left(D_{k_{c_i}} + \frac{D_{k_{c_i}} E_{c_i} V_{p_{k_{c_i}}}^2}{9RT} c_{k_{c_i}} \right) \frac{\partial^2 c_{k_c}}{\partial^2 x} + \frac{D_{k_{c_i}} E_{c_i} V_{p_{k_{c_i}}}^2}{9RT} \left(\frac{\delta c_{k_{c_i}}}{\delta t} \right)^2}{\frac{D_{k_c} V_{p_{k_{c_i}}}^2}{9RT} \frac{\delta c_{k_{c_i}}}{\delta t}} \end{aligned} \quad 3.18(b)$$

where σ'_T is the total stress resulted from diffusion induces stress $\frac{\partial \sigma_{d_{c_i}}}{\partial t}$ and residual stress $\frac{\partial \sigma_{r_{the c_i}}}{\partial x}$.

3.2.2 Fracture mechanics concept

The process of coating delamination of the multi-layered coating-substrate system can be investigated using concepts of fracture mechanics. The de-bonding driving force which defines the bonding strength of the multi-layered coating-substrate system has been derived (Faulhaber, S. et al., 2006). When the stresses generated within the coating-substrate system reaches a certain level at which the blistering failure initiates is called critical stress which is written as (Hutchinson, J. et al., 1992) :

$$\sigma_{cr} = 1.2235 \frac{E}{(1 - \nu^2)} \left(\frac{T_{th}}{r} \right)^2 \quad 3.19$$

Chapter 3: Blistering Failure

where ' T_{th} ', ' r ', ' E ' and ' ν ' are the total thickness of coating, radius of blister induced due to blistering failure between coating and substrate, Elastic modulus and Poisson's ratio of coating material, respectively.

The blistering failure in the multi-layered coating-substrate system has already been investigated using concepts of fracture mechanics (Choi, S. R. et al., 1999; Faulhaber, S. et al., 2006; Hutchinson, J. et al., 1992). The fracture mechanics concepts used for coating delamination of multi-layered thermal barrier coating can also be applied to other multi-layered coating-substrate systems (Choi, S. R. et al., 1999). The critical stress level for multi-layered coating-substrate systems can be defined as:

$$\sigma_{cr'} = \left(\frac{\pi}{r}\right)^2 \frac{1}{3} \sum_{i=1}^n \frac{E_i}{(1-\nu_i^2)} [(x_{i+1} - t_b)^3 - (x_i - t_b)^3] \quad 3.20$$

where ' $\sigma_{cr'}$ ', ' r ', ' x'_{i+1} ' and ' x'_i ' represents critical stress level for multi-layered coating, radius of blister, top and bottom locations of i^{th} coating layer, respectively.

The adhesion strength between coating and substrate depends on strain energy release rate. The strain energy release rate ' G_0 ' stored in the multi-layered coating-substrate system that can be released by plane strain without blistering failure is given as (Faulhaber, S. et al., 2006) :

$$G_0 = \frac{\sigma_c^2}{2} \sum_{i=1}^n \frac{(1-\nu_i^2)}{E_i} t_i \quad 3.21$$

The strain energy release rate ' G ' in the multi-layered coating-substrate system as a function of bending moment ' M ', resultant pre-buckling stress ' N ', bending stiffness ' B ' and stretching stiffness ' S ' can be defined as:

$$G = \frac{M^2}{2B} + \frac{N^2}{2S} \quad 3.22$$

$$B = \frac{1}{3} \sum_{i=1}^n \frac{E_i}{(1-\nu_i^2)} [(x_{i+1} - t_p)^3 - (x_i - t_p)^3] \quad 3.22(a)$$

$$S = \sum_{i=1}^n \frac{E_i}{(1-\nu_i^2)} t_i \quad 3.22(b)$$

Chapter 3: Blistering Failure

The Equation 3.22 can be solved by incorporating the parameters of bending stiffness ‘ B ’ and stretching stiffness ‘ S ’.

$$G' = \frac{3}{2} \sum_{i=1}^n \frac{(1 - v_i^2)}{E_i (x_{i+1} - t_p)^3 - (x_{i+1} - t_p)^3} M^2 \left[1 + \frac{1}{4} (\sqrt{\sigma_T / \sigma_{0'}} - 1)^2 \right] \quad 3.23$$

The resulting strain energy release rate Equation 3.23 is similar to the equation derived for the single-layered coating-substrate system in (Nazir, M. et al., 2015d). The de-bonding driving force which defines the adhesion strength of the coating-substrate system depends on the strain energy release rate G' and mode mix function ‘ j ’.

$$F = \frac{G'}{j} \quad 3.24$$

$$j = \sec^2 \left[\left(1 - \frac{\Gamma_{IC}}{E_c \lambda} \right) \psi \right] \quad 3.25$$

The strain energy release rate is mode dependent which can be adjusted by dimensionless mode mix function. The mode mix function for the isotropic coating-substrate system can be defined as:

$$\tan \psi = \frac{K_2}{K_1} = \frac{\sqrt{12} + (T_{th} \Delta N / \Delta M) \tan \omega}{-\sqrt{12} \tan \omega + (T_{th} \Delta N / \Delta M) \tan \omega} \quad 3.26$$

$$\frac{T_{th} \Delta N}{\Delta M} = \left(\sqrt{\frac{3(\sigma_{cT} - \sigma_{0'})}{B \left(\frac{\pi}{r} \right)^2}} \right) \quad 3.27$$

The research findings have revealed the dependency of delamination mechanism of the coating-substrate system on numerous multidisciplinary parameters. The de-bonding driving force has been formulated which is a function of various parameters including coating thickness, elastic modulus, Poisson’s ratio, interface roughness of the substrate toughness, bending moment, diffusion-induced and residual stresses. The relation has been experimentally validated for single layer coating-substrate system in (Nazir, M. et al., 2015d).

$$F = \frac{\frac{3}{2} \sum_{i=1}^n \frac{(1 - v_i^2)}{E_i (x_{i+1} - t_p)^3 - (x_i - t_p)^3} M^2 \left[1 + \frac{1}{4} (\sqrt{\rho} - 1)^2 \right]}{1 + \tan \left(\left(1 - \frac{\Gamma_{IC}}{E_c \lambda} \right) \frac{\sqrt{12} + (T_{th} \Delta N / \Delta M) \tan \omega}{-\sqrt{12} \tan \omega + (T_{th} \Delta N / \Delta M)} \right)^2} \quad 3.28(a)$$

The term ' ρ ' is defined as the de-bonding index which defines the safe, critical and fail states of the coating-substrate system. The state of the system depending on three conditions of the de-bonding index is given in Table 3.3. The safe state means that the blister has not occurred because the resultant stress hasn't exceeded the critical stress level ($\rho < 1$). The critical state of the coating-substrate system occurs when resultant stress is equal to critical stress level ($\rho = 1$). The fail state of the coating-substrate system is considered when resultant stress exceeds the critical stress level ($\rho > 1$). The mathematical relations of de-driving forces for the straight-sided blister have also been derived and discussed in (Khan, Z. A. et al., 2018) and Appendix B.

Table 3-3: De-bonding index for the coating-substrate system

Condition	State
$\rho < 1$	Safe
$\rho = 1$	Critical
$\rho > 1$	Fail

In order to derive the critical de-bonding driving force ' F_{cr} ', the condition $\rho = 1$ can be inserted into Equation 3.28(a) to derive the following expression as:

$$F_{cr} = \frac{\frac{3}{2} \sum_{i=1}^n \frac{(1 - v_i^2)}{E_i (x_{i+1} - t_p)^3 - (x_i - t_p)^3} M^2}{1 + \tan \left(\left(1 - \frac{\Gamma_{IC}}{E_c \lambda} \right) \frac{1}{-\tan \omega} \right)^2} \quad 3.28(b)$$

3.2.3 Blister growth rate model

The inflation of blister is controlled by the bending moment which establishes at the edges. The cantilever beam theory can be utilised to estimate the growth rate of the blister. The total bending moment as a function of total stress ' σ_T ', amplitude of blister ' w ' and coating thickness ' T_{th} ' can be written as:

Chapter 3: Blistering Failure

$$M_0 = T_{th} w \sigma_T \quad 3.29$$

The blister will not propagate if the value of bending moment is lower than the threshold level of bending moment (Chuang, T. et al., 1997). The equation of threshold level of bending moment for the multi-layered coating-substrate system can be written as:

$$M_{Th} = 0.73 \sqrt{\sum_{i=1}^n \frac{E_i}{(1 - v_i^2)}} \sqrt{a \sigma_T T_{th}^3} \quad 3.30$$

where ' E_i ' and ' v_i ' are the modulus of elasticity and Poisson's ratio of i^{th} coating layer, respectively. The growth rate of blister depends on various factors including stresses, temperature, material properties of coating and blister size. The blister will not grow if the velocity of blister growth is less than its threshold level. The expression for threshold velocity can be written as:

$$V_{min} = 1.83 \left(\frac{\sigma_f}{a}\right)^{1.25} \left[\frac{D_b \delta_b \Omega}{kT}\right] \left[\sum_{i=1}^n \frac{E_i}{(1 - v_i^2)} \frac{T_{th}^3}{12}\right]^{-0.25} \quad 3.31$$

where ' D_b ' and ' Ω ' represents the interfacial diffusivity and volume of the diffusing species, respectively. The dimensionless expression for blister growth velocity has been given as (Chuang, T. et al., 1997):

$$v = \left[m + \sqrt{m^2 - 1}\right]^{2.5} \quad 3.32$$

The relation in Equation 3.32 is also applicable for ' $m \geq 1$ ' and ' $v \geq 1$ ', where $v = \frac{V}{V_{min}}$ and $m = \frac{M_0}{M_{Th}}$. When the blister initiates, the bending moment is considered as initiation bending moment ' M_{ini} '. The bending moment at the initiation of blister can be estimated through the relation given in (Martin, J. et al., 1990) as:

$$M_{ini} = 3 \frac{\sum_{i=1}^n E_i T_{th}^3 w}{a^2} \quad 3.33$$

The Equations 3.30 and 3.33 can be used to predict whether the blister will grow or not. If the value of bending moment at blister initiation ' M_{ini} ' is greater than the threshold value of bending moment ' M_{Th} ', the blister will propagate. In the opposite condition, the blister will not propagate as shown in Table 3.4.

Table 3-4: Blister propagation criteria

If $M_{Th} < M_{ini}$	Blister = grow
If $M_{Th} > M_{ini}$	Blister \neq grow

3.3 Coating life assessment algorithm

The prognostic modelling for blister formation and propagation lead to the development of an algorithm for coating life assessment. The Nazir-Khan model proposed in recent research has been further extended for the multi-layered coating-substrate system (Nazir, M. et al., 2016a). The proposed prognostic algorithm calculates the de-bonding driving force as a function of multi-discipline parameters and also estimates the growth rate of the blister. It can be used for the assessment of effective life of coating and speed at which blister failure propagates.

The proposed coating life assessment algorithm has been shown in Figure 3.10. The algorithm takes various input parameters including material and mechanical properties of coating-substrate materials. The value of critical de-bonding driving is calculated at which coating-substrate system is considered in the critical state. At the next stage, the algorithm computes the current value of de-bonding driving force. The current value of de-bonding driving is then compared with the critical level to find the current state of the coating-substrate system. When the de-bonding driving force surpasses its critical level then the blister is considered to be developed and the system is in fail state as shown in Table 3.5.

Table 3-5: De-bonding driving force to define the state of the coating-substrate system

Condition	State
$F < F_{cr}$	Safe
$F = F_{cr}$	Critical
$F > F_{cr}$	Fail

Chapter 3: Blistering Failure

When the blister initiates, the bending moment is considered as initiation bending moment ' M_{ini} '. The algorithm computes threshold value of bending moment ' M_{Th} ' to estimate whether the blister will stop or propagate. If the condition is ' $M_{Th} < M_{ini}$ ' then the blister will propagate at a certain velocity. The algorithm can also estimate the growth rate of blister. The proposed prognostic algorithm provides a comprehensive solution for coating life assessment and the speed at which failure is propagating which can be used to estimate the coating failure on the component of structures.

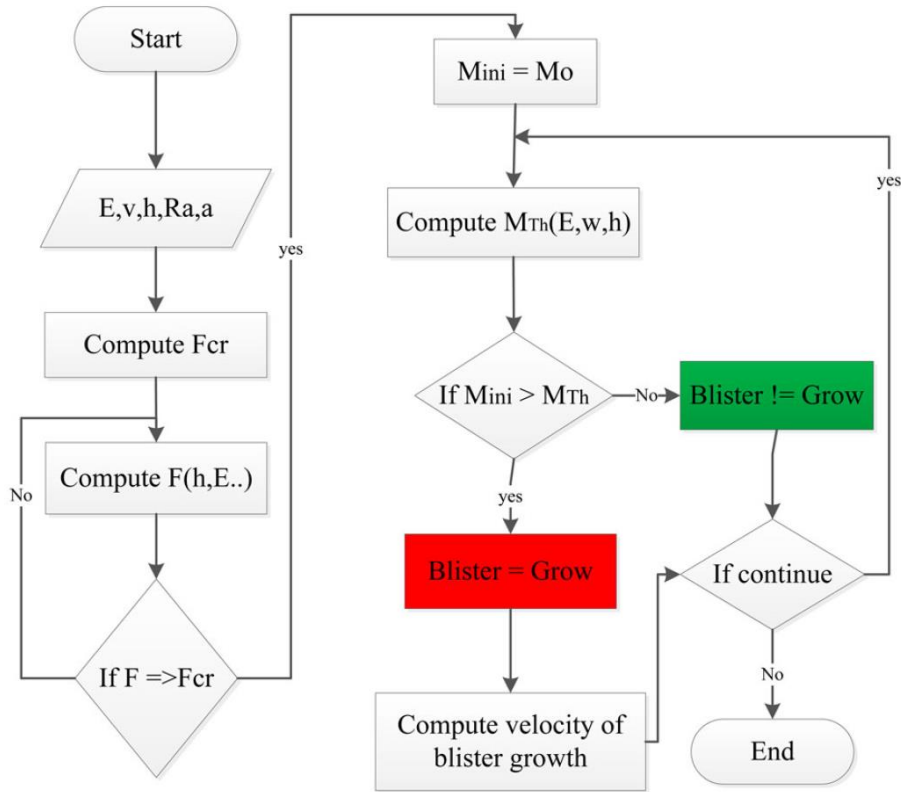


Figure 3.10: Coating life assessment algorithm (Latif, J. et al., 2018b)

3.3.1 Algorithm implementation

The algorithm is implemented by considering initial boundary conditions and the dimensionless form of all parameters for numerical simulation. Runge-Kutta method has been applied to estimate the de-bonding driving force as function diffusion-induced and residual stresses.

Chapter 3: Blistering Failure

Initial boundary conditions considered as:

$$c_{k_{c_i}}(x) = c_{k_s} = 0 \quad \text{for time } t = 0 \quad 3.34 \text{ (a)}$$

$$c_{k_{c_i}}(h) = c_{k_0} \quad \text{for time } t > 0 \quad 3.34 \text{ (b)}$$

All parameters are converted into a dimensionless form as:

$$\widetilde{c}_{k_{c_i}} = c_{k_{c_i}}/c_{k_0} \quad 3.34 \text{ (c)}$$

$$\check{E} = \frac{2}{3} \sum_{i=1}^n \frac{E_i}{(1 - v_i^2) E_s} \quad 3.34 \text{ (d)}$$

$$\widetilde{D}_k = D_{k_{c_i}}/D_{k_s} \quad 3.34 \text{ (e)}$$

$$\tilde{A} = \left(\frac{E_{c_i} V_{p_{k_{c_i}}}^2}{RT} \right) c_{k_0} \quad 3.34 \text{ (f)}$$

$$\frac{1}{\check{\rho}_{d_i}} = \frac{1}{\rho_{d_i} c_{k_0} V_{p_{k_0}}} = 6 \sum_{i=1}^n \frac{E_i t_i (c'_{k_i} \overline{V_{p_{k_i}}} - c'_{k_s} \overline{V_{p_{k_s}}})}{E_s s^2 c_{k_0} V_{p_{k_0}}} \quad 3.34 \text{ (g)}$$

$$\frac{1}{\check{\rho}_{r_i}} = \frac{1}{\rho_{r_i} \alpha_{k_0} \Delta T_{k_0}} = 6 \sum_{i=1}^n \frac{E_i t_i (\alpha_i - \alpha_s) \Delta T}{E_s s^2 \alpha_{k_0} \Delta T_{k_0}} \quad 3.34 \text{ (h)}$$

$$\check{x} = ((x_{i+1} - t_p)^3 - (x_i - t_p)^3)/(s + T_{th}) \quad 3.34 \text{ (i)}$$

Chapter 3: Blistering Failure

After inserting dimensionless parameters in Equations 3.28 (a) and 3.28 (b), the resulting Equation can be written as:

$$\tilde{F} = \frac{(1/\tilde{E}) \tilde{M} (1/\tilde{x})}{1 + \tan\left((1 - \tilde{B}) \frac{1}{-\tan \omega}\right)^2} \left[1 + \frac{1}{4} \left(\sqrt{n-1}\right)^2\right] \quad 3.35 (a)$$

$$\tilde{F}_{cr} = \frac{(1/\tilde{E}) \tilde{M} (1/\tilde{x})}{1 + \tan\left((1 - \tilde{B}) \frac{1}{-\tan \omega}\right)^2} \quad 3.35 (b)$$

Following are the steps for algorithm implementation:

- a) The algorithm begins by taking Input parameters including material and mechanical properties of coating-substrate materials such as Poisson's ratio, elastic modulus, thermal coefficients etc.
- b) The critical threshold values of stress and the de-bonding driving force is computed by using Equations 3.19, 3.20 and 3.35(b).
- c) Runge-Kutta method is applied to calculate the total resultant stress ' σ'_T '.
- d) The de-bonding driving force is computed by using Equation 3.30(a).
- e) The value of the de-bonding force is compared to identify the state of the coating-substrate system according to the criteria mentioned in Table 3.5.
- f) The convergence criterion is evaluated for debonding driving force by using the following Equation 3.36.

$$F_{max} = 100 \frac{(f^{t+1} - f^t)}{f^t} \quad 3.36$$

- g) If the coating-substrate system is in critical condition, the bending moment is saved as initiation bending moment as into fail state after critical state.
- h) The blister stoppage or propagation is identified according to the criteria mentioned in Table 3.4.
- i) The velocity such as blister growth rate can also be computed using Equation 3.32.

3.4 Results and discussions

In the experimental analysis, the blistering failure on all three samples has been observed. The surface profiles of samples recorded from White light Interferometry after immersion test have been compiled in Figures 3.11 and 3.12. The amplitude of average blister selected from each sample is plotted in Figure 3.11 for comparison. The blisters on each sample developed from non-osmotic and osmotic pressure resulted from material properties and diffusion-induced stress, respectively. The Mono-layered coated sample had a large number of blisters as compared to other samples because of its lowest adhesion strength due to coating thickness. The highest average blister size was recorded with amplitude and diameter of $\sim 25\mu\text{m}$ and 7 mm, respectively. The size of blister developed over Bi-layered coated sample was between Mono-layered and Tri-layered sample. The amplitude and diameter of average blister size were $\sim 23\mu\text{m}$ and 6mm which was high than expected. This could be the result of residual stresses which are developed during the application of the coating. The lowest blister size recorded over the Tri-layered coated sample as the amplitude of blister is $15\mu\text{m}$. The highest coating thickness resulted in highest adhesion strength which lowers the value of de-bonding driving force, so it takes more time to reach critical threshold level of de-bonding driving force. The samples are considered into fail state as the blisters have been developed.

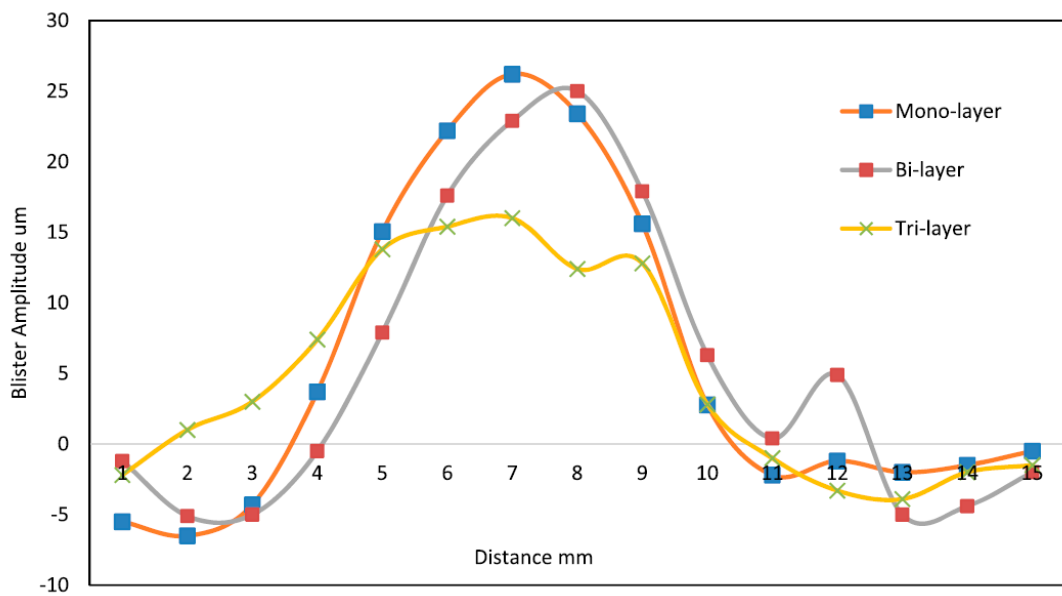


Figure 3.11: Blister height of each sample (Latif, J. et al., 2018b)

Chapter 3: Blistering Failure

The time when blisters on each sample started to develop and inflating to maximum has been shown in Figure 3.12. All three samples were in safe state when the immersion was started. The blisters started to develop over Mono-layered coated sample after ~72 hours during immersion test. It can be considered to be in fail state after blistering failure. The blisters started to develop over Bi-layered coated sample after ~96 hours during the immersion test. The Bi-layered coated sample takes more time to enter into fail state as it has more coating thickness as compare to Mono-layered coated sample. The blisters started to develop over Tri-layered coated sample after ~168 hours during immersion test. The Tri-layered sample has shown maximum adhesion strength as compared to rest of samples due to highest coating thickness.

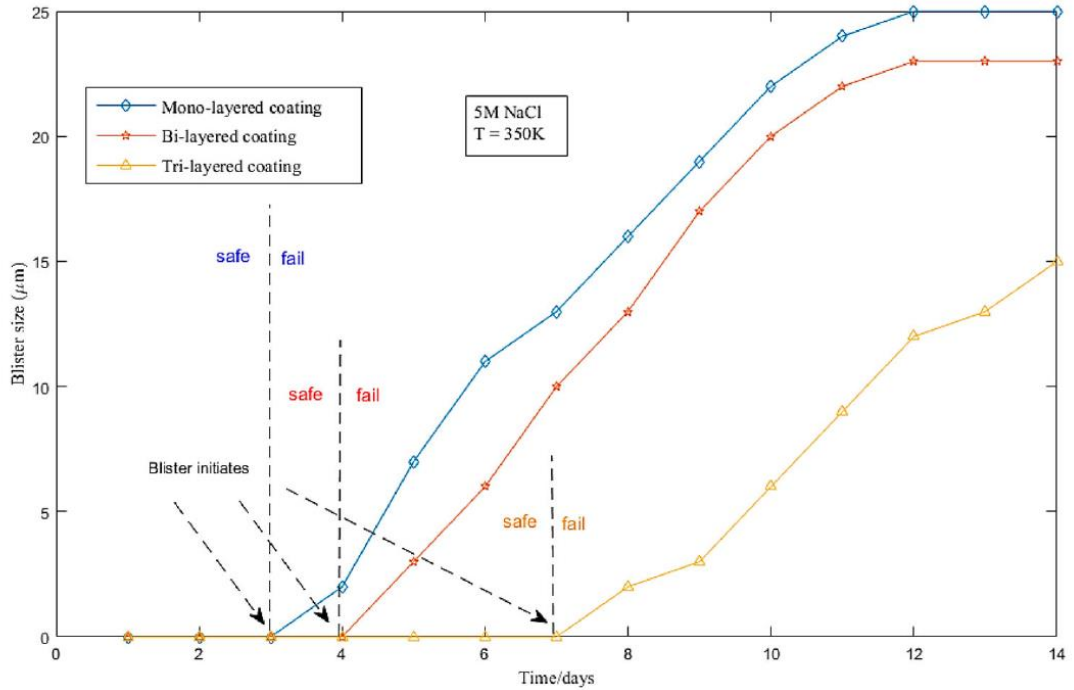


Figure 3.12: Blister propagation of each sample (Latif, J. et al., 2018b)

The simulation results for proposed prognostic algorithm have been shown in Figure 3.13. The critical de-bonding driving force computed for all three samples. The levels of critical de-bonding driving force for samples are labelled as ' F_{cr1} ', ' F_{cr2} ' and ' F_{cr3} '. It can be seen that all three samples has different critical de-bonding levels. It can vary depending on material properties and changing coating thickness. The de-bonding driving forces of each sample are calculated after updating the resultant stress. The Mono-layered sample is taking less time to reach its critical de-bonding level as

Chapter 3: Blistering Failure

compared to other samples. It enters into fail state while other samples are still in safe state. The critical de-bonding level of Bi-layered reaches after several time intervals to enter into fail state. The Tri-layered takes most time to enter into fail state. It can be concluded from simulation and experimental analysis that the increasing coating thickness lowers the de-bonding force.

The prognostic model also estimates the speed at which the blister will grow. The bending moment at the edges of the blister controls the stoppage and propagation of blistering failure. If the conditions of blister propagation as mentioned in Table 3.5 is applied to blister with amplitude $25\mu\text{m}$ and 7mm developed over the Mono-layered coated sample.

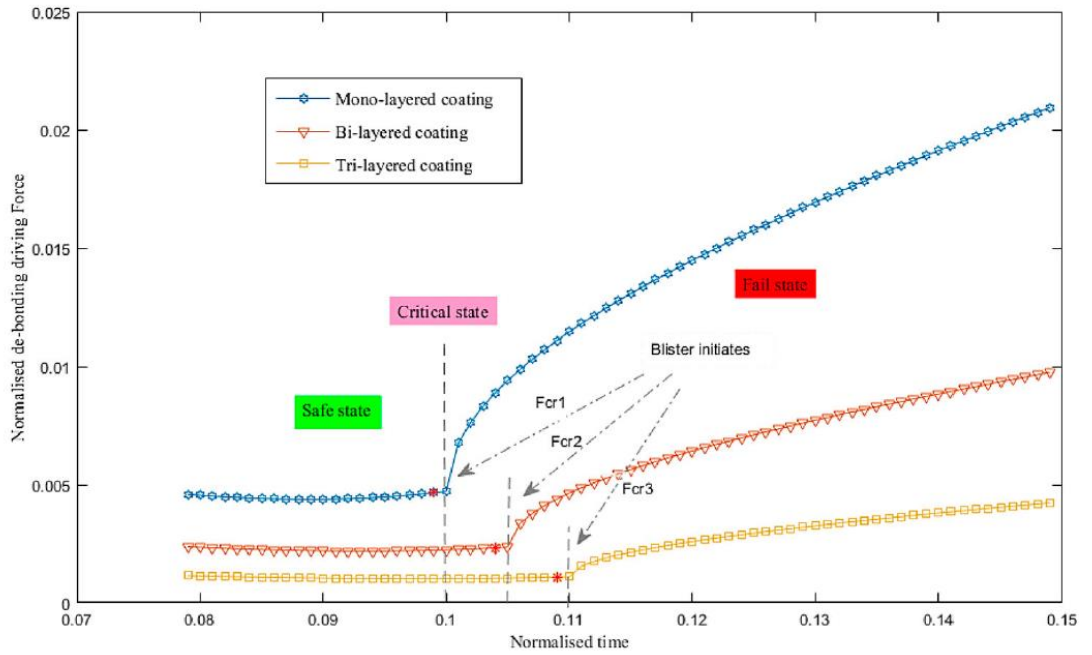


Figure 3.13: Simulation results for de-bonding driving force (Latif, J. et al., 2018b)

The initiation bending ' M_{ini} ' is greater than the threshold level of bending moment ' M_{Th} ', which means the blister will continue to grow. The simulations for blister propagation velocity also shown in Figures 3.14 and 3.15 with variable coating thickness. The proposed prognostic algorithm can be further investigated for various properties of coating materials to evaluate the development of number of blisters per area of specific coating and substrate material.

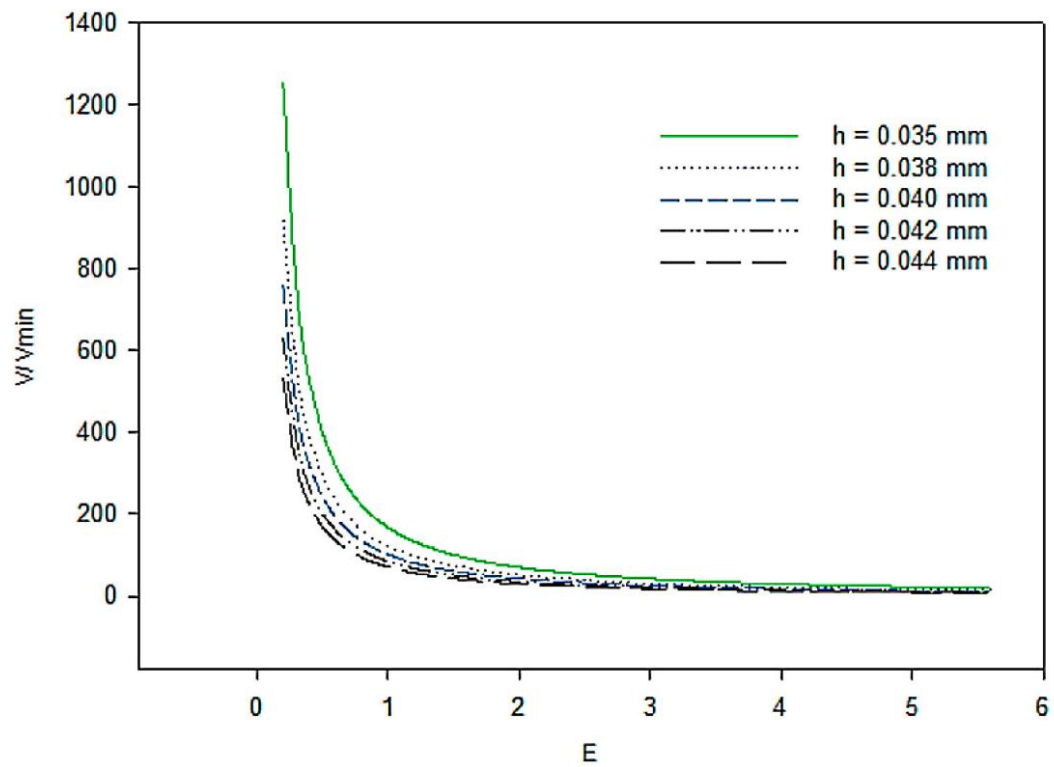


Figure 3.14: Simulation results for Velocity of blister vs Elastic modulus of the coating (Latif, J. et al., 2018b)

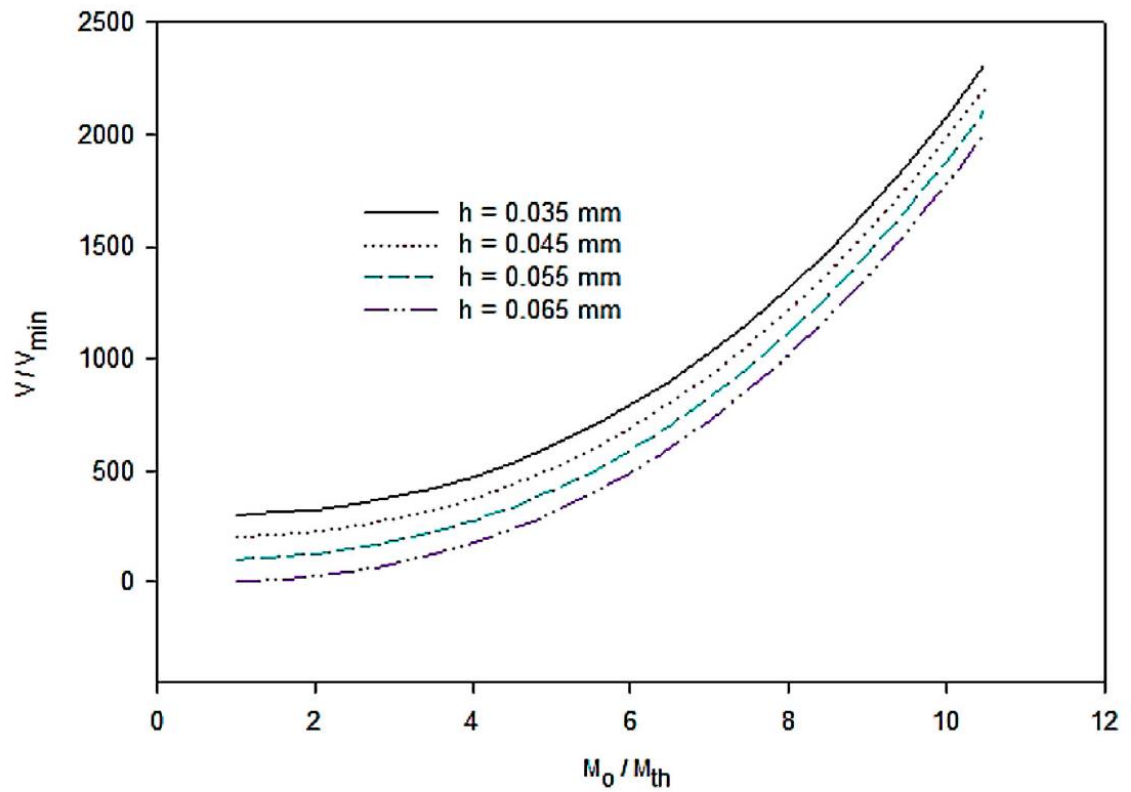


Figure 3.15: Simulation results for Velocity of blister vs bending moment (Latif, J. et al., 2018b)

3.5 Conclusion

A comprehensive prognostic algorithm based on various multi-discipline parameters has been proposed. The immersion test was performed on samples with variable coating thickness to validate the proposed algorithm. It classifies safe, critical and fail states of the coating-substrate system in terms of blistering failure. The speed of propagation can also be estimated using the proposed algorithm. It can be further investigated with numerous material properties to make useful coating life assessment. The investigation in propagation speed of blistering failure can lead to predicting the component failure of the structure.

Although, various prognostic models have been mentioned in the literature but the implementation of these models for proactive maintenance of complex structures in the industry is still a grey area. Therefore, the current prognostic model which incorporates complex parameters found in the latest research findings needs to be linked with maintenance strategies. In order to make accurate predictions and use the proposed algorithm more efficiently, real-time parameters of the operating conditions of structures are required along with maintenance history.

Chapter 4: Micro-cracks and Diffusion

The corrosive particles present in the atmosphere around metal structures can accumulate over the surface and diffuse through porous medium or micro-cracks within the coating. The development of micro-cracks due to mechanical damage and properties of the coating-substrate system provides the passage for corrosive particles to diffuse. Micro-cracks are one of the most common coating failures can be found in large structures such as military vehicles. The diffusion of corrosive elements activates electrochemical reactions beneath the coating which results in corrosion and decrease in adhesion strength of the coating and substrate (Huang, M.-W. et al., 2008). The coating over the electrochemically active cells become like a jelly medium and the adhesion strength of coating and substrate is driven by diffusion process (Fürbeth, W. and Stratmann, M., 2001; Grundmeier, G. et al., 1998; Grundmeier, G. et al., 2000). The corrosion rate under the coating can be estimated by measuring the diffusion rate that depends on meteorological factors. The diverse environmental conditions for the structures operating in different geographical locations make the prognostics of diffusion of corrosive particles more challenging. The Dorset environmental conditions have been investigated through corrosion monitoring techniques. The prognostic algorithm has been proposed to estimate the salinity transport rate for structures operating in different geographical locations. The contents of the chapter have been shown in Figure 4.1.

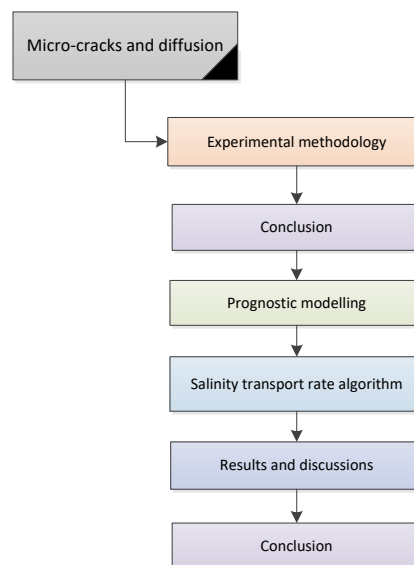


Figure 4.1: Contents of the chapter

Chapter 4: Micro-cracks and Diffusion

The properties of coating material and meteorological parameters are the major factors for the development of micro-cracks and corrosion damage beneath the coating, respectively. The large military vehicles at ‘The Tank Museum, UK’ operate stationary in a controlled environment and stationary at a remote location in uncontrolled environmental conditions. The weather conditions at Dorset, UK observed for last three years has shown critical operating environment for high-value military vehicles. The weather conditions in Dorset, UK have been comprehensively discussed in Chapter 2. The prediction of corrosion damage beneath the coating is very challenging because of diverse environmental conditions at remote locations. The corrosion beneath the coating is controlled by the diffusion of corrosive particles in the atmosphere such as salt particles. The experimental findings have shown that the accumulation of salt particles over the surface of the structure is highly influenced by the speed of the wind. Therefore, a comprehensive prognostic algorithm has been proposed to estimate the rate of diffusion for the structures operating in diverse operating conditions at different geographical locations.

4.1 Experimental methodology

The large military vehicles at ‘The Tank Museum, UK’ have been involved in several activities that include stationed inside the Museum for public display and some of the large vehicles are stationed outside for display or other event activity. The environmental conditions inside the Museum are controlled and suitable for the vehicle’s structure. When the military vehicles are taken outside of the Museum, they are exposed to harsh environmental conditions which pose a potential threat to their structural integrity. Therefore, the corrosion phenomena over the large military vehicles operating inside and outside of the Museum have been monitored for more than two years.

The Linear Polarisation Resistance (LPR) technique provides an effective method of corrosion detection due to meteorological parameters. The commercially available μ LPR sensors have been utilised for condition monitoring of military vehicles at ‘The Tank Museum’. The μ LPR sensor has been built on Linear Polarisation theory which is very sensitive to corrosion and allows the monitoring of corrosion in real-time. It provides the most feasible method for monitoring the atmospheric impact on high value

Chapter 4: Micro-cracks and Diffusion

and critical infrastructures such as buildings, bridges and aircraft. The bridge suspension cable has been monitored using μ LPR sensors to analyse the performance (Nims, D. K. and Colony, D. C., 2017). A photolithographic process is used for the fabrication of μ LPR sensor which contains shim. The Photolithographic and Electro-Chemical Etching techniques are used for preparing shim. It is further machined with Kapton to improve ductility and robustness of the sensor.

The three electrode system is applied to detect corrosion using working electrode, reference electrode and counter electrode as shown in Figure 4.2. The architecture of μ LPR sensor developed by ANALATOM is shown in Figure 4.3 (Brown, D. W. et al., 2014; Brown, D. W. et al.; Riemer, D. P. and Orazem, M. E., 2005).

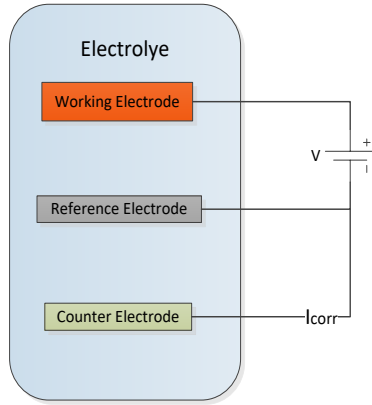


Figure 4.2: Three electrode system (Latif, J. et al., 2018a)

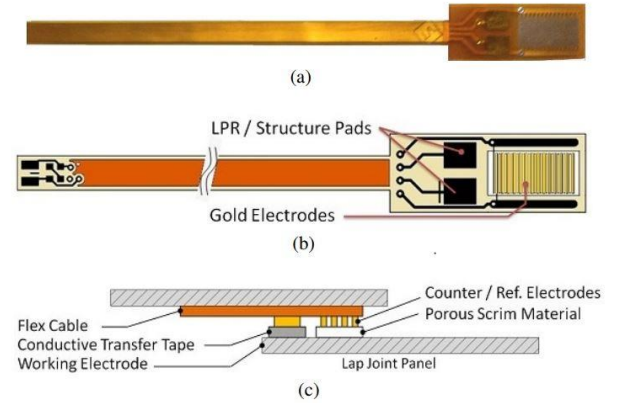


Figure 4.3: Architecture of μ LPR sensor [31]

The flow of current ' I_{corr} ' is measured between anodic and cathodic sites. The oxidation and reduction reactions within the material are responsible in the formation of cathodic and anodic sites. The Stern-Geary equation is applied to compute the corrosion current density as following (Brown, D. W. et al., 2014; Wagner, C. and Traud, W., 1938):

$$I_{corr} = \frac{B}{R_p} \quad 4.1$$

$$CR(t) = I_{corr} \left[\frac{w}{A * e * F} \right] = \frac{B}{R_p} \left[\frac{w}{A * e * F} \right] \quad 4.2$$

In Equation 4.1, ' I_{corr} ', ' R_p ' and ' B ' represents the corrosion current density, polarisation resistance and Stern-Geary constant, respectively. The value of Stern-Geary

Chapter 4: Micro-cracks and Diffusion

constant ' B ' for carbon steel 1010 is 30mV (Brown, D. W. et al., 2014; Nazir, M. et al., 2015b).

In Equation 4.2, ' $CR(t)$ ', ' F ', ' e ', ' w ' and ' A ' represents corrosion rate, Faraday's constant, the number of electrons exchanged, atomic weight and the area of corroding electrode, respectively.

The Valentine tank was selected for continuous corrosion monitoring for more than two years of duration. It operates inside the Museum in a controlled environment and also moved several times outside in harsh environment of Dorset during the calendar year. The μ LPR sensors were embedded at turret top location of Valentine tank as shown in Figure 4.4.



Figure 4.4: Corrosion monitoring system installed on Valentine Tank (Latif, J. et al., 2018a)

The complete corrosion monitoring system is illustrated in Figure 4.5. The sensors mounted at turret top are connected to Data acquisition unit (DAQ). The DAQ was also kept inside the Valentine tank throughout the monitoring. The battery life of the DAQ is ~5-7 years. It can store a large number of readings from 8 channels of μ LPR sensors. The stored data in the DAQ memory can be retrieved to the base station database using RS232 or RS-484 protocols. The Equations 4.1 and 4.2 can be applied to the reading to estimate the corrosion rate.

4.2 Experimental results

The μ LPR sensors have taken approximately 90K data samples during the corrosion monitoring period of more than two years. The measurements of two μ LPR sensors LPR_1 and LPR_2, which were mounted on turret top have been plotted in Figure 4.6. The Valentine tank was moved outside several times for remote activities during the monitoring period. These remote activities have been repeated 8 times which are labelled in the graph plot as A1, A2, A3....A8, respectively.

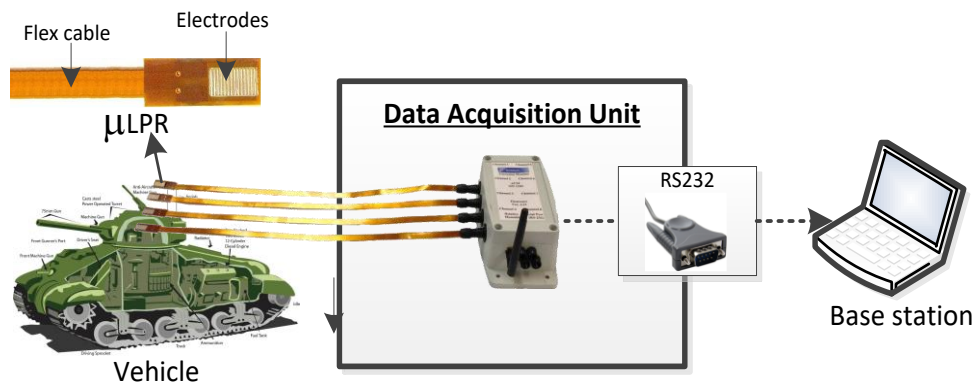


Figure 4.5: Corrosion monitoring system (Khan, Z. A. et al., 2017)

The corrosion monitoring system on the Valentine tank has not shown any sign of corrosion reaction during inside activity under the shed. The suitable environmental conditions for metal structures are maintained under the shed. Contrarily, the monitoring system has detected corrosion reactions several times during outside activity of the Valentine tank. The presence of salt particles in the atmosphere can be considered as a major factor for initiating and accelerating corrosion phenomena. The Museum is located near the coastal line of English Ocean, therefore a high amount of salinity can be expected in the atmosphere. The amount for salinity controls the rate of corrosion reaction and the amount of salinity is controlled by wind speed (Meira, G. et al., 2007; Morcillo, M. et al., 2000). The corrosion has been detected during all 8 outside activities. High corrosion rate has been observed during A1, A2 and A3 activities and low corrosion rate have been observed during A4, A5, A6, A7 and A8 activities. The data samples recorded during activities A1, A2 and A3 has been plotted as shown in Figures 4.7, 4.8 and 4.9, respectively. It can be concluded that the acceleration and variation in corrosion reactions during these activities are highly influenced by meteorological factors including wind speed, temperature, humidity and rain.

Chapter 4: Micro-cracks and Diffusion

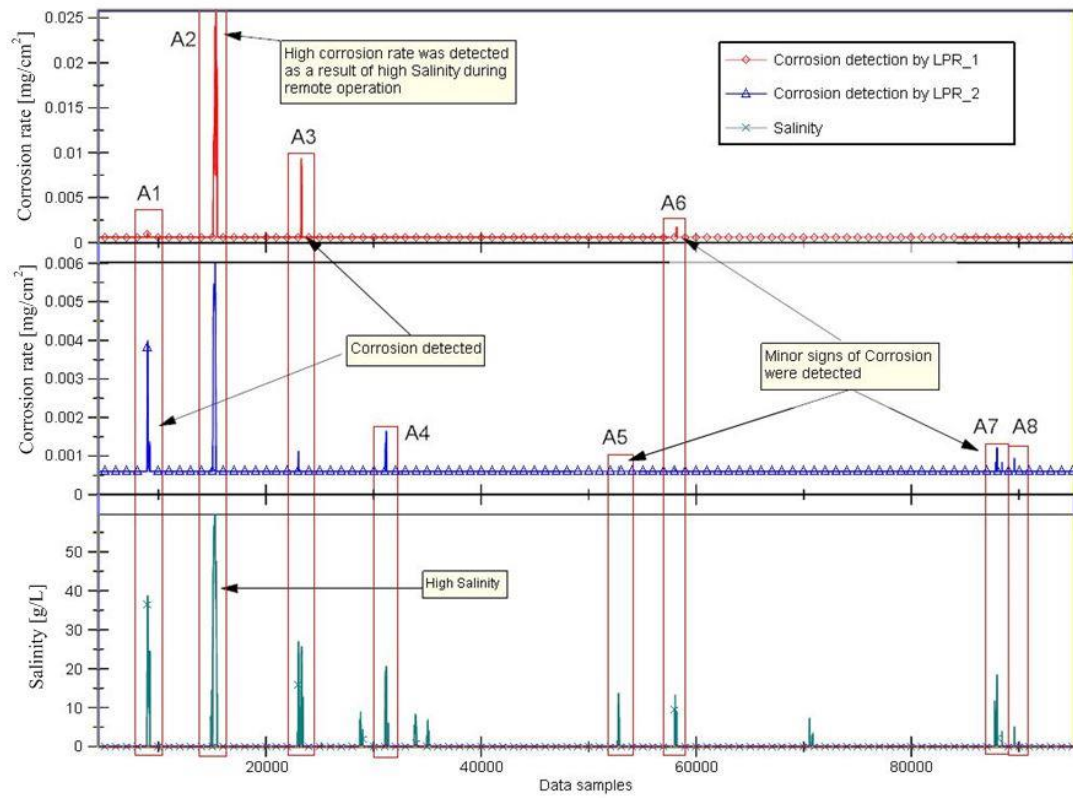


Figure 4.6: Corrosion monitoring at Turret top of Valentine tank during stationary and remote activities (Latif, J. et al., 2018a)

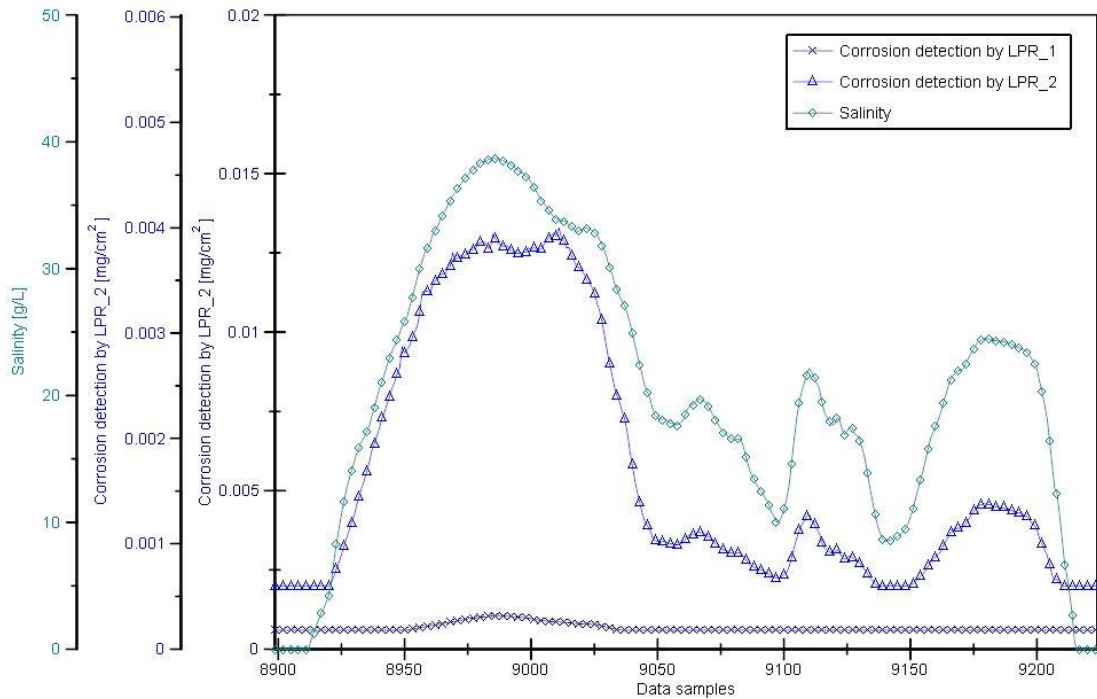


Figure 4.7: Corrosion rate and Salinity measurements during remote activity A1 (Latif, J. et al., 2018a)

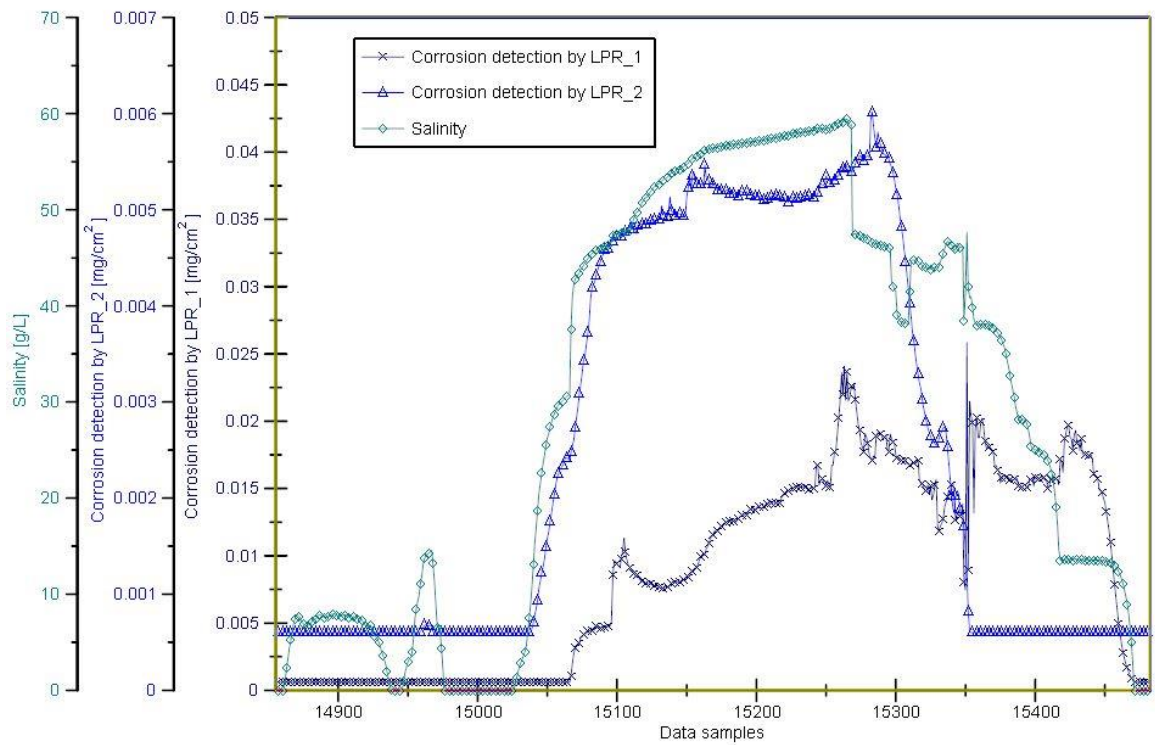


Figure 4.8: Corrosion rate and Salinity measurements during remote activity A2 (Latif, J. et al., 2018a)

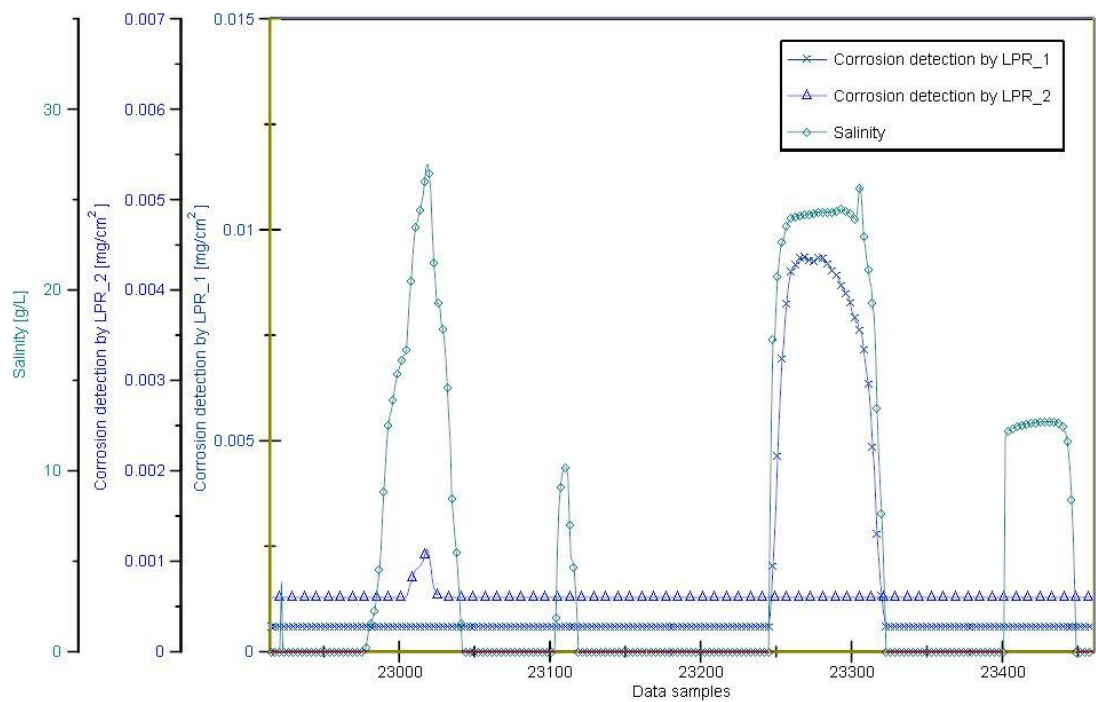


Figure 4.9: Corrosion rate and Salinity measurements during remote activity A3 (Latif, J. et al., 2018a)

4.3 Prognostic modelling

The salt particles accumulate over the surface of military vehicles and diffuse into the coating-substrate system through micro-cracks or porous medium within the coating. The water-soluble salt particles at the interface of the coating-substrate initiate and accelerate corrosion phenomena. The corrosion process continues to propagate which results in weakening of adhesion strength and metal loss. The corrosion current density is proportional to the concentration of salt particles. Therefore, the high diffusion rate of salt particles will result in an increase in corrosion rate which will result in an increase in metal loss. The temperature, relative humidity, time of exposure and the salt particles in the atmosphere are considered responsible for coating delamination and corrosion damage. The diverse weather condition makes the prognostic of delamination phenomena more challenging. The deposition rate of salt particles over the surface of the structure can be a considered controlling factor for coating delamination and corrosion damage. The salt particles deposition rate is highly affected by the speed of the wind and geographical location. The ISO classification of airborne salinity has divided the geographical location into four regions. It provides the deposition rate of salt particles for corresponding regions as shown in Table 4.1. The effect of wind speed has been incorporated in prognostic salinity model to propose a comprehensive algorithm for prediction of salt diffusion rate at various geographical regions.

Table 4-1: ISO classification of deposition rate of sodium chloride depending on different environmental conditions (Standardization, I. O. F.)

ISO Classification of Pollution by Airborne Salinity (Sodium Chloride deposition rate in Annual Average)		
Category	Deposition rate of NaCl, mg/m ² .day	Typical Environment
S ₀	≤ 3	Non-Coastal
S ₁	3 --- 60	Coastal Environment
S ₂	60 --- 300	Coastal Environment
S ₃	300 --- 500	Within 200 m. of Sea

Chapter 4: Micro-cracks and Diffusion

The change in concentration of salt particles ' $\frac{\partial S}{\partial t}$ ', depends on the accumulative effect of migration, diffusion and convection process (Bastidas-Arteaga, E. et al., 2011) .

$$\frac{\partial S}{\partial t} = \text{diffusion} + \text{migration} + \text{convection} \quad 4.3(a)$$

In the current research, the migration and convention phenomena have been neglected. The diffusion phenomenon depends on various parameters including the concentration of salt particles, relative humidity ' RH ', temperature ' T ' and time of exposure ' t ' which can be written as:

$$\frac{\partial S}{\partial t} = \frac{1}{n} \sum_{S_{e_{n=1}}}^n [D_{A_s}(T, RH, t) \nabla S_e] \quad 4.3(b)$$

where ' D_{A_s} ' represents the diffusion coefficient. The value of diffusion coefficient in the aqueous medium is higher by two order magnitude as compare to in porous medium (Allahar, K. N. et al., 2007).

$$D_{A_s} = \left[\frac{1}{D_{S,STA} f(T) f(RH) f(t)} \right]^2 \quad 4.4$$

where ' $D_{S,STA}$ ' represents standard diffusion coefficient.

4.3.1 Salinity Model

The deposition of hygroscopic particles on solid surfaces from the atmosphere is defined by the concepts of aerosol physics. The various physical processes generate aerosols over the surface of the sea. The wind stress is considered a major factor for the bursting of air bubbles during the development of Whitecap (Levin, Z. and Cotton, W. R., 2008). The threshold value of the speed of the wind at which the entrainment of marine aerosols begins has found to be $3ms^{-1}$ (Morcillo, M. et al., 2000).

During the operational activity of large structures, the deposition rate of salt particles depends on various factors including the direction of the wind, surface roughness, distance from the sea, particle density, geometrical configuration of the structure, local landscape and wind speed. The speed of wind is considered as a controlling factor for diffusion rate. The ISO classification of airborne salinity has classified the geographical location into four environmental regions. The deposition rate of salt particles

Chapter 4: Micro-cracks and Diffusion

corresponding to environmental regions has been specified as shown in Table 4.1. The environment has been classified into four regions such as S_0, S_1, S_2 and S_3 , respectively. The S_0 corresponds to the non-coastal region which is very far away from the coast. The deposition rate of sodium chloride (NaCl) over the solid surface in S_0 region is maximum 3 mg/m².day. The S_1 and S_2 are coastal regions in which S_2 is closer to coast. The deposition rate of sodium chloride (NaCl) over the solid surface in S_1 and S_2 regions are maximum 60 mg/m².day and 300 mg/m².day, respectively. The S_3 region contains the area which is maximum 200m away from the sea with maximum deposition rate as 500 mg/m².day. Comprehensive experimental research findings have shown increase in deposition rate of salt particles as wind speeds vary from 3.4 to 10 m/s (McDonald, R. et al., 1982; Meira, G. et al., 2007; Morcillo, M. et al., 2000). The cross wind affects are not included in current work.

The variation in wind speed from location to location will result in variation in corrosion damage and coating delamination. The uncontrolled environmental conditions for metal structures can also be classified into four categories based on ISO classification for airborne salinity. The deposition of salt particles over the surface of the structure as a function of wind speed has been modelled by using ISO classification for salinity deposition rate. For example, the maximum deposition rate of salt particles in S_0 region is 3 mg/m².day which can be considered for average wind speed. The deposition rate of salt particles is found to be a linear function of wind speed (Lovett, R., 1978; McDonald, R. et al., 1982). The following algorithmic approach has been adopted to estimate salt deposition rate for corresponding uncontrolled environmental conditions.

d = 1;

for i = 1:100

for k = 1:d

S = $S_{x_max} / ((W_{max} - W_{min}) * 100) + S_n(j-1)$;

$S_n(j) = S$;

j = j+1;

end

d = d+1;

$$j = 2;$$

$$St_c(i) = S;$$

end

where S_{x_max} represent the maximum deposition rate as mentioned in Table 4.1 which can be for any region (S_0, S_1, S_2 and S_3). The terms W_{max} and W_{min} represents the maximum and minimum wind speed, respectively.

The amount of salt particle in the atmosphere near the sea (S_3) decreases as distance increases. The relation for the rate of change of salt concentration as function of wind speed and distance can be written as:

$$\frac{dS_s}{dt} = - \frac{kS}{h} \quad 4.5$$

The exponential decay in the concentration of salt ' S_s ' has been observed as the distance from sea increase (Ailor, W. H., 1982; Basu, D. and Khan, D., 1972; McMahon, T. and Denison, P., 1979; Rajagopalan, K. et al., 1971) which can be written as:

$$S_s = S_0 \exp(-kx/Vh) \quad 4.6$$

where k , V and h represents coefficient (proportional to deposition velocity), wind speed and the height of air layer, respectively. The fusion of Equations 4.3(b) and 4.6 can be written as:

$$\frac{\partial S}{\partial t} = [D_{As}(T, RH, t) S_0 \exp(-\alpha x)] \quad 4.7$$

The addition of wind speed effect in predicting the diffusion of salt particles can give more accurate assessment of corrosion damage and coating delamination for structures which are operating at remote locations.

4.3.2 Temperature model

Temperature has a significant impact on electrochemical corrosion reaction and transport rate of salt particles. Arrhenius equation can be used to determine the rate of chemical reaction as (Laidler, K. J., 1984):

$$T' = A e^{\left[\left(\frac{G_a}{R}\right)\left(\frac{1}{T_{STA}} - \frac{1}{T}\right)\right]} \quad 4.8$$

Chapter 4: Micro-cracks and Diffusion

where ' A ', ' G_a ', ' R ', ' T ' and ' T_{STA} ' represents pre-exponential term, activation energy, universal gas constant, absolute temperature and standard temperature at standard diffusion coefficients ' D_{STA} ', respectively (Baştuğ, T. and Kuyucak, S., 2005; Samson, E. et al., 2003).

4.3.3 Relative humidity model

The relative humidity is one of the essential components for corrosion reaction to initiate. The following relation is utilised for relative humidity as:

$$RH' = \frac{1}{1 + \left(\frac{1 - RH}{1 - RH_s}\right)^m} \quad 4.9$$

where ' RH ' and ' RH_s ' represents actual pore relative humidity and relative humidity at which diffusion coefficient deviate between maximum and minimum values.

4.3.4 Exposure time

The structure deteriorates with respect to time of exposure as:

$$t' = \left(\frac{t_{STA}}{t}\right)^n \quad 4.10$$

where ' t_{STA} ', ' t ' and ' n ' represents time of exposure time at which standard diffusion coefficient is measured, actual exposure time and age reduction factor, respectively.

4.4 Proposed algorithm

The deposition rate of salt particles over the surface of the structure will vary significantly for structures operating at remote and multiple locations in diverse atmospheric condition as compared to stagnant structures. The variation in deposition rate will impact the diffusion of water-soluble salt particles which are responsible for corrosion damage and coating delamination. The algorithm has been proposed to estimate transport rate of salt particles over the surface of structures which are operating at different geographical locations in uncertain weather conditions.

The algorithm has four input parameters including wind speed, time of exposure, relative humidity and temperature as shown in Figure 4.10. The time iterative approach is implemented to simulate the parameters which have been explained comprehensively

Chapter 4: Micro-cracks and Diffusion

in our previous publication (Nazir, M. et al., 2015a). The deposition rate of salt is estimated through algorithmic logic mentioned and elaborated in Salinity model section. The algorithm will keep updating the deposition rate depending on wind speed and also change in operating location of structure e.g. the structure is moved from coastal region 'S₁' to the coastal region 'S₀'.

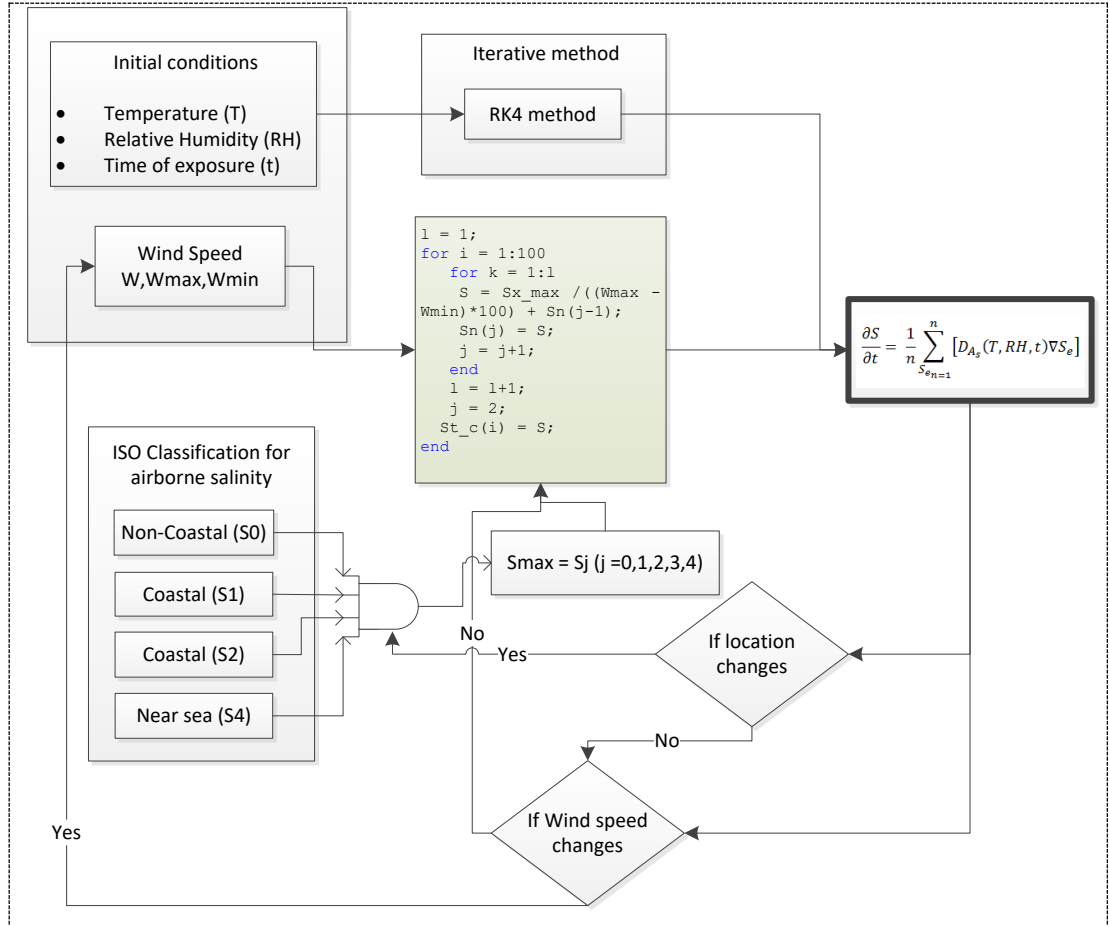


Figure 4.10: Algorithm for estimation of salinity transport rate depending on various geographical locations (Latif, J. et al., 2018a)

4.5 Results and discussions

The corrosion monitoring of the Valentine tank at 'The Tank Museum' have shown high variation in corrosion rates during outside activity. The water-soluble salt particles accelerate the corrosion reaction. The high amount of salt diffusion will result in high corrosion damage and coating delamination. The wind speed greatly influences the deposition rate of salt particles (Mcdonald, R. et al., 1982; Meira, G. et al., 2007, 2008;

Chapter 4: Micro-cracks and Diffusion

Morcillo, M. et al., 2000). The ambiguous nature of corrosion depends on wind speed and diffusion coefficient. The algorithm has been simulated by considering two scenarios of the winter season and two scenarios for the summer season to estimate the salinity transport rate as a function of wind speed.

In the summer season, the temperature is kept on increasing for 100 iterations in both scenarios, while the effect of wind speed is kept increasing from 3 m/s to 10 m/s in one scenario and decreasing from 10 m/s to 3 m/s in the second scenario. The simulation results of the first scenario for the structure operating in the summer season for increasing wind speed from 3 m/s to 10 m/s have been shown in Figure 4.11. The temperature is increasing from 1 to 100 iterations at a constant rate. The increase in temperature also increases the diffusion coefficient. The wind speed is also increasing from 3 m/s to 10 m/s for 100 iterations at a constant rate. The transport rate of salinity is varying corresponding to wind speed and diffusion coefficient. The increase in temperature results in an increased diffusion coefficient and an increase in wind speed is resulting in a high deposition rate of salt particles. High diffusion coefficient and salinity deposition rate are resulting in high salinity transport rate which can be considered as the worse situation for structural integrity. The corrosion rate will be maximum at high temperature and high wind speed.

The second scenario for the summer season is simulated for decreasing wind speed from 10 m/s to 3 m/s, while the temperature is increasing from 1 to 100 iterations at a constant rate as shown in Figure 4.12. Although, the increase in temperature results in an increase in diffusion coefficient but the decrease in wind speed accounts for a low deposition rate of salt particles. Therefore, the salinity transport rate is decreasing and these conditions will result in low corrosion rate for the structure.

Chapter 4: Micro-cracks and Diffusion

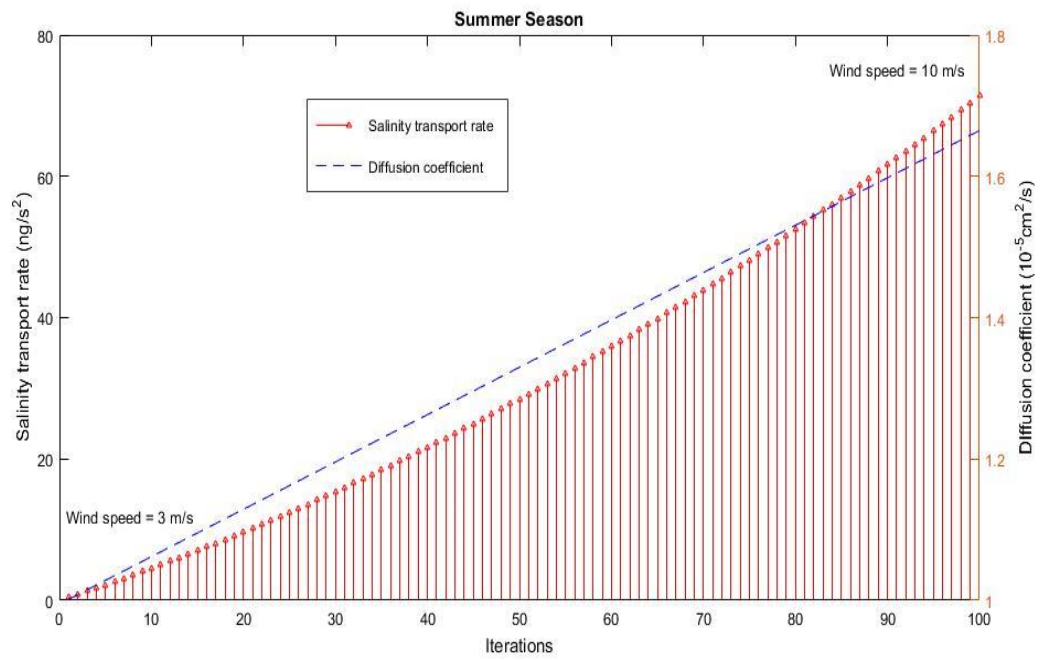


Figure 4.11: Salinity transport rate for increasing wind speed during the summer season (Latif, J. et al., 2018a)

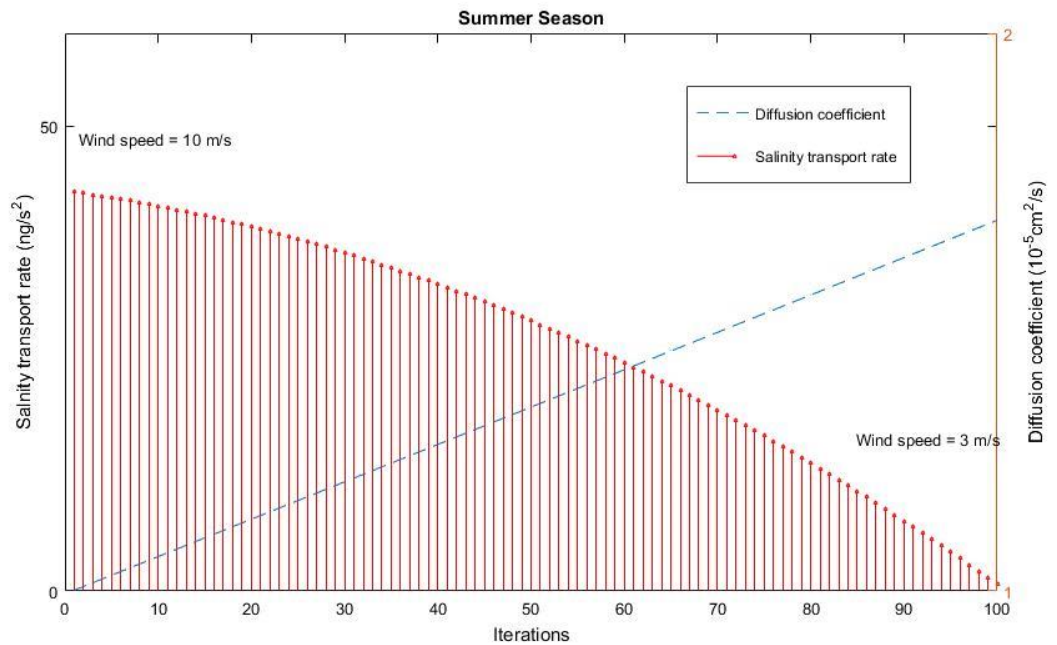


Figure 4.12: Salinity transport rate for decreasing wind speed during the summer season (Latif, J. et al., 2018a)

In the winter season, the temperature is kept on decreasing for 100 iterations in both scenarios, while the effect of wind speed is kept increasing from 3 m/s to 10 m/s in one scenario and decreasing from 10 m/s to 3 m/s in the second scenario. The simulation

Chapter 4: Micro-cracks and Diffusion

results for the structure operating in winter season for increasing wind speed have been shown in Figure 4.13. The temperature is decreasing from 1 to 100 iterations at a constant rate. The decrease in temperature also decreases the diffusion coefficient. The wind speed is increasing from 3 m/s to 10 m/s for 100 iterations at a constant rate. The transport rate of salinity is varying corresponding to wind speed and diffusion coefficient. The decrease in temperature is resulting in a reduction of the diffusion coefficient and an increase in wind speed is resulting in high deposition rate of salt particles. Although, the salt deposition rate is high but the low diffusion coefficient will result in low corrosion rate.

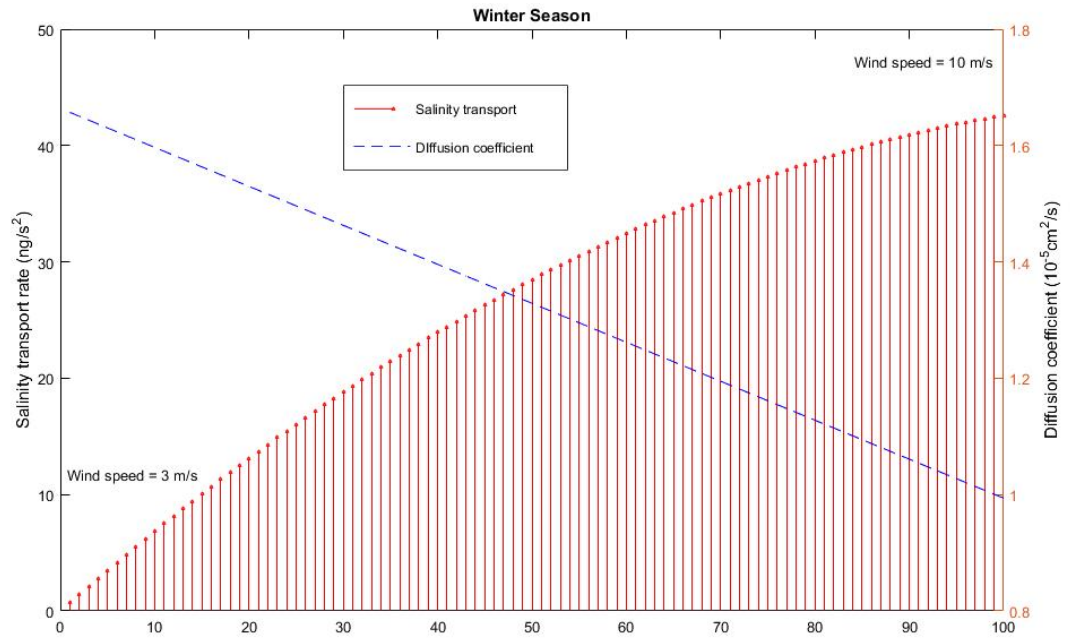


Figure 4.13: Salinity transport rate for increasing wind speed during the winter season (Latif, J. et al., 2018a)

The second scenario for the winter season is simulated for decreasing wind speed from 10 m/s to 3 m/s and the temperature is also decreasing from 1 to 100 iterations at a constant rate as shown in Figure 4.14. The decrease in temperature is accounting for decreasing diffusion coefficient and a decrease in wind speed is resulting in low salt deposition rate. Therefore, very low corrosion rate can be expected in these conditions because of low salt particles and low diffusion coefficient. These conditions can be considered more desirable and suitable for structural integrity.

Chapter 4: Micro-cracks and Diffusion

The salinity transport rate for the structure operating near the sea region ' S_3 ' has also been simulated. The simulation results for salinity transport rate as a function of distance from the sea has been shown in Figure 4.15. The salinity transport rate is highest near the sea and decreasing as the distance from the sea is increasing. The different levels of wind speeds are also resulting in different levels of salinity transport rate. The increase in wind speed accounts for high salinity transport rate.

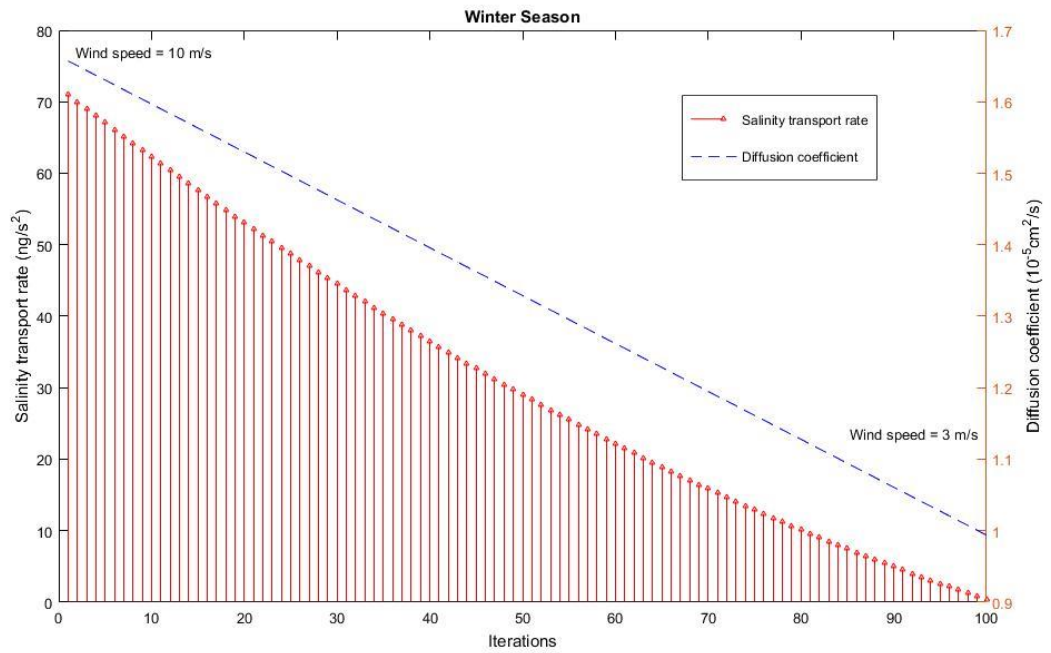


Figure 4.14: Salinity transport rate for decreasing wind speed during the winter season (Latif, J. et al., 2018a)

4.6 Conclusion

The impact of meteorological parameters has been incorporated in the proposed algorithm to predict the corrosion damage and coating delamination for the structures operating in diverse weather conditions at remote geographical locations. The simulation analyses for multiple scenarios of winter and summer seasons have been presented to evaluate the worse and suitable conditions for metal structures. The proposed algorithm will help maintenance professionals for proactive maintenance actions for structures operating remotely. The algorithm can be further extended and linked to the level of structural failure to decide appropriate maintenance strategy.

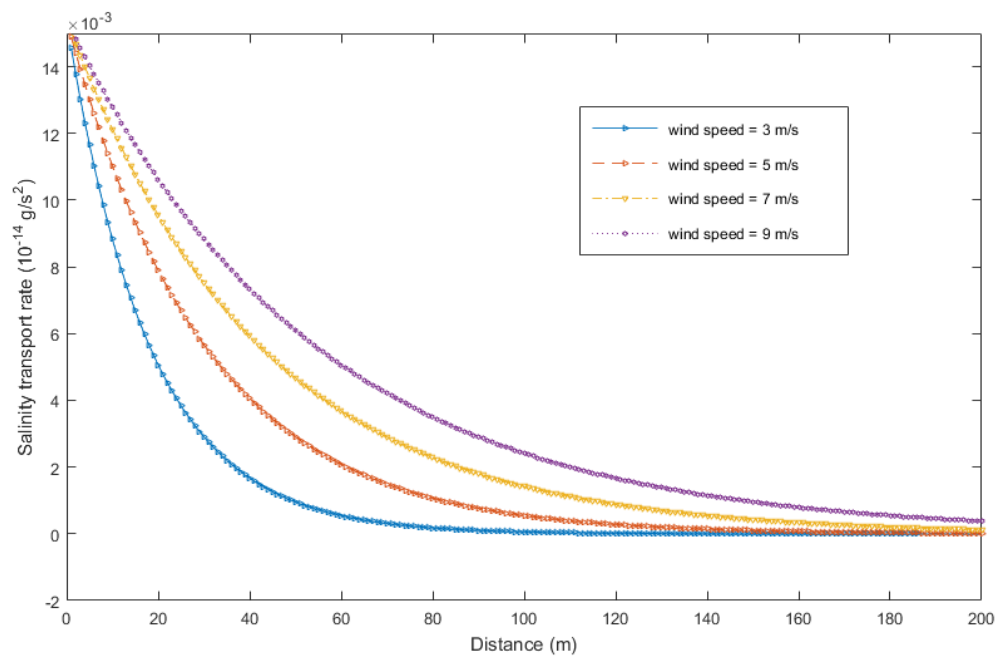


Figure 4.15: Salinity transport rate depending on the distance from the sea (Latif, J. et al., 2018a)

Chapter 5: Condition-based-Maintenance

The direct cost of corrosion estimated in recent years has found to be 3.4% of Gross Domestic Product (GDP). The indirect cost of corrosion is estimated to be almost equal to direct cost (Koch, G. E. A., 2016). A large number of organisations including automotive, aerospace, utilities and defence industry are affected by the financial impact of corrosion damage and maintenance of their structures. The report on the cost of corrosion and maintenance published by LMI has revealed that army equipment is costing almost \$3.1 billion which includes total maintenance cost of 15.5 % (Hertzberg, E., 2016). The maintenance activities associated with recoating and inspections incur the highest amount of maintenance cost. Latest research finding has revealed the influence of complex meteorological, mechanical and material parameters in the deterioration of structures integrity. The classical maintenance framework does not consider these complex parameters to schedule the optimal maintenance for metal structures. The Tank Museum follows complete recoating maintenance after fixed time duration without considering the cost implications. The inspections and maintenance decision based on accurate deterioration prediction model which incorporate complex parameters can assist organisations for cost-effective maintenance scheduling.

A comprehensive multidisciplinary algorithmic approach has been proposed in current research to provide optimal maintenance solutions to organisations. The prognostic models elaborated in previous chapters have been linked with maintenance cost to compute the cost-effective maintenance strategy for metal structures. The algorithm estimates the optimal recoating maintenance strategy based on specifications of coating material, structural material and operating conditions. The modelling and simulation results of the proposed algorithm have been elaborated in the current chapter as shown in Figure 5.1.

5.1 Maintenance Strategy Evaluation Algorithm

According to comprehensive literature, the Condition-based-maintenance is considered to be a most effective and cost-effective strategy for metal structures

Chapter 5: Condition-based-Maintenance

operating at remote locations. The proposed algorithm bridges the gap between modern prognostic algorithm and maintenance strategies to provide cost-effective solutions.

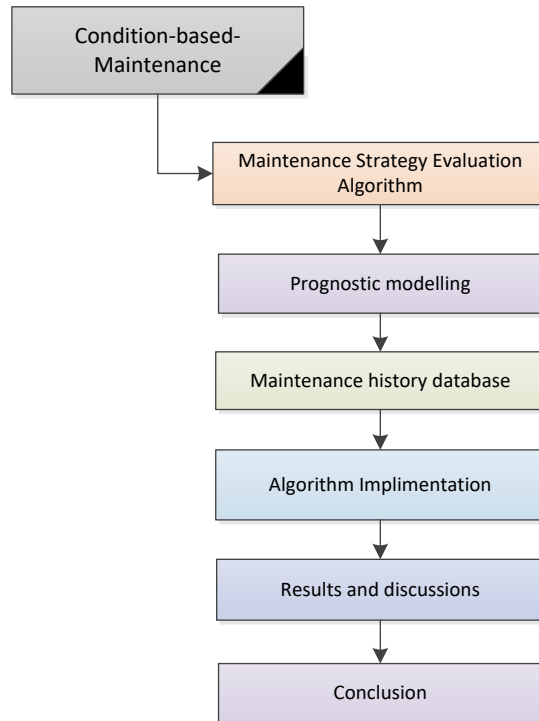


Figure 5.1: Contents of the chapter

The basic architecture of the proposed Condition-based-maintenance algorithm is shown in Figure 5.2. The input parameters for the algorithm include material properties of the coating-substrate system, operating conditions of structure and meteorological parameters. The prognostic models proposed in previous chapters can be applied to input parameters to estimate the useful coating life of the individual structure. The database of historical maintenance history will minimise the perdition error rate. The uniform database for maintenance history has also been proposed in current work. The decision for optimal recoating maintenance strategy will be based on the outcome of the prognostic model. The recoating maintenance has been divided into three different recoating strategies. The Patch recoat, Part recoat and Complete recoat. The Patch recoat involves the recoating of affected areas of the structure. The Part recoat involves the recoating maintenance of any component or part of the structure and the Complete recoat involves recoating of the complete structure.

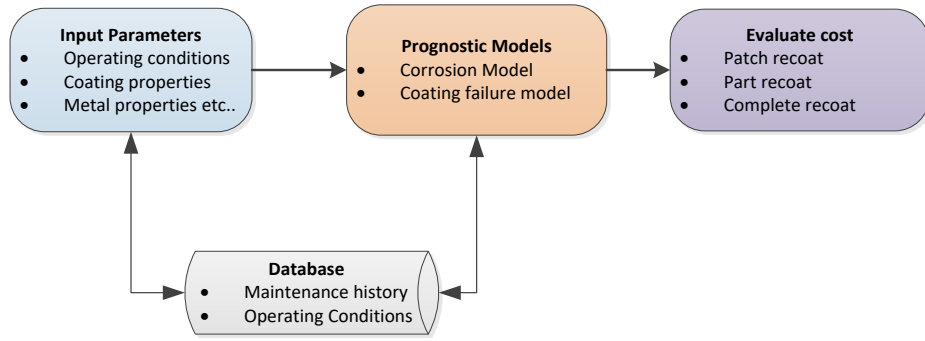


Figure 5.2: Basic Architecture of Maintenance Strategy Evaluation Algorithm

The proposed algorithm for optimal maintenance strategy evaluation has been illustrated compressively in Figure 5.3. The algorithm takes complex input parameters which includes the specifications of the coating-substrate system, material properties and cost associated with maintenance activities. The prognostic model for blistering failure identifies the critical threshold level and computes useful coating life until the development of patch failure/blister failure. The algorithm estimates the propagation speed of coating failure. The propagation speed can be used to identify the part failure of any individual metal structure. After evaluating the useful coating life, the models for calculating maintenance cost associated with Patch recoat, Part recoat and Complete recoat strategies are applied to find the best optimal maintenance strategy. The lack of real-time measurements and historical maintenance database are the major challenges for implementing the proposed algorithm. Therefore, a uniform database has also been proposed which is based on complex parameters evaluated in the latest research findings.

5.1.1 *Input parameters*

The performance of the coating-substrate system depends on numerous factors which need to be considered for prognostic modelling. The following are the input parameters for the proposed maintenance strategy evaluation algorithm along with temperature and humidity as shown in Figure 5.4.

5.1.1.1 *Mechanical and diffusion parameters*

The development of residual stresses and diffusion-induced stresses within coating are the controlling factors for blistering failure and micro-cracks (Latif, J. et al., 2018a; Nazir, M. et al., 2015a; Nazir, M. et al., 2015b; Nazir, M. et al., 2016b). These parameters are compressively elaborated in Chapter 2.

Chapter 5: Condition-based-Maintenance

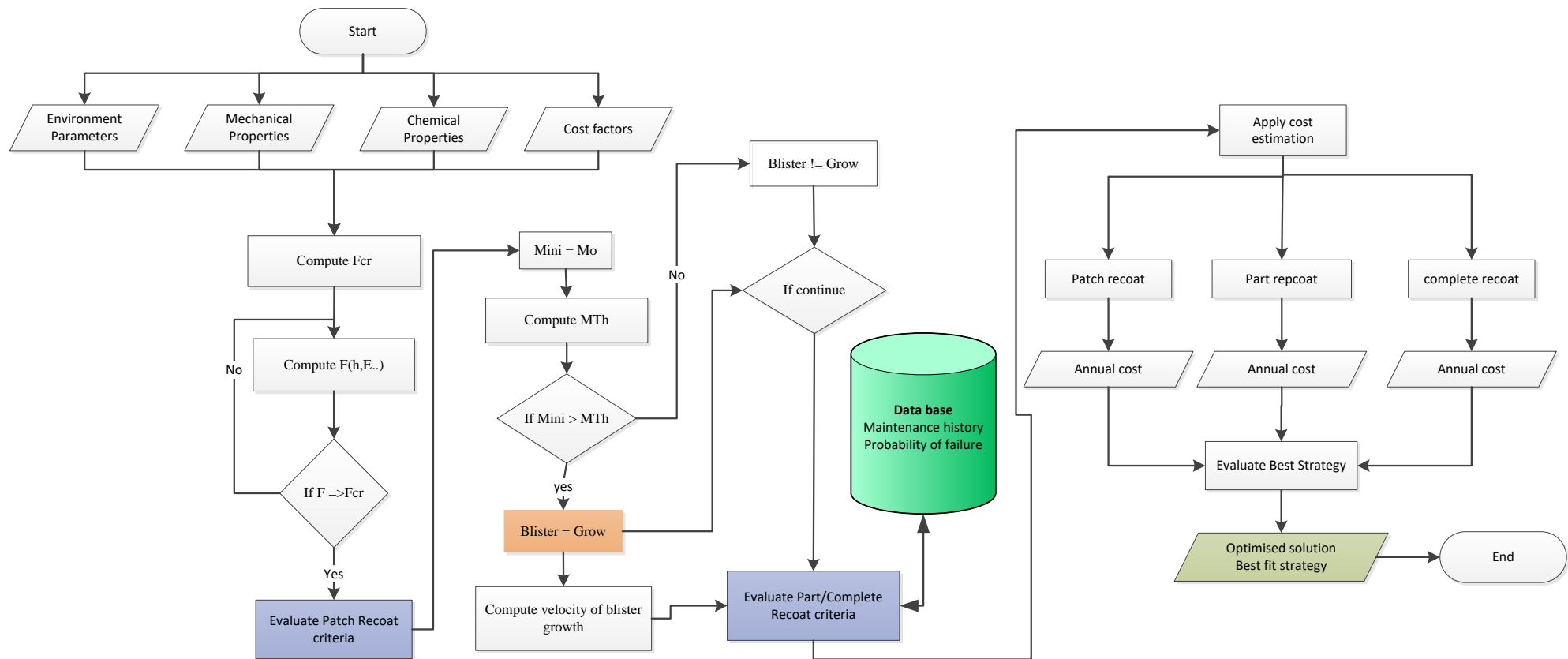


Figure 5.3: Recoating Maintenance Strategy Evaluation Algorithm

Chapter 5: Condition-based-Maintenance

5.1.1.2 Interfacial roughness

The interfacial roughness plays a vital role in adhesion strength between coating and substrate system. The appropriate increase in interfacial roughness can result in strong bonding (Nazir, M. et al., 2015d).

5.1.1.3 Coating thickness

The adhesion strength also increases with an increase in coating thickness which can extend the useful coating life (Nazir, M. et al., 2015d).

The screenshot shows a software window titled "CBR_GUI" with a subtitle "Maintenance Strategy Evaluation Application". The interface is organized into several sections for data entry:

- Select type of system:** A dropdown menu currently showing "Uni-layered coating".
- Select evaluation type:** Two radio buttons, "Single" (selected) and "Comparison".
- Substrate material properties:** Four input fields for "Poisson's ratio", "Elastic Modulus", "Diffusion coefficient", and "Thermal expansion".
- Coating material properties:** Four input fields for "Poisson's ratio", "Elastic Modulus", "Diffusion coefficient", and "Thermal expansion".
- Paint cost:** Two input fields for "Cost of paint per litre" and "Application cost", both followed by a "£" symbol.
- System specifications:** Three input fields for "Thickness of substrate", "Thickness of coating", and "Interfacial roughness", plus a dropdown for "Surface area" set to "1".
- Environmental conditions:** Two radio buttons, "Stationary" (selected) and "Mobile", followed by input fields for "Temperature range" and "Humidity range", each with a range indicator (e.g., "----").
- Time duration:** An input field followed by a dropdown menu set to "weeks".
- Generate Report:** A large green button at the bottom right.

Figure 5.4: Input parameters

5.1.1.4 Cost parameters

The cost of recoating maintenance involves the cost of washing, surface treatment, preparing equipment for application of recoating, drying, labour hours and other associated with recoating maintenance activities.

5.2 Prognostic modelling

The prognostic models for various modes of coating failure and corrosion damage has been proposed in current and previous research projects within the NCEM research group (Khan, Z. A. et al., 2018; Latif, J. et al., 2018a; Latif, J. et al., 2018b; Nazir, M. et al., 2015a; Nazir, M. et al., 2015b, 2016a; Nazir, M. et al., 2015c, 2015d, 2015e, 2016b; Nazir, M. et al., 2018; Nazir, M. H. and Khan, Z., 2015; Nazir, M. H. et al., 2018a; Nazir, M. H. et al., 2017). The prognostic algorithm for blistering coating failure illustrated in Chapter 3 has been utilised to develop the optimal condition-based-maintenance framework. The modelling equations presented in blistering failure have been integrated with the cost of maintenance to estimate optimal recoating maintenance for large metal structures.

5.2.1 Coating failure modelling

The adhesion between coating and substrate is driven by de-bonding driving force. The relation for the de-bonding driving force as a function of complex parameters derived and validated in previous research findings is given as (Latif, J. et al., 2018b):

$$F = \left\{ \frac{3}{2} \sum_{i=1}^n \frac{(1 - v_i^2)}{E_i (x_{i+1} - t_p)^3 - (x_i - t_p)^3} M^2 \left[1 + \frac{1}{4} (\sqrt{n-1})^2 \right] \right\} \left\{ 1 + \tan \left(\left(1 - \frac{\Gamma_{IC}}{E_c \lambda} \right) \tan \psi \right)^2 \right\}^{-1} \quad 5.1$$

The Equation 5.1 has been elaborated comprehensively in Chapter 3. The threshold level of de-bonding driving force at which coating enters into the critical state is termed as critical de-bonding driving force ' F_{cr} ' and the coating-substrate is considered in fail state when de-bonding driving force exceed its critical level. The relation for critical de-bonding driving force as function of complex parameters derived and validated in previous research findings is given as (Latif, J. et al., 2018b):

$$F_{cr} = \left\{ \frac{3}{2} \sum_{i=1}^n \frac{(1 - v_i^2)}{E_i (x_{i+1} - t_p)^3 - (x_i - t_p)^3} M^2 \right\} \left\{ 1 + \tan \left(\left(1 - \frac{\Gamma_{IC}}{E_c \lambda} \right) \frac{1}{-\tan \omega} \right)^2 \right\}^{-1} \quad 5.2$$

When de-bonding driving force exceeds critical level, the blister is considered to be developed and patch failure of the coating has occurred. The safe, critical and fail conditions of the coating-substrate system depending on de-bonding driving force is mentioned in Table 5.1.

Table 5-1: Conditions for patch failure

Condition	State
$F < F_{cr}$	Safe
$F = F_{cr}$	Critical
$F > F_{cr}$	Fail

The blister propagates which eventually results in exposing structure to surrounding environment. The propagation of blister is driven and controlled by the bending moment at edges of blister. (Tam, C. and Stiemer, S., 1996b) When the blister initiates, the bending moment is considered as initiation bending moment ' M_{ini} '. The bending moment at the initiation of blister can be estimated through the relation given in (Martin, J. et al., 1990) as:

$$M_{ini} = 3 \frac{\sum_{i=1}^n E_i T_{th}^3 w}{a^2} \quad 5.3$$

If the value of bending moment at blister initiation ' M_{ini} ' is greater than the threshold value of bending moment ' M_{Th} ', the blister will propagate. In the opposite condition, the blister will not propagate as shown in Table 2. The equation of threshold level of bending moment for the coating-substrate system can be written as:

$$M_{Th} = 0.73 \sqrt{\sum_{i=1}^n \frac{E_i}{(1 - v_i^2)}} \sqrt{a \sigma_T T_{th}^3} \quad 5.4$$

The Equations 5.3 and 5.4 can be used to predict whether the blister will grow or not. The parameters of these equations are elaborated in Chapter 3.

Table 5-2: Blister propagation criteria

If $M_{Th} < M_{ini}$	Blister = grow
If $M_{Th} > M_{ini}$	Blister \neq grow

Although, the prognostic models for blister propagation have been proposed but the model for blister failure leading to part failure of individual structure requires comprehensive experimental investigations and modelling. The profile for de-bonding driving force has been elaborated in Figure 5.5(a). The component-wise approach for predicting part failure is required that include various factors like number of blisters per area, growth rate of failure propagation and geometrical shape of parts of structure.

5.2.2 Maintenance cost modelling

The multidisciplinary coating failure prognostic model has been integrated with maintenance cost to evaluate cost-effective maintenance among Patch, Part and Complete recoating strategy. The annual cost can be computed using the following relation as (Tam, C. and Stierner, S., 1996b):

$$Annual\ cost = F_c \frac{ir}{(1 + ir)^t - 1} \quad 5.5$$

where ' F_c ', ' ir ' and exponent ' t ' represents future cost, interest rate and annual time, respectively. Several maintenance activities incur cost including maintenance facilities, surface preparation, inspection, preparation of coating instruments, blast abrasives and containment apparatus. The exponent time ' t ' is the useful life of coating-substrate system which depends on de-bonding driving force. The Equation 5.5 can be modified for annual cost of maintenance as:

$$Annual\ cost = (Area_Recoat)(Cost_factor)(unit_cost) \left[\frac{ir}{(1 + ir)^t - 1} \right] \quad 5.6$$

The standard ASTM D610 has classified the area to be recoated depending on degree of delamination which can also be utilised for Patch and Part recoating(Astm).

$$Area_Recoat_i = \left[\frac{Area_to_be_coated (\%)}{100} \right] (Surf_area_Part_i) \quad 5.7$$

The summation of area of individual parts of structure gives total area to be recoated as:

$$Total_Area_Recoat = \sum_{i=0}^n Area_Recoat_i \quad 5.8$$

The large metal structures are often assembled of numerous parts having various geometrical shapes. The area of individual parts and total area will vary from structure to structure. The measurements of parts of each individual structure need to be recorded in the database. The re-coating maintenance strategies can be classified into three different strategies such as Patch recoat, Part recoat and Complete recoat. The mathematical equations associated with each re-coating strategy can be written as (Tam, C. and Stierner, S., 1996a, 1996b):

Patch recoat

$$Annual\ cost = Area_{Recoat} * (surf_{prep_{cost}} + coating_{cost}) \left[\frac{ir}{(1 + ir)^t - 1} \right] \quad 5.9$$

Part recoat

$$Annual\ cost = (Area_{Recoat} * surf_{prep_{cost}}) + (area * coating_{cost}) \left[\frac{ir}{(1 + ir)^t - 1} \right] \quad 5.10$$

Complete recoat

$$Annual\ cost = area * (surf_{prep_{cost}} + coating_{cost}) \left[\frac{ir}{(1 + ir)^t - 1} \right] \quad 5.11$$

The cost of services and good varies according to the inflation rate. The factor $(1 + ir)^t$ is included in Equations 5.9, 5.10 and 5.11 to derive the following equations:

Patch recoat

$$Annual\ cost = Area_{Recoat} * (surf_{prep_{cost}} + coating_{cost}) \left[\frac{ir(1 + ir)^t}{(1 + ir)^t - 1} \right] \quad 5.12$$

Part recoat

$$\begin{aligned} \text{Annual cost} = & (Area_{Recoat} * surf_{prep_{cost}}) \\ & + (area * coating_{cost}) \left[\frac{ir(1+ir)^t}{(1+ir)^t - 1} \right] \end{aligned} \quad 5.13$$

Complete recoat

$$\begin{aligned} \text{Annual cost} = & area \\ & * (surf_{prep_{cost}} + coating_{cost}) \left[\frac{ir(1+ir)^t}{(1+ir)^t - 1} \right] \end{aligned} \quad 5.14$$

The profile of Patch recoating maintenance strategy is shown in Figure 5.5(b). The only delaminated area is recoated in Patch recoating strategy. The delamination could be micro-cracks, rusting or blisters. This strategy is very effective to halt the damage at an early stage but very frequent inspections are required than other strategies. The Patch can occur at different locations of the structure. The structure receiving Patch recoating maintenance strategy will also receive Complete recoating maintenance after an appropriate amount of time. The cost for patch recoats can also vary depending on the location of patch area within the structure, operating conditions and geometrical shape. The annual cost of Patch recoating maintenance can be written as:

$$\begin{aligned} \text{Annual cost}_{Patch\ repair} & \\ = & \sum_{p=0}^n Ar_p * (Sp_p + C_p) \left[\frac{ir(1+ir)^t}{(1+ir)^{t_n} - 1} \right] \\ & + \sum_{e=0}^n A_e * (Sp_e + C_e) \left[\frac{ir(1+ir)^t}{(1+ir)^{T_e} - 1} \right] \end{aligned} \quad 5.15$$

The description of all parameters in Equation 5.15 has been mentioned in the nomenclature of the report.

The blister or micro-cracks within coating propagates with time to expose metal structure to surrounding operating conditions leading to part failure of the structure. The profile of Part recoating maintenance strategy is shown in Figure 5.5(c). The large metal structures are often assembled of numerous parts with complex geometrical shapes. Some parts within the structure may require less frequent recoating maintenance and inspections as compare to other parts. The difference in the area of the part, location within the structure and geometrical shapes will also impact the cost of their maintenance. The structure receiving Part recoating maintenance strategy will also

Chapter 5: Condition-based-Maintenance

receive Complete recoating maintenance after an appropriate amount of time. The annual cost of Part recoating maintenance strategy can be written as:

$$\begin{aligned} \text{Annual cost}_{\text{Component repair}} &= \sum_{c=0}^n (Ar_c * Sp_c) + (Sp_c * C_c) \left[\frac{ir(1+ir)^t}{(1+ir)^{t_c} - 1} \right] \\ &+ \sum_{e=0}^n A_e * (Sp_e + C_e) \left[\frac{ir(1+ir)^t}{(1+ir)^{T_e} - 1} \right] \end{aligned} \quad 5.16$$

The description of all parameters in Equation 5.16 has been mentioned in the nomenclature of the report.

The complete structure is recoated in Complete recoating maintenance strategy once the structure exceeds its threshold level of deterioration. This strategy requires the least frequency of inspection but very inefficient for high value and critical structures. The profile of Complete recoating maintenance strategy is shown in Figure 5.5(d). The annual cost of Complete recoating maintenance strategy can be written as:

$$\text{Annual cost}_{\text{Complete repair}} = \sum_{e=0}^n A_e * (Sp_e + C_e) \left[\frac{ir(1+ir)^t}{(1+ir)^{T_e} - 1} \right] \quad 5.17$$

The description of all parameters in Equation 5.17 has been mentioned in the nomenclature of the report.

The frequency and degree of inspection depend on the operating conditions and complex architecture of structures. The cost relation for the cost related to movement of structure for inspection or for application of recoating can be written as:

$$\begin{aligned} x_Cost &= \sum_{i=0}^n i_Cost_i \left[\frac{ir(1+ir)^t}{(1+ir)^{t_i} - 1} \right] \\ &+ \sum_{m=0}^n m_Cost_m \left[\frac{ir(1+ir)^t}{(1+ir)^{t_m} - 1} \right] \end{aligned} \quad 5.18$$

where x_Cost is the accumulative cost associated with the number of inspections performed at different time intervals and cost incurred by the mobility of structure for inspection purpose or recoating. The Equation 22 can be incorporated in Equations 19, 20, 21 to include the cost associated with inspection activities as:

Annual cost_{patch repair}

$$\begin{aligned}
 &= \sum_{p=0}^n Ar_p * (Sp_p + C_p) \left[\frac{ir(1+ir)^t}{(1+ir)^{t_n} - 1} \right] \\
 &+ \sum_{e=0}^n A_e * (Sp_e + C_e) \left[\frac{ir(1+ir)^t}{(1+ir)^{T_e} - 1} \right] \\
 &+ \sum_{i=0}^n i_Cost_i \left[\frac{ir(1+ir)^t}{(1+ir)^{t_i} - 1} \right] \\
 &+ \sum_{m=0}^n m_Cost_m \left[\frac{ir(1+ir)^t}{(1+ir)^{t_m} - 1} \right]
 \end{aligned} \tag{5.19}$$

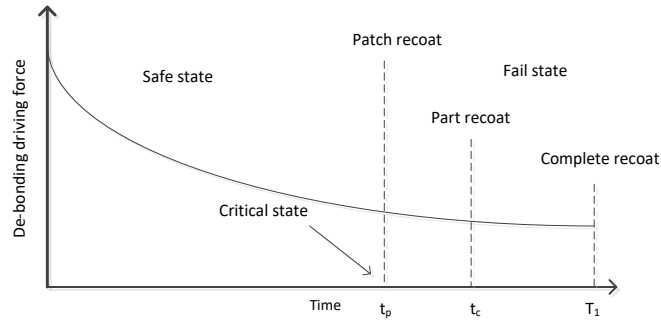
Annual cost_{component repair}

$$\begin{aligned}
 &= \sum_{c=0}^n (Ar_c * Sp_c) + (Sp_c * C_c) \left[\frac{ir(1+ir)^t}{(1+ir)^{t_c} - 1} \right] \\
 &+ \sum_{e=0}^n A_e * (Sp_e + C_e) \left[\frac{ir(1+ir)^t}{(1+ir)^{T_e} - 1} \right] \\
 &+ \sum_{i=0}^n i_Cost_i \left[\frac{ir(1+ir)^t}{(1+ir)^{t_i} - 1} \right] \\
 &+ \sum_{m=0}^n m_Cost_m \left[\frac{ir(1+ir)^t}{(1+ir)^{t_m} - 1} \right]
 \end{aligned} \tag{5.20}$$

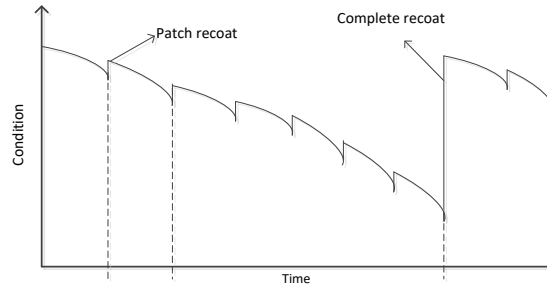
Annual cost_{Complete repair}

5.21

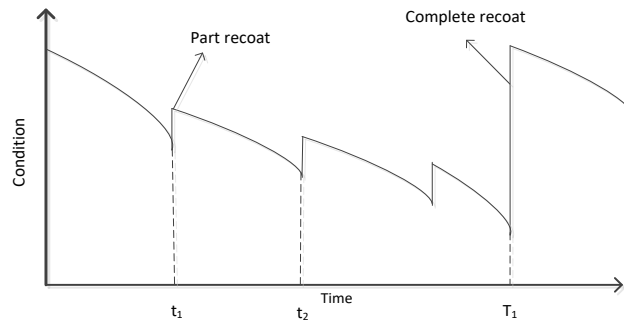
$$= \sum_{e=0}^n A_e * (Sp_e + C_e) \left[\frac{ir(1+ir)^t}{(1+ir)^{T_e} - 1} \right] \\ + \sum_{i=0}^n i_Cost_i \left[\frac{ir(1+ir)^t}{(1+ir)^{t_i} - 1} \right] + \sum_{m=0}^n m_Cost_m \left[\frac{ir(1+ir)^t}{(1+ir)^{t_m} - 1} \right]$$



(a) Profile for the de-bonding driving force



(b) Profile for Patch recoat maintenance strategy



(c) Profile for Part recoat maintenance strategy

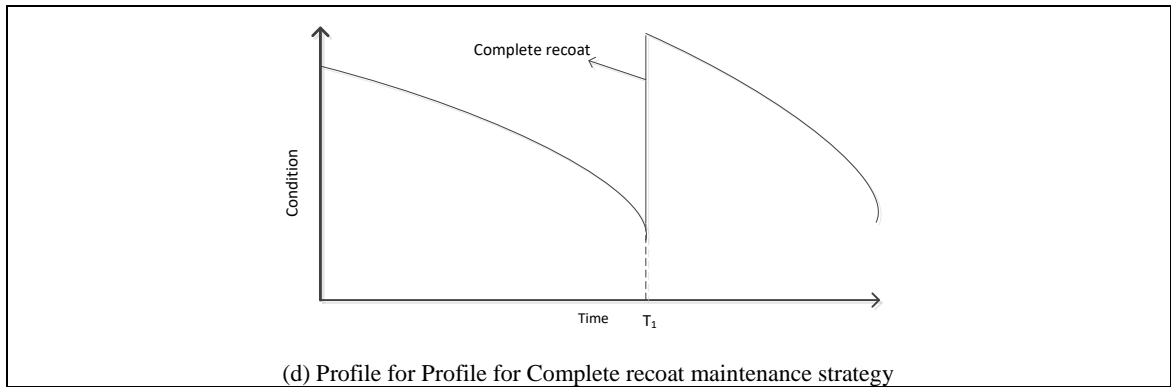


Figure 5.5: Profiles for de-bonding driving force and maintenance strategies

5.3 Maintenance history database

The proposed algorithm for optimal maintenance is based on various parameters which have not been considered in classical maintenance frameworks. The feedback system based on historical maintenance database and real-time monitoring will assist in minimising the error rate for individual structure. Therefore, a uniform database is required for collection of various important parameters. The required database has been elaborated comprehensively in Table 5.3.

Table 5-3: Uniform Database for Maintenance of metal structures

Parameter	Description
Inspection history	The inspection activity is very time-consuming for the organisations which are operating number of large metal structures such as museums, aerospace, automotive and defence industry. The historical data regarding the frequency of inspections with a degree of deterioration associated with the individual structure will help in minimising the inspection frequencies and cost incurred by inspection activities.
Coating thickness	According to experimental investigations, the appropriate application of coating thickness can increase the useful coating life. Some parts of the structure may require more thickness and some parts may require less coating thickness which can impact the coast of re-coting maintenance.

Interfacial roughness	The adhesion strength between coating and substrate system is affected by interfacial roughness. The appropriate selection of roughness can increase useful coating life.
Salinity	The diffusion of water-soluble salt particles at the interface of coating-substrate results in coating failure and corrosion damage (Latif, J. et al., 2018a). The record of accumulation of salt particles over the structure operating in any specific environmental will assist for accurate maintenance actions.
Stress/Strain	The temperature gradient is responsible for the development of stresses within the coatings which result in blistering and micro-cracks coating failure (Nazir, M. et al., 2016b). The real-time and historical data of stress/strain can assist in making accurate prediction of coating failure for any specific environmental conditions.
Meteorological factors	The variation in environmental conditions and complex architectures of structures may experience variable humidity and temperature within the structure also. For example, the inside parts of the structure may experience high temperature as to outside parts.
Geometrical shape	According to the visual inspection of military vehicles at “The Tank Museum”, the coating failure rate on curved surfaces was found higher than as compared to flat surfaces of military vehicles.
Failure frequency	The failure frequency of patch and parts of individual structures along with historical data of its operating conditions will assist in more efficient maintenance decisions for individual structures.
Time-to-	The time-to-maintenance of the individual structure will vary

maintenance	depending on the type of maintenance strategy. For example, the time for complete recoating of the structure undergoing Part recoating maintenance may come earlier than the structure undergoing only Complete recoating maintenance strategy.
Type of coating applied	The structures are often coated with number coatings for corrosion protection and also for decoration.
Operational activities	The operating condition of structures is one of the most important factors for accurate prediction of deterioration of individual structures. The historical data of operating conditions will assist in making efficient maintenance decision for specific structures.
Area recoated (specific to Part)	The standard ASTM D610 can be used to identify the degree of delamination and area to be re-coated.
Cost of maintenance activities	The cost of maintenance activities includes washing, preparing equipment for re-coating, surface treatment, drying, labour hours and other cost associated with maintenance activities.
Prediction error	The prediction error gap between theoretically calculated data and real-time events can be minimised by recording the error history and applying an efficient neural network to adjust future predations.

5.4 Algorithm implementation

The implementation of the proposed algorithm has been comprehensively elaborated in Figure 5.6. It computes useful coating life using prognostic models and applies maintenance cost analysis. The specification of structural steel S275 and red oxide primer coating has been considered for simulation analysis. The Elastics modulus and coefficient of thermal expansion of red oxide primer coating are 6.14 GPa and $21.6 \times 10^{-6}/^{\circ}\text{C}$, respectively. The Elastics modulus and coefficient of thermal expansion

Chapter 5: Condition-based-Maintenance

of structural steel S275 are 210 GPa and $12 \times 10^{-6}/^{\circ}\text{C}$, respectively. Two propositions have been considered for simulation analysis.

Proposition 1: The adhesion strength between coating and substrate has found to be proportional to the thickness of the coating. The useful coating life can be extended with an appropriate increase in coating thickness. The occurrence of the blister is considered as patch failure and algorithm is simulated for various coating thickness to find the financial impact on Patch recoating maintenance strategy.

Proposition 2: The annual cost of maintenance of Patch recoating and Part recoating maintenance strategies have been compared. The only damaged area is recoated in Patch recoating and complete part is recoated in Part recoating. In order to analyse all possible conditions, the algorithm is simulated for different size/area of the part while keeping the constant patch area. The number of patch failures and area of a part per year is increased for the next ten years (e.g. 2x means twice the size of patch area).

The equations of de-bonding driving forces are converted into dimensionless form as mentioned in Chapter 3.

$$\tilde{F} = \frac{(1/\tilde{E}) \tilde{M} (1/\tilde{x})}{1 + \tan\left((1 - \tilde{B}) \frac{1}{-\tan \omega}\right)^2} \left[1 + \frac{1}{4} (\sqrt{\eta - 1})^2\right] \quad 5.22$$

$$\tilde{F}_{cr} = \frac{(1/\tilde{E}) \tilde{M} (1/\tilde{x})}{1 + \tan\left((1 - \tilde{B}) \frac{1}{-\tan \omega}\right)^2} \quad 5.23$$

The description simulation steps of Equations 5.22 and 5.23 have been mentioned in nomenclature and Chapter 3 of the report.

For preposition 1, the algorithm estimates the annual cost for Patch recoating maintenance for various values of coating thickness. In proposition 2, the algorithm is calculating the annual cost for patch recoat and Part recoating strategy with one complete recoating of structure in both strategies. The annual cost of corrosion for the next ten years duration is calculated that starts from one patch failure per year. It also estimates the cost of maintenance by incrementing from 1 to 10 patches/year.

Chapter 5: Condition-based-Maintenance

After calculating the cost of maintenance for Patch recoating strategy, the algorithm calculates the cost of maintenance for Part recoating with increasing area of the part. The cost of maintenance for the next ten years is calculated by keeping the area of Part '2x' times of patch area. Similarly, the algorithm increases the area of part '3x' times and estimate cost for the next ten year. The calculation repeats 10 times with an increase in part area (such as '4x,'5x'...'10x').

Chapter 5: Condition-based-Maintenance

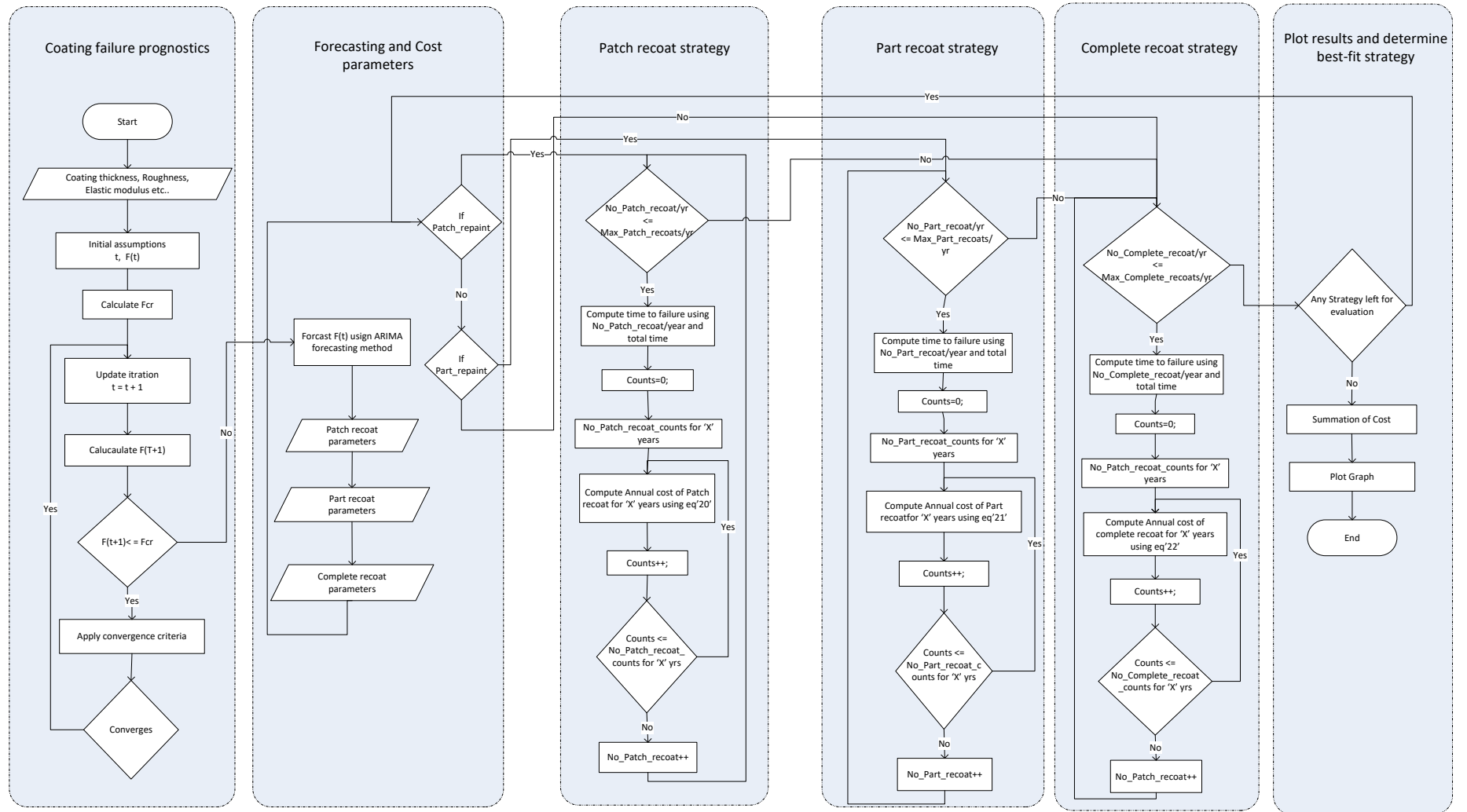


Figure 5.6: Recoating Maintenance Strategy Evaluation Simulation

5.5 Results and discussion

Proposition 1: The results in Figure 5.7 show the de-bonding driving force ' \tilde{F} ' as a function of de-bonding index ' \cap ' for different relative coating thickness ' T_{th}/s ' values. The increase in coating thickness has resulted in increasing critical de-bonding threshold level ' fcr_n '. The threshold level of critical de-bonding driving force ' fcr'_1 ' for relative coating thickness '0.1' is lower as compare to the critical threshold level de-bonding driving force ' fcr'_2 ' for relative coating thickness '0.2'. Similarly, the threshold level of critical de-bonding driving force ' fcr'_2 ' for relative coating thickness '0.2' is lower as compare to the critical threshold level de-bonding driving force ' fcr'_3 ' for relative coating thickness '0.3'. When the value of debonding index ' \cap ' is greater than 1, the system is considered in fail state and blister failure has occurred which is referenced as patch failure in current simulation.

The Patch recoating is required when the de-bonding driving force exceeds its critical threshold level. The increase in coating thickness raises the critical threshold level of de-bonding force which means the coating-substrate system will have more time to get into fail state. The increase in adhesion strength will result in a reduction of patch failures which will also reduce the cost of maintenance. The comparison for the annual cost of maintenance of the coating-substrate system with different coating thickness is shown in Figure 5.8. The increase in coating thickness also increases the cost of coating application but it also decreases the patch failures due to an increase in adhesion strength. Therefore, it can be concluded that the annual cost of maintenance can be reduced by increasing the appropriate increase in coating thickness.

Proposition 2: The comparison between Patch recoating and Part recoating maintenance strategies has been analysed for various conditions as shown in Figure 5.9. Every value in simulation result is showing the annual maintenance cost of 10 years of time duration. The unit cost of surface preparations and coating application is considered equal for both strategies for simulation analysis. At least one Complete recoat per year is included in both strategies with equal cost. The primary objective of simulation analysis in Proposition 2 is to evaluate optimal maintenance strategies among Patch recoat and Part recoat.

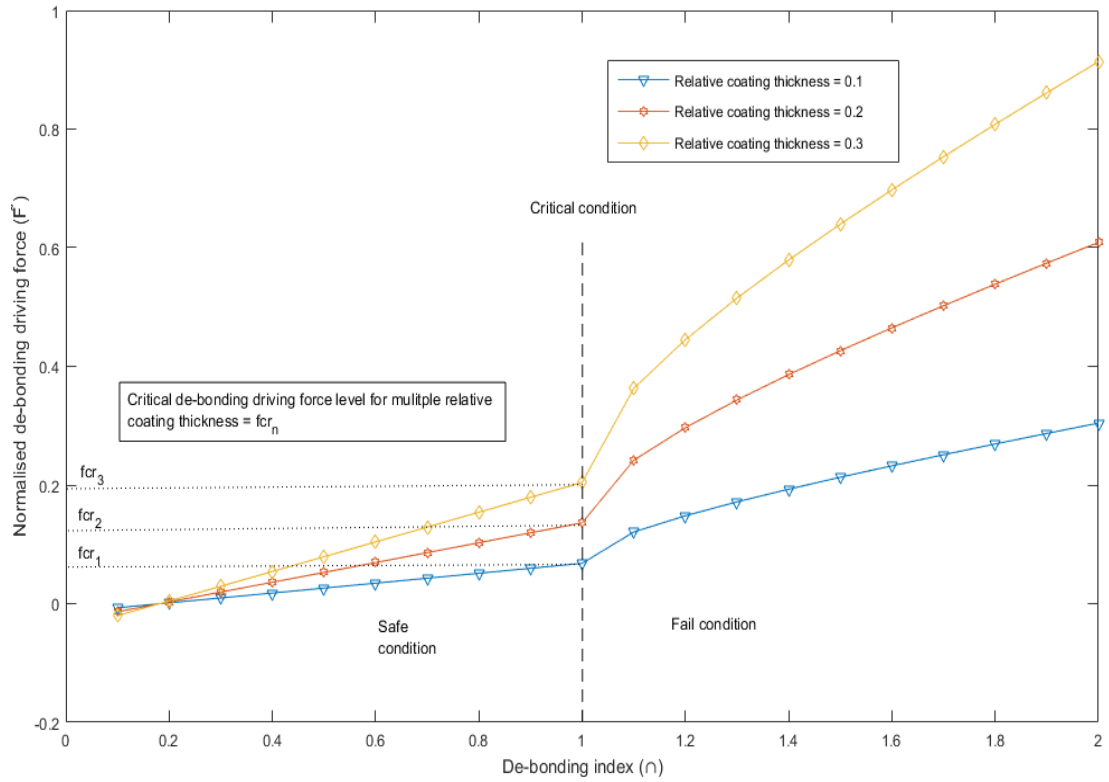


Figure 5.7: Simulation results for de-bonding driving force vs de-bonding index

The algorithm begins with calculating the annual cost of maintenance for Patch recoat strategy by considering one recoat of patch failure and one complete recoat. In the next iteration, the algorithm calculates the annual cost for the next 10 years by considering 2 patches per year. The cost of maintenance is proportional to the patch failures per year as shown in Figure 5.9 and maximum for 10 patch failures per year. The area is increasing in every iteration during the calculations for Part recoating strategy. The area of the part is considered '2x' in the second iteration which means twice the area as compared to Patch area. Similarly, the area of part increases in every next iteration and goes up to '10x'.

The algorithm has resulted in suggesting different recoating maintenance strategies depending on the area of patch failure and part failure. The trends of the cost associated with both maintenance strategies are crossing at point A. It is suggesting that the Patch recoat strategy is resulting in high cost when a number of patch recoats are greater than 4 per year and area of the Part is 5 times greater than the area of Patch failure. The Part

Chapter 5: Condition-based-Maintenance

recoating strategy is resulting in high cost when patch recoat is less than 4 per year and the Part area is 5 times greater than the area of patch failure that requires recoating.

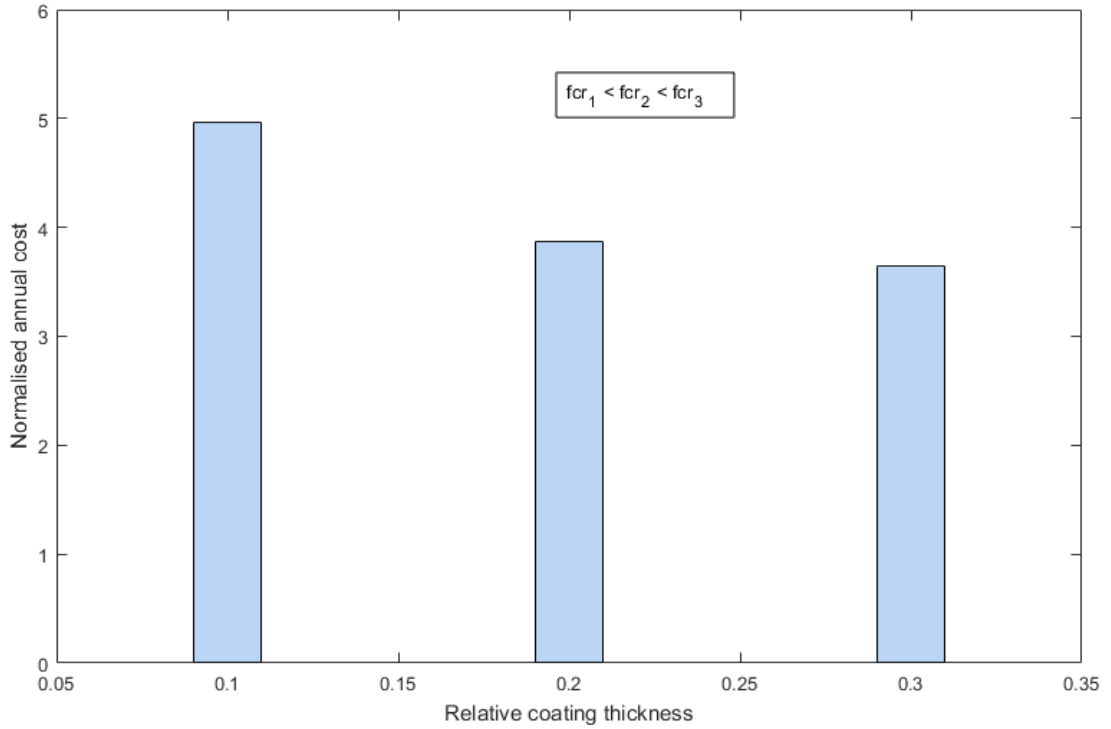


Figure 5.8: Annual cost of maintenance for coating-substrate system with different coating thickness

The conclusion can be drawn from point A that the Patch recoat is the optimal strategy for metal structure which has patch failure less than 4 per year and that area of its part is '5x' larger than patch area. Similarly, the Part recoat is the optimal strategy for metal structure which has patch failure more than 4 per year and that area of its part is '5x' larger than patch area. Several crossing points can be seen in simulation results that show the optimal recoating strategy for various conditions depending on area of parts.

5.6 Conclusion

The proposed framework does cost comparison based on the performance between coating-substrate systems of different specifications. The performance is defined by validated prognostic model of bonding driving force but in this case the output is in terms of cost. Systems with different specifications such as variable coating thickness can be compared that could help professionals in decision making process of maintenance strategy. The algorithm can also be simulated for various specifications

Chapter 5: Condition-based-Maintenance

and operating conditions for the coating-substrate system. The benchmarks for the part failure of the individual structure, historical maintenance data and real-time parameters are the major limitations for effective implementation of the proposed system. Therefore, the uniform database has been proposed and real-time monitoring system has been developed which is illustrated in the next Chapter.

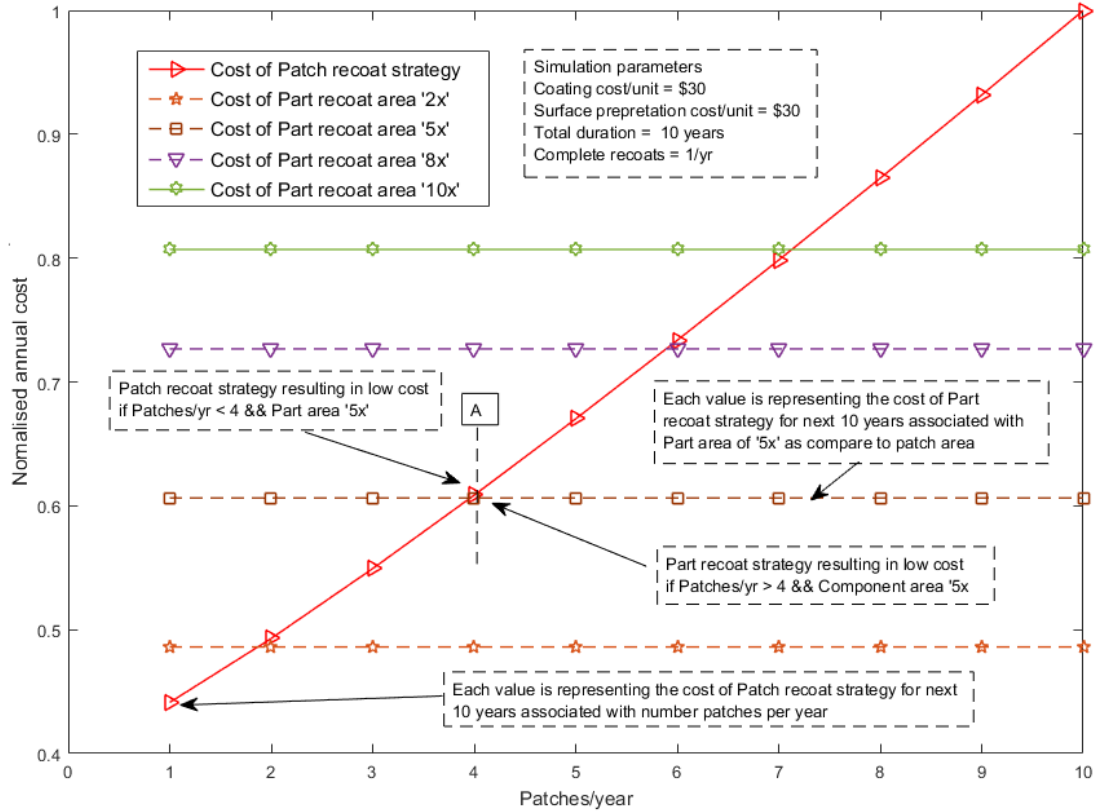


Figure 5.9: Simulation results for recoating maintenance strategy for metal structures

Chapter 6: Wireless Condition Monitoring System

The research findings within the NCEM research group in last few years have resulted in the development of state-of-the-art multidisciplinary prognostic solutions. These prognostic solutions are further extended to the development of algorithms for failure propagation and optimisation framework for maintenance strategies. The current work focuses on structures operating stationary and mobile at remote locations in diverse atmospheric conditions. The movement of structures and continues variation in environmental conditions make the accurate prediction more challenging. Therefore, the prediction based on real-time parameters is evident for critical structures for accurate life assessment and the selection of optimal maintenance strategy. Real-time monitoring systems have been developed for remote monitoring to further extend the research findings for accurate damage assessment prediction. The development of the condition monitoring system has been elaborated in the current chapter. The contents of the chapter have been mentioned in Figure 6.1.

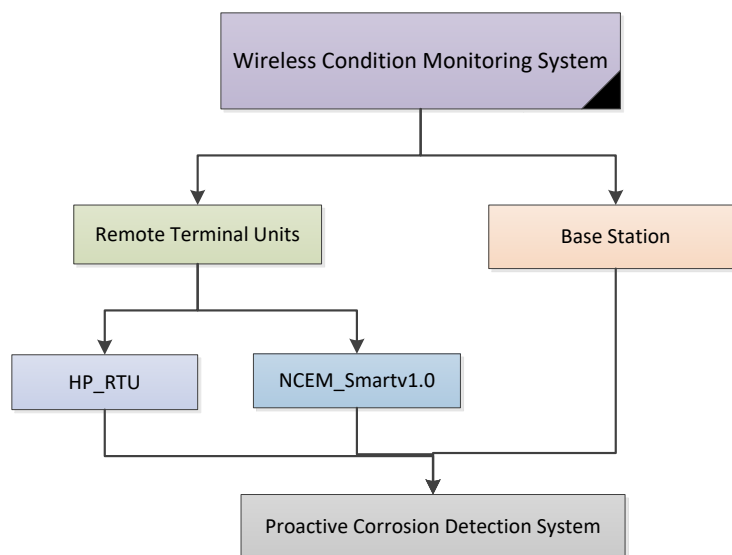


Figure 6.1: Contents of the chapter

6.1 Wireless Condition Monitoring System

The development of remote condition monitoring requires wireless remote terminal unit (RTU) and the base station. The wireless remote terminal unit attached with sensors for

Chapter 6: Wireless Condition Monitoring System

measurements of critical parameters and should be able to transmit data wirelessly to the base station. The base station needs to collect data and store in database for further data analysis. Two remote terminal units have been developed along with the base station system during the current project as shown in Figure. 6.2. The HP_RTU (High-Performance Remote Terminal Unit) is based on high-performance data acquisition systems developed by National Instruments (Instruments, N.). The second remote terminal unit is low cost based on commercially available Arduino boards and integrated circuits. The purpose of developing high-performance remote terminal unit is to utilise it for experimental purpose and set as a benchmark for low-cost remote terminal unit. The remote terminal units are attached with sensors which are embedded on a target object such as a vehicle. The current remote terminal system contains temperature, humidity, strain gauge and corrosion sensors. The base station is receiving data and storing it in a database for further analysis.

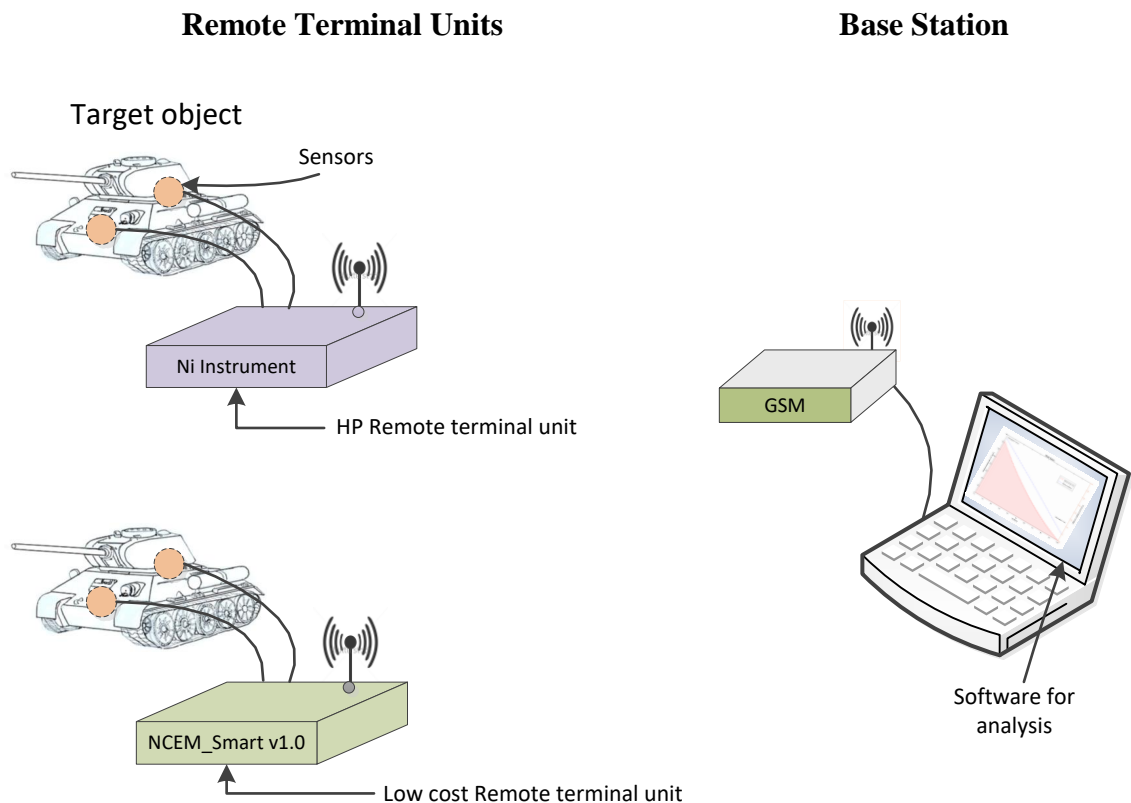


Figure 6.2: Wireless Condition Monitoring System

6.2 Remote Terminal Units (RTUs)

The algorithm for RTU is explained through flowchart shown in Figure. 6.3. The remote terminal unit initialises Global System for Mobile Communications (GSM) system and attempts to register with a network of corresponding SIM card. If the registration is successful, the system proceeds to the next stage otherwise it tries again by setting status LED for indication of an unsuccessful attempt. The next stage is to energise the electrical circuits which are connected with sensors to take measurements. The sensor suite includes corrosion, strain gauge, temperature and humidity sensors. After acquiring measurements from sensors, the values are concatenated in the form of a message. The date and time at which measurements have been taken are also included in the message. Every remote terminal unit has its own device address that needs to be added in a message to get recognised by the base station. The system will wait for time interval set by the user for the next measurement. The time interval depends on the operating conditions of the structure. If steady operating environment is expected then the time interval could be longer. If an unsteady and frequent change in operating conditions is expected then time interval could be small.

6.2.1 *HP_RTU*

The HP_RTU module based on commercially available NI systems have been developed for Laboratory experimentation and validation of results as compared to low-cost RTU module. Furthermore, it can be used for various other experimental purposes in Laboratory. The National Instruments provides various types of CompactDAQ and CompactRIO controllers which can be programmed and configured for a wide range of stand-alone applications including research and analysis, design validation and verification, manufacturing, quality testing, diagnosis, maintenance, automation and condition monitoring of structures. The CompactDAQ is data acquisition unit which integrates with compatible software and hardware modules that provide signal conditioning for sensors and data transmission. It enables the engineers for speedy development and implementation of the system application. On another hand, The CompactRIO is a real-time embedded controller which is a combination of reconfigurable I/O modules, field-programmable gate array (FPGA) module, real-time controller and Ethernet expansion chassis.

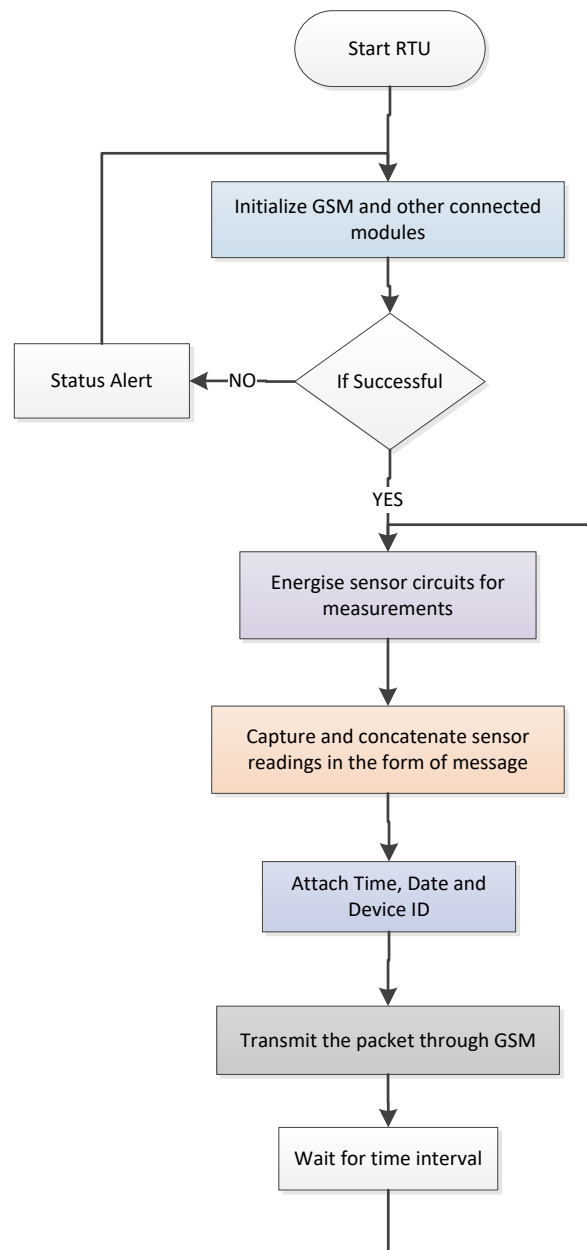


Figure 6.3: Flowchart for Remote terminal unit

It includes a real-time microprocessor to support a wide range of clock frequencies and implementation of the application based algorithm. The Third-party modules can also be attached with CompactRIO for additional features. The applications that require high-performance data computing can be implemented on Field Programmable Gate Arrays (FPGA) module in Compact RIO. Therefore, the cRIO-9063 controller is considered an ideal choice for research and development of real-time condition

Chapter 6: Wireless Condition Monitoring System

monitoring system and for future research. The cRIO-9063 controller as shown in Figure 6.4 is high-performance, reliable and rugged with industrial standard certification. The complete specifications of cRIO-9063 controller are given in Appendix F.



Figure 6.4: cRIO-9063 controller (Appendix G)

The sensors detect any change in the environment through change in resistance and they are also connected with electronic circuits for signal conditioning. The current, voltage and resistance within electronic circuit follow Ohm's Law ($\text{Voltage} = \text{Current} * \text{Resistance}$). The change in environment results changes in resistance of sensors and the change in resistance results in variation of current and voltage. The NI-9207 I/O module is used which contains current and also voltage inputs. The sensor with voltage or current output can be connected to NI-9207 which is embedded with cRIO-9063 controller. The NI-9207 provides 8 input voltage channels of ± 10 volts with 24-bit resolution and 8 current input channels of $\pm 20\text{mA}$. In the current project, the μLPR sensor and micro-strain gauge sensors are connected to NI-9207 for signal conditioning.

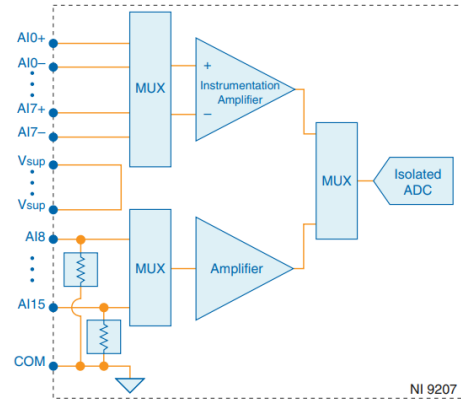
The corrosion rate is measured through the change in current using μLPR sensor which is connected to the current channel of NI-9207 and the $\mu\text{-strain}$ gauge sensor measures development of stresses on coating surface that is connected to voltage channel of NI-9207. The internal circuit diagram of NI-9207 is given in Figure 6.5(b) which contains multiplexers, amplifiers, and analog-to-digital converter. The input signals are scanned then amplified at an appropriate voltage or current level. The signals are then conditioned and sampled by using analogue-to-digital converter of 24-bit

Chapter 6: Wireless Condition Monitoring System

resolution. The complete description and specifications of NI-9207 are given in Appendix H.



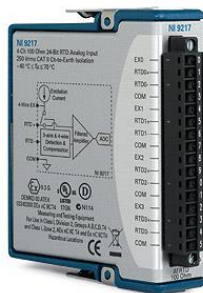
(a) NI-9207



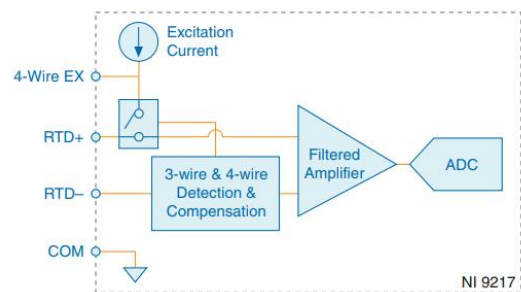
(b) Internal circuit diagram

Figure 6.5: NI-9207 module (Appendix H)

Another I/O module used for signal conditioning for temperature sensors is NI-9217. It provides four input channels for PT100 RTD. The internal circuit diagram of NI-9217 is shown in Figure. 6.6(b). The circuit contains connection for excitation current, detection module for 3-wire and 4-wire type PT100 RTD, amplifier and analogue-to-digital converter. It provides 1mA of excitation current per channel. The 3-wire and also 4-wire type of PT100 RTD are compatible and detected automatically by NI-9217. The signal is amplified and converted into digital signal with 24-bit resolution. The complete description and specifications of NI-9217 are given in Appendix I.



(a) NI-9217



(b) Internal circuit diagram

Figure 6.6: NI-9017 module (Appendix I)

Chapter 6: Wireless Condition Monitoring System

The third-party module SEA-9741 as shown in Figure 6.7 is used for wireless transmission of sensors measurements to the base station (Sea-Gmbh). It offers various features and support for text messaging (SMS), remote access via mobile network, web-based configuration and Global Positioning System. The SMS feature has been used for the development of a condition monitoring system in the current project. The complete description and specifications of SEA-9741 are given in Appendix J.



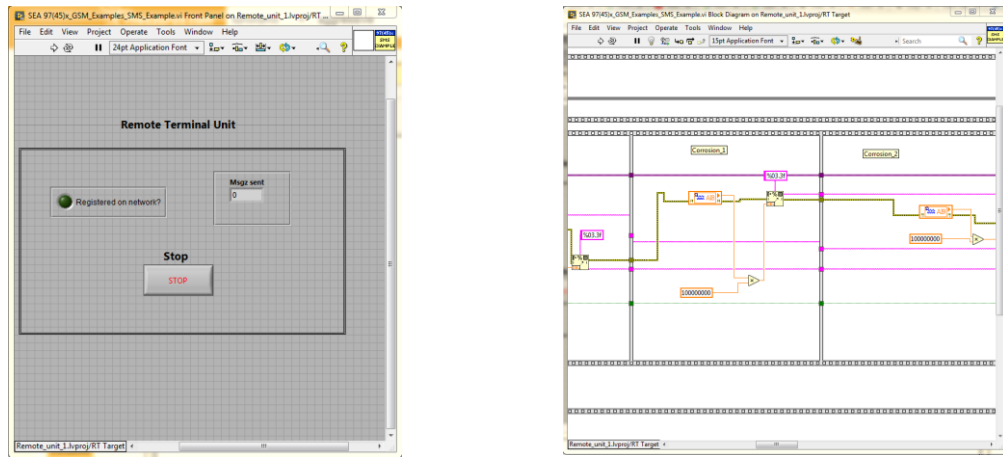
Figure 6.7: SEA-9741 module (Appendix J)

The I/O modules NI-9027 and NI-9217 along with third-party module SEA-9741 are connected with cRIO-9063 to form a high-performance wireless remote terminal unit. The sensors are attached with I/modules and the RTU is configured and programmed according to the flowchart shown in Figure 6.3 using Laboratory Virtual Instrument Engineering Workbench (LabVIEW) software. The programs-subroutines in LabVIEW are called Virtual Instruments (VIs) which has three components such as block diagram, front panel and connector panel. The block diagram contains functions, icons wires, subVIs and other objects as shown in Figure 6.8(a). The LabVIEW integrates the graphical program on block diagram into the development cycle. The front panel contains indicators and controls as shown in Figure 6.8(b). The connector panel includes terminals that correspond to the indicators and controls of VIs.

6.2.1.1 Application of strain gauge sensor

One of the major driving factors for de-bonding driving force is the development of stress/strain within the coating. The performance of μ -strain gauge sensor has been analysed with the aim of using it for real-time stress measurements at remote locations. Two samples were prepared to analyse the performance of μ -strain gauges.

Chapter 6: Wireless Condition Monitoring System



(a) Front panel

(b) Block diagram

Figure 6.8: Components in LabVIEW software

The μ -strain gauge sensor with grid resistance of $350\Omega \pm 0.2$ has been used to observe the stresses behaviour on the coating surface., the accessories mentioned in Figure 6.9 were used to mount the sensor on the coating surface of the sample. M-Prep neutralizer is applied on coating surface for conditioning before mounting sensor. PCT-2M tape is used to carefully place the sensor on the coating-substrate sample. The strain gauge sensor is then cleaned with M- Bond 200 catalyst-C. The sensor was then attached by using M-Bond 200. After a few minutes the PCT-2M gauge installation tape is removed. The sensor is then attached with wires to connect with Data acquisition unit. The soldering of wires with sensors also involves several steps as shown in Figure 6.10.



Figure.6.9: Accessories used for strain gauge installation



Figure 6.10: Several steps involved in the installation of the strain gauge sensor on the coated sample

The experimental analysis of μ -strain gauge sensor has shown promising results to utilise the configuration for real-time stress measurement. The sample was kept in an environmental chamber to provide different levels of temperature. The result of only one sample is shown in Figure 6.11. It can be seen that the change in temperature is resulting in the development of thermal stress and its behaviour can be observed through μ -strain gauge sensor.

The configuration for mounting the sensor on the sample explained in current work can also be applied on structures which are operating in outdoor environmental conditions by applying protective bonding on the sensor to avoid short circuit problem due to rain. The sensor on the sample was also covered with protective bonding as shown in Figure 6.12. It was dipped in an aqueous solution as shown in Figure 6.13 in the laboratory and checked for any short circuit problem.

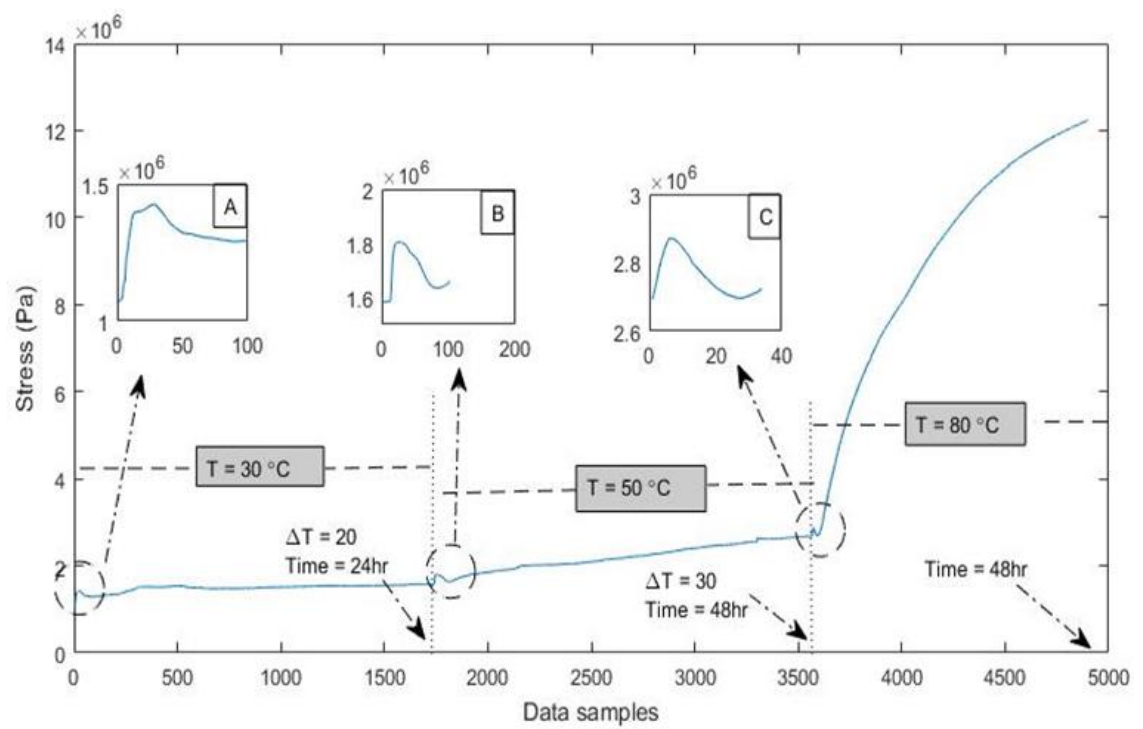


Figure 6.11: Experimental results acquired from strain gauge monitoring system from sample



Figure 6.12: Applying protective coating on the sensor

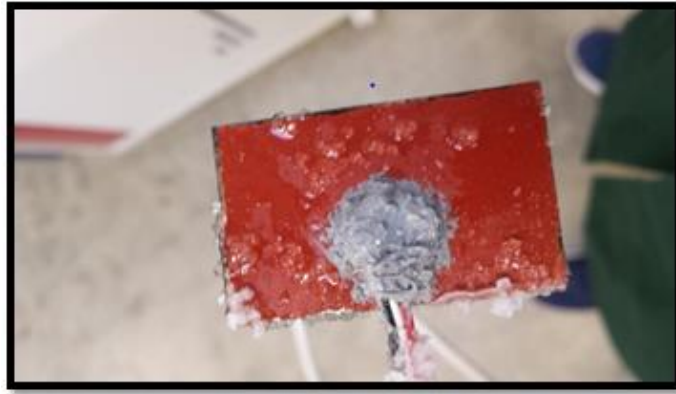


Figure 6.13: Sample after immersion test

The complete HP_RTU system is shown in Figure 6.14 that contains sensors connected with I/O Modules. These modules are attached to cRIO-9063 and SEA-9741 for wireless transmission. The LabVIEW program for HP_RTU system is given in Appendix L.

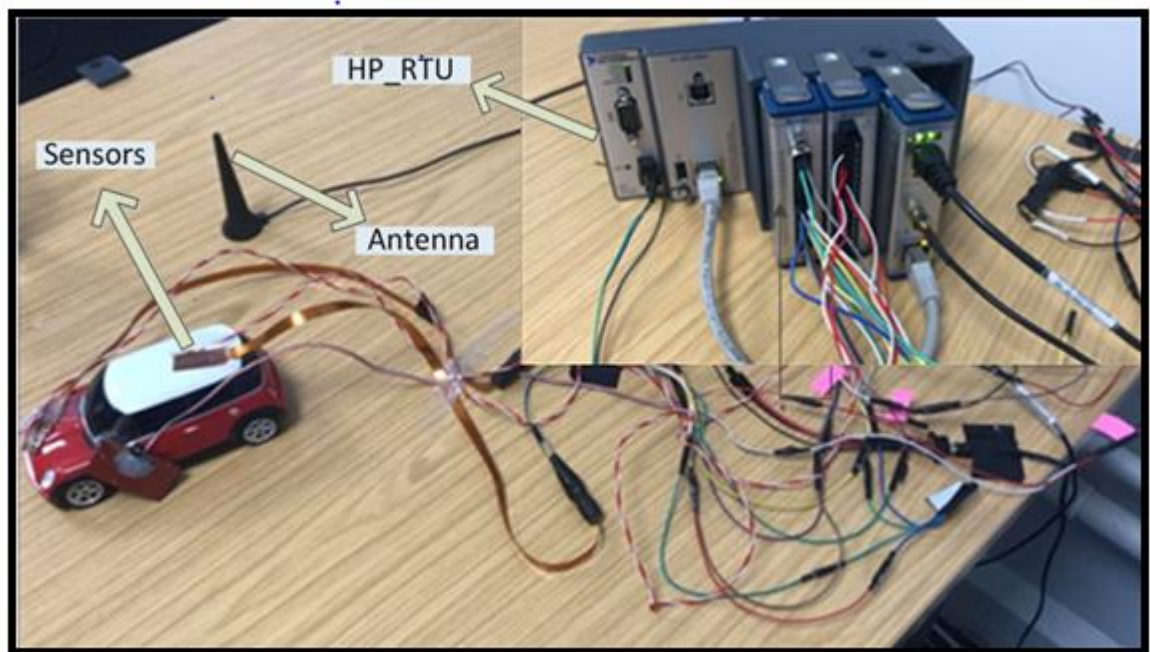


Figure 6.14: High-Performance Remote Terminal Unit

6.2.2 NCEM_Smartv1.0 RTU

The NCEM_Smartv1.0 RTU has been developed for the real-time condition monitoring system for structures operating at remote locations. The low-cost NCEM_Smartv1.0 is developed for monitoring numerous structures in the future to extend the research

Chapter 6: Wireless Condition Monitoring System

findings. The NCEM_Smartv1.0 RTU has multiple channels of Temperature, Humidity, Corrosion and Strain sensors. The flow chart shown in Figure 6.15 illustrates the working of NCEM_Smartv1.0 RTU in detail. The open-source and extendable electronic platform Arduino Mega 2560 Rev3 is selected for development as shown in Figure 6.16. It provides 16 analog inputs and 54 digital I/O's which are adequate to integrate Real Time Clock (RTC), GSM, status leds and multiple channels for sensors. Every NCEM_Smartv1.0 RTU will have its unique device ID to be recognised by the base station. The systems need to be configured for current Time and Date for the first time. The time interval between the sensors measurements can also be adjusted within Arduino IDE software. The NCEM_Smartv1.0 initialises all the attached modules which include GSM, RTC and set the status LED. The status LED indicates the successful initialisation of attached modules and registration of SIM card in GSM.

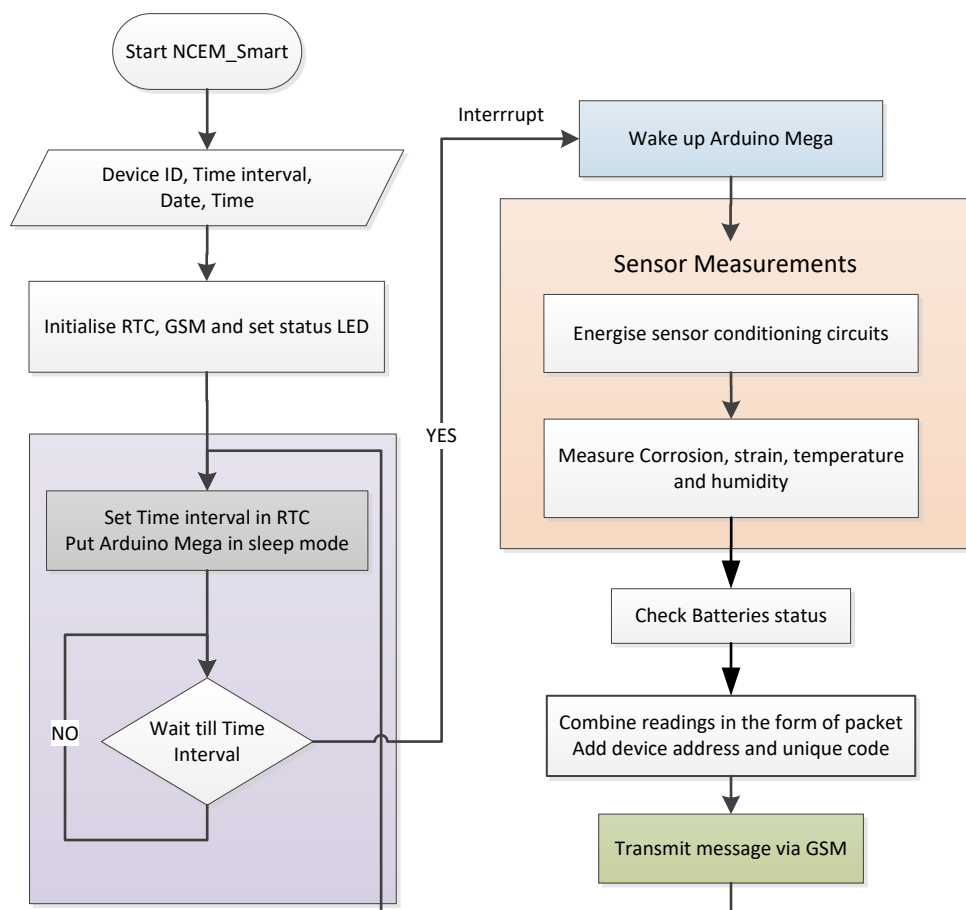


Figure 6.15: Flowchart for NCEM_Smartv1.0

Chapter 6: Wireless Condition Monitoring System

The time in the RTC module as shown in Figure 6.17 can be adjusted to generate an interrupt after a specified time interval. The system goes to sleep mode after adjusting next interval for an interrupt in RTC. This interrupt from RTC wakes up the system to perform interrupt service routine. During the interrupt service routine, the system performs signals conditioning for sensors to take measurements.



Figure 6.16: Arduino Mega 2560 Rev3



Figure 6.17: Real Time Clock

The electronic circuits for sensors were built and attached to Arduino Mega. Figure 6.18 shows the electronic circuit for μ LPR sensor. The DC voltage is converted into a low voltage of $\sim 20\text{mV}$ and applied across sensor and resistor. The corrosion reaction results in a change in resistance which changes current within the circuit. The low current is amplified using non-inverting Operational amplifier IC-741 to make it measurable by Arduino Mega. The gain (G) for IC-741 amplified is given by the following relation:

$$G = 1 + \frac{R_f}{R} \quad 6.1$$

where $R_f = 100k$ and $R = 10k$ in the circuit. The equations to calculate the corrosion rate are implemented in Arduino Mega.

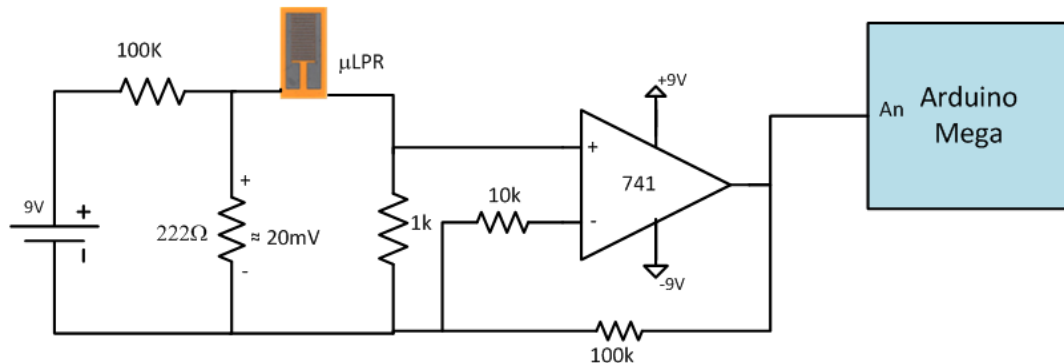


Figure 6.18: Electronic circuit for μ LPR sensor

Chapter 6: Wireless Condition Monitoring System

The electronic circuit for μ -strain gauge sensor connected to Arduino Mega is shown in Figure 6.19. The μ -strain gauge sensor is connected within the Wheatstone bridge. The low voltage of $\sim 20\text{mV}$ is applied across the Wheatstone bridge with known resistances and followed by the following relation:

$$\frac{R_1}{R_2} = \frac{R_0}{R_x} = 1 \quad 6.2$$

Any change in strain results in variation of current within the circuit. The low current is amplified and input into Arduino Mega to record the measurement.

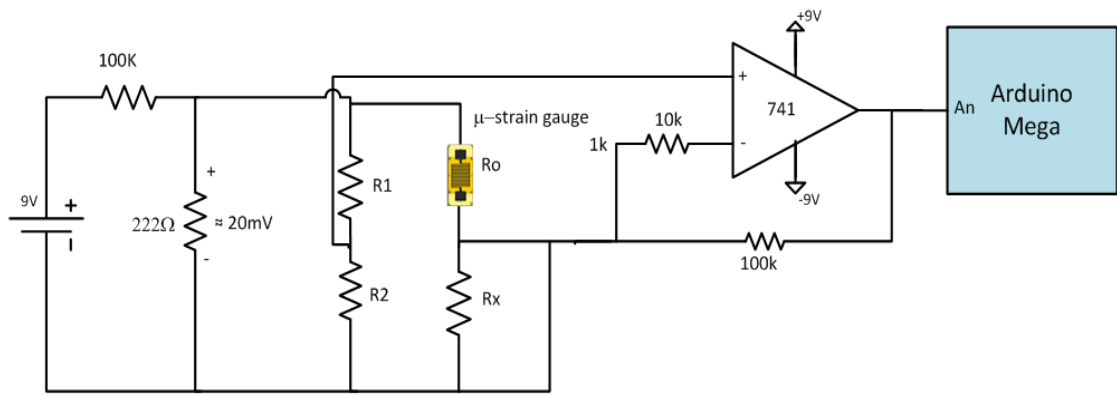


Figure 6.19: Electronic circuit for μ -strain gauge sensor

The DHT22 sensor has been integrated for temperature humidity measurements. The specifications of DHT22 sensor has been mentioned in Appendix K. The electronic circuit for DHT22 sensor is shown in Figure 6.20. The NCEM_Smart system also monitors the power life of the battery. The circuit diagram is shown in Figure 6.21.

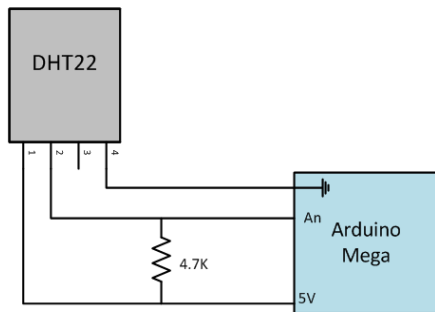


Figure 6.20: Electronic circuit for DHT22 sensor

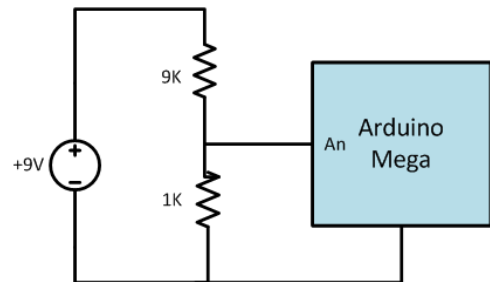


Figure 6.21: Electronic circuit for battery life

After executing the signal conditioning for sensor measurements, all the readings are combined in the form of the message. The device address and unique codes associated

Chapter 6: Wireless Condition Monitoring System

with sensors are included in the message. The GSM module shown in Figure 6.22 transmits the data to the base station using SIM card.



Figure 6.22: GSM module

The system will set up next time in RTC for next interrupt and goes to sleep mode till next measurements. The developed NCEM_Smartv1.0 RTU system is shown in Figure 6.23. The data sheet and program code of NCEM_Smartv1.0 are given in Appendices M and N, respectively.

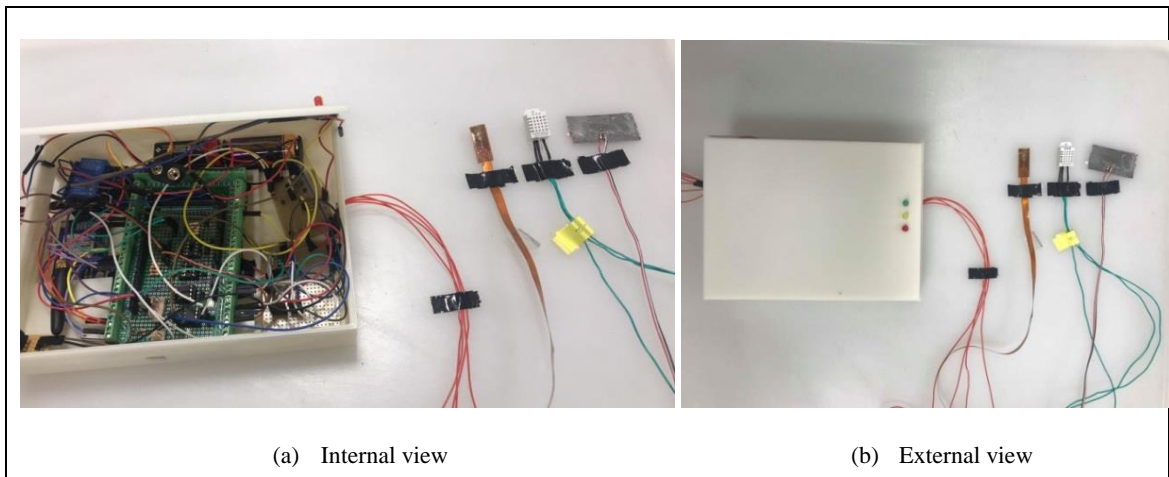


Figure 6.23: NCEM_Smartv1.0 RTU

6.3 Base Station

The algorithm executing at the base station is explained through the flowchart shown in Figure 6.24. The software at the base station attempts to register for network connection. It constantly checks for incoming messages from any remote terminal unit. If any message is received from the remote terminal unit then it identifies the remote terminal unit through device address, decrypts the message to extract sensors readings and store into the database. Each remote terminal unit has its own database file. The real-time measurements are also visible on the graphical user interface which also

Chapter 6: Wireless Condition Monitoring System

shows the location of the corresponding sensor on the structure. The Graphical user interface of software at the base station attached with GSM is shown in Figures 6.25 and 6.26. The LabVIEW program of base station is given in Appendix O.

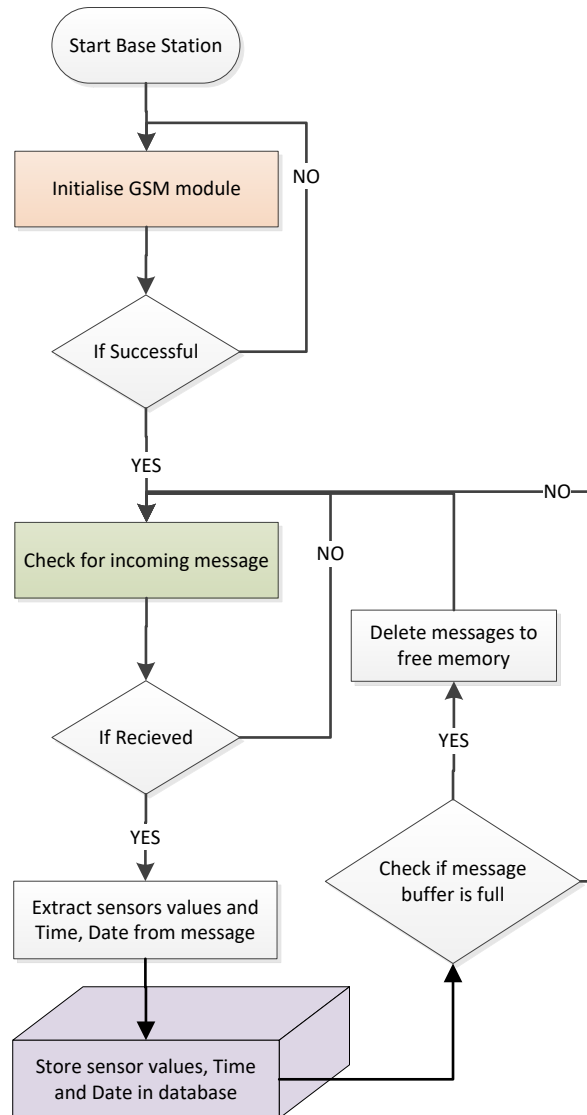


Figure 6.24 Flow chart for Base Station

The sensors were also tested in the laboratory to validate the sensor measurements and wireless monitoring. The sensors were kept in a salt spray chamber to observe the behaviour according to the environment in the chamber as shown in Figures 6.27 to 6.31.

Chapter 6: Wireless Condition Monitoring System

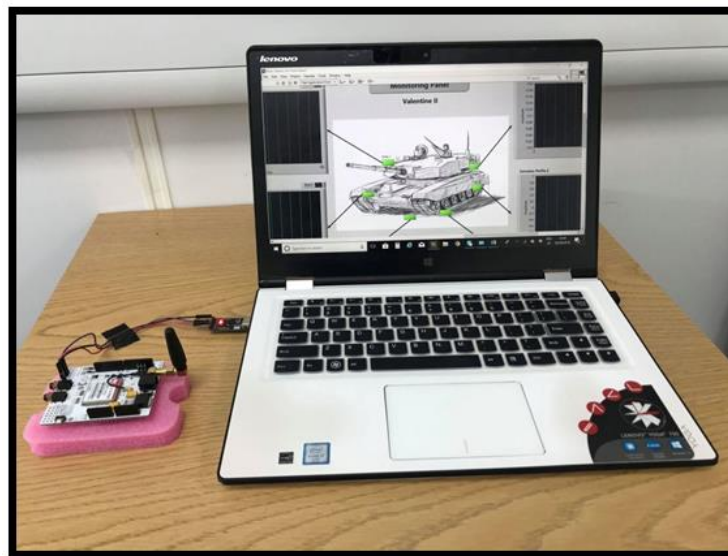


Figure 6.25: Base Station system

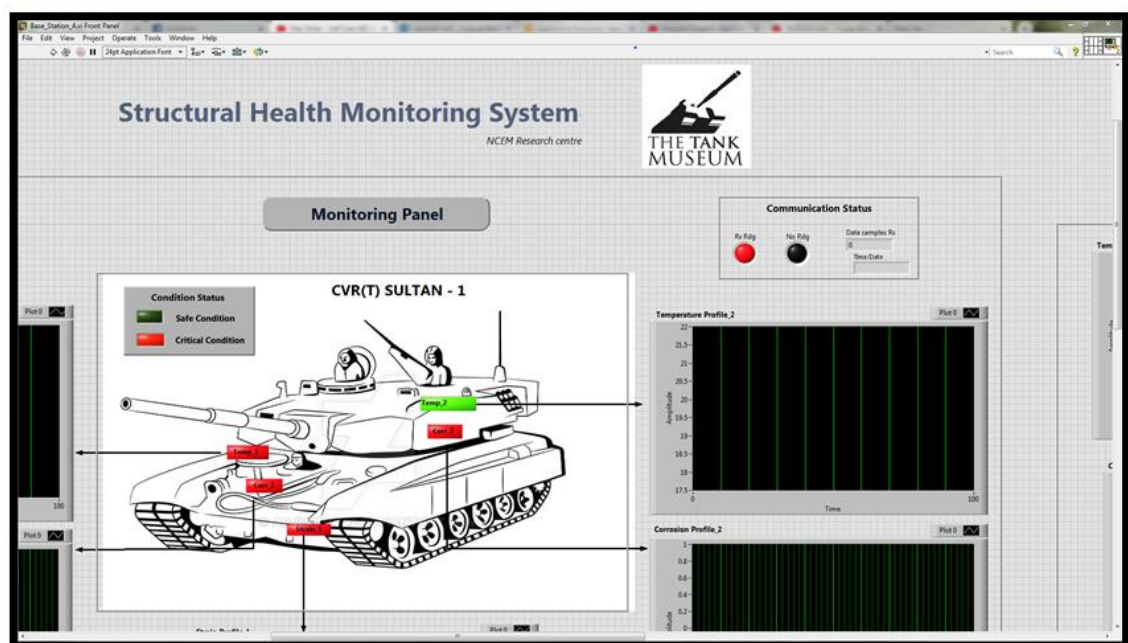


Figure 6.26: Graphical user interface of software at the base station

Chapter 6: Wireless Condition Monitoring System

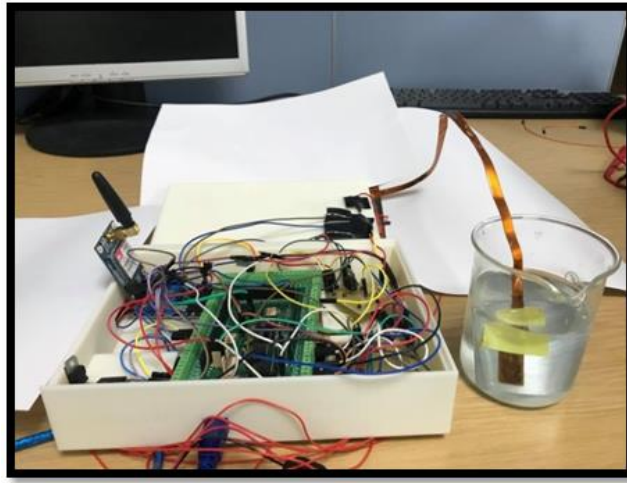


Figure 6.27: Inserting a corrosion sensor in an aqueous salt solution to verify the corrosion detection

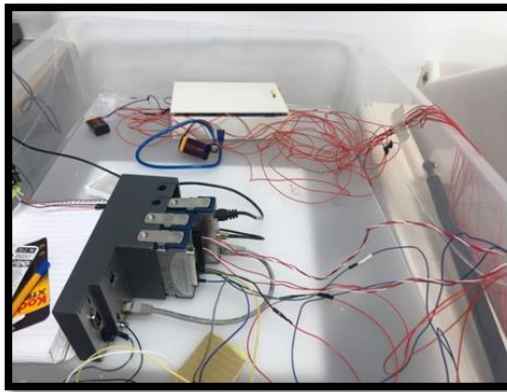


Figure 6.28: The RTU's connected with sensors

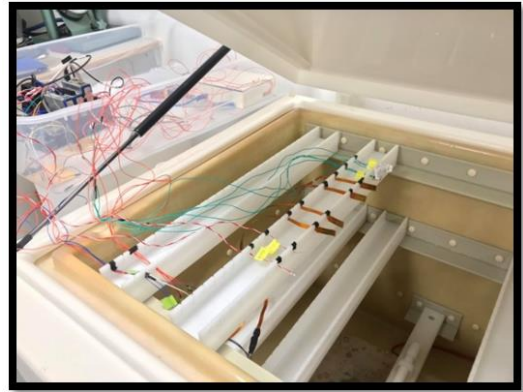


Figure 6.29: Sensors are kept inside the salt spray chamber

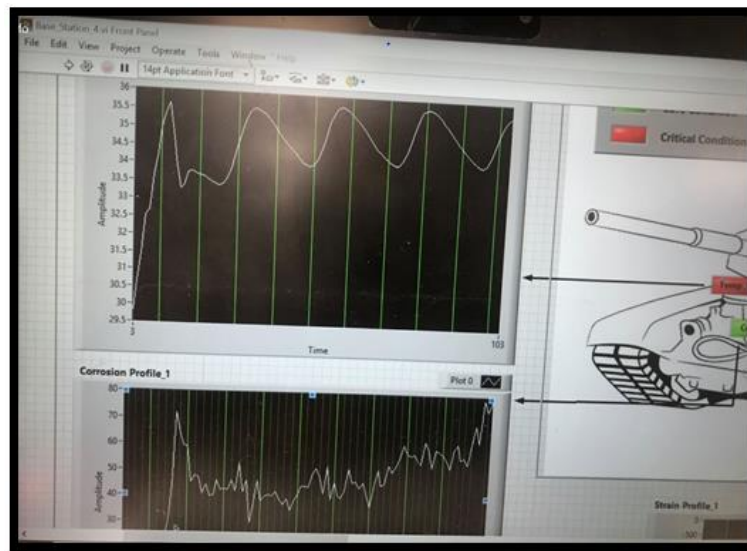


Figure 6.30: The base station system displaying measurements from RTUs

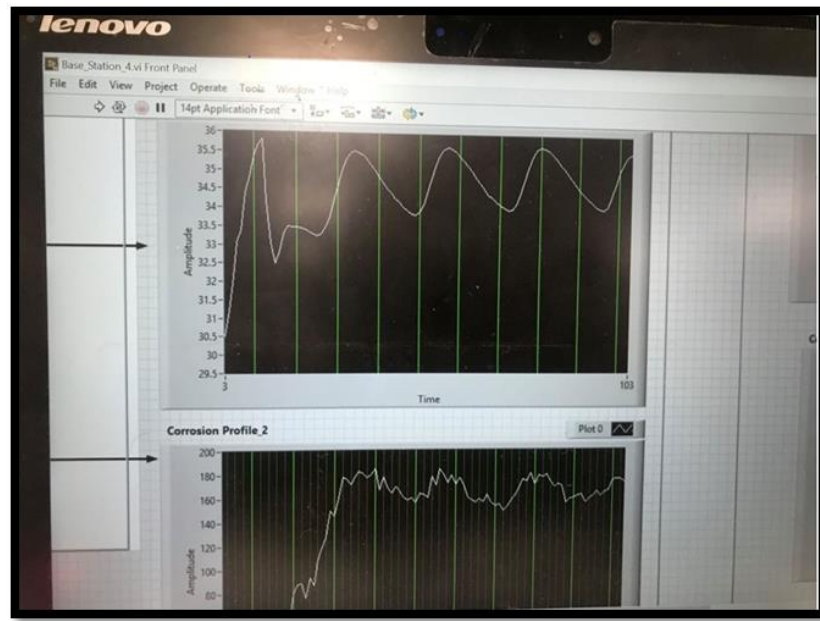


Figure 6.31: The base station system displaying measurements from RTUs

6.4 Proactive Corrosion Detection System

The military vehicles in ‘The Tank Museum’, Bovington, UK are often operated in diverse and harsh atmospheric conditions in the coastal region of Dorset, UK. The wind speed, high amount of salinity in the air and variation in temperature as vehicles moves to different locations and environment causes a potential threat to high-value large vehicles. The past study has revealed that the tensile stresses due to temperature gradient are responsible for the opening of micro-cracks which controls the number of corrosive particles diffusing into the coating-substrate interface. The proposed system based on chemical and mechanical sensors to detect any potential threat to structure in two stages. In the first stage, the μ -strain gauge sensor monitors the opening and contraction of micro-cracks by measuring residual stresses due to change in temperature. In the second stage, the corrosion sensor under the coating will detect corrosion reaction due to the diffusion of corrosive particles into coating-substrate. The experimental setup based on the proposed technique is well illustrated in Figure 6.32.

The stresses developed in coating depend on the differential thermal expansion of coating and substrate material. The difference in coefficient of thermal expansion between coating and substrate plays a major role in the behaviour of stresses in the coating as the increase in difference results increase in stress level. Consider a coating-substrate system with an applied coating having a higher value of the coefficient of

thermal expansion than the substrate. In past experimental study, It was observed that when the temperature drops, the coating tries to shrink but the substrate having low value of the coefficient of thermal expansion restricts the coating to contract as a result the coating experiences tensile stress which opens the crack and allows corrosive particles to diffuse (Nazir, M. et al., 2015b). The development of tensile stress in coating resulting in the opening of crack and allowing corrosive particles to diffuse as shown in Figure 2.12. The sensor suite in the current work contains temperature sensor, μ -strain gauge sensor and μ LPR sensor. The strain gauge temperature sensor monitors change in temperature, μ -strain gauge monitors the development of residual stresses and μ LPR sensor detects corrosion reaction.

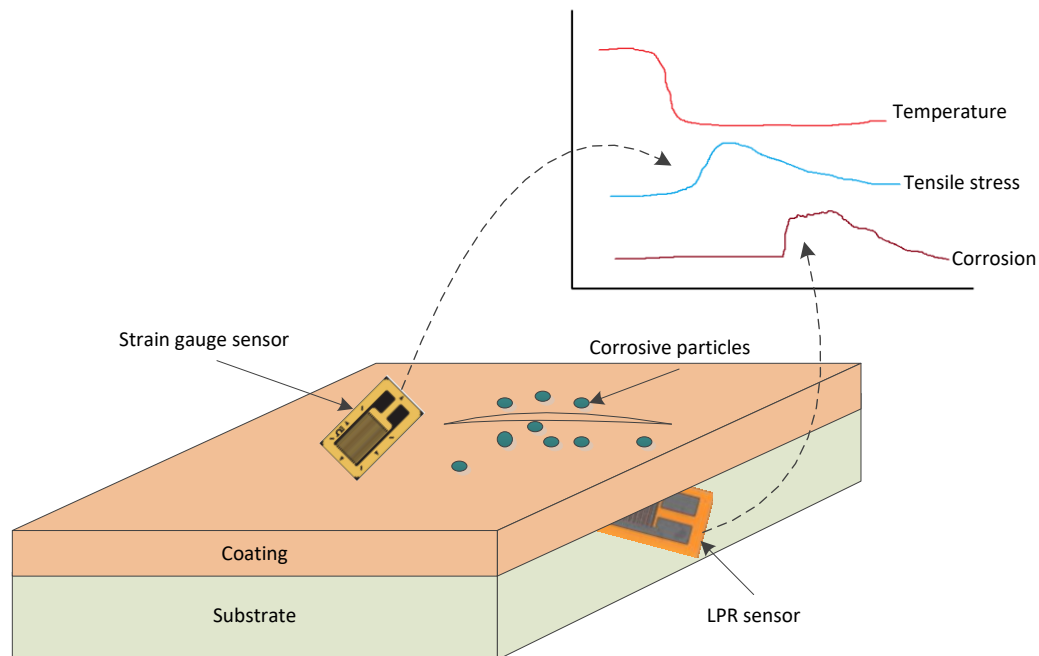


Figure 6.32: Proactive corrosion detection system

6.5 Experimental methodology

The proactive corrosion monitoring system has been validated through accelerated corrosion testing in laboratory. Three aluminium 6082 samples with 33mm of thickness with 2'' x 2'' dimensions were prepared for experiments. The Modulus of elasticity and coefficient of thermal expansion of aluminium 6082 are 70GPa and $24 \times 10^{-6} \text{ K}^{-1}$, respectively. Preparation of samples involved following steps:

- Polishing the surface interface of samples

Chapter 6: Wireless Condition Monitoring System

- Installation of μ LPR sensor on surface interface of sample
- Coating the sample with red-oxide primer
- Installation of μ -strain gauge sensor on coated surface of sample

The samples surface were polished using emery paper with grit size of 80 as shown in Figure 6.33. The Optical Inferometry was used to measure the surface roughness at 8 different locations of each sample. Table 6.1 shows the average roughness value of each sample. The samples were cleaned with deionised water after the polishing.



Figure 6.33 Polished samples

Table 6-1 Surface roughness of each sample

	Sample 1 Ra(μm)	Sample 2 Ra(μm)	Sample 3 Ra(μm)
Average Roughness	1.501	1.197	1.335

The working electrode of μ LPR sensor was attached to the sample interface. The μ LPR sensor has 40mm x 20mm x 0.1mm of dimensions. Adhesive tape is applied on back of sensor to keep it in place and in touch with sample surface as shown in Figure 6.34. RTU system attached to μ LPR sensor transmits measurements to the base station.

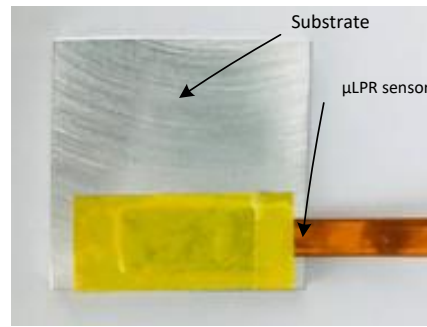


Figure 6.34 Sample with μ LPR sensor

The red-oxide primer was applied on sample using conventional spray gun at 300K temperature. It has Elastic modulus of 6.14 GPa and coefficient of thermal expansion of $21 \times 10^{-6} \text{K}^{-1}$. The samples were dried for next 24hrs before another coating. Coating was applied three times to entirely cover the sample surface as shown in Figure 6.35 .



Figure 6.35 Sample with μ LPR sensor

The μ -strain gauge sensor was embedded on coated sample as shown in Figure 6.36. It requires careful soldering and placement due its sensitivity and small size. The sample with μ LPR and μ -strain gauge sensor is shown in Figure 6.37. Number of experiments were carried out on samples in environmental chamber as shown in Figure 6.38. The samples were placed inside 10% salt solution excluding strain gauge sensor area to avoid short circuit.



Figure 6.36 Accessories for installation of μ -strain gauge sensor



Figure 6.37 Sample with μ -strain gauge sensor

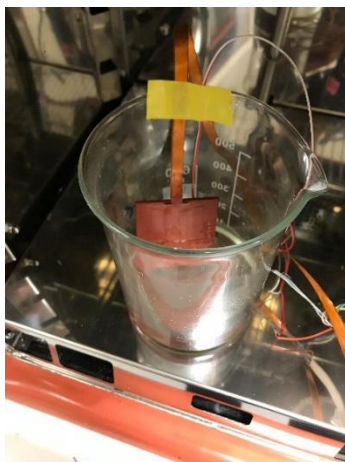


Figure 6.38 Sample inside environmental chamber

6.6 Results and discussions

The response of RTU system that consists of μ -strain gauge, μ LPR, temperature and humidity sensors have been investigated through experiments in laboratory. The accelerated corrosion environmental conditions were provided to the samples with

different temperature gradients. Three experiments were performed to observe the stress/strain behaviour and corrosion reaction under the coating. The measurements from sensors were continuously recorded at regular time intervals. The measurements from μ LPR sensor were recorded at 1min time interval and the measurements from μ -strain gauge were recorded at 30s of time interval.

Experiment 1: First experiment was initiated at $313.14\text{K} \pm 2$ temperature and the increase in strain was recorded as temperature rises from room temperature as shown in Figure 6.39. The strain produced during installation of sensor is considered as offset which is subtracted from initial value of strain measurement to start the reading from zero. The measurements from μ -strain gauge sensor has shown that the development of tensile strain reaching to $1200\mu\epsilon$. The temperature was kept constant for next three hours and reduced to 283.15 ± 2 after 3 hours. High negative temperature gradient resulted in development of compressive strain and the value of strain was recorded to be decreasing from $1200\mu\epsilon$ to $-200\mu\epsilon$. The μ LPR sensor installed under the coating is monitoring the corrosion reaction. The front face of μ LPR sensor is attached to substrate interface which acts as working electrode. The resistance of μ LPR sensor is maximum in the absence of corrosion. The corrosion was detected as sample was placed inside the beaker containing salt solution as shown in Figure 6.40. It shows the presence of micro-cracks that weakens the coating barrier and allows salt particles to diffuse which resulted in corrosion.

Experiment 2: Small temperature gradient was applied in second experiment. The temperature in environmental chamber was set up at room temperature for 30mins in the beginning of experiment. No significant variation in strain measurements was observed as shown in Figure 6.41. The change in temperature ($\Delta T = -18\text{K}$) resulted in development of compressive strain and value of strain recorded as decreasing from $0\mu\epsilon$ to $-900\mu\epsilon$. In the beginning of experiment, the sample was not placed inside the salt solution to monitor the corrosion reaction without any corrosive solution. Therefore, No signs of corrosion has been found as shown in Figure 6.42 during 30mins of an experiment. The corrosion was detected as the sample was inserted into the salt solution.

Chapter 6: Wireless Condition Monitoring System

Experiment 3: Small and large temperature gradients were applied in third experiment. Initial temperature resulted in compressive strain at $292.15\text{K} \pm 2$ temperature. Small change in temperature ($\Delta T = -3.3\text{K}$) resulted in slight increase in compressive strain as shown in Figure 6.43. Increase in temperature after almost 2.8hrs resulted in development of strain. Low magnitude of corrosion was recorded during first 2.8hrs of experiment, while high magnitude of corrosion was recorded as temperature was increased from $290.15\text{K} \pm 2$ to $298.15\text{K} \pm 2$. This behaviour can be linked to the development of strain subjected to change in temperature. The increase in temperature resulting in tensile strain which allowed more salt particles to diffuse and increase the magnitude of corrosion reactions as shown Figure 6.44.

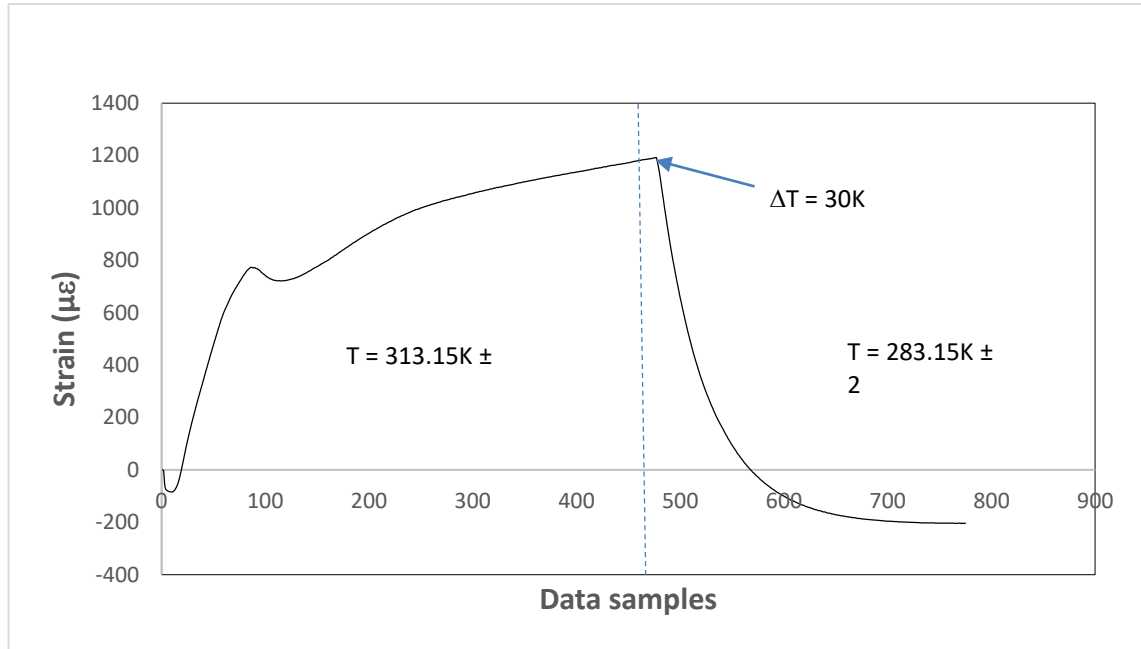


Figure 6.39 Measurements of μ -strain gauge sensor during 1st experiment

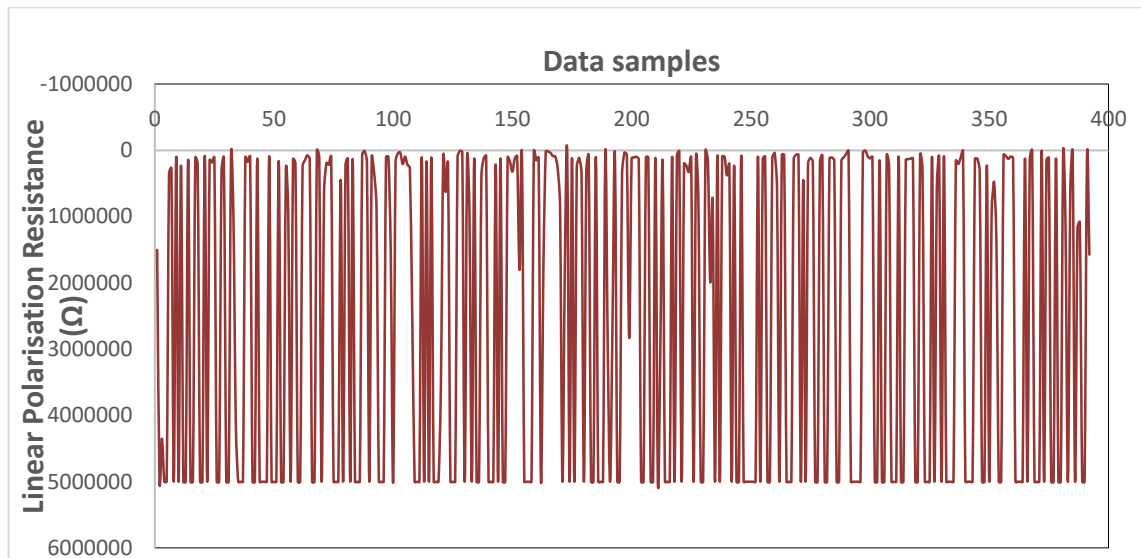


Figure 6.40 Measurements of μ LPR sensor during 1st experiment

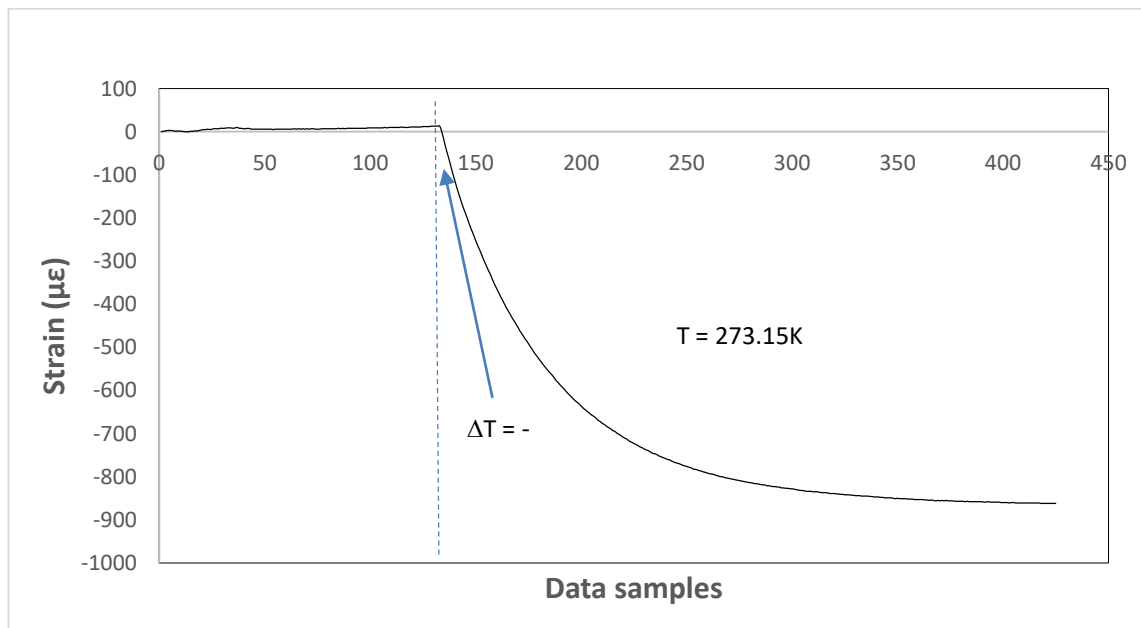


Figure 6.41 Measurements of μ -strain gauge sensor during 2nd experiment

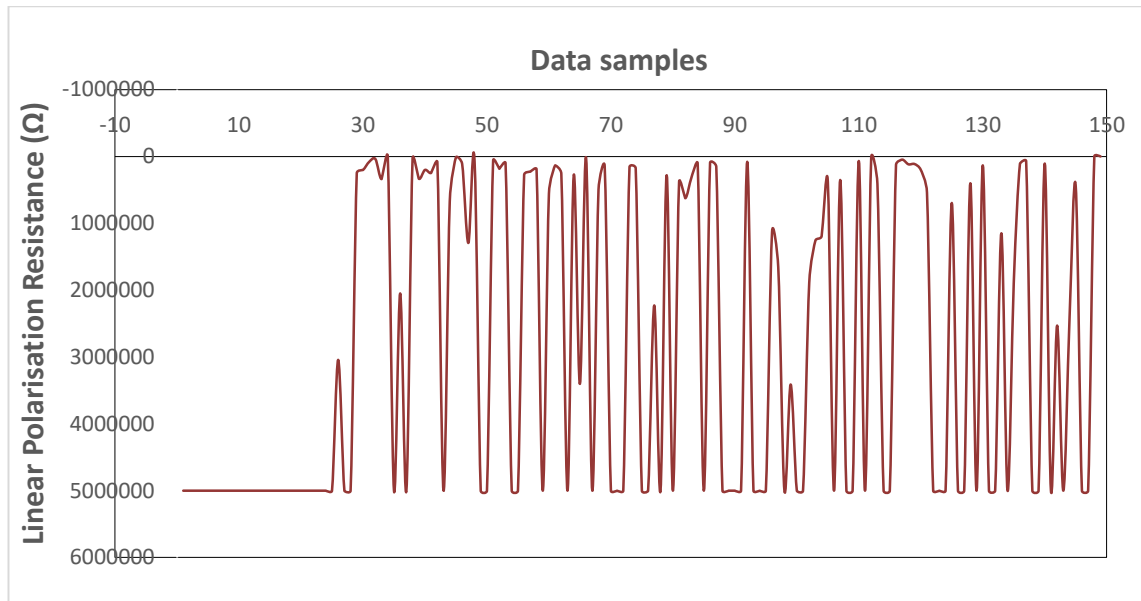


Figure 6.42 Measurements of μ LPR sensor during 2nd experiment

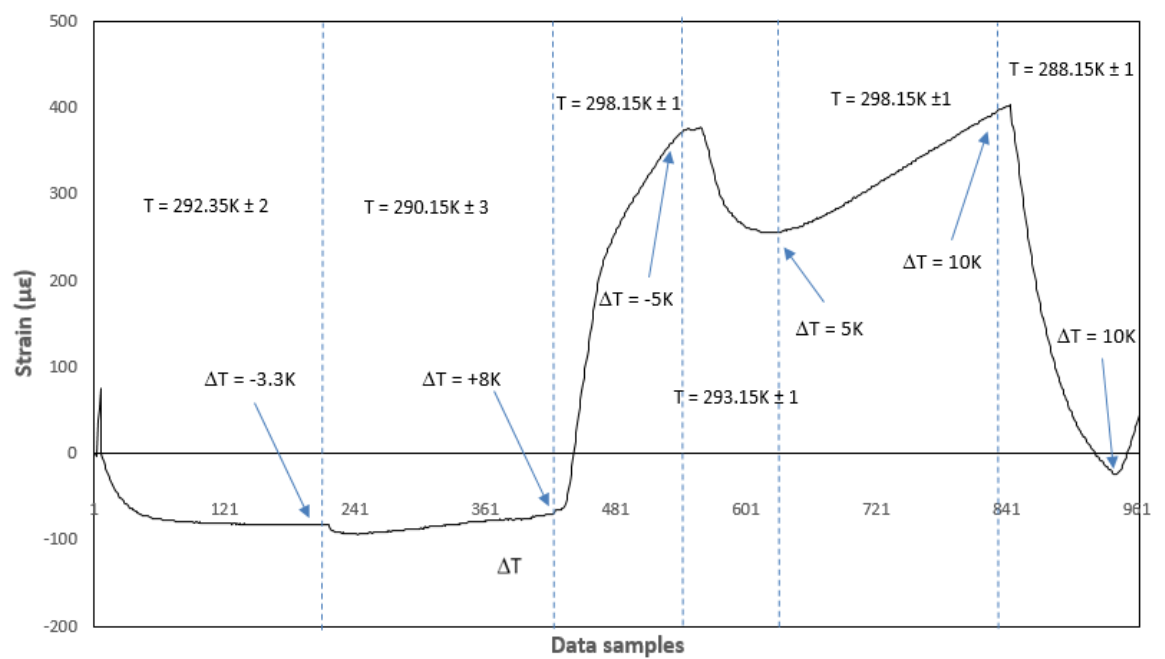


Figure 6.43 Measurements of μ -strain gauge sensor during 3rd experiment

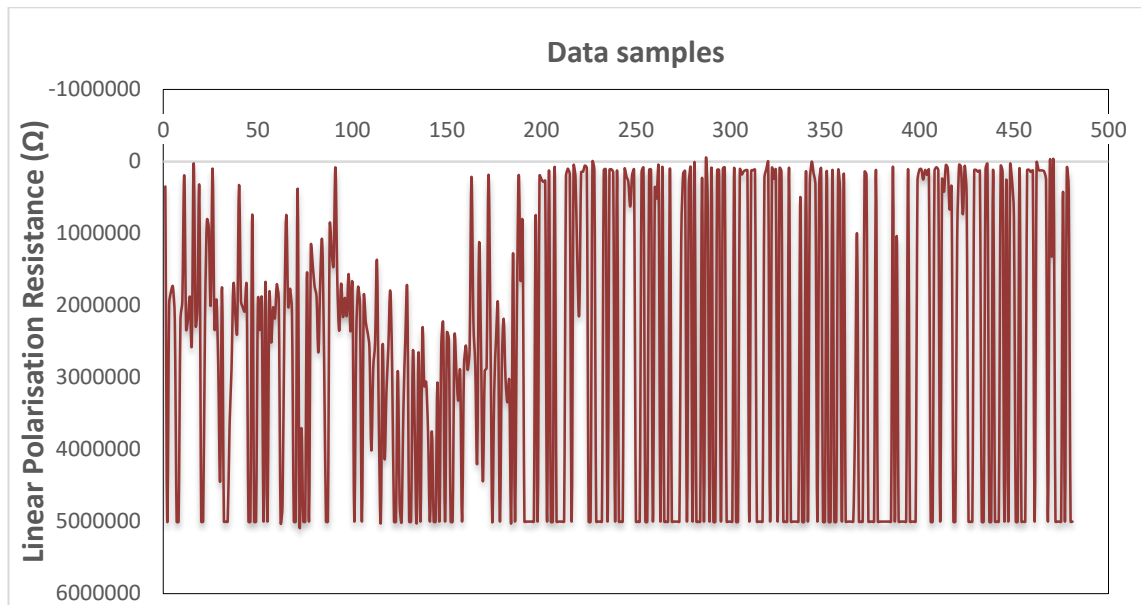


Figure 6.44 Measurements of μ LPR sensor during 3rd experiment

The inspection and assessment of corrosion damage beneath the coating are very challenging to schedule the maintenance especially for structures at remote locations. The existence of micro-cracks within the coating is not visible during visual inspection. The analysis of results from all three experiments has shown that the combination of μ -LPR and μ -strain gauges provides an effective solution for proactive detection of corrosion in real time. When structures are moved from location such as Museum environment and exposed to the outside environment, the change in temperature results in the development of residual stresses. The measurements from μ -strain gauge in response to small temperature gradients can provide instant information regarding the development of tensile or compressive stresses within the coating of structures as observed in experiments. The μ -LPR attached directly to the structure beneath the coating working as the third electrode provide instant detection of corrosion reaction that could occur due to the diffusion of salt particles.

6.7 Conclusion

The wireless condition monitoring system has been developed and tested in the laboratory. The HP_RTU has been designed for experimental work and low-cost NCEM_Smartv1.0 has been built to monitor multiple structures in future research instead of buying expensive systems. The corrosion sensor was already used in previous research and the performance of μ -strain gauge sensor has been observed in current

Chapter 6: Wireless Condition Monitoring System

research. The developed RTUs contains corrosion and also μ -strain gauge sensors which can be used for the proactive corrosion detection system.

Chapter 7: Conclusion and Future work

Modern prognostic solutions are limited to structures operating at a stationary location. Several milestones have been achieved in current research to bridge the gap between the predictions based on operating conditions and specifications of structural systems. The current solution are applicable for structures operating mobile and at various geographical locations. The solutions proposed in the current project will allow the professionals to implement state-of-the-art condition monitoring system for optimising maintenance activities without compromising the integrity of the structure. However, this chapter provides explicit recommendations to extend the current solutions for an inclusive condition monitoring system.

The objectives mentioned in Chapter 1. Section 1.4 have been achieved as follows:

1. The bending moment at the crack tips of blister controls the stoppage and propagation of criteria of blistering failure. The threshold level of bending moment also depends on residual and diffusion-induced stresses. The criteria for the propagation of blister is re-defined as a function of residual and diffusion-induced stresses. Comprehensive prognostic algorithm for the development and propagation of blister based on various multidiscipline parameters has been proposed in Chapter 3. The algorithm can be further extended to estimate the propagation speed of blistering failure that leads to predict the component/part failure of the structure. According to the visual inspections at The Tank Museum. The frequent number of coating damages has been identified on large vehicles with complex architecture.
2. The structures often operate in diverse environmental conditions at remote geographical locations. The salinity in the atmosphere along with other environmental factors diffuse through micro-cracks in coating and results in corrosion damage. Current research has analysed the deterioration factors such as wind speed for the structures operating at remote locations and proposed solutions that include the effect of speed of wind along with the temperature, humidity and time of exposure. Therefore, the solutions proposed in the current work are applicable to various geographical locations. The corrosion monitoring

of large vehicle has been carried out using Linear Polarisation Resistance method at 'The Tank Museum' for more than 2.5 years, recording around 90k measurements. The significantly varying wind speed is also identified as one of the major reason to control the corrosion beneath the coating. A comprehensive algorithm that predicts the diffusion of salinity due to the effect of meteorological factors along with wind speed has been proposed in Chapter 4. The simulation analyses for multiple scenarios of winter and summer seasons have been presented to evaluate the worse and suitable conditions for metal structures. The proposed model can be used for making maintenance decision for structures operating at remote locations.

3. The maintenance activities including recoating of metal structures incur the highest amount of cost. The present Condition-based-Maintenance solutions do not incorporate critical features of structures such as coating thickness, surface roughness, coating and substrate properties to decide maintenance schedule. Experimental findings have shown significant impact of critical features on the useful life of structures. Current research has evaluated the impact of critical features in terms of cost by bridging the gap between parameters of different disciplines. Therefore, a multidisciplinary research approach has been adopted to propose optimal condition-based-maintenance framework. The results have shown that the cost-effective maintenance strategy among Patch and Component recoat can be selected depending on number patch failures and size of the component. The uniform database that includes all possible parameters to implement the optimal CBM framework has been proposed in Chapter 5. The organisations and research academia should also focus on providing and implementing the mechanism to record the maintenance history of large metal structures with all critical parameters.
4. When structures are moved from location such as Museum environment and exposed to the outside environment, the change in temperature results in the development of residual stresses. These stresses result in the development of micro-cracks and allows salt particles to diffuse. Current work evaluated the performance of μ -strain gauge for small and large temperature gradients on metal samples coated with red oxide primer. The instant response of μ -strain gauge subjected to variation in temperature and wireless communication system

makes it suitable for real-time monitoring for residual stresses. The wireless real-time condition monitoring systems have been developed to record real-time complex parameters including corrosion reaction, residual stresses, temperature and humidity and maintain a database of maintenance history. The system contains a remote terminal unit and base station. One high-performance RTU and one low-cost RTU have been developed with corrosion, strain, temperature and humidity sensors. These systems were tested in a laboratory experiment for any functional error.

7.1 Inclusive Condition Monitoring System

The solutions and systems developed in a current research project can be utilised to build an Inclusive condition monitoring system for complex metal structures operating at remote locations. The basic architecture of an Inclusive condition monitoring system has been shown in Figure 7.1. The system contains input parameters and prognostic models of various failure modes. The Uniform data base provides the system specifications of structures, maintenance history and information about past events of structural deterioration. The addition of machine learning algorithms in condition monitoring system can assist in predicting the structural failures more accurately in real-world scenarios.

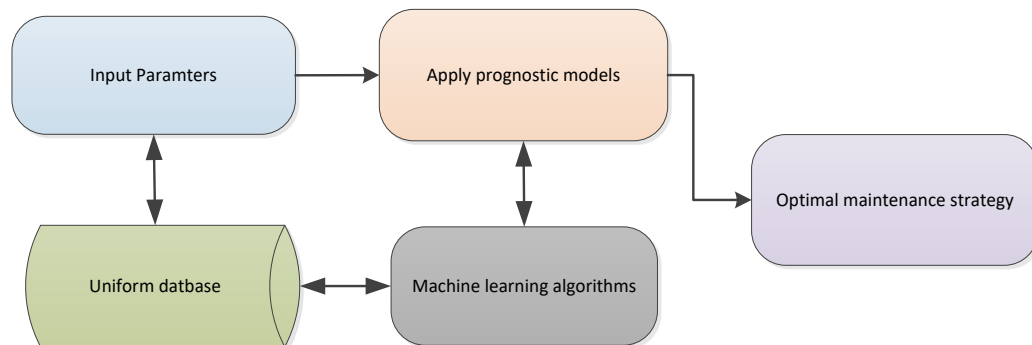


Figure 7.1: Basic architecture of an Inclusive Condition Monitoring System

The comprehensive illustration of Inclusive Condition Monitoring System has been shown in Figure 7.2. The real-time monitoring system will provide measurements of critical parameters acting in operating conditions. The real-time monitoring system has been developed with various sensors as explained in Chapter 6. The system specifications and cost associated parameters can be provided through the uniform

Chapter 7: Conclusion and Future work

database system. The next stage is to apply various prognostic models of potential structural failure mode. For example, if the structure is operating near a coastal area in dynamic weather conditions. The high corrosion damage through micro-cracks due to salinity and blistering failure due to temperature change is expected. The condition monitoring system applies both prognostic models as proposed in Chapter 3 and Chapter 4 to identify the reason and decide corrective maintenance measures using the framework as proposed in Chapter 5.

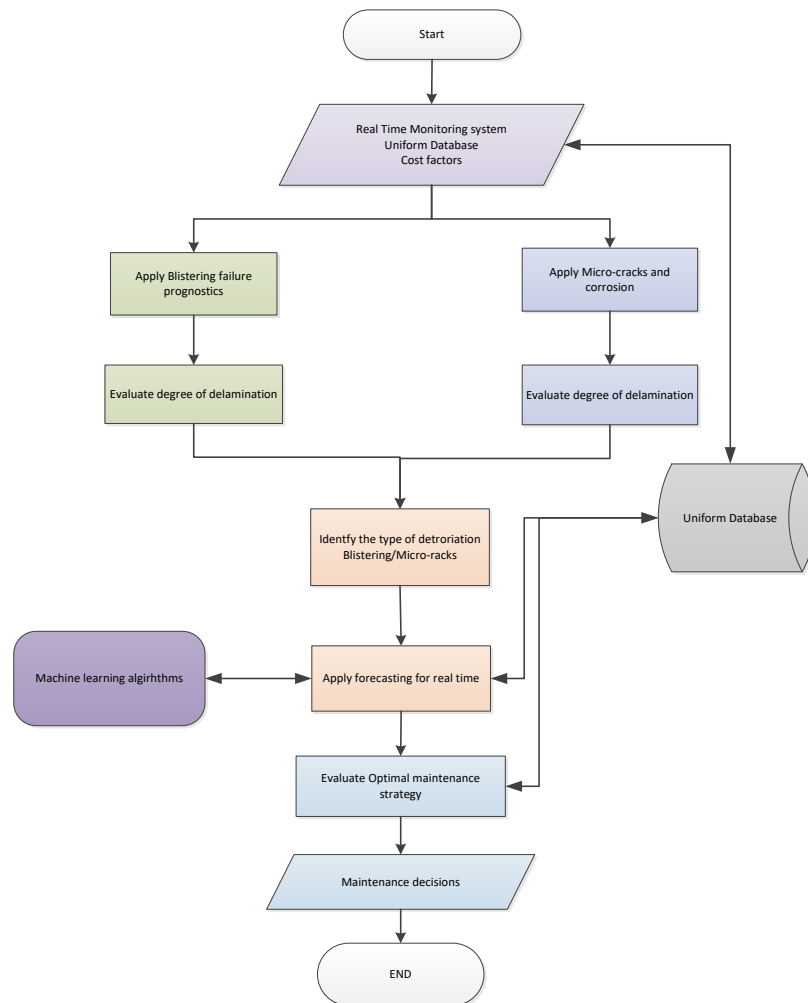


Figure 7.2: Inclusive Condition Monitoring System

7.2 Recommendations

The prognostic algorithm needs to be extended for the particular part failure of an individual structure. The organisations need to set up benchmarks for the complete

Chapter 7: Conclusion and Future work

failure of structures and parts of structures operating in particular operating conditions. The mechanism should be introduced to maintain a comprehensive uniform database that should contain previous error rates along with meteorological parameters of operating conditions, structural system specifications and previous maintenance history.

The machine learning can be incorporated to make predictions more accurate for specific structures operating in any particular environment. The machine learning algorithms keeps the track of previous difference in estimation of failure and learns to minimise the gap between theoretical calculations and the actual time of any structural breakdown event as shown in Figure 7.3. The critical parameters and algorithms proposed in the project can also be used with machine learning methods to make more accurate maintenance predictions. Machine learning algorithms are the mathematical models based on training data set. The accuracy of predictive maintenance using machine learning algorithms depends on the availability of historical data containing all possible parameters regarding events that leads to failure, appropriate framing of the problem and proper evaluation of predictive algorithms. The domain experts and data scientists would be involved in the process of data collection to make sure that the data is suitable for the model to be developed. Once the data collection process is complete, the next task is to select appropriate algorithm subject to the problem. The machine learning methods are mainly characterised as following:

- Instance-based algorithm
- Regression analysis
- Regularization algorithm
- Classifiers

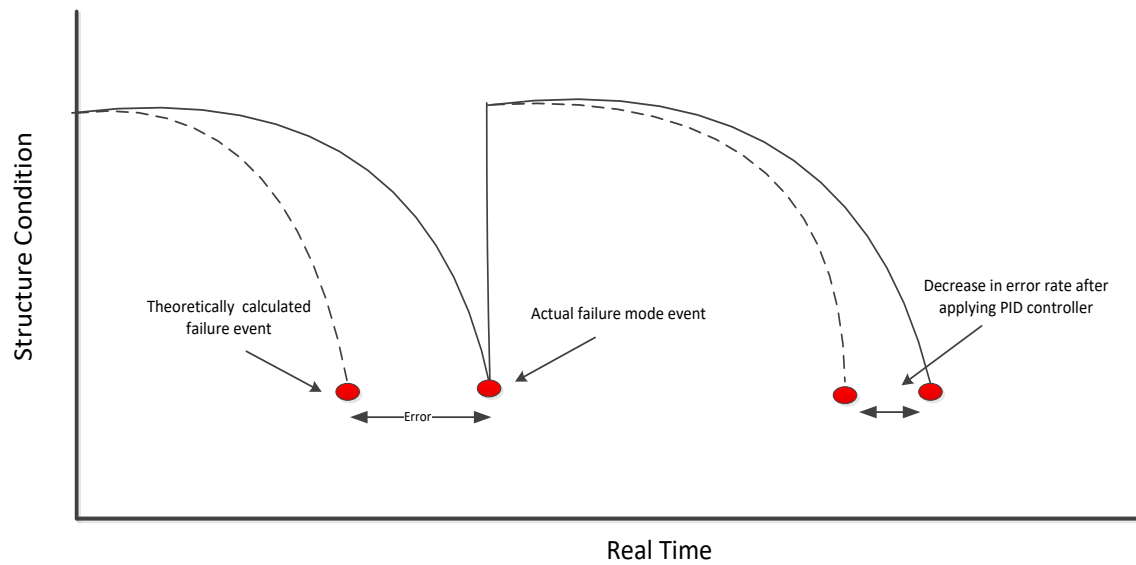


Figure 7.3: Application of machine learning algorithms

7.3 Summary

The milestones achieved in the current multidisciplinary research project have provided very comprehensive Structural Health Monitoring System for large metal structures operating remote locations at various geographical locations. The wireless monitoring system has also been developed to further expand the research findings not limited to SHMS. The future recommendations to take this project forward have been explained explicitly.

References

- Ailor, W. H., 1982. Atmospheric corrosion. *W. H. Ailor, Ed., 1028 pages, hard cloth, 7 X 10 in. (18 X 25 cm), Electrochemical Society Monograph Series, John Wiley and Sons, New York, New York, 1982.* \$ 150.
- Alaswad, S., and Xiang, Y., 2017. A review on condition-based maintenance optimization models for stochastically deteriorating system. *Reliability Engineering & System Safety*, 157, 54-63.
- Allahar, K. N., Orazem, M. E., and Ogle, K., 2007. Mathematical model for cathodic delamination using a porosity–ph relationship. *Corrosion Science*, 49 (9), 3638-3658.
- Astm. Standard practice for evaluating degree of rusting on painted steel surfaces.
- Au-Yong, C. P., Ali, A. S., and Ahmad, F., 2013. Significant characteristics of scheduled and condition-based maintenance in office buildings. *Journal of Performance of Constructed Facilities*, 28 (2), 257-263.
- Bastidas-Arteaga, E., Chateauneuf, A., Sánchez-Silva, M., Bressolette, P., and Schoefs, F., 2011. A comprehensive probabilistic model of chloride ingress in unsaturated concrete. *Engineering Structures*, 33 (3), 720-730.
- Baştuğ, T., and Kuyucak, S., 2005. Temperature dependence of the transport coefficients of ions from molecular dynamics simulations. *Chemical physics letters*, 408 (1-3), 84-88.
- Basu, D., and Khan, D., 1972. Short communication on role of different variables on atmospheric corrosion in marine environment-effect of proximity to sea. *NML Technical Journal*, 14 (1), 34-36.
- Bressers, J., Peteves, S., and Steen, M. 2000. Coatings for hot section gas turbine components, *European Structural Integrity Society* (Vol. 26, pp. 115-134): Elsevier.
- Brown, D. W., Connolly, R. J., Darr, D. R., and Laskowski, B., 2014. *Linear polarization resistance sensor using the structure as a working electrode*. Paper presented at the Proceedings of the Second European Conference of the Prognostics and Health Management Society, Nantes, France.
- Brown, D. W., Connolly, R. J., Laskowski, B., Garvan, M., Li, H., Agarwala, V. S., and Vachtsevanos, G., A novel linear polarization resistance corrosion sensing methodology for aircraft structure.
- Choi, S. R., Hutchinson, J. W., and Evans, A., 1999. Delamination of multilayer thermal barrier coatings. *Mechanics of Materials*, 31 (7), 431-447.
- Chuang, T.-J., Nguyen, T., and Lee, S., 1999. Micro-mechanic model for cathodic blister growth in painted steel. *Journal of Coatings Technology*, 71 (895), 75-85.
- Chuang, T., Nguyen, T., and Li, S., 1997. *A non-osmotic blister growth model in coating systems*. Paper presented at the Damage and failure of interfaces. 1st International Conference. Proceedings.
- Corrosion. Corrosion fundamentals. Available from: <https://corrosion.ksc.nasa.gov/unifcor.htm> [Accessed.
- Corvo, F., Pérez, T., Martín, Y., Reyes, J., Dzib, L., González-Sánchez, J., and Castañeda, A., 2008. Time of wetness in tropical climate: Considerations on the estimation of tow according to iso 9223 standard. *Corrosion Science*, 50 (1), 206-219.
- Faulhaber, S., Mercer, C., Moon, M.-W., Hutchinson, J., and Evans, A., 2006. Buckling delamination in compressed multilayers on curved substrates with accompanying ridge cracks. *Journal of the Mechanics and Physics of Solids*, 54 (5), 1004-1028.

References

- Feliu, S., Morcillo, M., and Feliu Jr, S., 1993a. The prediction of atmospheric corrosion from meteorological and pollution parameters—i. Annual corrosion. *Corrosion Science*, 34 (3), 403-414.
- Feliu, S., Morcillo, M., and Feliu Jr, S., 1993b. The prediction of atmospheric corrosion from meteorological and pollution parameters—ii. Long-term forecasts. *Corrosion Science*, 34 (3), 415-422.
- Fürbeth, W., and Stratmann, M., 2001. The delamination of polymeric coatings from electrogalvanised steel—a mechanistic approach.: Part 1: Delamination from a defect with intact zinc layer. *Corrosion Science*, 43 (2), 207-227.
- Galindo, R. E., Van Veen, A., Evans, J., Schut, H., and De Hosson, J. T. M., 2005. A modified blister test to study the adhesion of thin coatings based on local helium ion implantation. *Thin Solid Films*, 471 (1-2), 170-176.
- Gilber, N. Structural steel. Available from: <https://www.azom.com/article.aspx?ArticleID=6022#> [Accessed.
- Goldstein, J. I., Newbury, D. E., Michael, J. R., Ritchie, N. W., Scott, J. H. J., and Joy, D. C., 2017. *Scanning electron microscopy and x-ray microanalysis*. Springer.
- Grundmeier, G., Reinartz, C., Rohwerder, M., and Stratmann, M., 1998. Corrosion properties of chemically modified metal surfaces. *Electrochimica acta*, 43 (1-2), 165-174.
- Grundmeier, G., Schmidt, W., and Stratmann, M., 2000. Corrosion protection by organic coatings: Electrochemical mechanism and novel methods of investigation. *Electrochimica Acta*, 45 (15-16), 2515-2533.
- Hall, C. E., 1953. *Introduction to electron microscopy*. McGra-hill Publishing Company Ltd; London.
- Harris, S., Mishon, M., and Hebborn, M., 2006. *Corrosion sensors to reduce aircraft maintenance*. Paper presented at the Rto avt-144 workshop on enhanced aircraft platform availability through advanced maintenance concepts and technologies. Vilnius, Lithuania.
- Hertzberg, E. 2016. Estimated impact of corrosion on cost and availability of dod weapon systems: Fy2016: Report SAL4IT2.
- Herzberg, E. F., Ambrogio, E. D., Barker, C. L., Harleston, E. F., Haver, W. M., O'meara, N. T., Marafioti, R. J., Stimatze, G. L., Timko, A., and Tran, J. C., 2006. The annual cost of corrosion for army ground vehicles and navy ships. *LMI Report SKT50T1*.
- Holmberg, K., and Mathews, A., 1994. Coatings tribology: A concept, critical aspects and future directions. *Thin Solid Films*, 253 (1-2), 173-178.
- Hornbacher, A. Steel vs aluminum. Available from: <https://www.wenzelmetal spinning.com/steel-vs-aluminum.html> [Accessed.
- Hsueh, C.-H., 2002. Modeling of elastic deformation of multilayers due to residual stresses and external bending. *Journal of Applied Physics*, 91 (12), 9652-9656.
- Huang, M.-W., Allely, C., Ogle, K., and Orazem, M. E., 2008. A mathematical model for cathodic delamination of coated metal including a kinetic ph–porosity relationship. *Journal of the Electrochemical Society*, 155 (5), C279-C292.
- Hutchinson, J., Thouless, M., and Liniger, E., 1992. Growth and configurational stability of circular, buckling-driven film delaminations. *Acta metallurgica et materialia*, 40 (2), 295-308.
- Hutchinson, J. W., 1996. Stresses and failure modes in thin films and multilayers. *Notes for a Dcamm Course. Technical University of Denmark, Lyngby*, 1-45.
- Hutchinson, J. W., and Suo, Z., 1991. Mixed mode cracking in layered materials. In: *Advances in applied mechanics* Vol. 29: Elsevier, 63-191.

References

- Inspectioneering. Nace study estimates global cost of corrosion at \$2.5 trillion annually. Available from: <https://inspectioneering.com/news/2016-03-08/5202/nace-study-estimates-global-cost-of-corrosion-at-25-trillion-ann> [Accessed].
- Instruments, N. National instruments. Available from: <http://www.ni.com/en-gb.html> [Accessed].
- Irwin, G. R., 1957. Analysis of stresses and strains near the end of a crack traversing a plate. *Journal of Applied Mechanics*, 24, 351-369.
- Jahnsen, H., 2001. *Delamination of coatings. Handbook of materials behavior models*.
- Javaherdashti, R., 2000. How corrosion affects industry and life. *Anti-corrosion methods and materials*, 47 (1), 30-34.
- Kappes, M., Frankel, G., and Sridhar, N., 2010. Adhesion and adhesion degradation of a pressure sensitive tape on carbon steel. *Progress in Organic Coatings*, 69 (1), 57-62.
- Keytomets. Classification of carbon and low-alloy steels. Available from: <http://www.keytomets.com/Articles/Art62.htm> [Accessed].
- Khan, Z. A., Latif, J., Hammad Nazir, A. S., and Stokes, K., 2018. Predictive and prognostic modelling and simulation of coatings subject to corrosion and mechanical failures. *Materials Characterisation*, 6 (3), 487-498.
- Khan, Z. A., Latif, J., Nazir, M. H., Stokes, K., and Plummer, J., 2017. Sensor based corrosion condition monitoring of coating substrate system informed by fracture mechanics, electrochemistry and heat transfer concepts. In: *Department of Defense - Allied Nations Technical Corrosion Conference*, Birmingham, AL, USA.
- Klinesmith, D. E., Mccuen, R. H., and Albrecht, P., 2007. Effect of environmental conditions on corrosion rates. *Journal of Materials in Civil Engineering*, 19 (2), 121-129.
- Koch, G. E. A., 2016. *Nace international impact*.
- Laidler, K. J., 1984. The development of the arrhenius equation. *Journal of Chemical Education*, 61 (6), 494.
- Latif, J., Khan, Z. A., Nazir, M. H., Stokes, K., and Plummer, J., 2018a. Condition monitoring and predictive modelling of coating delamination applied to remote stationary and mobile assets. *Structural Health Monitoring*.
- Latif, J., Khan, Z. A., Nazir, M. H., Stokes, K., and Plummer, J., 2018b. Life assessment prognostic modelling for multi-layered coating systems using a multidisciplinary approach. *Materials Science and Technology*, 34 (6), 664-678.
- Levin, Z., and Cotton, W. R., 2008. *Aerosol pollution impact on precipitation: A scientific review*. Springer Science & Business Media.
- Li, J. C.-M., 1978. Physical chemistry of some microstructural phenomena. *Metallurgical Transactions A*, 9 (10), 1353-1380.
- Lim, C., Yan, B., Yin, L., and Zhu, L., 2012. Simulation of diffusion-induced stress using reconstructed electrodes particle structures generated by micro/nano-ct. *Electrochimica Acta*, 75, 279-287.
- Lin, S., and Hwang, C. C., 1995. Nonlinear effect of self-induced electric field on diffusion-induced stresses. *Journal of applied physics*, 78 (12), 7035-7039.
- Liu, X., and Frankel, G., 2006. Effects of compressive stress on localized corrosion in aa2024-t3. *Corrosion science*, 48 (10), 3309-3329.
- Lovett, R., 1978. Quantitative measurement of airborne sea-salt in the north atlantic. *Tellus*, 30 (4), 358-364.
- Ma, Y., Wang, G., Chen, Y., Long, D., Guan, Y., Liu, L., and Zhang, Z., 2018. Extended hencky solution for the blister test of nanomembrane. *Extreme Mechanics Letters*.
- Machen, J. D. Coating failure. Available from: <https://ktauniversity.com/blistering-bubbling-coatings/> [Accessed].

References

- Maiti, S. K., 2015. *Fracture mechanics: Fundamentals and applications*. Cambridge University Press.
- Martin, J., Embree, E., and Tsao, W., 1990. Non-osmotic, defect-controlled cathodic disbondment of a coating from a steel substrate. *JCT, Journal of coatings technology*, 62 (790), 25-33.
- Mcdonald, R., Unni, C., and Duce, R., 1982. Estimation of atmospheric sea salt dry deposition: Wind speed and particle size dependence. *Journal of Geophysical Research: Oceans*, 87 (C2), 1246-1250.
- Mcmahon, T., and Denison, P., 1979. Empirical atmospheric deposition parameters—a survey. *Atmospheric Environment* (1967), 13 (5), 571-585.
- Meira, G., Andrade, C., Alonso, C., Padaratz, I., and Borba, J., 2007. Salinity of marine aerosols in a brazilian coastal area—influence of wind regime. *Atmospheric Environment*, 41 (38), 8431-8441.
- Meira, G., Andrade, C., Alonso, C., Padaratz, I., and Borba, J., 2008. Modelling sea-salt transport and deposition in marine atmosphere zone—a tool for corrosion studies. *Corrosion Science*, 50 (9), 2724-2731.
- Mejlbro, L., 1996. The complete solution of fick's second law of diffusion with time-dependent diffusion coefficient and surface concentration. *Durability of concrete in saline environment*, 127-158.
- Mendoza, A. R., and Corvo, F., 2000. Outdoor and indoor atmospheric corrosion of non-ferrous metals. *Corrosion Science*, 42 (7), 1123-1147.
- Morcillo, M., Chico, B., Mariaca, L., and Otero, E., 2000. Salinity in marine atmospheric corrosion: Its dependence on the wind regime existing in the site. *Corrosion Science*, 42 (1), 91-104.
- Nazir, M., Khan, Z., and Stokes, K., 2015a. Modelling of metal-coating delamination incorporating variable environmental parameters. *Journal of Adhesion Science and Technology*, 29 (5), 392-423.
- Nazir, M., and Khan, Z. A., 2017. A review of theoretical analysis techniques for cracking and corrosive degradation of film-substrate systems. *Engineering Failure Analysis*, 72, 80-113.
- Nazir, M., Khan, Z. A., Saeed, A., and Stokes, K., 2015b. Modeling the effect of residual and diffusion-induced stresses on corrosion at the interface of coating and substrate. *Corrosion*, 72 (4), 500-517.
- Nazir, M., Khan, Z. A., Saeed, A., and Stokes, K., 2016a. A model for cathodic blister growth in coating degradation using mesomechanics approach. *Materials and Corrosion*, 67 (5), 495-503.
- Nazir, M., Khan, Z. A., and Stokes, K., 2015c. A holistic mathematical modelling and simulation for cathodic delamination mechanism—a novel and an efficient approach. *Journal of Adhesion Science and Technology*, 29 (22), 2475-2513.
- Nazir, M., Khan, Z. A., and Stokes, K., 2015d. Optimisation of interface roughness and coating thickness to maximise coating–substrate adhesion—a failure prediction and reliability assessment modelling. *Journal of Adhesion Science and Technology*, 29 (14), 1415-1445.
- Nazir, M., Khan, Z. A., and Stokes, K., 2015e. A unified mathematical modelling and simulation for cathodic blistering mechanism incorporating diffusion and fracture mechanics concepts. *Journal of Adhesion Science and Technology*, 29 (12), 1200-1228.
- Nazir, M., Khan, Z. A., and Stokes, K., 2016b. Analysing the coupled effects of compressive and diffusion induced stresses on the nucleation and propagation of circular coating blisters in the presence of micro-cracks. *Engineering Failure Analysis*, 70, 1-15.

References

- Nazir, M., Saeed, A., and Khan, Z. A., 2018. Electrochemical corrosion failure analysis of large complex engineering structures by using micro-lpr sensors. *Sensors and Actuators B: Chemical*, 268, 232-244.
- Nazir, M. H., 2015. *In-situ corrosion health monitoring and prediction in military vehicle*. Thesis. Bournemouth University.
- Nazir, M. H., and Khan, Z., 2015. Maximising the interfacial toughness of thin coatings and substrate through optimisation of defined parameters. *International Journal of Computational Methods and Experimental Measurements*, 3 (4), 316-328.
- Nazir, M. H., Khan, Z. A., and Saeed, A., 2018a. A novel non-destructive sensing technology for on-site corrosion failure evaluation of coatings. *IEEE Access*, 6, 1042-1054.
- Nazir, M. H., Khan, Z. A., Saeed, A., Siddaiah, A., and Menezes, P. L., 2018b. Synergistic wear-corrosion analysis and modelling of nanocomposite coatings. *Tribology International*, 121, 30-44.
- Nazir, M. H., Saeed, A., and Khan, Z., 2017. A comprehensive predictive corrosion model incorporating varying environmental gas pollutants applied to wider steel applications. *Materials Chemistry and Physics*, 193, 19-34.
- Ni, Y., and Soh, A., 2014. On the growth of buckle-delamination pattern in compressed anisotropic thin films. *Acta materialia*, 69, 37-46.
- Nielsen, J. S., and Sørensen, J. D., 2018. Computational framework for risk-based planning of inspections, maintenance and condition monitoring using discrete bayesian networks. *Structure and Infrastructure Engineering*, 14 (8), 1082-1094.
- Nims, D. K., and Colony, D. C., 2017. *Luc-2-1682 long term maintenance of the anthony wayne suspension bridge main cables*. Ohio Department of Transportation, Office of Statewide Planning & Research.
- Perez, N., 2004. *Electrochemistry and corrosion science*. Vol. 412: Springer.
- Prajapati, A., Bechtel, J., and Ganesan, S., 2012. Condition based maintenance: A survey. *Journal of Quality in Maintenance Engineering*, 18 (4), 384-400.
- Prawoto, Y., 2013. Unified model for blister growth in coating degradation using weight function and diffusion concepts. *Materials and Corrosion*, 64 (9), 794-800.
- Prawoto, Y., and Dillon, B., 2012. Failure analysis and life assessment of coating: The use of mixed mode stress intensity factors in coating and other surface engineering life assessment. *Journal of failure analysis and prevention*, 12 (2), 190-197.
- Rajagopalan, K., Annamalai, P., Sundaram, M., and Rajagopal, C., 1971. Atmospheric corrosion of steel in some tropical locations in india. *Proc. 3rd Int. Cong. on Metallic Corrosion*, 4, 532.
- Revie, R. W., 2008. *Corrosion and corrosion control: An introduction to corrosion science and engineering*. John Wiley & Sons.
- Riemer, D. P., and Orazem, M. E., 2005. Modeling coating flaws with non-linear polarization curves for long pipelines. *Corrosion and Cathodic Protection Modelling and Simulation*, 12, 225-259.
- Roberge, P. R., *Corrosion inspection and monitoring*. a john wiley & sons ltd. publication.
- Roylance, D., 2001. Introduction to fracture mechanics. *Massachusetts Institute of Technology, Cambridge*, 1.
- Saeed, A., 2013. *Sustainable methodology of conserving historic military vehicles*. Thesis (Doctrate). Bournemouth University.
- Saeed, A., Khan, Z. A., Nazir, H., Hadfield, M., and Smith, R., 2017. Research impact of conserving large military vehicles through a sustainable methodology. *International Journal of Heritage Architecture*, 1 (2), 267-274.
- Saeed, A., Khan, Z. A., and Nazir, M. H., 2015. An optimised approach of protecting and sustaining large vehicle system. *Sustainability*, 7 (12), 16451-16464.

References

- Saeed, A., Khan, Z. A., and Nazir, M. H., 2016. Time dependent surface corrosion analysis and modelling of automotive steel under a simplistic model of variations in environmental parameters. *Materials Chemistry and Physics*, 178, 65-73.
- Samson, E., Marchand, J., and Snyder, K. A., 2003. Calculation of ionic diffusion coefficients on the basis of migration test results. *Materials and structures*, 36 (3), 156-165.
- Schmauder, S., and Meyer, M., 1992. Correlation between dundurs' parameters and elastic constants. *Z. Metallkd*, 83 (7), 525.
- Sea-Gmbh. Sea 9741 3g/gps communication module. Available from: <https://www.sea-gmbh.com/en/products/compactrio-products/mobile-communications/sea-9741-3ggps/> [Accessed].
- Si, X.-S., Wang, W., Hu, C.-H., and Zhou, D.-H., 2011. Remaining useful life estimation—a review on the statistical data driven approaches. *European journal of operational research*, 213 (1), 1-14.
- Standardization, I. O. F. Iso 9223:2012
- corrosion of metals and alloys -- corrosivity of atmospheres -- classification, determination and estimation.
- Stratmann, M., Feser, R., and Leng, A., 1994. Corrosion protection by organic films. *Electrochimica Acta*, 39 (8-9), 1207-1214.
- Suo, Z., and Hutchinson, J. W., 1990. Interface crack between two elastic layers. *International Journal of Fracture*, 43 (1), 1-18.
- Tam, C., and Stiemer, S., 1996a. Bridge corrosion cost model implementation and coating maintenance model using dynamic programming. *Journal of performance of constructed facilities*, 10 (2), 57-66.
- Tam, C., and Stiemer, S., 1996b. Development of bridge corrosion cost model for coating maintenance. *Journal of performance of constructed facilities*, 10 (2), 47-56.
- Totalmateria. Aluminum alloys in military vehicles and equipment. Available from: <http://www.totalmateria.com/Article102.htm> [Accessed].
- Totten, G. E., 2002. *Handbook of residual stress and deformation of steel*. ASM international.
- Ventsel, E., and Krauthammer, T., 2001. *Thin plates and shells: Theory: Analysis, and applications*. CRC press.
- Volinsky, A., Moody, N., and Gerberich, W., 2002. Interfacial toughness measurements for thin films on substrates. *Acta materialia*, 50 (3), 441-466.
- Wagner, C., and Traud, W., 1938. Concerning the evaluation of corrosion reactions by superposition of electrochemical partial reactions and concerning the potential formation on mixed electrodes. *Z. Elektrochem*, 44 (391), 52.
- Wan, K.-T., and Liao, K., 1999. Measuring mechanical properties of thin flexible films by a shaft-loaded blister test. *Thin Solid Films*, 352 (1-2), 167-172.
- Worldweatheronline. Worldweatheronline. Available from: <https://ja.worldweatheronline.com/> [Accessed].
- Ye, Z. S., and Xie, M., 2015. Stochastic modelling and analysis of degradation for highly reliable products. *Applied Stochastic Models in Business and Industry*, 31 (1), 16-32.
- Zhang, N.-H., and Xing, J.-J., 2006. An alternative model for elastic bending deformation of multilayered beams. *Journal of applied physics*, 100 (10), 103519.
- Zhang, X., Shyy, W., and Sastry, A. M., 2007. Numerical simulation of intercalation-induced stress in li-ion battery electrode particles. *Journal of the Electrochemical Society*, 154 (10), A910-A916.
- Zhao, X., Munroe, P., Habibi, D., and Xie, Z., 2013. Roles of compressive residual stress in enhancing the corrosion resistance of nano nitride composite coatings on steel. *Journal of Asian Ceramic Societies*, 1 (1), 86-94.

Appendices

Appendix A: Paper I

MATERIALS SCIENCE AND TECHNOLOGY, 2018
VOL. 34, NO. 6, 664–678
<https://doi.org/10.1080/02670836.2017.1410358>



Life assessment prognostic modelling for multi-layered coating systems using a multidisciplinary approach

Jawwad Latif^a, Zulfiqar Ahmad Khan ^a, Mian Hammad Nazir^a, Keith Stokes^b and Joseph Plummer^c

^aNanoCorr, Energy and Modelling (NCEM), Faculty of Science & Technology, Bournemouth University, Poole, UK; ^bNational Centre for Advanced Tribology at Southampton (nCATS) Faculty of Engineering and the Environment, University of Southampton, Southampton, UK; ^cPhysical Sciences Division, Defence Science & Technology Laboratory DSTL, Ministry of Defence, Salisbury, UK

ABSTRACT

The multidisciplinary approach has been adopted to model the formation and propagation of blistering effect for evaluation of useful coating life in the multi-layered coating–substrate system. A prognostic model of de-bonding driving force has been formulated as a function of material science, solid mechanics and fracture mechanics properties to estimate critical, safe and fail conditions of the coating–substrate system. The blister growth velocity rate is also included in the developed model to estimate the blister propagation as a function of diffusion-induced stress and residual stress. The proposed prognostic modelling for the formation and propagation of blistering effect are combined to form an assessment model for the evaluation of useful coating life of the multi-layered coating–substrate system and validated through experimental observation.

ARTICLE HISTORY

Received 21 July 2017
Revised 21 September 2017
Accepted 22 September 2017

KEYWORDS

Multi-layered coating;
delamination; blistering;
modelling

Nomenclature

σ_{di}	Diffusion-induced stress of substrate material
σ_{dci}	Diffusion-induced stress for the i th coating material
σ_{ri}	Residual stress for the i th coating material
σ_{rs}	Residual stress of substrate material
V_{pk}	Partial molar volume
c'_k	Concentration gradient
s	Thickness of substrate
ε_{ud}	Uniform bending strain due to diffusion-induced stress
ε_{ur}	Uniform bending strain due to residual stress
ρ_d	Bending curvature due to diffusion-induced stress
ρ_r	Bending curvature due to residual induced stress
μ_k^Q	Chemical potential for isotropic material
r	Radius of blister
E_i	Elastic modulus of the i th coating material
h_i	Thickness of the i th layer of coating
ν_i	Poisson's ratio of the i th material
σ_{cr}	Critical stress of single layer coating
$\sigma_{cr'}$	Critical stress of multi-layered coating
G_o	Resultant strain energy release rate
T_{th}	Total thickness of coating
σ_T	Total unbuckled stress
\cap	De-bonding index
Γ_{IC}	Interface toughness

j	Mode mixity ratio
λ	Roughness parameter
ψ	Mode adjustment term
F_{cr}	Critical de-bonding driving force
F	De-bonding driving force
M_{Th}	Threshold bending moment
M_{ini}	Initiation bending moment
a	Blister diameter
w	Blister amplitude

Introduction

Thin film coatings cover a wide range of applications in the field of optics, chemistry, mechanics, magnetism, electricity, automobiles, civil infrastructure, aerospace and medical field; computer hard disks, video and audio tapes are also coated with thin films. In optics, coatings are applied for anti-reflection and decorative purposes. Coatings act as a diffusion barrier to preserve the materials from environmental factors which cause oxidation reactions that lead to coating and structural failure. In aircraft and automobiles, structures are protected from corrosion under severe environmental conditions by applying an appropriate coating system. Factors that lead to coating failure are mainly environmental factors, inappropriate sample preparation, incorrect selection of coating, service environment, poor application, improper drying of coating times and mechanical

CONTACT Jawwad Latif jlatif@bournemouth.ac.uk NanoCorr, Energy and Modelling (NCEM), Faculty of Science & Technology, Bournemouth University, Poole House, Fern Barrow, Poole BH12 5BB, UK

© 2017 Institute of Materials, Minerals and Mining.

damage. Coating failures cause such immense amount of financial loss that the cost of repairing defected areas commonly exceeds the initial cost of coating. The maintenance cost can be reduced by identifying the coating failure at the earliest possible stage [1–3].

The factors which are responsible for coating failures affect the materialistic and mechanical properties of coating, which results in different forms of coating failures such as blistering (osmotic and non-osmotic), micro-cracks, edge delamination, ridge cracks, bubbling, abrasion and adhesion failure. Buckling in the multi-layered coating has been investigated for initiation of buckling through experimental analysis, and a prognostic model and growth rate has been formulated to find the de-bonding driving force to predict critical, fail and safe states. The change in temperature, thermal expansion mismatch between coating and substrate and in-plane compressive stress are key factors in the formation of blisters. Researchers have incorporated multiple parameters to model failure mechanism of coated systems. Mathematical solutions for elastic deformation of multi-layered beams due to residual stresses and external bending have been formulated by Zhang et al. [4]. Stress in multi-layered coating system has been investigated and a closed form solution is proposed in Ref. [5]. Loss of adhesion and variation in electrical properties in multi-layered films due to the effect of stresses has also caused major concerns for semiconductor industry [6]. Solutions to analyse deformation in multi-layered coating system affected by stresses, in-plane loading and external bending are presented in Ref. [7] and these relations can be further utilised to determine the stiffness, thickness, thermal expansion coefficient or thermal gradient.

Comprehensive experimental and theoretical studies have been conducted by researchers to investigate the improvement in mechanical properties of multi-layered coating by evaluation of various types of material compositions, varying the thickness of coating layers and evaluating the mechanical, thermal and magnetic properties via buckling test, nanoindentation test, scratching test, tensile test, corrosion and high-temperature test [8–12]. It has been found that oxidation has an inverse relationship to the number of interfaces in the multi-layered coating, which makes it more resistive towards corrosion [13]. Osmotic and non-osmotic phenomena between substrate and coating play a major role in the formation and growth of blisters. The presence of salt particles in water acting as cations drives the osmotic pressure with hydroxide acting as anions that appear through an electrochemical reaction due to microstructural defects in materials [14]. Several models in mathematical form have been developed to observe the phenomena of blisters formation and propagation. Bressers et al. [15] presented a discussion on premature cracking of oxidation-resistant coatings using fracture mechanisms

and mechanics concepts. An investigation of blistering effect in Ti/Al multi-layered coating through a modified experimental blister test is given by Galindo et al. [16]. Blister propagates in a pressure-sensitive tape on a steel substrate before approaching to maximum pressure. Dry cycles are responsible for degradation in tape adhesion and support in making a path for transport of species [17]. Strain energy density factor using mix mode conditions with stress intensity factors to estimate the durability of the coating was derived [18]. Prawoto [19] found that the strain energy density factor could be further combined with fracture mechanics to observe the growth of blister as crack propagation and diffusion of corrosive species concept to estimate the critical and safe condition of a coating system.

The NanoCorr, Energy and Modelling Group at Bournemouth University has developed several models to compute the de-bonding driving force and corrosion current rate as a function of residual and diffusion-induced stresses using material science, solid mechanics and fracture mechanics concepts. The mobility of corrosive products induces diffusion stress that can also alter the residual stress from 15 to 5 MPa compression. The proliferation of blistering does not depend on the thickness ratio of coating and substrate but adhesion between coating and substrate can be improved by increasing the ratio of elastic modulus of coating and substrate material [20]. Normalised stress, at the substrate interface, depends on the chemical potential of diffusive elements and blister formation takes place when it exceeds the critical stress level. Interfacial toughness is a function of elastic mismatch parameters and angular deflection which varies the mix mode parameter between $-\pi/2$ and $\pi/2$. It has been shown that mobility and concentration of cations plays a vital role in coating de-bonding from substrate [21]. A prognostic model for life assessment of exhaust mufflers has been developed by incorporating electrochemical reactions at the surface of the metal and dropwise condensation process [22]. In the presence of residual stress, a coefficient of thermal expansion (CTE) mismatch and negative change in temperature induces tensile stress which expands the micro-cracks already present in coating before the corrosive species approach saturation level [23]. Nucleation and Propagation of blisters in the cracks of the coating have also been modelled by coupling the effects of residual and diffusion-induced stresses [24]. Previous investigation of coating failures, that is, blistering, delamination, micro-cracks and corrosion damage measurement in real time has been reported [25–45].

Experimental observation

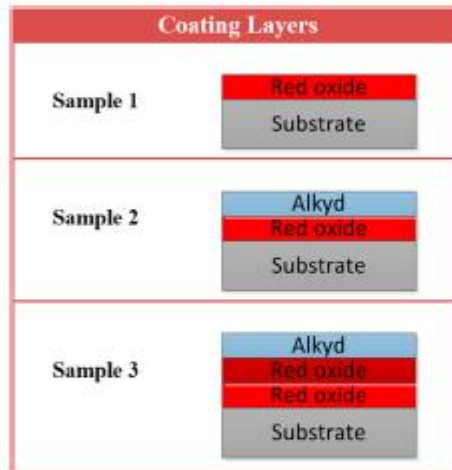
The S275 material has been used as a substrate in the experimental analysis; it is a structural steel grade which has been designed with specific chemical com-

Table 1. Steel S275 composition [25].

Composition and properties of S275					
Elements	C%	Mn%	P%	S%	S%
Quantity	0.25 max	1.60 max	0.04 max	0.05 max	0.05 max
Yield strength at nominal thickness 16 mm		275 N mm ⁻²			370–530 MPa
Tensile strength at thickness between 3 and 16 mm					

positions and mechanical properties formulated for particular applications. S275 has a Young modulus of 210 GPa and CTE as $12 \times 10^{-6}/^{\circ}\text{C}$. Composition and properties of S275 are shown in Table 1 [46]. Samples were conditioned before coating with the same grit size to produce roughness on the substrate interface. The roughness of each sample is measured through an optical interferometer. Samples were coated with primers along with alkyd topcoat, as shown in Figure 1. Properties of alkyd coatings have been investigated by

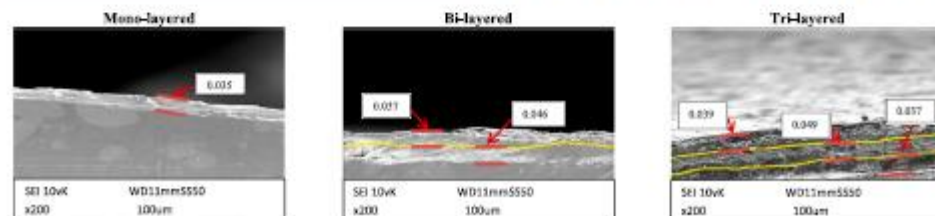
Armelin et al. [47] in detail. Red oxide primer coating has a Young's modulus of 6.14 GPa and the CTE is $21.6 \times 10^{-6}/^{\circ}\text{C}$ [24]. Sample 1 has mono-layer coating, sample 2 has bi-layer coating and sample 3 has tri-layer coating, respectively. Total thickness of each sample was measured using scanning electron microscopy (SEM). Thickness and average roughness of each sample before and after coating are given in Table 2. Samples were degreased with acetone before exposing them to corrosive aqueous solution, a solution of 5 M NaCl in distilled water. The thickness of coatings was measured through SEM, as shown in Figure 2. Layers are labelled with yellow lines to differentiate between them. It was observed that more application defects were measured as the number of coatings applied on the samples increases. After corrosion testing, surface profiles of all samples have been investigated through a 3D optical surface profilometer. Multiple blisters have been identified on the surface of samples due to the osmotic process, mismatch of thermal coefficient, diffusion-induced stresses and residuals stresses. The blisters with maximum amplitude from each sample are considered for comparison and are shown in Figure 3. Sample 1 with mono-layered coating has the largest number and size of blisters observed. The maximum blister amplitude for the mono-layered coated sample was $26.03 \mu\text{m}$ while bi-layered coated sample had the maximum blister amplitude of $24.8 \mu\text{m}$. The amplitude of the largest blister in the tri-layered coated sample is $16.64 \mu\text{m}$, which is comparatively small to mono-layered and bi-layered coated samples (Figure 4).

**Figure 1.** Coating layers.**Table 2.** Substrate roughness and coating thickness.

Sample no.	Average roughness (Ra)		Coating thickness (mm)
	Pre-coating	Post-coating	
1	0.328	1.63	0.035
2	0.468	1.72	0.083
3	0.384	1.53	0.125

Modelling of multi-layered coating

The aim of current research is to develop a prognostic model for failure prediction and the reliability assessment of multi-layered coating on metals using a multidisciplinary approach, as shown in Figure 5. Residual stress depends on the change in temperature and

**Figure 2.** Coating thickness using SEM.

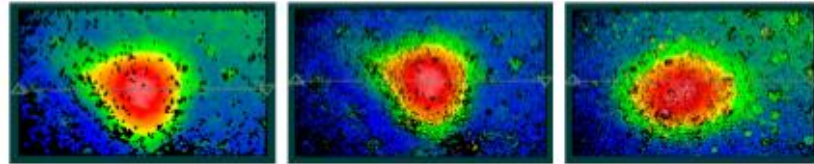


Figure 3. Average blisters after corrosion test using a 3D optical surface profilometer.

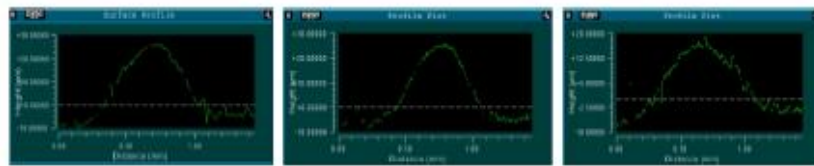


Figure 4. Blister amplitude using a 3D optical surface profilometer.

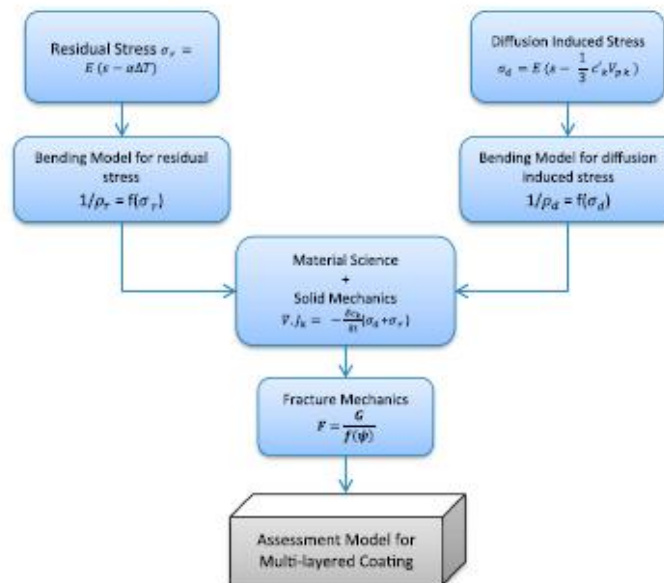


Figure 5. Multidisciplinary modelling approach.

CTE while corrosive species generate diffusion-induced stress which causes delamination. Bending models are derived for residual and diffusion-induced stresses. Material science and solid mechanics concepts are then combined to compute the change in concentration of corrosive species with respect to time, incorporating the effects of stresses in the multi-layered system. The energy release rate lies under the fracture mechanics concept defined as the de-bonding driving force which is released when the coating is separated from the substrate. The relationship for the de-bonding driving force as a function of residual and diffusion-induced stresses

is derived to compute critical, safe and fail states of multi-layered coatings.

Deformation in film coating systems depends on changes in temperature, the CTE mismatch and Young's modulus of material and substrate. Delamination of multi-layers due to the effect of residual stresses has previously been formulated [48]. The product of thermal expansion coefficient α and change in temperature ΔT dictate thermal stress-strain. The relation between thermal stress-strain and normal stress in cantilever beam is $\sigma = E(\epsilon - \alpha\Delta T)$ where ϵ strain and E represents Young's modulus. Temperature gradient can

be taken equal to concentration gradient and thermal expansion α to partial molar volume $\overline{V}_{pk}52$.

$$\sigma_d = E \left(\varepsilon - \frac{1}{3} c'_k \overline{V}_{pk} \right) \quad (1)$$

Deformation of multi-layers caused by residual stress has been modelled [48] using solid mechanics concept. These models can be used in conjunction with the diffusion model to assess the life of multi-layered coatings. The relation for the normal stress of a substrate and multi-layered coating system [49] can be given as:

$$\sigma_{di} = E_i \left(\varepsilon - \frac{1}{3} c'_{ki} \overline{V}_{pki} \right) \quad (2)$$

$$\sigma_{dci} = E_{ci} \left(\varepsilon - \frac{1}{3} c'_{kci} \overline{V}_{pkci} \right) \quad \text{where } i = 1 \dots n \text{ layers} \quad (3)$$

The diffusion-induced strain is a composition of uniform bending and bending component as $\varepsilon = \varepsilon_u + \varepsilon_b$. If the thickness of substrate is given as s , the thickness of the coating is h and the curvature is represented by ρ then the relation of uniform strain ε_u is given as $\varepsilon_u = x - t_b/\rho$ for $(-s \leq x \leq h)$. When the coating remains intact with the substrate, $x = t_b$ then bending strain is zero ($\varepsilon_b = 0$) and strain in a system becomes equal to uniform strain as $\varepsilon = \varepsilon_u$. To simplify calculations, it is assumed that $c'_{kj} = (1/3)c'_{ki}$ and $\overline{V}_{pkj} = (1/3)\overline{V}_{pkci}$ where $j = s, ci$ for the rest of calculations. The average stress distribution of multi-layered coatings, using Equations 2(a) and 2(b) can be given as:

$$\int_{-s}^0 E_s \left(\varepsilon_{ud} - \frac{1}{3} c'_{ks} \overline{V}_{pks} \right) dx_s + \sum_{i=1}^n \int_{h_{i-1}}^{h_i} E_{ci} \left(\varepsilon_{ud} - \frac{1}{3} c'_{kci} \overline{V}_{pkci} \right) dx_{ci} = 0 \quad (4)$$

The solution of Equation (3) gives uniform bending strain ε_u for multi-layered coating when the coating is intact with the substrate.

$$\varepsilon_{ud} = \frac{(E_s c'_{ks} \overline{V}_{pks} + \sum_{i=1}^n E_{ci} c'_{kci} \overline{V}_{pkci})}{E_s s + \sum_{i=1}^n E_{ci} t_i} \quad \text{where } i = 1 \dots n \text{ layers} \quad (5)$$

Using first-order approximation, uniform bending strain can write as:

$$\varepsilon_{ud} = \overline{V}_{pkc} c'_{k_s} + \sum_{i=1}^n \frac{E_{ci} t_i (c'_{k_i} \overline{V}_{pk_i} - c'_{k_s} \overline{V}_{pk_s})}{E_s s} \quad \text{where } i = 1 \dots n \text{ layers} \quad (6)$$

The applied moment is in equilibrium with the summation of bending moment with respect to the bending

axis ($x = t_b$). If M is the applied moment per unit width of multi-layered system, then

$$\int_{-s}^0 \sigma_{ds} (x - t_b) dx + \sum_{i=1}^n \int_{h_{i-1}}^{h_i} \sigma_{dci} (x - t_b) dx = M \quad (7)$$

By incorporating Equation 2(a), Equation 2(b), Equation (4) in Equation (6) gives

$$\int_{-s}^0 E_s \left(\varepsilon_u - \frac{1}{3} c'_{ks} \overline{V}_{pks} \right) (x - t_b) dx_s + \sum_{i=1}^n \int_{h_{i-1}}^{h_i} E_{ci} \left(\varepsilon_u - \frac{1}{3} c'_{kci} \overline{V}_{pkci} \right) (x - t_b) dx_{ci} = M \quad (8)$$

The solution of above equation gives us a relation for bending equation. Bending curvature is represented as ρ_d .

$$\frac{1}{\rho_d} = \frac{3[E_s(\varepsilon_u - c'_{ks} \overline{V}_{pks})s^2 - \sum_{i=1}^n E_{ci} t_i (\varepsilon_u - c'_{kci} \overline{V}_{pkci})(2h_{i-1} + t_i)] + 6M}{E_s s^2 (2s + 3t_b) + \sum_{i=1}^n E_{ci} t_i [6h_{i-1}^2 + 6h_{i-1} t_i + 2t_i^2 - 3t_b(2h_{i-1} + t_i)]} \quad (9)$$

Assuming the resultant force due to uniform stress components for multi-layers is zero, Equation (6) can be written as:

$$\int_{-s}^0 \sigma_{ds} (x - t_b) dx + \sum_{i=1}^n \int_{h_{i-1}}^{h_i} \sigma_{dci} (x - t_b) dx = 0 \quad (10)$$

By incorporating Equation 2(a), Equation 2(b), Equation (4) in Equation (9) gives

$$\int_{-s}^0 E_s \left(\varepsilon_{ud} - \frac{1}{3} c'_{ks} \overline{V}_{pks} \right) (x - t_b) dx_s + \sum_{i=1}^n \int_{h_{i-1}}^{h_i} E_{ci} \left(\varepsilon_{ud} - \frac{1}{3} c'_{kci} \overline{V}_{pkci} \right) (x - t_b) dx_{ci} = 0 \quad (11)$$

The thickness of the multi-layered coating is less than the thickness of substrate which simplifies the solution. The bending moment M has been ignored to study residual stress in the multi-layered system [48]. Using first-order approximation and ignoring applied moment the relationships of bending curvature can be given as:

$$\frac{1}{\rho_d} = 6 \sum_{i=1}^n \frac{E_{ci} t_i (c'_{k_i} \overline{V}_{pk_i} - c'_{k_s} \overline{V}_{pk_s})}{E_s s^2} \quad (12)$$

Bending curvature for each coating can be formulated as:

$$\frac{1}{\rho_{di}} = 6 \frac{E_{ci} t_i (c'_{k_i} \overline{V}_{pk_i} - c'_{k_s} \overline{V}_{pk_s})}{E_s s^2} \quad (13)$$

Thus Equation 11(a) can be written as:

$$\frac{1}{\rho_d} = \sum_{i=1}^n \rho_{d_i} \quad (14)$$

The above bending curvature relationship is similar to the relation derived by Hsueh et al. [48], but the thermal expansion and temperature gradient are taken analogues to partial molar volume and change in concentrations of species. This analogous relationship has been used to determine the effect of diffusion-induced stress in Li-Ion battery electrode particles [49]. The relation for deformation of multi-layered coating system due to residual stress has been derived by [48]. Uniform bending strain due to residual stress is given as:

$$\varepsilon_{ur} = \alpha_s \Delta T + \sum_{i=1}^n \frac{E_i t_i (\alpha_i - \alpha_s) \Delta T}{E_s s} \quad (15)$$

where $i = 1 \dots n$ layers

Bending curvature due to residual stress is formulated as:

$$\frac{1}{\rho_r} = 6 \sum_{i=1}^n \frac{E_i t_i (\alpha_i - \alpha_s) \Delta T}{E_s s^2} \quad (16)$$

Integration of diffusion and bending model

Fick's laws of diffusion describe diffusion and were derived as provided in Ref. [50]. According to Fick's first law, diffusion flux is proportional to the change in chemical potential. According to Li [51], chemical potential for isotropic materials can be defined as:

$$\mu_k^Q = \mu_k^s + RT \ln(c_k) - \bar{V}_{pk} \sigma_d \quad (17)$$

where J_k represents diffusion flux, D_k is diffusion coefficient, c_k represents concentration of the species, $\nabla \mu_k$ represents the gradient of chemical potential and R is the molar gas constant. A change in chemical potential defines a change in the thermodynamics state of system. The μ_k^s is chemical potential in standard state, μ_k^Q represents chemical potential corresponding to the stressed state of coating. \bar{V}_{pk} represents partial molar volume of component k . σ_d is diffusion-induced stress due to mobility of corrosive species, R is the molar gas constant and T is temperature. Fick's second law, which defines change in the concentration of species with respect to time, can be utilised to compute transport of corrosive species in coating material [24].

$$\begin{aligned} \frac{\delta c_k}{\delta t} = & D_k \nabla^2 c_k - \frac{\bar{V}_{pk} D_k}{RT} \nabla c_k \nabla (\sigma_d + \sigma_r) \\ & - \frac{\bar{V}_{pk} D_k}{RT} c_k \nabla^2 (\sigma_d + \sigma_r) \end{aligned} \quad (18)$$

By incorporating the above relations in the diffusion model, the relation for change in concentration of

species in the multi-layered system can be derived. The diffusion model for substrate and multi-layered coating is given as:

$$\begin{aligned} \frac{\delta c_k}{\delta t} = & D_k \nabla^2 c_k - \frac{\bar{V}_{pk} D_k}{RT} \nabla c_k \nabla (\sigma_r + \sigma_d) \\ & - \frac{\bar{V}_{pk} D_k}{RT} c_k \nabla^2 (\sigma_r + \sigma_d) \end{aligned} \quad (19)$$

The model for change in concentration of species due to residual and diffusion-induced stress has been derived and experimentally validated in Ref. [23].

$$\begin{aligned} \frac{\delta c_{k_i}}{\delta t} = & \left\{ \left(D_{k_i} + \frac{D_{k_i} E_{c_i} V_{pk_i}^2}{9RT} c_{k_i} \right) \frac{\partial^2 c_{k_i}}{\partial x^2} \right. \\ & + \frac{D_{k_i} E_{c_i} V_{pk_i}^2}{9RT} \left(\frac{\delta c_{k_i}}{\delta t} \right)^2 \\ & \left. - \frac{D_{k_i} E_{c_i} V_{pk_i}^2}{9RT} \frac{\delta c_{k_i}}{\delta t} \left(\frac{1}{\rho_{d_i}} + \frac{1}{\rho_{r_i}} \right) \right\} \end{aligned} \quad (20)$$

Terms can be written as $E_{c_i} / \rho_{d_i} = \partial \sigma_{d_i} / \partial t E_{c_i} / \rho_{r_i} = \partial \sigma_{r_i} / \partial x$,

$$\sigma_T = \sigma'_d + \sigma'_r = \frac{\partial \sigma_{d_i}}{\partial t} + \frac{\partial \sigma_{r_i}}{\partial x} \quad (21)$$

$$\begin{aligned} & \frac{\partial \sigma_{d_i}}{\partial t} + \frac{\partial \sigma_{r_i}}{\partial x} \\ & = \frac{\left(D_{k_i} + \frac{D_{k_i} E_{c_i} V_{pk_i}^2}{9RT} c_{k_i} \right) \frac{\partial^2 c_{k_i}}{\partial x^2} + \frac{D_{k_i} E_{c_i} V_{pk_i}^2}{9RT} \left(\frac{\delta c_{k_i}}{\delta t} \right)^2}{\frac{D_{k_i} V_{pk_i}^2}{9RT} \frac{\delta c_{k_i}}{\delta t}} \end{aligned} \quad (22)$$

Fracture mechanics concept

Propagation and initiation of delamination can be investigated under the umbrella of fracture mechanics. The de-bonding driving force, which is a function of substrate and coating material properties, roughness and thickness, defines detachment of coating from the substrate [52]. When stress reaches a certain value, which is defined as critical stress, buckling initiates and its propagation depends on the toughness of the material. Critical stress as defined in Ref. [53] is given as:

$$\sigma_{cr} = 1.2235 \frac{E}{(1 - \nu^2)} \left(\frac{T_{th}}{r} \right)^2 \quad (23)$$

where T_{th} is the total thickness of coating, r is the radius of blister induced by buckling between coating and substrate, E is Young's modulus and ν is the Poisson's ratio of coating material.

Examination of buckling delamination in multi-layered coatings using fracture mechanics concept was

performed in Refs. [52–54]. The relations given by [54] for delamination of multi-layered thermal barrier coating are applicable for other multi-layered coating systems. The critical value of stress in multi-layered system at which buckling initiates is given as:

$$\sigma_{cr} = \left(\frac{\pi}{r}\right)^2 \frac{1}{3} \sum_{i=1}^n \frac{E_i}{(1-v_i^2)} [(x_{i+1} - t_b)^3 - (x_i - t_b)^3] \quad (24)$$

σ_{cr} represents critical stress level for multi-layered coating, r is the radius of blisters induced by buckling between coating and substrate, x_{i+1} and x_i are the top and bottom locations of i th coating layer.

The strain energy release rate defines the de-bonding driving force which is required to generate buckling between coating and substrate. High fracture toughness means the de-bonding force will experience more resistance. Strain energy in the multi-layered coating system depends on mechanical properties of the coating materials. Energy stored in the multi-layered system that can be released by plane strain without any buckling or bending is given as [52]:

$$G_0 = \frac{\sigma_c^2}{2} \sum_{i=1}^n \frac{(1-v_i^2)}{E_i} t_i \quad (25)$$

Diffusion-induced stress in the multi-layered model is incorporated in the proposed prognostic model to find the value of strain energy release rate. The relation of the strain energy release rate in the multi-layered system is given as:

$$G = \frac{M^2}{2B} + \frac{N^2}{2S} \quad (26)$$

G represents the strain energy release rate, which can be defined as a de-bonding driving force. M is the bending moment, N is the resultant pre-buckling stress, B and S are bending stiffness and stretching stiffness of the multi-layered coating system, respectively. Relations for B and S are given in Appendix.

Solving Equation (21) by incorporating B and S relations gives the following equation to calculate strain energy release rate as a function of stresses. Equation (23) seems similar to the equation derived in Ref. [36] for the single layered coating system. The solution of Equation (23) is given in Appendix.

$$G' = \frac{3}{2} \sum_{i=1}^n \frac{(1-v_i^2)}{E_i(x_{i+1} - t_p)^3 - (x_{i+1} - t_p)^3} M^2 \left[1 + \frac{1}{4} \left(\sqrt{\frac{\sigma_T}{\sigma_0}} - 1 \right)^2 \right] \quad (27)$$

Propagation depends on mode adjusted de-bonding driving force. The de-bonding driving force, which defines the detachment of coating from the substrate,

is a function of strain energy release rate and mode mix function [36].

$$F = \frac{G'}{j} \quad (28)$$

$$j = \sec^2 \left[\left(1 - \frac{\Gamma_{IC}}{E_c \lambda} \right) \psi \right] \quad (29)$$

where λ is the ratio between square of average roughness amplitude (R_{av}) and average roughness wavelength (L_{av}) as $\lambda = R_{av}^2/L_{av}$. ψ represents the mode adjustment term. The dimensionless mode mix function can be used to adjust the mode-dependent strain energy release rate for isotropic materials attached to each other; the mode mixing relation can be given as:

$$\tan \psi = \frac{K_2}{K_1} = \frac{\sqrt{12} + (T_{th} \Delta N / \Delta M) \tan \omega}{-\sqrt{12} \tan \omega + (T_{th} \Delta N / \Delta M) \tan \omega} \quad (30)$$

$$\frac{T_{th} \Delta N}{\Delta M} = \left(\sqrt{\frac{3(\sigma_{cr} - \sigma_0)}{B \left(\frac{\pi}{r} \right)^2}} \right) \quad (31)$$

The de-bonding driving force can be written as a function of toughness, stresses, bending moment, total coating thickness, elastic modulus, Poisson ratio and interface roughness of the substrate. The following relation is similar to the relation derived and experimentally validated [36] for single layered coating optimisation:

$$F = \frac{\frac{3}{2} \sum_{i=1}^n \frac{(1-v_i^2)}{E_i(x_{i+1} - t_p)^3 - (x_{i+1} - t_p)^3} M^2 \left[1 + \frac{1}{4} (\sqrt{\Gamma} - 1)^2 \right]}{1 + \tan \left(\left(1 - \frac{\Gamma_{IC}}{E_c \lambda} \right) \frac{\sqrt{12} + (T_{th} \Delta N / \Delta M) \tan \omega}{-\sqrt{12} \tan \omega + (T_{th} \Delta N / \Delta M) \tan \omega} \right)^2} \quad (32)$$

where Γ is the de-bonding index. From the above relation, critical, safe and fail conditions for isotropic coating layers can be found. De-bonding force is dependent on the ratio of resultant stress and critical stress which defines the threshold level for coating failure. When $\Gamma < 1$, the coating is in the safe condition because stress generated has not exceeded the critical stress and blistering has not been initiated. $\Gamma = 1$ defines the critical threshold level at which blistering effect starts. When $\Gamma > 1$, the coating lies in the fail state, which means the blistering effect has been initiated. Optimised values for the isotropic multi-layered coating system can be computed from the above relation. To find the threshold level $\Gamma = 1$, the above equation reduces to Equation (28b) which can be used to find critical values of multi-layered isotropic coatings.

$$F_{cr} = \frac{\frac{3}{2} \sum_{i=1}^n \frac{(1-v_i^2)}{E_i(x_{i+1} - t_p)^3 - (x_{i+1} - t_p)^3} M^2}{1 + \tan \left(\left(1 - \frac{\Gamma_{IC}}{E_c \lambda} \right) \frac{1}{-\tan \omega} \right)^2} \quad (33)$$

Blister growth velocity model

Once the blister has formed, the moment at the verge of blister establishes and causes the formation of cathodic reaction products to accelerate the diffusion process to inflate the blister. The growth rate of blister can be predicted by taking coating as a cantilever beam loaded by bending moment at the edge. The total bending moment as a function of stress, coating thickness and amplitude of blister is given by the following relation:

$$M_0 = T_{th} w \sigma T \quad (34)$$

where T_{th} is the coating thickness, w is the amplitude of blister and σ is stress formed by the diffusion process of corrosive environment and the defects that were formed during the manufacturing processes. The threshold bending moment is given in Equation (30). If the value of bending moment is below the threshold value calculated from the following relation, then the blister will not continue to grow [55].

$$M_{Th} = 0.73 \sqrt{\sum_{i=1}^n \frac{E_i}{(1 - \nu_i^2)}} \sqrt{a \sigma T_{th}^3} \quad (35)$$

where E_i is the modulus of elasticity and ν_i is the Poisson's ratio of coating material. After the formation of blister, it grows with a velocity that depends on coating properties, temperature, stress induced and the size of blister. The relation for threshold velocity below which the blister will not continue can be calculated as:

$$V_{min} = 1.83 \left(\frac{\sigma_f}{a} \right)^{1.25} \left[\frac{D_b \delta_b \Omega}{kT} \right] \left[\sum_{i=1}^n \frac{E_i}{(1 - \nu_i^2)} \frac{T_{th}^3}{12} \right]^{-0.25} \quad (36)$$

where $D_b \delta_b$ is the interfacial diffusivity and Ω represents volume of the diffusing species. The dimensionless relation for blister growth velocity can be given as:

$$v = [m + \sqrt{m^2 - 1}]^{2.5} \quad (37)$$

The above relation is applicable for $v \geq 1$ and $m \geq 1$, where $v = V/V_{min}$ is dimensionless velocity and $m = M_0/M_{Th}$ is dimensionless moment at blister crack tip, respectively. The relation for critical bending moment to predict the blistering initiation process has been derived by Martin et al. [56] and can be given as:

$$M_{ini} = 3 \frac{\sum_{i=1}^n E_i T_{th}^3 w}{a^2} \quad (38)$$

According to the above relation, M_{ini} is a function of blister diameter a and amplitude w . After the formation of blister following conditions can be utilised to estimate whether the blister will grow or stop growing. If the value estimated through Equation (30) is greater

If $M_{Th} < M_{ini}$ Blister → grow	If $M_{Th} > M_{ini}$ Blister ≠ grow
---	---

than the value estimated through Equation (33), then blister will grow after initiation and in opposite scenario blister will not grow, which can be summarised as:

Coating life assessment model

Atmospheric pollutants are a major source of corrosion, and the diffusion of these corrosive species plays a significant role in the coating failure mechanism. The corrosive species present at a coating defect starts diffusing into the delamination region and forms an electrochemical cell, which drives the cathodic delamination process [57]. Research findings have shown that blisters form due to the electrochemical process and growth of a blister depends on the bending moment, which induces at the edge of the blister. In early research, cathodic blistering mechanisms have been modelled by applying the concept of semi-double cantilever beam theory. In past several years, researchers have adopted a multidisciplinary approach to model the transportation of corrosion products and blister growth phenomena under the umbrella of material science, thermodynamics and fracture mechanics.

Several models have previously been proposed to explain the process of cathodic delamination. Wan and Liao [58] formulated the elastic energy release rate for blister formation and growth as a function of blister height and pressure. The relationship proposed by Bresser et al. [15] models the elastic energy release rate as a function of blister amplitude, pressure and thickness of the coating. Jensen [59] has also developed identical kind of relations. Later on, the relation between energy release rate as a function of stiffness, pressure, blister amplitude, blister radius and coating thickness was developed by Kappes et al. [60]. Prawoto and Dillon [18] have combined the material science concepts with fracture mechanics and also modelled blister mechanism by including J-integral concept. Strattmann et al. [61] investigated the cathodic deamination process through various experimental techniques and developed a corrosion model. Later on, an extensive model was proposed by Allahar et al. [62] based on the experimental observation that the rate of diffusion of corrosive species and formation of OH^- ions define the adhesion loss between coating and substrate. Hutchinson [52,53,63] has done comprehensive work on explaining the blister formation and propagation mechanism using fracture mechanics concepts, which are modified by Khan-Nazir [21] for interfacial toughness and mod mix equations.

The de-bonding driving force as a function of mechanical and chemical characteristics of coating and substrate modelled by Khan-Nazir is further extended

672 J. LATIF ET AL.

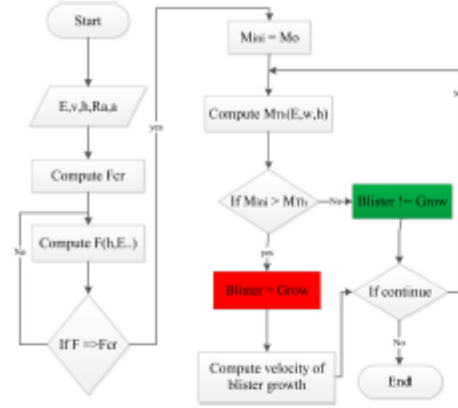


Figure 6. Coating life assessment model.

for multi-layered coated systems and combined with blister velocity growth to propose a coatings useful life assessment model. The model can be utilised to evaluate and compare multiple coatings in terms of adhesion loss and the speed at which a blister will propagate once it has appeared. The model takes material and mechanical parameters of coating and substrate as input. It computes the critical level de-bonding driving force at which blister initiates. After calculating the critical level of de-bonding force, the current value of de-bonding force is being computed and continuously monitored and compared with critical level to predict the formation of a blister. If the current de-bonding force is less than the critical level than a blister has not formed, while a blister appears when de-bonding force surpasses its critical level. The bending moment at blister initiation is taken as the initiation bending moment. The threshold bending moment is computed after blister formation to compare it with the initiation bending moment. The conditions for blister growth or stops given in the previous section are evaluated to predict the propagation of blister. If blister continues to grow then its growth velocity can be computed to estimate the rate at which coatings are losing adhesion with the substrate. The model provides a prediction of adhesion loss for multi-layered coatings as well as the failure rate after losing adhesion and can be used to differentiate the performance of coatings useful life and behaviour after falling into a fail state (Figure 6).

Mathematical model implementation

Initial boundary conditions are given as:

$$c_{k_i}(x) = c_{k_e} = 0 \quad \text{for time } t = 0 \quad (39)$$

$$c_{k_i}(h) = c_{k_0} \quad \text{for time } t > 0 \quad (40)$$

All parameters and variables are converted into a dimensionless form for numerical simulation as:

$$\tilde{c}_{k_i} = \frac{c_{k_i}}{c_{k_0}} \quad (41)$$

$$\tilde{E} = \frac{2}{3} \sum_{i=1}^n \frac{E_i}{(1 - \nu_i^2)E_s} \quad (42)$$

$$\tilde{D}_k = \frac{D_{k_i}}{D_{k_e}} \quad (43)$$

$$\tilde{A} = \left(\frac{E_G V_{p_{k_i}}^2}{RT} \right) c_{k_0} \quad (44)$$

$$\frac{1}{\tilde{\rho}_{d_i}} = \frac{1}{\rho_{d_i} c_{k_0} V_{p_{k_0}}} = 6 \sum_{i=1}^n \frac{E_i t_i (c'_{k_i} \overline{V_{p_{k_i}}} - c'_{k_e} \overline{V_{p_{k_e}}})}{E_s s^2 c_{k_0} V_{p_{k_0}}} \quad (45)$$

$$\frac{1}{\tilde{\rho}_{r_i}} = \frac{1}{\rho_{r_i} \alpha_{k_0} \Delta T_{k_0}} = 6 \sum_{i=1}^n \frac{E_i t_i (\alpha_i - \alpha_s) \Delta T}{E_s s^2 \alpha_{k_0} \Delta T_{k_0}} \quad (46)$$

$$\tilde{x} = ((x_{i+1} - t_p)^3 - (x_i - t_p)^3) / (s + T_{th}) \quad (47)$$

After applying dimensionless parameters and variables Equation 28(a) and 28(b) can be written as:

$$\tilde{F} = \frac{(1/\tilde{E})\tilde{M}(1/\tilde{x})}{1 + \tan \left((1 - \tilde{B}) \frac{1}{\tan \omega} \right)^2} \left[1 + \frac{1}{4} (\sqrt{\gamma - 1})^2 \right] \quad (48)$$

$$\tilde{F}_{cr} = \frac{(1/\tilde{E})\tilde{M}(1/\tilde{x})}{1 + \tan \left((1 - \tilde{B}) \frac{1}{\tan \omega} \right)^2} \quad (49)$$

For numerical solution the Runge-Kutta method has been utilised to find the de-bonding driving force as a function of change in the stress with the following steps:

- Input parameters into prognostic model, for example, Poisson's ratio, elastic modulus, thermal coefficients, etc.
- Calculate the critical stress levels and critical de-bonding driving force using Equations (19), (20) and (35b).
- Apply the Runge-Kutta method to update the change in σ_T using Equation (18).
- Use the updated value obtained in step (c) to find the de-bonding driving force using Equation (30a).
- Compare the value of de-bonding driving force obtained in step (d) to find critical, safe and fail conditions. If $\tilde{F} < \tilde{F}_{cr}$ shows coating is in the safe condition, $\tilde{F} > \tilde{F}_{cr}$ represents the fail condition while $\tilde{F} = \tilde{F}_{cr}$ means coating is in the critical condition.

- (f) Evaluate the convergence criteria for de-bonding driving force using Equation (A3) in Appendix and repeat the process if it converges.
- (g) When the coating enters into the critical condition the bending moment at that stage is taken as the initiation bending moment.
- (h) Threshold bending moment is computed to find the possibility of blister growth.
- (i) If the initiation bending moment is greater than the threshold bending moment then the blister will not grow.
- (j) If the initiation bending moment is less than the threshold bending moment then the blister will grow.
- (k) The velocity of blister growth can be calculated from Equation (32).

Results and discussions

Buckle-driven blistering delamination has been modelled in terms of de-bonding driving force as a function of diffusion induced and residual stresses for multi-layered organic isotropic coatings to predict useful coating life. The proposed model can be utilised to compare and measure the performance of multiple coating materials. Using a multi-layered model, the effect of multiple layers can be incorporated for more reliable prediction of coating failure as most of the substrates in different applications are coated with multiple coats. Experimental and simulation analyses show a very strong agreement. Multiple coating layers reduce the de-bonding driving force, so the blister formation takes more time to appear and propagate. Experiments were conducted and the results show the behaviour of blistering initiation and propagation in single and multi-layered coated substrates. The three samples which were subjected to a corrosive environment at 350 K showed blisters of variable sizes and at

different times, depending on the properties. After the surface analysis of samples, the average size of a blister from each sample is selected for observation and analysis. Blister formation in multi-layered coated samples is assumed to be between substrate and coatings while coating layers remain intact.

The blister size distribution is plotted in Figure 7 to show the difference of blister size among samples. The mono-layered coated sample has the lowest strength and it showed the largest number of blisters and the average blister had 25 μm amplitude with approximately 7 mm of diameter. The average blister amplitude of bi-layered coated sample is 23 μm with a diameter of 6 mm between the other two samples that were 23 mm which was more than expected, which may be the effect of stresses developed within coating during the application. Meanwhile, the average blister that formed on the tri-layered coated sample was much smaller than others, with an amplitude of approximately 15 μm with a diameter of 8 mm. The point of interest is to identify the critical stage at which blister initiates. The blister initiation stages are shown in Figure 8 which is observed through experimental analysis. The result plotted in Figure 8 shows the relation of blister formation and time. The sample prior to the blistering effect is considered in a safe state while after formation of a blister the sample is considered in the fail state.

According to the experimental observation, blisters started forming on the sample after approximately 72 h. Sample 1 is then considered in the fail state because the de-bonding driving force has surpassed its critical level due to osmosis and non-osmosis factors and coating started deteriorating from sample substrate. The time taken by sample 2 to reach its critical level then drop into the fail state was approximately after 96 h under the corrosive environmental conditions. The dual layers of coats have lowered the de-bonding driving force as it took more time than sample 1 to surpass its critical

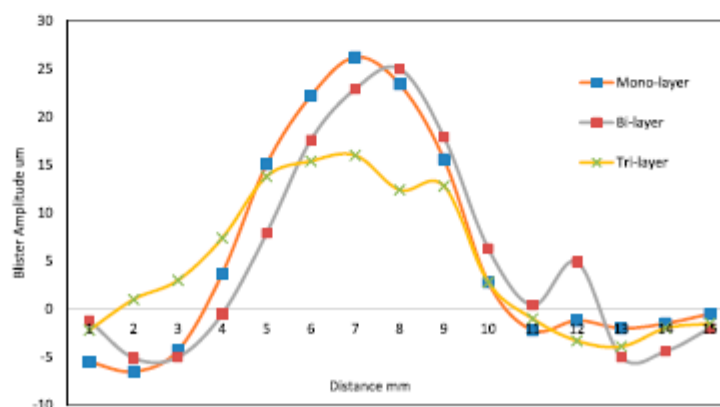


Figure 7. Comparison of average blister size of each sample.

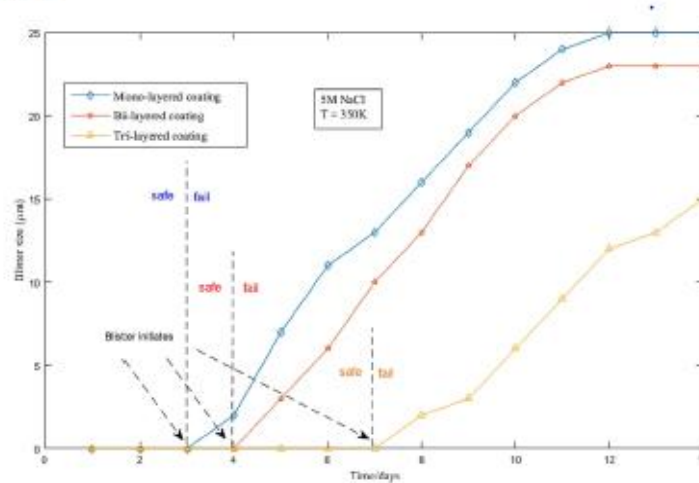


Figure 8. Experimental observation of blisters initiation and propagation.

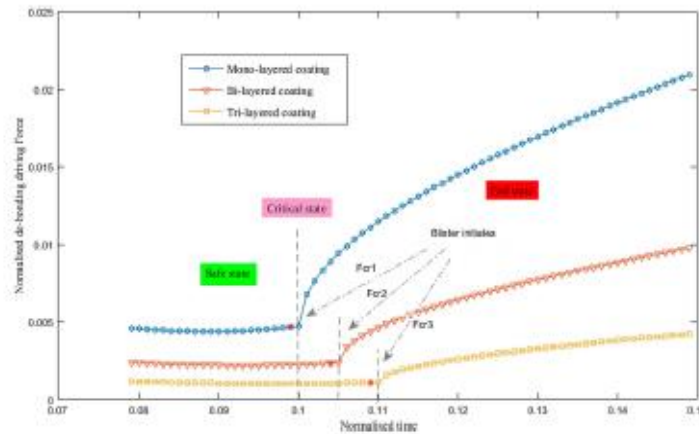


Figure 9. Simulation analysis of safe and fail states of each sample.

level. Sample 3 had the highest adhesion strength as compared to the rest of the samples; the top coat also assisted in lowering the de-bonding force. The buckling effect took approximately 168 h to start forming blisters on the sample 3 surface and continued increasing until it gained its maximum amplitude. Simulation results for the mathematical model are shown in Figure 9. The de-bonding driving force is the parameter that defines the blister initiation through which safe, critical and fail conditions can be defined. The simulation of the algorithm is described in the mathematical model implementation section. The critical de-bonding driving force is computed initially and the de-bonding force is compared to the critical level to

find whether it is lying in the safe state or fail state. The relationship between the normalised de-bonding driving force and normalised time is plotted and shows a similar behaviour to that observed in the experiments. The model can be used to scale it with real time to find and predict the duration at which coating would be in their critical and fail conditions. According to simulation results, the de-bonding driving force has been reduced by multiple coatings depending on their mechanical and chemical properties. Once a blister has formed, it then propagates at a particular velocity depending on bending moment at the edge of the blister. Hence, the prognostic model is further extended to blister growth velocity. If the conditions of blister

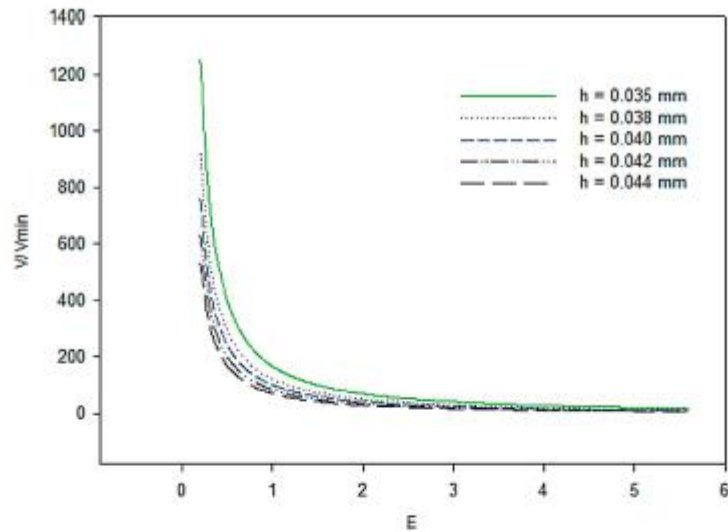


Figure 10. Blister velocity vs. elastic modulus.

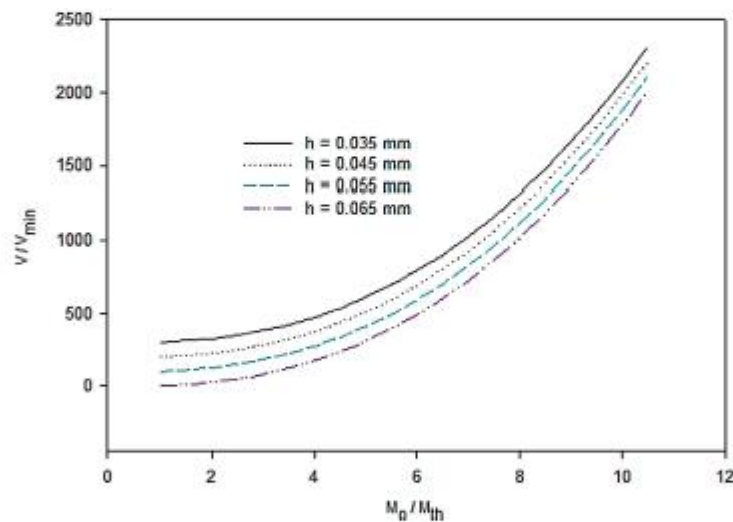


Figure 11. Blister velocity vs. bending moment.

growth or stoppage as described in the section 'Blister growth velocity model' are applied by taking the amplitude and diameter of a blister as $25\text{ }\mu\text{m}$ and 7 mm gives the initiation bending moment large than the threshold bending moment, hence the blister tends to keep growing. The velocity of blister growth depends on elastic modulus and with variable coating thicknesses as shown in Figure 10. As shown in Figures 10 and 11 the blister growth velocity also depends on properties of the coating materials. The proposed model of coating life assessment can be further investigated

and evaluated through experimental and simulation by varying coating materials, by measuring blisters per area of particular coating and the effect of variable multiple coating thicknesses with different mechanical and chemical properties.

Conclusion

The coating failure and corrosion phenomena can cause the whole structure to complete failure which costs human loss, delay in industrial production and huge

financial loss. It is very important to design prognostic models by incorporating all the possible parameters in order to evaluate the useful life of protective coatings and schedule the maintenance strategies accordingly. The coating failure mechanism involves various fields of study. Therefore, a comprehensive coating life assessment model has been developed using a multi-disciplinary approach to formulate de-bonding driving force. The specimens with protective coatings are tested through experimental analysis to validate the proposed model. The de-bonding driving force predicts three stages as safe, critical and fails states of coating-substrate system operating under corrosive environmental conditions. The formation and propagation of blistering effect were observed during experimental analysis and average blister size is selected from each sample for experimental observation. Further experimental analysis can be carried out to investigate the model in more detail on different types of substrate and coating materials.

Acknowledgements

The authors acknowledge their financial support and in-kind contributions.

Disclosure statement

No potential conflict of interest was reported by the authors.

Funding

This research is jointly funded by Defence Science and Technology Laboratory (DSTL), Ministry of Defence (MoD) UK and Bournemouth University.

ORCID

Zulfiqar Ahmad Khan  <http://orcid.org/0000-0002-8725-5166>

References

- [1] Herzberg E. The annual cost of corrosion for DoD. Proceedings of the Department of Defense Corrosion Conference; 2009.
- [2] Revie RW. Corrosion and corrosion control. Hoboken New Jersey: Wiley; 2008.
- [3] Du YJ, Damron M, Tang G, et al. Inorganic/organic hybrid coatings for aircraft aluminum alloy substrates. *Prog Org Coat*. 2001;41:226–232.
- [4] Zhang N-H, Xing J-J. An alternative model for elastic bending deformation of multilayered beams. *J Appl Phys*. 2006;100:103519.
- [5] Hu Y, Huang W. Elastic and elastic-plastic analysis of multilayer thin films: closed-form solutions. *J Appl Phys*. 2004;96:4154–4160.
- [6] Liu H, Murarka S. Elastic and viscoelastic analysis of stress in thin films. *J Appl Phys*. 1992;72:3458–3463.
- [7] Malzbender J. Mechanical and thermal stresses in multilayered materials. *J Appl Phys*. 2004;95:1780–1782.
- [8] Moody N, Venkataraman S, Nelson J, et al. Interface roughness effects on adhesion of Ta 2 N films. *MRS proceedings*; 1993; Cambridge University Press, 337.
- [9] Sarikaya O. Effect of some parameters on microstructure and hardness of alumina coatings prepared by the air plasma spraying process. *Surf Coat Technol*. 2005;190:388–393.
- [10] Yagmur L. Effect of microstructure on internal friction and Young's modulus of aged Cu–Be alloy. *Mater Sci Eng A*. 2009;523:65–69.
- [11] Fauchais P, Vardelle A. Thermal sprayed coatings used against corrosion and corrosive wear. 2012, INTECH Open Access Publisher.
- [12] Chirima GT, Zied KM, Ravirala N, et al. Numerical and analytical modelling of multi-layer adhesive-film interface systems. *Phys Status Solidi B Basic Solid State Phys*. 2009;246:2072–2082.
- [13] Nordin M, Herranen M, Hogmark S. Influence of lamellae thickness on the corrosion behaviour of multilayered PVD TiN/CrN coatings. *Thin Solid Films*. 1999;348:202–209.
- [14] Pommersheim JM, Nguyen T, Hartzfeld K. Prediction of blistering in coating systems. Washington, DC: ACS symposium series; 1998.
- [15] Bressers J, Petevs S, Steen M. Coatings for hot section gas turbine components. *Eur Struct Integr Soc*. 2000;26:115–134.
- [16] Galindo RE, Van Veen A, Evans J, et al. A modified blister test to study the adhesion of thin coatings based on local helium ion implantation. *Thin Solid Films*. 2005;471:170–176.
- [17] Gent A, Lewandowski L. Blow-off pressures for adhering layers. *J Appl Polym Sci*. 1987;33:1567–1577.
- [18] Prawoto Y, Dillon B. Failure analysis and life assessment of coating: the use of mixed mode stress intensity factors in coating and other surface engineering life assessment. *J Fail Anal Prev*. 2012;12:190–197.
- [19] Prawoto Y. Unified model for blister growth in coating degradation using weight function and diffusion concepts. *Mater Corros*. 2013;64:794–800.
- [20] Nazir M, Khan ZA, Saeed A, et al. A model for cathodic blister growth in coating degradation using mesomechanics approach. *Mater Corros*. 2016;67:495–503.
- [21] Nazir M, Khan ZA, Stokes K. A holistic mathematical modelling and simulation for cathodic delamination mechanism – a novel and an efficient approach. *J Adhes Sci Technol*. 2015;29:2475–2513.
- [22] Nazir M, Khan ZA, Saeed A, et al. A predictive model for life assessment of automotive exhaust mufflers subject to internal corrosion failure due to exhaust gas condensation. *Eng Fail Anal*. 2016;63:43–60.
- [23] Nazir M, Khan ZA, Saeed A, et al. Modeling the effect of residual and diffusion-induced stresses on corrosion at the interface of coating and substrate. *Corrosion*. 2015;72:500–517.
- [24] Nazir M, Khan ZA, Stokes K. Analysing the coupled effects of compressive and diffusion induced stresses on the nucleation and propagation of circular coating blisters in the presence of micro-cracks. *Eng Fail Anal*. 2016;70:1–15.
- [25] Saeed A, Khan Z, Montgomery E. Corrosion damage analysis and material characterization of Sherman and Centaur – the historic military tanks. *Mater Perform Charact*. 2013;2:20120016.
- [26] Saeed A, Khan ZA, Hadfield M, et al. Material characterization and real-time wear evaluation of pistons

- and cylinder liners of the tiger 131 military tank. *Tribol Trans.* 2013;56:637–644.
- [27] Nazir MH, Khan ZA, Saeed A, et al. A model for cathodic blister growth in coating degradation using mesomechanics approach. *Mater Corros.* 2016;67:495–503.
- [28] Nazir MH, Khan ZA, Saeed A, et al. Modeling the effect of residual and diffusion-induced stresses on corrosion at the interface of coating and substrate. *Corrosion.* 2015;72:500–517.
- [29] Saeed A, Khan Z, Clark M, et al. Non-destructive material characterisation and material loss evaluation in large historic military vehicles. *Insight Non-Destr Test Cond Monit.* 2011;53:382–386.
- [30] Saeed A. Sustainable methodology of conserving historic military vehicles. Bournemouth, UK: Bournemouth University; 2013.
- [31] Saeed A, Khan ZA, Nazir MH. Time dependent surface corrosion analysis and modelling of automotive steel under a simplistic model of variations in environmental parameters. *Mater Chem Phys.* 2016;178:65–73.
- [32] Nazir MH, Khan ZA, Stokes K. A holistic mathematical modelling and simulation for cathodic delamination mechanism – a novel and an efficient approach. *J Adhes Sci Technol.* 2015;29:2475–2513.
- [33] Khan ZA, Grover M, Nazir MH. The implications of wet and dry turning on the surface quality of EN8 steel. *Trans Eng Technol.* 2015;413–423. Springer.
- [34] Nazir MH, Khan Z, Stokes K. Modelling of metal-coating delamination incorporating variable environmental parameters. *J Adhes Sci Technol.* 2015;29:392–423.
- [35] Nazir M, Khan Z, Saeed A, et al. Modelling the effect of residual and diffusion induced stresses on corrosion at the interface of coating and substrate. *Corrosion.* 2016;72:500–517.
- [36] Nazir MH, Khan ZA, Stokes K. Optimisation of interface roughness and coating thickness to maximise coating-substrate adhesion – a failure prediction and reliability assessment modelling. *J Adhes Sci Technol.* 2015;29:1415–1445.
- [37] Nazir M, Khan ZA, Stokes K. A unified mathematical modelling and simulation for cathodic blistering mechanism incorporating diffusion and fracture mechanics concepts. *J Adhes Sci Technol.* 2015;29:1200–1228.
- [38] Nazir MH, Saeed A, Khan Z. A comprehensive predictive corrosion model incorporating varying environmental gas pollutants applied to wider steel applications. *Mater Chem Phys.* 2017;193:19–34.
- [39] Saeed A, Khan ZA, Nazir H, et al. Research impact of conserving large military vehicles through a sustainable methodology. *Int J Herit Arch.* 2017;1:267–274.
- [40] Nazir M, Khan Z. A review of theoretical analysis techniques for cracking and corrosive degradation of film-substrate systems. *Eng Fail Anal.* 2017;72:80–113.
- [41] Bajwa R, Khan Z, Nazir H, et al. Wear and friction properties of electrodeposited Ni-based coatings subject to nano-enhanced lubricant and composite coating. *Acta Metall Sin (English Letters).* 2016;29:902–910.
- [42] Khan ZA, Pashaei P, Bajwa R, et al. Fabrication and characterization of electrodeposited and magnetron-sputtered thin films. *Int J Comput Methods Exp Meas.* 2015;3:165–174.
- [43] Nazir MH, Khan Z. Maximising the interfacial toughness of thin coatings and substrate through optimisation of defined parameters. *Int J Comput Methods Exp Meas.* 2015;3:316–328.
- [44] Bajwa RS, Khan Z, Bakolas V, et al. Effect of bath ionic strength on adhesion and tribological properties of pure nickel and Ni-based nanocomposite coatings. *J Adhes Sci Technol.* 2016;30:653–665.
- [45] Bajwa RS, Khan Z, Bakolas V, et al. Water-lubricated Ni-based composite (Ni–Al₂O₃, Ni–SiC and Ni–ZrO₂) thin film coatings for industrial applications. *Acta Metall Sin (English Letters).* 2016;29:8–16.
- [46] Anon. Available from: <http://www.azom.com/article.aspx?ArticleID=6022>
- [47] Armelin E, Ocampo C, Liesa F, et al. Study of epoxy and alkyd coatings modified with emeraldine base form of polyaniline. *Progr Org Coat.* 2007;58:316–322.
- [48] Hsueh C-H. Modeling of elastic deformation of multilayers due to residual stresses and external bending. *J Appl Phys.* 2002;91:9652–9656.
- [49] Zhang X, Shyy W, Sastry AM. Numerical simulation of intercalation-induced stress in Li-ion battery electrode particles. *J Electrochem Soc.* 2007;154:A910–A916.
- [50] Mejlbro L. 1996 Cementa AB, Lund, Sweden.
- [51] Li JC-M. Physical chemistry of some microstructural phenomena. *Metall Trans A.* 1978;9:1353–1380.
- [52] Faulhaber S, Mercer C, Moon M-W, et al. Buckling delamination in compressed multilayers on curved substrates with accompanying ridge cracks. *J Mech Phys Solids.* 2006;54:1004–1028.
- [53] Hutchinson J, Thouless M, Liniger E. Growth and configurational stability of circular, buckling-driven film delaminations. *Acta Metall Mater.* 1992;40:295–308.
- [54] Choi SR, Hutchinson JW, Evans A. Delamination of multilayer thermal barrier coatings. *Mech Mater.* 1999;31:431–447.
- [55] Chuang T, Nguyen T. 1997 Proceedings of the First International Conference DFI-1, Vienna, Austria, CRC Press.
- [56] Martin J, Embree E, Tsao W. Non-osmotic, defect-controlled cathodic disbondment of a coating from a steel substrate. *J Coat Technol.* 1990;62:25–33.
- [57] Stratmann M, Leng A, Fürbeth W, et al. The scanning Kelvin probe; a new technique for the in situ analysis of the delamination of organic coatings. *Prog Org Coat.* 1996;27:261–267.
- [58] Wan K-t, Liao K. Measuring mechanical properties of thin flexible films by a shaft-loaded blister test. *Thin Solid Films.* 1999;352:167–172.
- [59] Jensen H. Delamination of coatings Handbook of materials behavior models. Lyngby, Denmark: Academic press; 2001. p. 582–586
- [60] Kappes M, Frankel G, Sridhar N. Adhesion and adhesion degradation of a pressure sensitive tape on carbon steel. *Prog Org Coat.* 2010;69:57–62.
- [61] Stratmann M, Feser R, Leng A. Corrosion protection by organic films. *Electrochim. Acta.* 1994;39:1207–1214.
- [62] Allahar KN, Orazem ME, Ogle K. Mathematical model for cathodic delamination using a porosity–pH relationship. *Corros Sci.* 2007;49:3638–3658.
- [63] Hutchinson JW, Suo Z. Mixed mode cracking in layered materials. *Adv Appl Mech.* 1991;29:63–191.

Appendix

The relations for bending stiffness (B) and stretching stiffness (s) are given in Equations (A1) and (A2), when

$x = t_p$ is at neutral point of axis where coating is attached to substrate, ν represents Poisson ratio of coating materials, t_i is the thickness of i th coating layer.

$$B = \frac{1}{3} \sum_{i=1}^n \frac{E_i}{(1 - \nu_i^2)} [(x_{i+1} - t_p)^3 - (x_i - t_p)^3] \quad (A1)$$

$$S = \sum_{i=1}^n \frac{E_i}{(1 - \nu_i^2)} t_i \quad (A2)$$

$$F_{\max} = 100 \frac{(f^{t+1} - f^t)}{f^t} \quad (A3)$$

Appendix B: Paper II

Z. A. Khan, et al., *Int. J. Comp. Meth. and Exp. Meas.*, Vol. 6, No. 3 (2018) 487–498

PREDICTIVE AND PROGNOSTIC MODELLING AND SIMULATION OF COATINGS SUBJECT TO CORROSION AND MECHANICAL FAILURES

ZULFIQAR AHMAD KHAN¹, JAWWAD LATIF¹, HAMMAD NAZIR¹, ADIL SAEED² & KEITH STOKES³

¹NanoCorr, Energy & Modelling (NCEM), Department of Design and Engineering, Faculty of Science & Technology, Bournemouth University, United Kingdom.

²Global College of Engineering and Technology, Muscat Sultanate Oman.

³University of Southampton, National Centre for Advanced Tribology at Southampton (nCATS)
Faculty of Engineering and the Environment, Southampton.

ABSTRACT

This research presents analytical and mathematical modelling of coating failures within industrial components, structures, mobile assets and systems due to corrosive degradation and mechanical fracture. These failures lead to several surface problems; therefore, contact mechanics and electrochemistry approaches incorporating induced residual stresses have been adopted to develop a comprehensive solution for the prediction and prognostic of such failures. Experimental study of film cracking and its propagation into substrates, interfacial transient behaviours and film-substrate system has been conducted. A parallel study of corrosive degradation to include cathodic delamination, cathodic blistering and tribo-corrosion of films has been conducted. Experimental and analytical studies of induced residual stresses within the coating and their effects on failure mechanisms and propagation have been completed. A detailed investigation of elastic mismatch at the interfacial contact and interfacial crack tip field has been performed and a complex stress intensity factor is presented. Mathematical derivation of oscillatory singularity, mode mix and interfacial fracture criterion to include adhesion are presented. This paper presents novel mathematical modelling incorporating interfacial crack propagating, diffusion of corrosive species and cathodic blistering for prediction and prognoses of coating failures.

Keywords: coating failure, compressive residual stress, diffusion induced stress.

1 INTRODUCTION

Protective coatings on industrial components and structures act as a barrier to preserve them from chemical and physical attack. Various environmental and mechanical factors are involved in the breakdown of coating on metallic surfaces. Defects in coating and substrate are formed during the fabrication process and during the application of system. The difference in coefficient of thermal expansion between coating and the substrate is the major cause of producing micro-cracks in coating. Cracks can also occur due to abrasion, physical or mechanical contact. The presence of residual stresses in coating and substrate system causes compressive and tensile stress. In corrosive environment, tensile residual stress results in crack opening, which leads to stress corrosion cracking. Micro-cracks provide passageway to corrosive species to diffuse into substrate and cause electrochemical reactions which results in coating delamination [1]. However, compressive residual stress closes the micro-cracks, but it causes the blister delamination when these stresses are sufficiently high [2]. Compressive residual stress and diffusion induced stress play a major role in adhesion loss of coating from the substrate. Various mathematical models have been formulated to model these two parameters for reliability assessment. Current work presents predictive modelling for the propagation of coating deformation in the presence of micro-cracks as a function of compressive residual and diffusion induced stresses.

© 2018 WIT Press, www.witpress.com

ISSN: 2046-0546 (paper format), ISSN: 2046-0554 (online), <http://www.witpress.com/journals>

DOI: 10.2495/CMEM-V6-N3-487-498

2 BACKGROUND

A model for de-bonding driving force as a function of stress to predict the duration of useful life of isotropic coatings is presented in [2]. Elastic modulus and residual stress play a major role in the formation and propagation of blisters [3]. Stress-driven viscoplastic deformation conditions were also proposed to explain blistering mechanism [4]. Modified model to explain the deformation induced by residual stress for multilayer structure has been proposed in [5]. Later on, closed form solutions have been proposed in [6–8] by incorporating residual stress parameter. Diffusion induced stress factor is also a major cause for coating delamination, which cannot be neglected and has drawn considerable interest of researchers in the past decade. Various mathematical models have been proposed to model the concentration and diffusion of corrosive species inducing stress in the system. The effects of diffusion stress has been investigated in [9]. A theory has been presented in [10] that describes the delamination initiation when ions migrate through conductive passages which are usually formed in the presence of water molecules in hydrophilic and low molecular weight regions. Prognostic model designed in [10] was a function of blister size, ion diffusivity, potential gradient and distance between defect and blister. Diffusion induced stress is also a major problem in lithium ion batteries. The surface energy has been modelled by merging diffusion induced stress problem [11]. Considering diffusion induced stress and residual stress as important delamination parameters, it is very important to investigate and model the coupling behaviour of both factors.

Nanocorr, Energy and Modelling (NCEM) research group has been investigating corrosion and coating failure problems in isotropic organic coatings. Various parameters have been investigated and modelled to explain the behaviour of corrosion and coating failures [12–25]. Recently, the coupling effects of compressive residual stress and diffusion induced stress have been investigated through experimental analysis to model the formation and propagation of circular blisters in the presence of micro-cracks over coated surface. In this research, the de-bonding driving forces for straight-sided blister are modelled to explain blister formation and propagation mechanism in the presence of micro-crack.

3 EXPERIMENTAL ANALYSIS

In order to analyse the effect of compressive residual stress and diffusion induced stress, corrosion test was applied on coated samples having micro-crack over coating [16]. Seven samples were used to obtain cross-sectional measurements. AISI-1020 carbon steel samples 0.18%–0.23% C, 0.3%–0.6% Mn with balanced Fe were used for experimental analysis as substrates. The thicknesses of samples were 0.01 cm with elastic modulus of 200 GPa and coefficient of thermal expansion as $11.7 \times 10^{-6} \text{ K}^{-1}$ [26]. Sample were polished with emery paper of grit size 200 then conditioned with distilled water and dried with cold air.

Spray gun was used to apply red oxide primer coating on samples. The elastic modulus of red-oxide is 6.14 GPa with coefficient of thermal expansion as $21.6 \times 10^{-6} \text{ K}^{-1}$. Coating thickness was 20 μm . Micro-cracks were induced over the coating surface with initial aperture size of 2.1 μm . Residual stresses were measured through charge coupled device (CCD) detector and laser optics, which measures stress by monitoring substrate curvature. When samples were exposed to corrosive environment and monitored through the microscope, it was observed that several blisters and micro-cracks started to appear over the surface of coated samples. All the micro-cracks have shown almost similar behaviour but single micro-crack from each sample is considered for cross-sectional observation and analysis which is a destructive method.

The purpose of experimental work was to analyse the effects of residual induced stress in presence of diffusion induced stress. Samples were kept at fabrication temperature of 318K then transported to corrosive atmospheric chamber for accelerated testing. The fog, 5 parts of NaCl in 95 parts of distilled water, was simulated. The samples were placed at 60°C to avoid any direct pathways of crystallisation into the coating. The corrosive atmosphere was accelerated by gradually increasing the temperature. The temperature was raised 1K for every one hour. Cross-sectional images of each sample were taken during the temperature values i.e. 319K, 321K, 328K, 333K, 353K. During microscopic analysis, temperature is maintained similar to that in the corrosion simulation chamber for precision. Diffusion induced stress was induced by the presence of corrosive species in the environmental chamber and residual stress was induced by the change in temperature due to elastic mismatch. Micro-cracks provide channels for the species to diffuse into the system. Tensile and compressive behaviour of residual stress controls the opening and closing of pre-existing micro-cracks in the coating. The experimental compressive residual stress and diffusion induced stress with respect to change in temperature are shown in Fig. 2. The investigation of micro-crack propagation is divided into three regions and the resultant stress for controlling blister propagation was derived.

Region 1:

The experiment was initiated from fabrication temperature (318K) of system and increased to 319K. The aperture size of micro-crack was measured to be 2.1 μm , as shown in Fig. 1(a), which provided channel for the corrosive species to diffuse into the system, as a result the

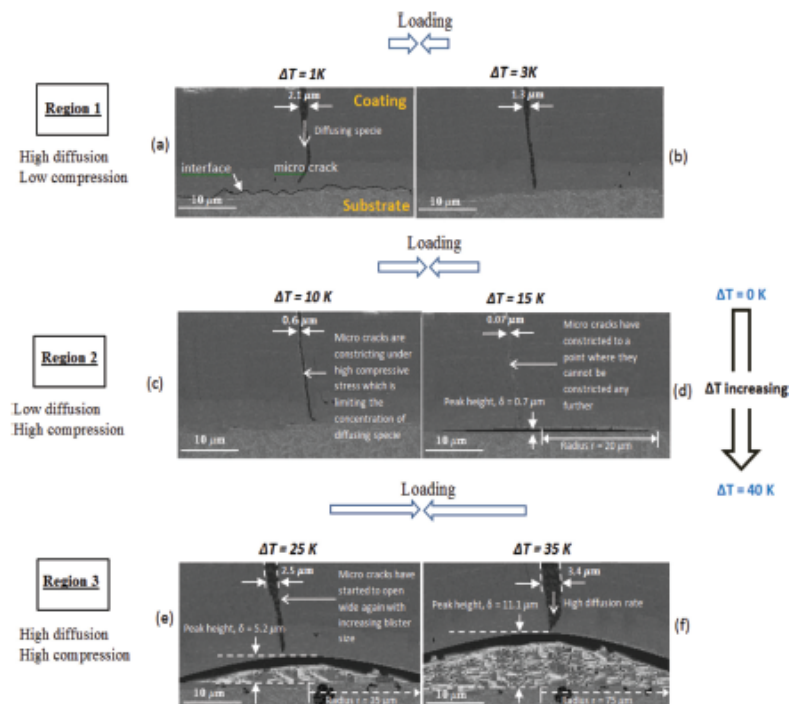


Figure 1: Samples micrographs at various temperature values [16].

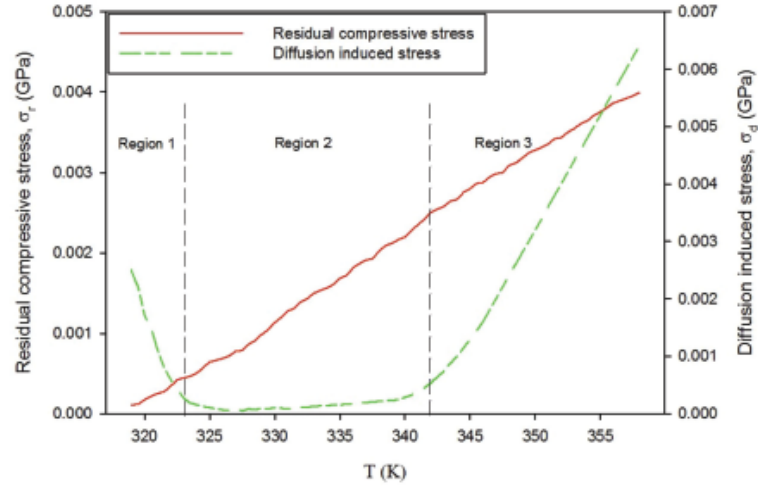


Figure 2: Experimental results of residual compressive stress and diffusion induced stress [16].

diffusion stress was high at the beginning of the experiment, as shown in Fig. 2. When the temperature is further increased to 321K the micro-crack started to shrink due to the rise in compressive residual stress but no major blistering effect was observed. The aperture of micro-crack decreased to $1.3 \mu\text{m}$, as shown in Fig. 1(b). Small decrease in diffusion induced stress was observed due to minor rise in temperature. Diffusion induced stress in this region appears to be a major controlling factor. According to the theory of linear superposition the following relation can be concluded.

$$\sigma = \sigma_r + \sigma_d \cong \sigma_d. \quad (1)$$

Region 2:

When the temperature was raised to 328K, the aperture size of micro-crack decreased to $0.6 \mu\text{m}$. The reason of this decrease in the size is the increase in compressive residual stress that can be seen in the results, which are plotted in Fig. 2. The compressive residual stress continued to increase from 0.004 GPa to 0.0023 GPa in region 2. The decrease in channel size for the corrosive species to diffuse into the system also decreased the diffusion induced stress. Further increase in the temperature to 331K, increased the compressive residual stress which reduced the aperture size to $0.07 \mu\text{m}$. This increase in compressive residual stress initiated the blistering effect, which can be seen in Fig. 1(d). Residual compressive stress can be considered as a significant influential parameter and can be written as:

$$\sigma = \sigma_r + \sigma_d \cong \sigma_r. \quad (2)$$

Region 3:

When the temperature was increased to 341K, compressive residual stress increased significantly which leads to blistering delamination. The size of the blister increased thus making the aperture size of micro-crack to further increase to $2.5 \mu\text{m}$. The widening of micro-crack provided more space for corrosive species to diffuse into the system, hence diffusion induced stress started to rise after 341K. In region 3, the behaviour of increase in compressive residual stress and diffusion induced stress was observed to be identical. The amplitude and radius of

blister as observed was $5.2 \mu m$ and $35 \mu m$, which continually increased and reached up to a radius as $75 \mu m$ and amplitude as $11 \mu m$. After applying the principle of linear superposition on coupling effect of compressive residual stress and diffusion induced stress for blister growth and propagation, the following relation can be derived as:

$$\sigma = \sigma_r - \sigma_d . \quad (3)$$

The relation of compressive residual stress and diffusion induced stress proposed in eqn (3) is considered as a major controlling factor in blistering delamination mechanism. The coupling effect relation for compressive residual and diffusion induced stress has been previously incorporated for de-bonding driving force of circular blister growth and propagation. In current research the de-bonding driving force for straight-sided blister growth and propagation is proposed. Modelling of circular blister and straight-sided blister is derived in the next section.

4 MATHEMATICAL MODEL

The coupling effect of compressive residual stress and diffusion induced stress has been investigated through experimentation and the relation for stress as a function of compressive residual stress and diffusion induced stress has been proposed by using the principle of linear superposition theory. This paper discusses the incorporation of observed stress behaviour in circular blister propagation and based on that theory, relations for de-bonding force of straight-sided blisters are also proposed. Multi-disciplinary modelling approach has been adopted to explain the effect of stresses in coating delamination process. The designed and proposed models are based on the concepts of thermodynamics, mechanics and bi-layer cantilever beam theory. The critical stress level in the system can be calculated by using the following relation [2]:

$$\sigma_{cr} = 1.2235 \frac{E}{(1-\nu^2)} \left(\frac{h}{r} \right)^2 \quad (4)$$

Here, σ_{cr} is the critical stress, which computes critical threshold for the initiation of delamination, h is coating thickness, r is radius of blister, E is elastic modulus and ν poisson's ratio. The coupling effect of compressive residual stress and diffusion induced stress controlling the transport of corrosive species as observed through experimental analysis [16] can be written as follows:

$$\sigma_0 = \frac{\partial \sigma_c}{\partial x} - \frac{\partial \sigma_d}{\partial t} , \quad (5)$$

σ_0 represents total stress according to linear superposition theory, $\frac{\partial \sigma_c}{\partial t}$ is the change in compressive residual stress with respect to location x and $\frac{\partial \sigma_d}{\partial t}$ is the change in diffusion induced stress with respect to time t , change in concentration of corrosive species as a function of environmental parameters and the coupling effects of diffusion induced and compressive stress was derived [16] as:

$$\frac{\partial c_{k_c}}{\partial t} = \left\{ \left(D_{k_c} + \frac{D_{k_c} E_c V_{k_c}^2}{9RT} c_{k_c} \right) \frac{\partial^2 c_{k_c}}{\partial x^2} + \frac{D_{k_c} E_c V_{k_c}^2}{9RT} \left(\frac{\partial c_{k_c}}{\partial t} \right)^2 - \frac{D_{k_c} E_c V_{k_c}^2}{9RT} \frac{\partial c_{k_c}}{\partial t} \left(\frac{\partial \sigma_c}{\partial x} - \frac{\partial \sigma_d}{\partial t} \right) \right\} \quad (6)$$

$\frac{\partial c_{k_c}}{\partial t}$ represents a change in the concentration of corrosive species on coating and substrate system through micro-cracks, D_{k_c} diffusion coefficient of coating, T is temperature, R is molar gas constant and V_{k_c} is partial molar volume of coating material. Coupling effect of stress using eqn (2) can be written as:

$$\sigma_0 = \frac{\partial \sigma_{\epsilon}}{\partial x} - \frac{\partial \sigma_{d_c}}{\partial t} = \left(D_{k_c} + \frac{D_{k_c} E_c V_{p k_c}^2}{9RT} \right) \frac{\partial^2 c_{k_c}}{\partial x^2} + \frac{D_{k_c} E_c V_{p k_c}^2}{9RT} \left(\frac{\partial c_{k_c}}{\partial t} \right)^2 \left(\frac{D_{k_c} V_{p k_c}^2}{9RT} \frac{\partial c_{k_c}}{\partial t} \right)^{-1} \quad (7)$$

4.1 De-bonding driving force for circular blister

When coating remains intact with the substrate, there is no de-bonding driving force. The blistering effect appears when de-bonding driving force exceeds critical threshold value. The blisters shapes can be circular which end up in telephonic cord like shape and blister can also lead to straight-sided shape which ends up as snakes back forth shape [27]. In this research paper the coupling effect of compressive residual stress and diffusion induced stress, which was investigated for circular blister through experimental results, is incorporated for straight-sided blister to model de-bonding driving force [16]. First, the derivation of de-bonding driving force for circular blister is discussed and then, relations for straight-sided blisters are proposed. The model for circular blister is already analysed and validated through experiments while strain energy release rate for straight-sided blister has already been discussed and validated [16, 27]. So, new relations for straight side blister are based on two verified and validated theories. Strain energy release rate stored for circular blister can be written as:

$$G_0 = \frac{(1-\nu)h\sigma^2}{E} \quad (8)$$

Strain energy release rate for crack propagation derived in Ref. [2] is given as:

$$G = 6 \frac{(1-\nu^2)}{E h^3} \left(M^2 + \frac{1}{12} h^2 \Delta N^2 \right) \quad (9)$$

G represents strain energy release rate for circular blister propagation, M is bending moment and N is resultant stress force ($\sigma = \sigma_r - \sigma_d$) acting on coating. By incorporating the coupling effect of compressive residual stress and diffusion induced stress in crack propagation can be derived as:

$$G' = 6 \frac{(1-\nu^2)}{E h^3} M^2 \left(1 + \frac{1}{4} \left(\sqrt{\left(\frac{\partial \sigma_{\epsilon}}{\partial x} - \frac{\partial \sigma_{d_c}}{\partial t} \right) \sigma_{cr}^{-1} - 1} \right)^2 \right) \quad (10)$$

The term $\bigcirc = \left(\frac{\partial \sigma_{\epsilon}}{\partial x} - \frac{\partial \sigma_{d_c}}{\partial t} \right) \sigma_{cr}^{-1}$ is de-bonding index which controls blister formation and propagation. By using relation of mode dependent strain energy release rate the following model can be formulated for de-bonding driving force.

$$F = 6 \frac{(1-\nu^2)}{Eh^3} M^2 \left(1 + \frac{1}{4} (\sqrt{\Gamma-1})^2 \right) \left(\sec^2 \left[\left(1 - \frac{\Gamma_{IC}}{E_c \lambda} \right) \psi \right] \right)^{-1}. \quad (11)$$

F represents de-bonding driving force, Γ_{IC} is coating toughness, λ is roughness of substrate interface and ψ is the ratio of coating crack edge from mode II to mode I.

4.2 De-bonding driving force for straight-sided blister

The derivation of de-bonding driving force for straight-sided blister propagation is proposed and derived in this section. The straight-sided blister proliferates after the complete formation of curved ‘front’ of blister. The straight-sided blister is thought to provide accurate measure of primary area of de-bonded interface needed to initiate buckle delamination along with energy release rate [27]. The strain energy release rate [27] in direction parallel to crack front can be written as:

$$G_0 = \frac{(1-\nu^2)}{2E} \sigma_0^2 h. \quad (12)$$

By incorporating the $\sigma_0 = \frac{\partial \sigma_{\epsilon}}{\partial t} - \frac{\partial \sigma_{d_c}}{\partial t}$ stress, which has been concluded in previous section in the above equation, the strain energy release rate for straight-sided blister due to coupling effect of compressive residual stress and diffusion induced stress can derived as:

$$G'_0 = \frac{(1-\nu^2)h}{2E} \left(\frac{\partial \sigma_{\epsilon}}{\partial t} - \frac{\partial \sigma_{d_c}}{\partial t} \right)^2. \quad (13)$$

In straight-sided blister, the energy release rate relation for crack propagation at ‘side’ and ‘front’ has separate relations [27]. The ‘side’ and ‘front’ sides of straight-sided blister is labelled in Fig. 3. For blister side strain energy as a function of stresses can be written as:

$$G_{side} = G_0 \left(1 - \frac{\sigma_c}{\sigma_0} \right) \left(1 + 3 \frac{\sigma_c}{\sigma_0} \right). \quad (14)$$

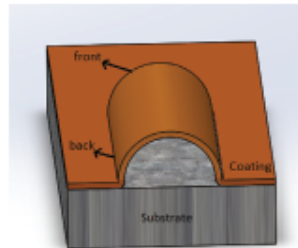


Figure 3: Schematic of straight-sided blister.

By incorporating the $\sigma_0 = \frac{\partial \sigma_c}{\partial t} - \frac{\partial \sigma_d}{\partial t}$ in the above relation the strain energy for 'side' of blister as a function of coupling effect of compressive residual stress and diffusion induced stress can be written as:

$$G'_{side} = \frac{(1-\nu^2)h}{2E} \left(\frac{\partial \sigma_c}{\partial t} - \frac{\partial \sigma_d}{\partial t} \right)^2 \left(1 - \sigma_c \left(\frac{\partial \sigma_c}{\partial t} - \frac{\partial \sigma_d}{\partial t} \right)^{-1} \right) \left(1 + 3\sigma_c \left(\frac{\partial \sigma_c}{\partial t} - \frac{\partial \sigma_d}{\partial t} \right)^{-1} \right). \quad (15)$$

De-bonding driving force for the 'side' of blister as a function of mode mix can be derived as:

$$F_{side} = \frac{(1-\nu^2)h}{2E} \sigma_0^2 (1 - \Gamma^{-1}) (1 + 3\Gamma^{-1}) \left(\sec^2 \left[\left(1 - \frac{\Gamma_{IC}}{E_c \lambda} \right) \Psi \right] \right)^{-1}. \quad (16)$$

F_{side} is the de-bonding driving force for 'side' of straight-sided blister, which is a function of mod mix and de-bonding index. Similarly, the de-bonding driving force for 'front' of blister can be derived as follows:

$$G'_{front} = G_0 \left(1 - \frac{\sigma_c}{\sigma_0} \right). \quad (17)$$

By including de-bonding index in eqn (13), it can be modified as:

$$G'_{front} = \frac{(1-\nu^2)h}{2E} \left(\frac{\partial \sigma_c}{\partial t} - \frac{\partial \sigma_d}{\partial t} \right)^2 \left(1 - \sigma_c \left(\frac{\partial \sigma_c}{\partial t} - \frac{\partial \sigma_d}{\partial t} \right)^{-1} \right). \quad (18)$$

De-bonding driving force for the 'front' of blister as a function of mode mix can be derived as:

$$F_{front} = \frac{(1-\nu^2)h}{2E} \sigma_0^2 (1 - \Gamma^{-1}) \left(\sec^2 \left[\left(1 - \frac{\Gamma_{IC}}{E_c \lambda} \right) \Psi \right] \right)^{-1}. \quad (19)$$

The 'front' and 'side' de-bonding driving forces for straight-sided blister are proposed by incorporating the coupling effect of compressive residual stress and diffusion induced stress.

5 SIMULATION RESULTS

5.1 Simulation results for circular blister

The resultant stress force due to coupling effect of compressive residual stress and diffusion induced stress proposed for circular blister formation and propagation has been validated which shows strong agreement between experimental observation and mathematical modelling [16]. Experimental and simulation results for normalised de-bonding driving force as a function of change in temperature are shown in Fig. 4. All parameters are converted into dimensionless form for simulation of normalised de-bonding driving force. In region 1, the coating and substrate system was in safe condition and there was no change in pre-existing micro-crack and de-bonding driving force was also zero. In region 2, micro-crack

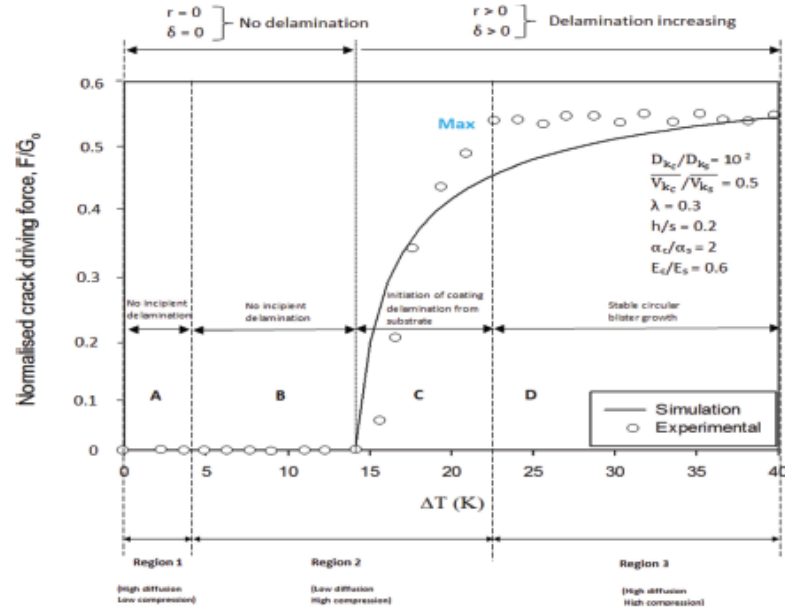


Figure 4: Simulation and experimental results of de-bonding driving force for circular blister [16].

aperture size started to reduce due to high compression rate. Diffusion rate decreased due to the reduction in aperture size of micro-crack. Normalised de-bonding driving force was zero till $\Delta T = 14\text{K}$; hence, coating can be considered in safe condition. Further increase in temperature resulted in adhesion loss in the form of blistering and de-bonding driving force continued to increase and reach at maximum level. In region 3, compressive residual stress continues to increase and the behaviour of diffusion rate seems similar to compressive residual stress. In this region the size of blister increased significantly and micro-crack also expanded.

5.2 Simulation results for straight-sided blister

The proposed mathematical models for straight-sided blister is based on validated theory as explained in previous sections [16, 27]. The simulation result of straight-sided blister is shown in Fig. 5. The mathematical equations for simulating de-bonding driving forces for 'side' and 'front' were converted into normalised form. It is worth noting that the de-bonding driving force for the 'side' of straight-sided blister is always greater as compared to the de-bonding driving force for the 'front' but crack propagates at the 'front'. The reason is that the 'front' experiences lower effective interface toughness [27]. For sufficiently wide straight-sided blister, the energy release rate along curved front exceeds than that of 'side' for large (by a factor of ten or more) coating modulus than substrate which would allow propagation of straight-sided blisters despite of interface toughness is mode independent [28].

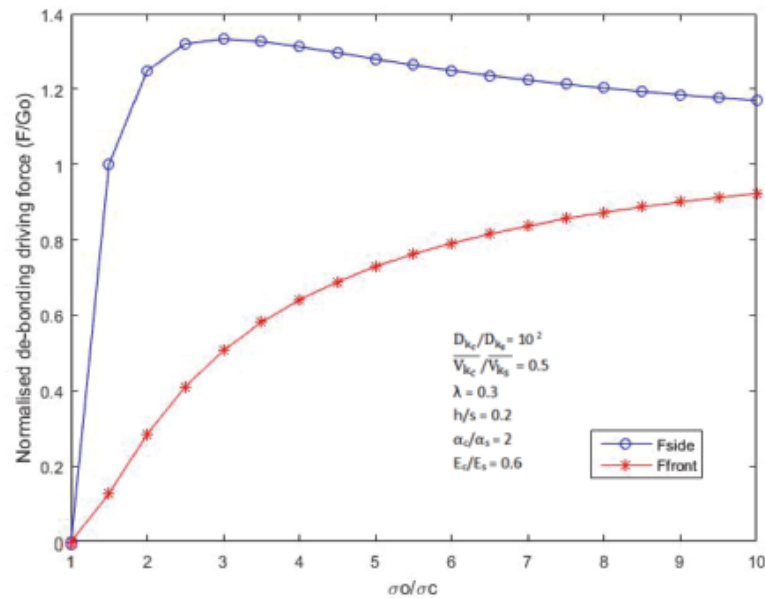


Figure 5: Simulation results of de-bonding driving forces for straight-sided blister.

6 CONCLUSIONS

This paper presents the mathematical modelling for circular and straight-sided blister growth and propagation by incorporating coupling effect of compressive residual stress and diffusion induced stress. The effects of stresses are investigated in the presence of micro-cracks. The difference in coefficient of thermal expansion between coating and substrate system induced compressive residual stress which continued to increase due to an increase in temperature while the corrosive species produced diffusion induced stress. Initially, increase in temperature caused pre-existing micro-crack to shrink and reduce diffusion induced stress while further increase in temperature caused de-bonding driving force to exceed its critical level which resulted in blister formation and it started propagating in circular shape. The rising trend of diffusion induced stress appears to be similar as compressive residual stress at high temperature. Based on experimental observations, resultant stress for blister formation and growth is proposed and incorporated in circular and straight-sided blisters formation and propagation to propose the de-bonding driving forces. De-bonding driving forces are proposed for blisters growth and propagation which can be used for coating life assessment. Proposed mathematical models can be further extended for 'telephonic cord' which appears after the propagation of circular blister and for 'back and forth' shape which appears after the propagation of straight-sided blister. Comprehensive analyses of circular blister formation and propagation has been conducted through experimentation and by simulating the effects of various parameters (modulus of elasticity, coefficient of thermal expansion, coating thickness and poisson's ration) in previous NCEM papers. In future, further analysis of proposed de-bonding driving forces of straight-sided blisters will be presented.

ACKNOWLEDGEMENT

This research is joint funded by the Defence Science and Technology Laboratory (DSTL), Ministry of Defence (MoD) and Bournemouth University UK. The authors acknowledge their financial support and in kind contributions.

REFERENCES

- [1] Parkins, R., *Stress Corrosion Cracking*, Uhlig's Corrosion Handbook, p. 191, 2011.
<https://doi.org/10.1002/9780470872864.ch14>
- [2] Hutchinson, J., Thouless, M. & Liniger, E., Growth and configurational stability of circular, buckling-driven film delaminations. *Acta metallurgica et materialia*, **40**(2), pp. 295–308, 1992.
[https://doi.org/10.1016/0956-7151\(92\)90304-W](https://doi.org/10.1016/0956-7151(92)90304-W)
- [3] Chuang, T. & Nguyen, T., A non-osmotic blister growth model in coating systems. in damage and failure of interfaces. *1st International Conference. Proceedings*, 1997.
- [4] Malerba, C., Valentini, M., Ricardo, C.A., Rinaldi, A., Cappelletto, E., Scardi, P. & Mittiga, A., Blistering in Cu 2 ZnSnS 4 thin films: correlation with residual stresses. *Materials & Design*, **108**, pp. 725–735, 2016.
<https://doi.org/10.1016/j.matdes.2016.07.019>
- [5] Huang, S. & Zhang, X., Gradient residual stress induced elastic deformation of multilayer MEMS structures. *Sensors and Actuators A: Physical*, 2007, **134**(1), pp. 177–185.
<https://doi.org/10.1016/j.sna.2006.05.026>
- [6] Zhang, X., Xu, B.S., Wang, H.D. & Wu, Y.X., An analytical model for predicting thermal residual stresses in multilayer coating systems. *Thin Solid Films*, **488**(1), pp. 274–282, 2005.
<https://doi.org/10.1016/j.tsf.2005.04.027>
- [7] Widjaja, S., Limarga, A.M. & Yip, T.H., Modeling of residual stresses in a plasma-sprayed zirconia/alumina functionally graded-thermal barrier coating. *Thin Solid Films*, **434**(1), pp. 216–227, 2003.
[https://doi.org/10.1016/S0040-6090\(03\)00427-9](https://doi.org/10.1016/S0040-6090(03)00427-9)
- [8] Soliman, H. & Waheed, A., Effect on differential thermal expansion coefficient on stresses generated in coating. *Journal of Materials Science & Technology (China) (USA)*, **15**(5), pp. 457–462, 1999.
- [9] Podstrigach, Y.S. & Shevchuk, P., Effect of surface layers on diffusion processes and the resulting stress state in solids. *Materials Science*, **3**(5), pp. 420–426, 1968.
<https://doi.org/10.1007/BF00716058>
- [10] Nguyen, T., Hubbard, J. & Pommersheim, J., Unified model for the degradation of organic coatings on steel in a neutral electrolyte. *JCT, Journal of Coatings Technology*, **68**(855), pp. 45–56, 1996.
- [11] Deshpande, R., Cheng, Y.T. & Verbrugge, M.W., Modeling diffusion-induced stress in nanowire electrode structures. *Journal of Power Sources*, **195**(15), pp. 5081–5088.
<https://doi.org/10.1016/j.jpowsour.2010.02.021>
- [12] Nazir, M., Khan, Z.A., Saeed, A. & Stokes, K., A model for cathodic blister growth in coating degradation using mesomechanics approach. *Materials and Corrosion*, 2015.
<https://doi.org/10.1016/j.engfailanal.2016.02.014>
- [13] Nazir, M., Khan, Z.A., Saeed, A. & Stokes, K., A predictive model for life assessment of automotive exhaust mufflers subject to internal corrosion failure due to exhaust gas condensation. *Engineering Failure Analysis*, **63**, pp. 43–60, 2016.
<https://doi.org/10.1016/j.engfailanal.2016.02.014>
- [14] Nazir, M., Khan, Z.A., Saeed, A. & Stokes, K., Modeling the effect of residual and diffusion-induced stresses on corrosion at the interface of coating and substrate. *Corrosion*, **72**(4), pp. 500–517, 2015.
<https://doi.org/10.1080/01694243.2015.1071023>

- [15] Nazir, M., Khan, Z.A. & Stokes, K., A holistic mathematical modelling and simulation for cathodic delamination mechanism—a novel and an efficient approach. *Journal of Adhesion Science and Technology*, **29**(22), pp. 2475–2513, 2015.
<https://doi.org/10.1016/j.engfailanal.2016.07.003>
- [16] Nazir, M., Khan, Z.A. & Stokes, K., Analysing the coupled effects of compressive and diffusion induced stresses on the nucleation and propagation of circular coating blisters in the presence of micro-cracks. *Engineering Failure Analysis*, **70**, pp. 1–15, 2016.
<https://doi.org/10.1080/01694243.2015.1026870>
- [17] Nazir, M., Khan, Z.A. & Stokes, K., Optimisation of interface roughness and coating thickness to maximise coating–substrate adhesion—a failure prediction and reliability assessment modelling. *Journal of Adhesion Science and Technology*, **29**(14), pp. 1415–1445, 2015.
<https://doi.org/10.1080/01694243.2015.1026870>
- [18] Khan, Z.A., Chacko, V. & Nazir, H., A review of friction models in interacting joints for durability design. *Friction*, 2017.
- [19] Khan, Z.A., Pashaei, P., Bajwa, R., Nazir, H. & Cakmak, M., Fabrication and characterisation of electrodeposited and magnetron-sputtered thin films. *International Journal of Computational Methods & Experimental Measurements*, **3**(2), pp. 165–174, 2015.
<https://doi.org/10.2495/CMEM-V3-N2-165-174>
- [20] Nazir, M. and Khan, Z., A review of theoretical analysis techniques for cracking and corrosive degradation of film-substrate systems. *Engineering Failure Analysis*, 2016.
- [21] Nazir, M., Khan, Z.A. & Stokes, K., A unified mathematical modelling and simulation for cathodic blistering mechanism incorporating diffusion and fracture mechanics concepts. *Journal of Adhesion Science and Technology*, **29**(12), pp. 1200–1228, 2015.
<https://doi.org/10.1080/01694243.2015.1022496>
- [22] Nazir, M.H. & Khan, Z., Maximising the interfacial toughness of thin coatings and substrate through optimisation of defined parameters. *International Journal of Computational Methods and Experimental Measurements*, **3**(4), pp. 316–328, 2015.
<https://doi.org/10.2495/cmeme-v3-n4-316-328>
- [23] Saeed, A., Khan, Z.A., Nazir, H., Hadfield, M. & Smith, R., Research impact of conserving large military vehicles through a sustainable methodology. *International Journal of Heritage Architecture*, **1**(2), pp. 267–274, 2017.
<https://doi.org/10.1016/j.matchemphys.2016.04.068>
- [24] Saeed, A., Khan, Z.A. & Nazir, M.H., Time dependent surface corrosion analysis and modelling of automotive steel under a simplistic model of variations in environmental parameters. *Materials Chemistry and Physics*, **178**, pp. 65–73, 2016.
<https://doi.org/10.3390/su71215825>
- [25] Saeed, A., Khan, Z.A. & Nazir, M.H., An optimised approach of protecting and sustaining large vehicle system. *Sustainability*, **7**(12), pp. 16451–16464, 2015.
<https://doi.org/10.3390/su71215825>
- [26] Lide, D.R., *CRC Handbook of Chemistry and Physics*, CRC Press, 85, 2004.
- [27] Choi, S.R., Hutchinson, J.W. & Evans, A., Delamination of multilayer thermal barrier coatings. *Mechanics of Materials*, **31**(7), pp. 431–447, 1999.
[https://doi.org/10.1016/S0167-6636\(99\)00016-2](https://doi.org/10.1016/S0167-6636(99)00016-2)
- [28] Yu, H.-H. & Hutchinson, J.W., Influence of substrate compliance on buckling delamination of thin films. *International Journal of Fracture*, **113**(1), pp. 39–55, 2002.
<https://doi.org/10.1023/A:1013790232359>

Appendix C: Paper: III



Original Article

Condition monitoring and predictive modelling of coating delamination applied to remote stationary and mobile assets

Jawwad Latif¹, Zulfiqar Ahmad Khan¹ , Mian H Nazir¹ , Keith Stokes² and Joseph Plummer³

Abstract

The ambiguous nature of meteorological parameters in uncontrolled environmental conditions makes it difficult to determine the structural integrity of stationary and mobile assets. The weather conditions for large vehicles, at The Tank Museum at Bovington, UK, which are operating in controlled and uncontrolled environmental conditions are investigated through weather history and corrosion monitoring techniques applied to large military vehicles by using linear polarisation resistance method. Corrosion initiation and propagation was found on several occasions during the operation of large vehicles within uncontrolled environment due to critical level of metrological parameters including salinity, relative humidity and rainfall. Comprehensive solutions have been proposed to detect damage initiation at the earliest possible stage to prompt maintenance professionals to take necessary actions to avoid damage. Early detection techniques will help to prolong the service life of large vehicles or metal structures which are operating or installed remotely. The analysis of diffusion of salt particles into coating during summer and winter season is also presented by estimating the salt concentration by taking linear relationship between wind speed and salt deposition rate based on ISO classification of airborne salinity. The proposed solutions can be applied to valuable assets operating in coastal, non-coastal and near the sea regions to predict and estimate the damage. The research will directly impact the maintenance and reliability of the automotive, oil and gas pipelines, aerospace and defence applications through remote condition monitoring technique.

Keywords

Corrosion, coating delamination, condition monitoring, diffusion, predictive modelling

Background

According to NACE International report, the global cost of corrosion is 3.4% of the global gross domestic product (GDP) which is equal to the US\$2.5 trillion.¹ Corrosion-related repairs and maintenance costs are around 23% of the budget within the military applications in the United States. It will lead to significant cost savings in the range of 15%–35% by preventive measures, avoiding malfunctions and downtime and enhancing reliability.² Several methods and techniques have been adopted for predicting corrosion damage by using the neural network, mathematical models and probabilistic approaches. Literature provides extensive experimental observations regarding the influence of meteorological factors on materials' corrosion behaviour subject to various geographical locations and operating conditions. The attempt has been made to propose universal equations by finding the correlation

between exponent of power-law and meteorological parameters to predict corrosion damage in Feliu and Morcillo.^{3,4} The information about annual corrosion data of rural and urban atmospheric quality from almost 28 countries was compiled to develop a mathematical equation for estimation of corrosion damage of

¹Department of Design & Engineering, NanoCorr, Energy & Modelling (NCEM) Research Group, Bournemouth University, Poole, UK

²National Centre for Advanced Tribology at Southampton (nCATS), Faculty of Engineering and the Environment, University of Southampton, Southampton, UK

³Physical Sciences Division, Defence Science and Technology Laboratory (DSTL), Ministry of Defence, Porton Down, Salisbury, UK

Corresponding author:

Zulfiqar Ahmad Khan, Department of Design & Engineering, NanoCorr, Energy & Modelling (NCEM) Research Group, Bournemouth University, Fern Barrow, Poole BH12 5BB, Bournemouth, UK.
Email: zkhan@bournemouth.ac.uk



Structural Health Monitoring
1–18
© The Author(s) 2018
Reprints and permissions:
sagepub.co.uk/journalsPermissions.nav
DOI: 10.1177/1475921718773524
journals.sagepub.com/home/shm

several materials including mild steel, aluminium, copper and zinc. The mathematical relations derived from the data recorded were not promising to estimate the corrosion damage. The complexity and uncertainty in corrosion phenomena have encouraged researchers to include the effect of other potential meteorological factors which are responsible for corrosion damage into the mathematical models to derive generalised equations which could be suitable for any location. The annual corrosion rate of carbon steel was observed in 43 different sites and regression equations were proposed to estimate corrosion rate.⁵ The corrosion study of carbon steel under indoor and outdoor Cuban atmospheres was conducted to propose corrosion model.⁶ The results from experimental data have shown significant variations in corrosion under various atmospheric conditions and exposure time.

In previous mathematical models, the corrosion loss is not zero even in the absence of water. The model was proposed,⁷ which incorporates time-of-wetness, salinity, sulphur dioxide and temperature to predict corrosion loss, and the appropriate form of time-of-wetness is added to show zero corrosion in the absence of water. The field exposure tests were conducted in an urban, rural-wet, rural-dry and marine environment of Sri Lanka for the development of corrosion model.⁸ The results concluded that the prediction of corrosion loss from models show good performance when they are calibrated according to their location. After applying power law function on field exposure corrosion data, the concave functionality of power law function does not sound to be an appropriate solution for real-time corrosion prediction assessment as the environmental factors vary significantly over the location and from location to location.⁹ The probabilistic techniques had also been applied to model the corrosion growth phenomena. In Altynova et al.,¹⁰ the prediction of corrosion damage has been developed by using the current corrosion condition of material and growth of corrosion rate as input parameters for the probabilistic model.

Various types of metal coatings including thermal spray coating, organic coating, corrosion-resistant coating and chemically resistant coating are applied to civil, automotive and engineering infrastructures to make a physical barrier between metal structures and atmosphere to provide protection from meteorological factors such as moisture, corrosive ions and oxygen.¹¹ The coating barrier also leads to failure in the form of porous medium, cracks and blisters. The corrosive ions can diffuse into the coating-substrate system through defected coating or porous medium and activates electrochemical reaction which results in the degradation of the metal structure and coating-substrate bond weakening.¹² Various techniques have been adopted to

investigate the role of corrosive ions diffusing into the coating-substrate system in the past. Special electrochemical cell was developed to investigate the relation between cathodic or anodic current and coating delamination under the coating for zinc polymer system.¹³ The diffusion of water and oxygen into the coating-substrate system was investigated in the presence electrochemically active sites.^{14,18} It was found that the organic coating does not provide sufficient protection against dissolution of water and oxygen which decreases the adhesion between coating and substrate. According to the conclusion derived from research findings in Stratmann and colleagues,^{15,17} the delamination of coating in the defected area is driven by the strength and diffusion of corrosive ions as the coating starts behaving like a jelly medium where electrochemical cells are active. The mathematical model¹⁹ was developed to describe the delamination behaviour of coating by using the relation between porosity and pH which was an adequate approach to couple the experimental findings in the past¹⁷ and analytical modelling. The concept proposed in Allahar et al.¹⁹ was adopted to further develop a mathematical model for coating delamination in the presence of homogeneous reactions, electrochemical reactions and precipitation of corrosive ions in Huang et al.¹² Currently, researchers have been using multi-disciplinary approaches to model the coating delamination process by using solid mechanics, material science and fracture mechanics concepts. Coating life assessment models were developed by using weight functions, diffusion concepts and stress intensity factors based on the principles of mesomechanics and approach.^{20,21}

NanoCorr, Energy & Modelling (NCEM) research group have been working to provide solutions to detect and mitigate the potential threats posed to large vehicles stationed at The Tank Museum, Bovington, UK²²⁻⁴⁹ by electrochemical degradation combined with mechanical failures. Current research provides contribution towards detection, prevention and the assessment of material and coating degradation of high-value assets in operation or stationed indefinitely and could be at remote locations both under controlled and uncontrolled environmental conditions.

The past weather history at The Tank Museum, Bovington, UK is reported in this work where linear polarisation technique was applied to measure the environmental impact on large vehicle operating under both controlled and uncontrolled environmental conditions. The solution is also proposed for large vehicles operating at remote locations to detect the critical environmental conditions at the earliest stage. The analysis of the diffusion of corrosive ions into the coating-substrate system is also presented by estimating salt concentration. According to literature, the deposition

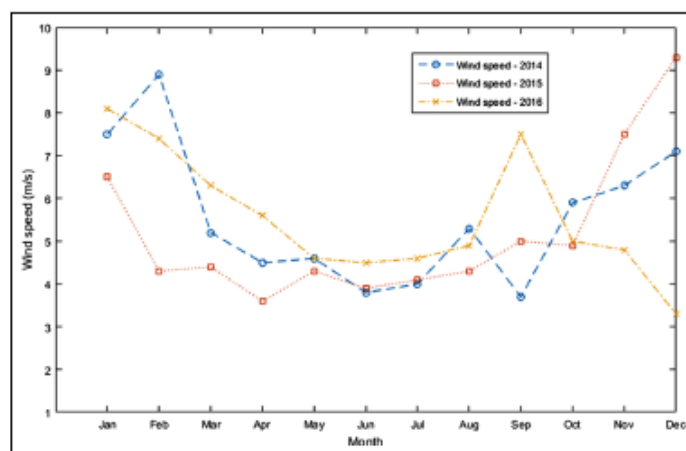


Figure 1. Wind speed in Dorset, UK during last 3 years.⁵⁶

rate of salt depends on wind speed.^{50–53} The classification of airborne salinity which defines salt deposition rate based on location is utilised to estimate the concentration of salt by assuming linear relationship between wind speed and deposition rate based on experimental observations performed in the past.^{50,54,55} The analysis is conducted for summer and winter seasons. Furthermore, the mathematical relation is also presented for the diffusion of salt particles for assets near the sea.

Weather conditions

The weather conditions of last few years at The Tank Museum are analysed by using data taken from world weather online.⁵⁶ The minimum wind speed for entrainment of salt particles is 3 m/s. The wind speed during last year at Dorset, The South West Coast of England, UK is provided in Figure 1. It can be seen that the average wind speed remains greater than the threshold level for aerosol entrainment of salt particles. The presence and deposition of salt particles over large vehicles can be expected throughout the year in an uncontrolled environment. The relative humidity at Dorset for the last 3 years is shown in Figure 2. According to the literature, the critical humidity level above which corrosion process is more likely to take place is around 80%. The history of relative humidity shows that most of the time during a calendar year, the relative humidity level remains greater than the critical level. One of the most important factors which are responsible for corrosion reaction is the rain. The data of number of rainy days during the last three years is presented in Figure 3. The

water and salt are the main ingredients for corrosion reaction. The speed of wind greater than the threshold level for entrainment and large number of rainy days throughout the calendar year makes large vehicles more vulnerable to corrosion damage.

The source of salinity is the English Channel within the vicinity of the Bovington which is 5.6 miles away from the Atlantic Ocean. Several tanks are also stationed at random locations in Dorset near the Atlantic Ocean under significantly harsh environments. One of the large vehicles, Valentine, which is operating in controlled and uncontrolled environmental conditions from the past several years in The Tank Museum, UK was considered for investigation of corrosion reaction. Significant corrosion damage has been found on several parts of Valentine tanks.²⁸ The Tank Museum, Bovington, UK owns a large number of around 300+ large military vehicles (military tanks). These military tanks were exposed to harsh working and operating conditions in the battlefields in their past service life and therefore showing various modes of degradation in their structures. Corrosion can be classified as one of the major contributors to the structural ageing of the military tanks. NCEM has investigated several vehicles to identify corrosion problem and other associated damages and risks. The investigation has revealed that the several types of corrosion were prevalent and some vehicles have shown severe corrosion problems in their structures. The large vehicles were operated under controlled and uncontrolled environmental conditions at The Tank Museum. The surface coating failure on Challenger 1 has been observed.⁵⁶ The breakdown of the coating reveals the structure of tank and that the

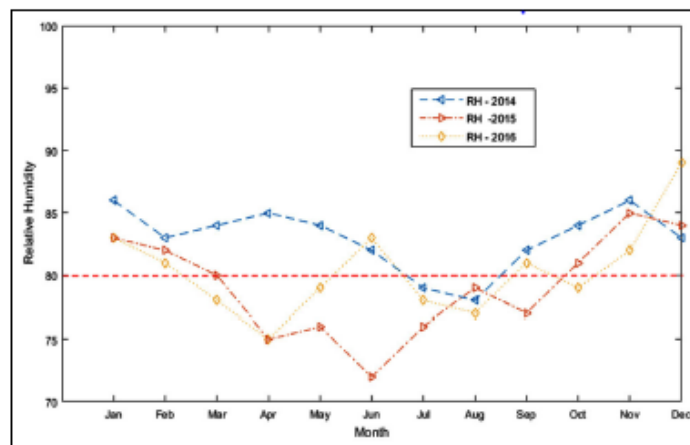


Figure 2. Relative humidity in Dorset, UK during last 3 years.⁵⁶

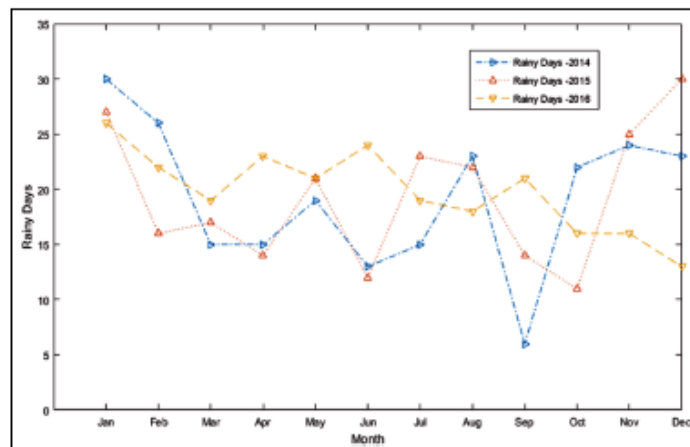


Figure 3. Rainy days in Dorset, UK during last 3 years.⁵⁶

failure is propagating with time due to meteorological factors and properties of the coating-substrate system. Centaur was badly affected by various corrosion modes.²⁸ Inter-granular corrosion (IGC) is a localised corrosion attack on or at the grain boundaries propagating into the material. IGC damage was identified in Centaur armoured skirt.²⁸ Conclusively, the large number of rainy days, wind speed and relative humidity makes the conditions critical for large vehicles and structures to be prone to corrosion.

Experimental analysis

Corrosion is an electrochemical reaction in which metals in manufactured states turn back to its natural states which results in deterioration and losses in the functional stability of metals. The oxidation reaction occurs on the metal surface due to its surrounding environment including water and oxygen to form rust. A corrosion reaction is illustrated in Figure 4 in which the anodic site of metal is losing electrons to produce Fe^{2+} ions

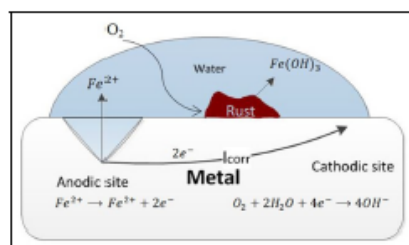
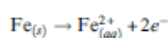


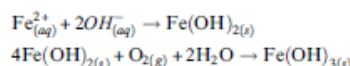
Figure 4. Corrosion reaction.



The cathode site reacts with electrons, water and oxygen to form hydroxide (OH^{-}) ions



The Fe^{2+} and OH^{-} reacts with each other to form $\text{Fe}(\text{OH})_2$ which is called rust.



The existence of salt particles in water acting as electrolyte boost the conductivity of water which results in an effective increase in the concentration of ions and so stimulating the oxidation process (corrosion) of metal. In electrochemical techniques, linear polarisation resistance method provides an effective technique for condition monitoring of metal infrastructures by detecting corrosion reaction due to environmental effects. The μLPR sensor has been developed on linear polarisation theory to directly detect the corrosion in real time caused by water, oxygen and salt. The modern research on corrosion is based on mixed potential theory hypothesised by Wagner and Traud that the overall corrosion reaction is the summation of autonomously occurring oxidation–reduction reactions.⁵⁸ The corrosion is measured by computing the flow of current (I_{corr}) during oxidation–reduction reaction between anodic and cathodic sites. The sensor has three electrodes including working electrode, counter electrode and reference electrode.

The oxidation reaction takes place at working electrode while counter electrode completes the circuit. The reference electrode acts as a half cell which allows the potential of the other half cell to be measured. The three electrode system and structure of μLPR sensor are shown in Figures 5 and 6, respectively.

The performance of μLPR sensors was tested for degradation detection in bridge suspension cable.⁶⁰ It has been found that one of the most feasible solutions

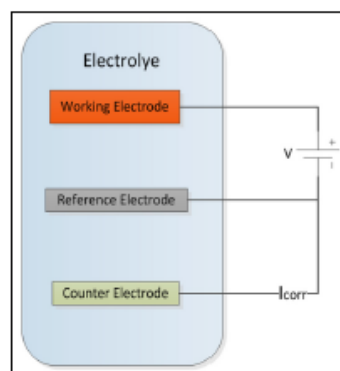


Figure 5. Three-electrode system.

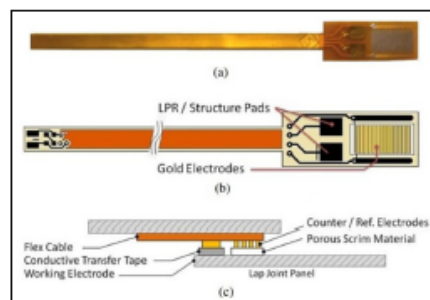


Figure 6. (a) The μLPR sensor as fabricated on a flexible circuit, (b) Labelling each electrode, and (c) using the structure as the three electrode system.⁵⁹

for monitoring the environmental impact on high-value infrastructures such as aircrafts, bridges and buildings. The micro-linear polarisation resistance (μLPR) sensor very sensitive to corrosion is fabricated through a photolithographic process. It contains shim which is prepared using electrochemical etching and photolithographic techniques. The shim is further machined on the Kapton to enhance robustness and ductility. In this research, μLPR sensors have been utilised to detect the corrosion reactions due to the environmental impact on large vehicles at The Tank Museum, UK. In order to analyse the condition of large vehicles operating in uncontrolled environmental condition, μLPR sensors were installed at turret top of valentine tank as shown in Figure 7 and the conditions were monitored for the duration of over 2 years. Sensors were further

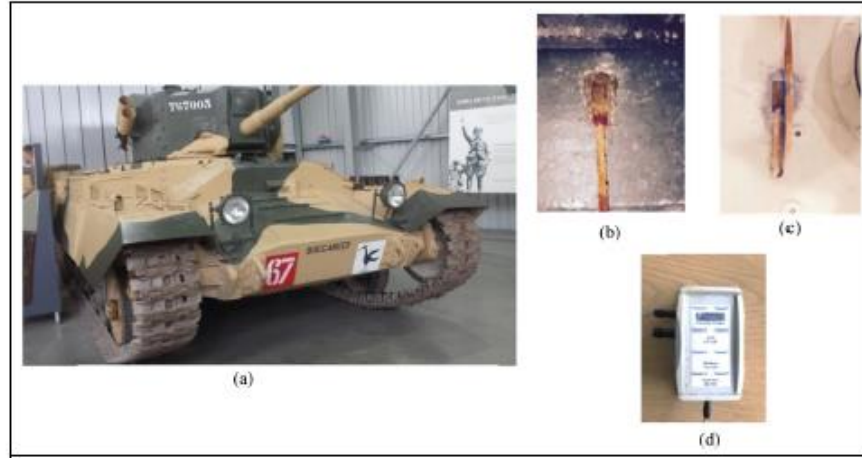


Figure 7. Valentine tank and sensing instruments at The Tank Museum, UK. (a) Valentine Tank stationed at The Tank. (b) μ LPR-1 sensor. (c) μ LPR-2 sensor. (d) DAQ connected to sensors.

connected with data acquisition units to perform signal conditioning and data acquisition. The Stern-Geary equation can be used to calculate the corrosion current density after acquiring polarisation resistance values from the μ LPR sensors^{58,59}

$$I_{Corr} = \frac{B}{R_p} \quad (1)$$

$$CR(t) = I_{Corr} \left[\frac{w}{A * e * F} \right] = \frac{B}{R_p} \left[\frac{w}{A * e * F} \right] \quad (2)$$

In equation (1), I_{Corr} represents the corrosion current density which can be computed by taking the ratio of polarisation resistance (R_p) and Stern-Geary constant (B). The value of Stern-Geary constant (B) is 30 mV for carbon steel 1010.^{25,59} In equation (2), $CR(t)$ represents corrosion rate, F represents Faraday's constant, e represents the number of electrons exchanged, w represents atomic weight and A is the area of corroding electrode.

At The Tank Museum, Bovington, large vehicles are involved in several activities as some of them are stationed inside the museum for display under the shed, where the controlled environmental conditions are provided and some of the vehicles are moved outside in uncontrolled environmental conditions. The μ LPR sensors were installed at turret top of Valentine tank which was operated inside the shed in controlled environmental conditions and also operated remotely outside shed under uncontrolled and harsh environmental conditions of Dorset as described in previous sections. The μ LPR

sensors were constantly monitoring the corrosion process during inside operation and remote activity.

Approximately, 90,000 data samples have been recorded from μ LPR sensors. The measurements taken from sensors are plotted in Figure 8 where remote activities which were repeated several times are labelled as A1, A2, ..., A8. The Valentine tank was operated remotely 8 times during the corrosion monitoring period. It can be seen in the results plotted in Figure 8 that no sign of corrosion has been detected in controlled environmental conditions, while corrosion has been detected several times during remote activity of Valentine tank. The salinity in outside atmosphere can be considered as a major contributor to corrosion reaction as the increase in salinity results in high corrosion rate. The highest corrosion rate was detected by both μ LPR sensors during remote activity A2 as the corresponding value of salinity also highest. The accumulative corrosion detected by both μ LPR sensors during remote activities A1 and A3 is less than the corrosion detected during A2 as the salinity level is also low. The measurements have been recorded during all the remote activities, while the results of activities A1, A2 and A3 are shown in Figures 9 to 11, respectively. The μ LPR sensors have shown similar behaviour in all activities as the salinity level is increasing, the corrosion rate is also increasing and decrease in salinity level making corrosion rate decrease accordingly. The corrosion rate detected during activities A5, A6, A7 and A8 is very low as the corresponding salinity level is also very low.

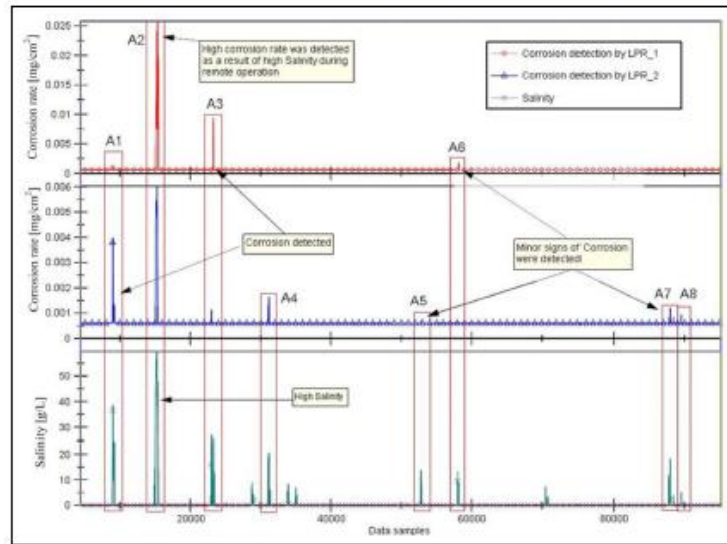


Figure 8. Corrosion detection from μ LPR sensors at turret top of Valentine tank during stationary and remote activities.

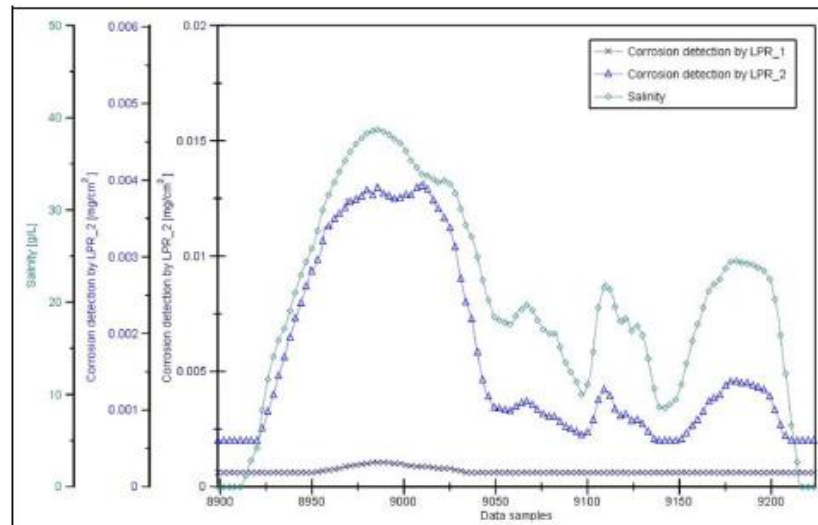


Figure 9. Corrosion rate and salinity measurements during remote activity A1.

The conclusion can be drawn that in uncontrolled environmental conditions, the salinity in the atmosphere is a major element to cause corrosion damage as other

factors including rain, temperature and humidity are already above the critical level for most of the time during a calendar year.

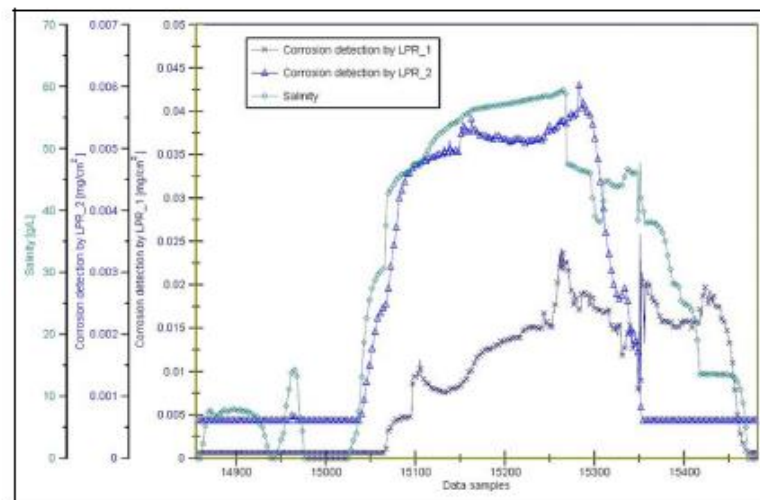


Figure 10. Corrosion rate and salinity measurements during remote activity A2.

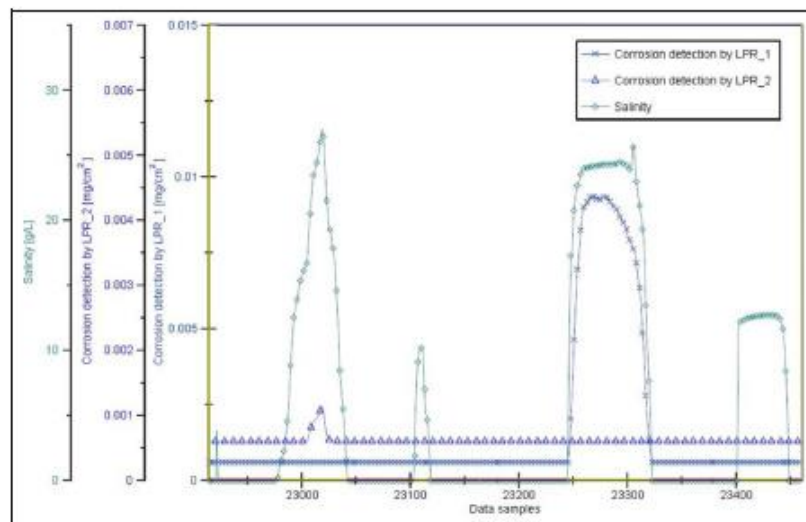


Figure 11. Corrosion rate and salinity measurements during remote activity A3.

Corrosion monitoring for remote assets

Due to the uncertainty in meteorological factors for stationary and remote vehicles operating in an uncontrolled environment, it is very important to find a solution to detect the threat to vehicles at the earliest

possible stage to avoid any damage and prolong the service life. The performance of μ LPR sensors to measure the environmental impact on the large military vehicle has been investigated at The Tank Museum as mentioned in the previous section. The complex structure of vehicles makes it difficult to access and assess every part

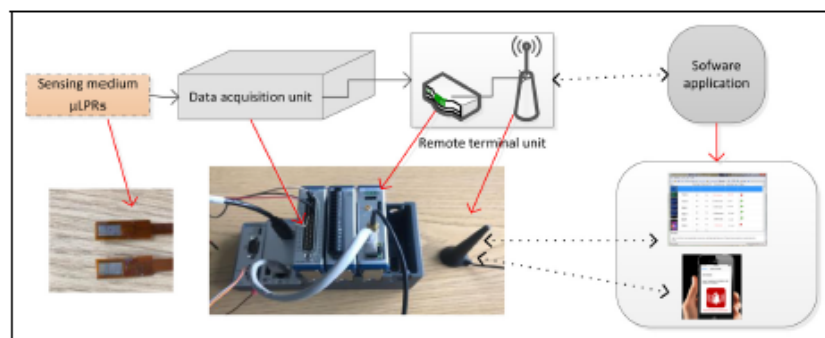


Figure 12. Corrosion monitoring system model for remote assets.

of large vehicles on a continuous basis. The corrosion monitoring system which was implemented for corrosion detection had data acquisition unit with internal memory to store data values, and data were retrieved by connecting an external device such as a laptop for further analytical investigations.

A comprehensive solution is required for high-value assets which are operating at remote locations such as large military vehicles to receive real-time information about critical conditions on time. The use of μ LPR sensors and wireless system technology can provide an efficient way for detection of critical environmental conditions. The system consists of a suite of μ LPR sensors, data acquisition unit and remote terminal unit. The sensor is responsible for measuring the impact of environmental changes as described in the previous section. The data acquisition unit performs signal condition and forwards it to the remote terminal unit. The wireless transmission is carried out at a remote terminal unit which has General Packet Radio Service (GPRS) technology. It utilises cellular network to send and receive messages from remote locations. The advantage of using GPRS technology is that the information regarding corrosion damage can be transmitted or received even from mobile vehicle operating at a remote location. The information regarding the impact of environmental conditions on vehicles or high-value assets stationed or operating at mobile locations will help the maintenance professionals to take necessary steps in order to avoid costly damages due to corrosion. Maintenance or precautionary actions by the professionals could be the movement of vehicle or asset to the appropriate location and it could be the dusting or cleaning mechanism to remove any corrosive products over the body surface to stop corrosion or delamination process. The remote monitoring system has shown in Figure 12 which consists of sensors,

data acquisition unit, remote terminal unit and application software.

Modelling of coating delamination

The delaminated porous region in coating allows the salt particles to diffuse into the interface of the coating-substrate system and propagate towards the intact region. The rate of corrosion current density is directly related to salt concentration which means high diffusion rate will result in high delamination due to corrosion current density which is proportional to metal loss. The salinity in the atmosphere, relative humidity, temperature, time of exposure, rain and wind speed around the high-value assets such as large vehicles are responsible for coating delamination process. The variation in weather conditions makes it difficult to estimate the delamination phenomenon in a more realistic way. The deposition of an amount of salt particles over the body of a large vehicle is the major factor to decide the level of damage. According to research findings in the past, wind speed plays a major role in the deposition rate of salt particles and both are proportional to each other unless other factors like crosswind or shape of body affects the accumulated salt concentration. ISO classification of airborne salinity for atmospheric salinity as shown in Table 1 has been utilised to estimate the salt concentration over body depending on the location of an asset such as coastal region, non-coastal region or near the sea.

The diffusion of hygroscopic ions into metal coating

The accumulation of corrosive ions on large military vehicles at The Tank Museum depends on uncertain vehicle movement and variation in the environmental conditions. The diffusion process depends on various

factors including the concentration of ions, temperature, relative humidity and time of exposure. The change in the concentration of ions can be interpreted as a summation of diffusion, migration and convection process⁶¹

$$\frac{\partial S}{\partial t} = \text{diffusion} + \text{migration} + \text{convection} \quad (3a)$$

$$\frac{\partial S}{\partial t} = \frac{1}{n} \sum_{S_n=1}^n [D_{A_i}(T, RH, t) \nabla S_e + z D_{A_i} S_f \nabla \phi + j_m S_f + R_i + S_j] \quad (3b)$$

The migration and convection processes are neglected in the current research. D_{A_i} is the diffusion coefficient which is smaller by two orders of magnitude in a porous medium as compared to aqueous medium¹⁹

$$D_{A_i} = \left[\frac{1}{D_{S, STAF}(T)f(RH)f(t)} \right]^2 \quad (4)$$

Salinity model. The concept of aerosol physics describes the deposition of hygroscopic particles from the atmosphere on the solid surfaces. The aerosols are generated by various physical processes over the sea surface, but the bursting of air bubbles is one of the common causes due to wind stress during the formation of Whitecap.⁶² The wind speed is a key factor to determine the deposition rate of hygroscopic particles on the solid surface. The threshold level of wind speed for initiation of entrainment of marine aerosol was found to be 3 ms^{-1} .⁵¹

The deposition of salt particles over solid surface depends on many factors including wind speed, wind direction distance from the sea, surface roughness, particle density, shape of body and local landscape. The ISO classification of airborne salinity as shown in Table 1 has classified the deposition rate into four categories and specified the range for a deposition rate of salt particles for the corresponding environmental category. It has four categories such as non-coastal environment denoted as S_0 . It has a maximum deposition rate of $3 \text{ mg/m}^2 \text{ day}$. The coastal environment has categories having a maximum deposition rate of $60 \text{ mg/m}^2 \text{ day}$ denoted as S_1 and $300 \text{ mg/m}^2 \text{ day}$ denoted as S_2 . The location near the sea (S_4) can have a maximum deposition rate of $1500 \text{ mg/m}^2 \text{ day}$. Experimental observations conducted in the past has shown an increase in salt deposition rate as wind speed increases from 3.4 to 10 m/s , and other factors including crosswind affecting deposition rate is not included in the proposed algorithm.

Corrosion and coating delamination will vary from location to location as the deposition rate varies

depending on wind speed. The uncontrolled environmental conditions can also be classified into four categories as UC_0 for deposition rate S_0 non-coastal region, UC_2 for the deposition rate S_2 , UC_3 for deposition rate S_3 and UC_4 for S_4 deposition rate near the sea. In this work, the ISO classification for salinity deposition rate has been utilised to estimate the accumulation of deposited particles over the solid body surface as a function of wind speed for coastal and non-coastal environmental conditions. For example, in the non-coastal environment, the maximum deposition rate is $3 \text{ mg/m}^2 \text{ day}$ and can be assumed for average wind speed. On the basis of experimental observations,^{50,55} considering wind speed as a linear function of deposition rate and ignoring crosswind effects. Following algorithm is used to distribute the salt deposition rate over wind speed for simulation of various typical environments.

```
d = 1;
for i = 1:100
    for k = 1:d
        S = Sx_max / ((Wmax-Wmin)*100) + Sn(j-1);
        Sn(j) = S;
        j = j + 1;
    end
    d = d + 1;
    j = 2;
    St_c(i) = S;
end
```

Sx_max is the maximum deposition rate as specified in the ISO standard. It can be for non-coastal and coastal uncontrolled environmental conditions. $Wmax$ is the maximum wind speed and $Wmin$ is the minimum wind speed depending on location.

The high amount of salt is present in the atmosphere near the sea. The equation is derived for transport rate of salt particles for structures near the sea as a function of distance and wind speed. The rate of change of concentration can be given as

$$\frac{dS_s}{dt} = -\frac{kS}{h} \quad (5)$$

According to experimental observations in the past,^{63–66} the exponential decay of salinity was found as the distance from the sea increases, which was mathematically described as follows

$$S_s = S_0 \exp\left(-\frac{kx}{Vh}\right) \quad (6)$$

where k is the coefficient proportional to deposition velocity,⁶⁷ V is the wind speed and h is the height of air layer. The combination of diffusion mechanism and

Table 1. ISO classification of deposition rate of sodium chloride depending on different environmental conditions.

ISO classification of pollution by airborne salinity (sodium chloride deposition rate in annual average)

Category	Deposition rate of NaCl (mg/m ² day)	Typical environment
S ₀	≤3	Non-coastal
S ₁	3–60	Coastal environment
S ₂	60–300	Coastal environment
S ₃	300–500	Within 200 m of sea

Note. International Organization for Standardization. 2012 2017; Corrosion of metals and alloys – Corrosivity of atmospheres – Classification, determination and estimation]. Available from: <https://www.iso.org/standard/53499.html>.

estimation of corrosive particles depending on wind speed and distance from the sea gives a comprehensive coating delamination model for more accurate and efficient prognostics of coating and corrosion near the sea. The fusion of equations 3(b) and 5 results in the following relation

$$\frac{\partial S}{\partial t} = [D_A(T, RH, t)S_0 \exp(-\alpha x)] \quad (7)$$

The proposed solutions can be used to estimate salt particles depending on the location as classified in ISO standard for airborne salinity. The transport rate of salt particles with a varying deposition rate as linear relation to the wind speed is simulated for summer and winter scenarios and also for near sea environment.

Temperature model. The atmospheric temperature plays a significant part in electrochemical corrosion reaction. The rate of chemical reaction depending on temperature can be computed from Arrhenius equation⁶⁸

$$T' = Ae^{\left[\left(\frac{G_a}{R}\right)\left(\frac{1}{T_{STA}} - \frac{1}{T}\right)\right]} \quad (8)$$

where A represents pre-exponential term, G_a represents activation energy, R represents universal gas constant, T is the absolute temperature in Kelvin and T_{STA} represents standard temperature. The standard diffusion coefficients D_{STA} for standard temperature T_{STA} are calculated in previous works.^{69,70}

Relative humidity model. The presence of moisture is an essential part for most of the corrosion reactions. If RH is a actual pore relative humidity and RH_c represents relative humidity at which diffusion coefficient falls between maximum and minimum values, then relation for relative humidity variation function can be given as

$$RH' = \frac{1}{1 + \left(\frac{1-RH}{1-RH_c}\right)^m} \quad (9)$$

Exposure time. The deteriorating function depending on the time of exposure is given as Nazir et al.³²

$$t' = \left(\frac{t_{STA}}{t}\right)^n \quad (10)$$

where t_{STA} is the time of exposure at which standard diffusion coefficient is measured, t represents actual exposure time and n is the age reduction factor.

Algorithm implementation

The accumulation of salt particles over the structure of an asset which is changing its location and operating in dynamic and uncontrolled environmental conditions will vary significantly as compared to the asset operating stagnant in uncontrolled environmental conditions. The variation in concentration salt accumulation will vary the amount of transportation of salt particles into the coating-substrate system. The algorithm for estimating transport rate of salt particles is shown in Figure 13 which can be used for the assets operating in stationary conditions and also for those assets which are installed remotely and moved to several locations in variable atmospheric conditions.

The algorithm takes temperature, relative humidity, time of exposure and wind speed as input parameters. The implementation of the algorithm using time iterative approach has been reported comprehensively in Nazir et al.³² It also estimates the salinity transport rate by using deposition rate as mentioned in the ISO standard for airborne salinity. The reason behind using wind speed as an input is to estimate salt concentration by using wind speed readings of a particular location and to utilise the value to make a more realistic prediction of transportation of salt particles into the coating-substrate system. The algorithm also has two decisional statements which depend on the change in the wind speed and change of location. If the location of asset changes (e.g. from non-coastal to coastal environment), the salt deposition rate values can be switched to the corresponding environment as defined in the ISO standard.

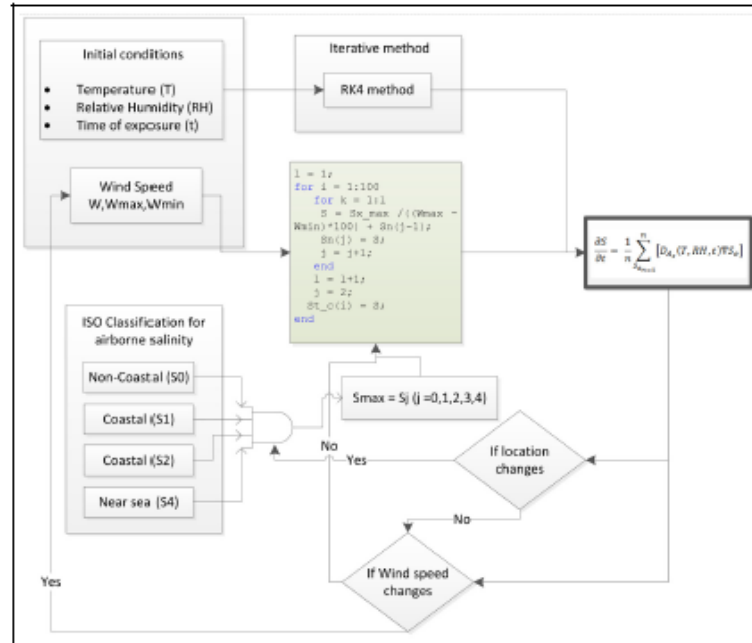


Figure 13. Algorithm for estimating salinity transport rate depending on various environmental conditions.

Results and discussions

Multiple scenarios are considered to simulate the transportation of salt particles into the coating through porous medium. Various factors are responsible for the accumulation of salt particles over solid surfaces including surface roughness, location, wind speed, nature of pollutant, particle density and particle diameter. According to the literature,⁵⁰⁻⁵³ the wind speed also plays a major role in the accumulation of salt particles. The experimental observations performed at The Tank Museum by using μ LPR sensors have detected different levels of corrosion rates at several times depending on salinity contents. The ambiguous nature of corrosion rates depending on diffusion coefficient and wind speed is simulated by considering multiple scenarios for deposition rate of salt particles depending on the increase and decrease in wind speeds for summer and also for winter seasons. The ranges specified in the ISO standard for the deposition of salinity in different environmental conditions is utilised to distribute the deposition rate over different levels of wind speeds from 3 to 10 m/s. According to environmental categories specified in ISO standard, the uncontrolled environmental condition can also be classified into non-

coastal, coastal and near sea uncontrolled environmental conditions (Figure 13).

The transport rate of salt particles in winter and summer seasons is considered with varying wind speed to understand ambiguous nature of delamination process. In the simulation, for the summer season, the temperature is kept on increasing; the increase in temperature also increases diffusion coefficient. The summer season is simulated by increasing temperature at a constant rate from 1 to 100 iterations. There are other many factors which can change the concentration of salt particles including the shape of the substrate or crosswind effects. These effects are not included in this study. The results plotted in Figures 14 and 15 show the behaviour of transport rate of salinity into coating when the concentration of salt particles varies depending on wind speed. The wind speed increases from 3 to 10 m/s for the summer season as shown in Figure 14 and decreases from 10 to 3 m/s for the summer season as shown in Figure 15. High diffusion coefficient in summer accounts for the rise in transport rate of salt particles at high wind speed, but in Figure 15, simulation results show that although the diffusion coefficient is increased, the transport rate decreased due to decrease in salt deposition rate as a function of wind speed. Similarly, the varying salt

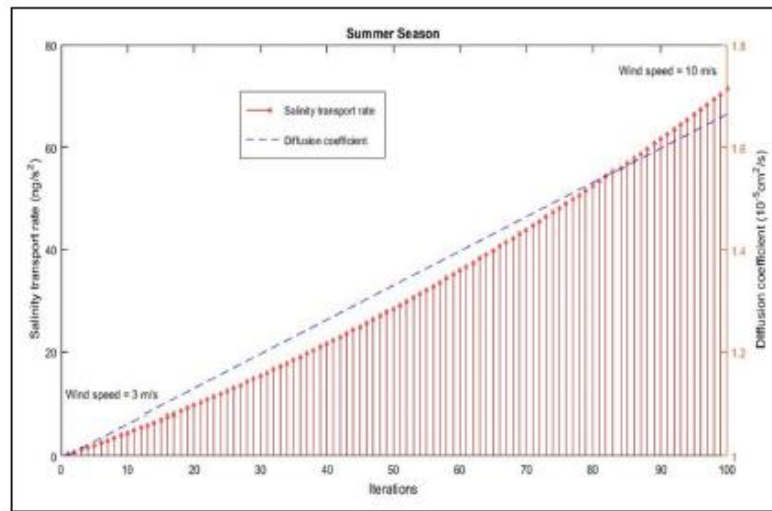


Figure 14. Salinity transport rate during the summer season for increasing wind speed.

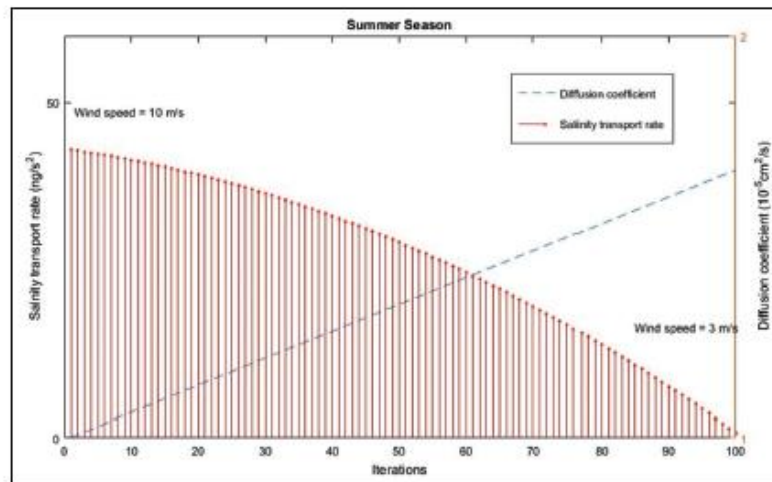


Figure 15. Salinity transport rate during the summer season for decreasing wind speed.

concentration for winter season depending on wind speed is also simulated as shown in Figures 16 and 17. The winter season is simulated by decreasing temperature which accounts for decrease in diffusion coefficient from 1 to 100 iterations. The decrease in diffusion coefficient also decreases the transport of salt particles and decreasing wind speed also decreases the concentration of salt particles which is shown in Figure 16.

Generally, the increase in deposition rate also increases the transport rate of salt particles, but the variation in wind speed from high as 10 m/s to low as 3 m/s deposit low salt contents over the surface, and decrease in diffusion coefficient significantly reduces the salinity transport rate as shown in Figure 16. The increase in wind speed from 3 to 10 m/s is simulated for winter environment with decreasing diffusion

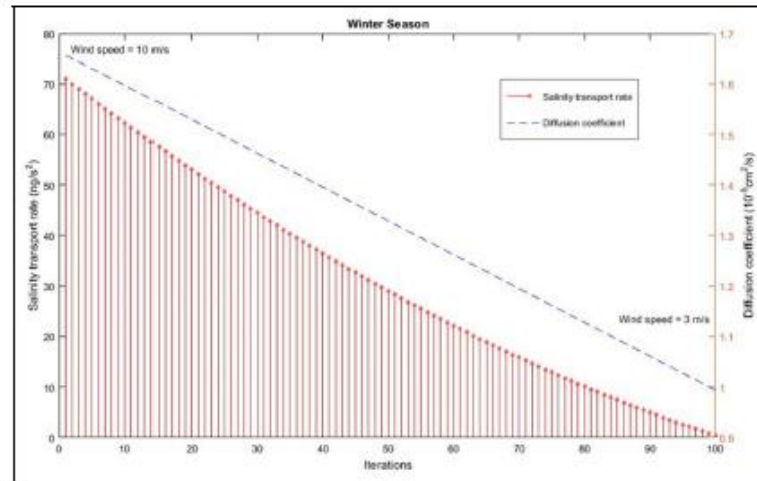


Figure 16. Salinity transport rate during the winter season for decreasing wind speed.

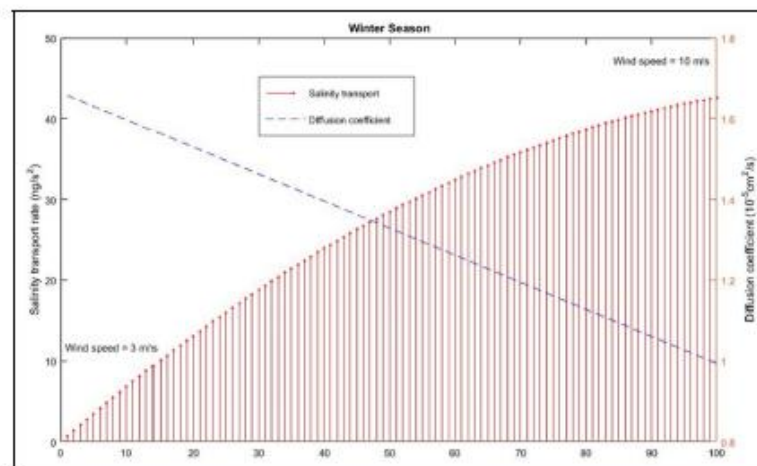


Figure 17. Salinity transport rate during the winter season for increasing wind speed.

coefficient in Figure 17. Although the diffusion coefficient decreases, high diffusion rate of salt particles resulted due to the presence of high salt particles due to high wind speed.

The transport rate of salinity depending on wind speed in uncontrolled environmental conditions near the sea is simulated by using equation (7) as shown in Figure 18. The increase in the distance from sea also

results in low salt deposition. The salt deposition rate is the highest near the sea and decreases as distance increases. The deposition rate of salt concentration also varies with wind speed. The transport rate of salt particles is simulated for different levels of wind speed as shown in Figure 18. As the wind speed increases, the deposition rate and transport rate of salt particles also increase.

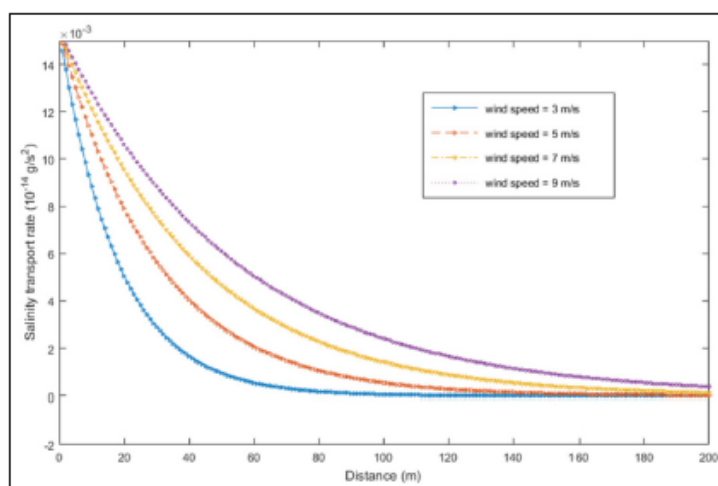


Figure 18. Salinity transport rate near sea depending on the distance from the sea.

Conclusion

This research provides a cost-effective yet efficient and reliable methodology to sustainably mitigate structural integrity issues within large vehicles and structures mainly through corrosion. The impact of meteorological parameters on large vehicles of historical importance operating under uncontrolled environmental conditions is measured by using linear polarisation resistance method. The solution for prior detection of corrosion damage at the initial stage for stationary as well as mobile vehicles operating remotely is also proposed in this work. The deposition of salt particles from the atmosphere is a major parameter which accounts for the amount of coating delamination and corrosion damage. The simulation study of coating delamination in winter and summer environmental conditions is also presented. The salinity transport rate near the sea is also modelled as a function of wind speed and simulation results are also reported. The algorithm presented in this work can be applied to asset operating at remote locations such as non-coastal, coastal and near sea environmental conditions to estimate the corrosion and coating damage using wind speed, temperature, humidity and time of exposure as input parameters. This framework is also applicable to conserve large vehicles of significant cultural and historical biographies for the future generations.



Dedation of conflicting interests

The author(s) declared no potential conflicts of interest with respect to the research, authorship and/or publication of this article.

Funding

The author(s) disclosed receipt of the following financial support for the research, authorship, and/or publication of this article: This research is jointly funded by Defence Science and Technology Laboratory (DSTL), Ministry of Defence (MoD) UK and Bournemouth University. The authors acknowledge their financial support and in-kind contributions.

ORCID iDs

Zulfiqar Ahmad Khan  <https://orcid.org/0000-0002-8725-5166>
 Mian Hammad Nazir  <https://orcid.org/0000-0002-7623-0625>

References

1. NACE study estimates global cost of corrosion at \$2.5 trillion annually, 2016, <https://inspectioneering.com/news/2016-03-08/5202/nace-study-estimates-global-cost-of-corrosion-at-25-trillion-ann>
2. Hertzberg. Cost of corrosion to DoD, 2010, <http://www.sac.org/events/dod/presentations/2010/B3EricHertzberg.pdf>
3. Feliu S and Morcillo M. The prediction of atmospheric corrosion from meteorological and pollution parameters-I: annual corrosion. *Corros Sci* 1993; 34(3): 403-414.
4. Feliu S and Morcillo M. The prediction of atmospheric corrosion from meteorological and pollution parameters-II: long-term forecasts. *Corros Sci* 1993; 34(3): 415-422.
5. Revie RW. *Uhling's corrosion handbook (The ECS series of text and monographs)*. New York: John Wiley & Sons, 2005.

6. Mendoza AR and Corvo F. Outdoor and indoor atmospheric corrosion of non-ferrous metals. *Corros Sci* 2000; 42(7): 1123–1147.
7. Klinesmith DE, McCuen RH and Albrecht P. Effect of environmental conditions on corrosion rates. *J Mater Civil Eng* 2007; 19(2): 121–129.
8. Adikari M and Munasinghe N. Development of a Corrosion Model for Prediction of Atmospheric Corrosion of Mild Steel. *Am J Constr Build Mater* 2016; 2: 91–96.
9. Melchers RE. *Modelling the long term atmospheric corrosion of aluminium alloys*. Callaghan, NSW, Australia: The University of Newcastle.
10. Altnova M, Kelly RG, Scully JR, et al. Engineering corrosion prediction model for aircraft structures. In: *6th joint FAA/DOD/NASA aging aircraft conference*, San Francisco, CA, 16–19 September 2002.
11. Burns RM and Bradley WW. *Protective coatings for metals*. New York: Reinhold Publishing Corporation 1967.
12. Huang M-W, Allely C, Ogle K, et al. A mathematical model for cathodic delamination of coated metal including a kinetic pH-porosity relationship. *J Electrochem Society* 2008; 155(5): C279–C292.
13. Ogle K, Morel S and Meddahi N. An electrochemical study of the delamination of polymer coatings on galvanized steel. *Corros Sci* 2005; 47(8): 2034–2052.
14. Grundmeier G, Reinartz C, Rohwerder M, et al. Corrosion properties of chemically modified metal surfaces. *Electrochimica Acta* 1998; 43(1): 165–174.
15. Grundmeier G, Schmidt W and Stratmann M. Corrosion protection by organic coatings: electrochemical mechanism and novel methods of investigation. *Electrochimica Acta* 2000; 45(15): 2515–2533.
16. Stratmann M, Feser R and Leng A. Corrosion protection by organic films. *Electrochimica Acta* 1994; 39(8–9): 1207–1214.
17. Fürbeth W and Stratmann M. The delamination of polymeric coatings from electrogalvanized steel—a mechanistic approach, part 1: delamination from a defect with intact zinc layer. *Corros Sci* 2001; 43(2): 207–227.
18. Stratmann M, Fürbeth W, Streckel H, et al. The scanning Kelvin probe: a new technique for the in situ analysis of the delamination of organic coatings. *Prog Org Coatings* 1996; 27(1): 261–267.
19. Allahar KN, Orazem ME and Ogle K. Mathematical model for cathodic delamination using a porosity–pH relationship. *Corros Sci* 2007; 49(9): 3638–3658.
20. Prawoto Y and Dillon B. Failure analysis and life assessment of coating: the use of mixed mode stress intensity factors in coating and other surface engineering life assessment. *J Fail Anal Prev* 2012; 12(2): 190–197.
21. Prawoto Y. Unified model for blister growth in coating degradation using weight function and diffusion concepts. *Mater Corros* 2013; 64(9): 794–800.
22. Saeed A, Khan ZA and Montgomery E. Corrosion damage analysis and material characterization of Sherman and Centaur: the historic military tanks. *Mater Perform Character* 2013; 2(1): 30–44.
23. Saeed A, Khan ZA, Hadfield M, et al. Material characterization and real-time wear evaluation of pistons and cylinder liners of the tiger 131 military tank. *Tribol Trans* 2013; 56(4): 637–644.
24. Nazir MH, Khan ZA, Saeed A, et al. A model for cathodic blister growth in coating degradation using mesomechanics approach. *Mater Corros*. Epub ahead of print 23 November 2015. DOI: 10.1002/maco.201508562.
25. Nazir MH, Khan ZA, Saeed A, et al. Modeling the effect of residual and diffusion-induced stresses on corrosion at the interface of coating and substrate. *Corrosion* 2015; 72(4): 500–517.
26. Saeed A, Khan ZA, Clark M, et al. Non-destructive material characterisation and material loss evaluation in large historic military vehicles. *Insight* 2011; 53(7): 382–386.
27. Nazir MH, Khan ZA, Saeed A, et al. A predictive model for life assessment of automotive exhaust mufflers subject to internal corrosion failure due to exhaust gas condensation. *Eng Fail Anal* 2016; 63: 43–60.
28. Saeed A. *Sustainable methodology of conserving historic military vehicles*. Poole: Bournemouth University, 2013.
29. Saeed A, Khan ZA and Nazir MH. Time dependent surface corrosion analysis and modelling of automotive steel under a simplistic model of variations in environmental parameters. *Mater Chem Phys* 2016; 178: 65–73.
30. Nazir MH, Khan ZA and Stokes K. A holistic mathematical modelling and simulation for cathodic delamination mechanism – a novel and an efficient approach. *J Adhes Sci Tech* 2015; 29: 2475–2513.
31. Khan ZA, Grover M and Nazir MH. The implications of wet and dry turning on the surface quality of EN8 steel. In: Ao S-L, Kim HK and Amouzgar MA (eds) *Transactions on engineering technologies*. London: Springer, 2015, pp. 413–423.
32. Nazir MH, Khan Z and Stokes K. Modelling of metal-coating delamination incorporating variable environmental parameters. *J Adhes Sci Tech* 2014; 29(5): 392–423.
33. Nazir M, Khan ZA, Saeed A, et al. Modelling the effect of residual and diffusion induced stresses on corrosion at the interface of coating and substrate. *Corrosion* 2015; 72: 500–517.
34. Nazir MH, Khan ZA and Stokes K. Optimisation of interface roughness and coating thickness to maximise coating-substrate adhesion: a failure prediction and reliability assessment modelling. *J Adhes Sci Tech* 2015; 29(14): 1415–1445.
35. Nazir M, Khan ZA and Stokes K. A unified mathematical modelling and simulation for cathodic blistering mechanism incorporating diffusion and fracture mechanics concepts. *J Adhes Sci Tech* 2015; 29(12): 1200–1228.
36. Nazir MH, Khan ZA and Stokes K. Analysing the coupled effects of compressive and diffusion induced stresses on the nucleation and propagation of circular coating blisters in the presence of micro-cracks. *Eng Fail Anal* 2016; 70: 1–15.
37. Nazir MH, Saeed A and Khan Z. A comprehensive predictive corrosion model incorporating varying

- environmental gas pollutants applied to wider steel applications. *Mater Chem Phys* 2017; 193: 19–34.
38. Saeed A, Khan Z, Nazir MH, et al. Research impact of conserving large military vehicles through a sustainable methodology. *Int J Heritage Archit* 2017; 1(2): 267–274.
 39. Nazir M and Khan Z. A review of theoretical analysis techniques for cracking and corrosive degradation of film-substrate systems. *Eng Fail Anal* 2016; 72: 80–113.
 40. Bajwa R, Khan Z, Nazir MH, et al. Wear and friction properties of electrodeposited Ni-based coatings subject to nano-enhanced lubricant and composite coating. *Acta Metallurgica Sinica* 2016; 29(10): 902–910.
 41. Khan ZA, Pashaei P, Bajwa RS, et al. Fabrication and characterization of electrodeposited and magnetron-sputtered thin films. *Int J Computat Met Exp Measure* 2015; 3(2): 165–174.
 42. Nazir MH and Khan Z. Maximising the interfacial toughness of thin coatings and substrate through optimisation of defined parameters. *Int J Computat Met Exp Measure* 2015; 3(4): 316–328.
 43. Bajwa RS, Khan Z, Bakolas V, et al. Effect of bath ionic strength on adhesion and tribological properties of pure nickel and Ni-based nanocomposite coatings. *J Adhes Sci Tech* 2016; 30(6): 653–665.
 44. Bajwa RS, Khan Z, Bakolas V, et al. Water-lubricated Ni-based composite (Ni–Al₂O₃, Ni–SiC and Ni–ZrO₂) thin film coatings for industrial applications. *Acta Metallurgica Sinica* 2015; 29(1): 8–16.
 45. Khan ZA, Latif J, Nazir H, et al. Predictive and prognostic modelling and simulation of coatings subject to corrosion and mechanical failures. *Int J Computat Met Exp Measure* 2017; 6: 487–498.
 46. Latif J, Khan Z, Nazir H, et al. Life assessment prognostic modelling for multi-layered coating systems using a multidisciplinary approach. *Mater Sci Tec* 2017; 34: 664–678.
 47. Khan ZA, Latif J, Nazir H, et al. Sensor based corrosion condition monitoring of coating substrate system informed by fracture mechanics, electrochemistry and heat transfer concepts. In: *Department of defense – allied nations technical corrosion conference*, Birmingham, AL, 7–10 August 2017.
 48. Nazir H, Khan ZA, Saeed A, et al. Synergistic wear-corrosion analysis and modelling of nanocomposite coatings. *Tribol Int* 2018; 121: 30–44.
 49. McDonald R, Unni C and Duce R. Estimation of atmospheric sea salt dry deposition: wind speed and particle size dependence. *J Geophys Res* 1982; 87(C2): 1246–1250.
 50. Morcillo M, Chico B, Mariaca L, et al. Salinity in marine atmospheric corrosion: its dependence on the wind regime existing in the site. *Corros Sci* 2000; 42(1): 91–104.
 51. Meira G, Andrade C, Alonso C, et al. Modelling sea-salt transport and deposition in marine atmosphere zone—a tool for corrosion studies. *Corros Sci* 2008; 50(9): 2724–2731.
 52. Meira G, Andrade C, Alonso C, et al. Salinity of marine aerosols in a Brazilian coastal area – influence of wind regime. *Atmos Environ* 2007; 41(38): 8431–8441.
 53. Blanchard DC and Woodcock AH. The production, concentration, and vertical distribution of the sea-salt aerosol. *Ann N Y Acad Sci* 1980; 338(1): 330–347.
 54. Lovett R. Quantitative measurement of airborne sea-salt in the North Atlantic. *Tellus* 1978; 30(4): 358–364.
 55. World Weather Online. <https://worldweatheronline.com/>
 56. Saeed A, Khan ZA and Nazir MH. An optimised approach of protecting and sustaining large vehicle system. *Sustainability* 2015; 7(12): 16451–16464.
 57. Wagner C and Traud W. Concerning the evaluation of corrosion reactions by superposition of electrochemical partial reactions and concerning the potential formation on mixed electrodes. *Z Elektrochem* 1938; 44(391): 52.
 58. Brown DW, Connolly RJ, Darr DR, et al. Linear polarization resistance sensor using the structure as a working electrode. In: *Proceedings of the second European conference of the prognostics and health management society*, Nantes, 8–10 July 2014.
 59. Nims DK and Colony D. *LUC-2-1682 long term maintenance of the Anthony Wayne Suspension Bridge main cables*. Columbus, OH: Ohio Department of Transportation and Office of Statewide Planning & Research, 2017.
 60. Bastidas-Arteaga E, Chateaufort A, Sánchez-Silva M, et al. A comprehensive probabilistic model of chloride ingress in unsaturated concrete. *Eng Struct* 2011; 33(3): 720–730.
 61. Levin Z and Cotton WR. *Aerosol pollution impact on precipitation: A scientific review*. London: Springer, 2008.
 62. Basu D and Khan D. Short communication on role of different variables on atmospheric corrosion in marine environment—Effect of proximity to sea. *NML Tech J* 1972; 14: 34–36.
 63. Rajagopalan K, Annamalai PL, Sundarara M, et al. *Atmospheric corrosion of steel in some tropical locations in India*. *Proc Int Cong on Metal Corros* 1971; 4: 532.
 64. Dutra A and Vianna R. *Atmospheric corrosion*. New York: John Wiley, 1982.
 65. Dutra A and Vianna R. Atmospheric corrosion testing in Brazil. In: *International Symposium on Atmospheric Corrosion* 1980. 5–10 October 1980, Hollywood, Florida.
 66. McMahon T and Denison P. Empirical atmospheric deposition parameters—a survey. *Atmos Environ* 1979; 13: 571–585.
 67. Laidler KJ. The development of the Arrhenius equation. *J Chem Educ* 1984; 61(6): 494.
 68. Samson E, Marchand J and Snyder K. Calculation of ionic diffusion coefficients on the basis of migration test results. *Mater Struct* 2003; 36(3): 156–165.
 69. Baştuğ T and Kuyucak S. Temperature dependence of the transport coefficients of ions from molecular dynamics simulations. *Chem Phys Lett* 2005; 408(1): 84–88.

Appendix I

Notation

A	area of corroding electrode
B	proportionality constant

$CR(t)$	corrosion current rate	S_s	salt concentration near sea
dS_s/dt	rate of change of salt concentration near sea	S_0	initial salt concentration
D_{A_s}	standard diffusion coefficient	t	time of exposure
e	number of electrons exchanged	T	temperature
F	Faraday's constant	v_d	deposition velocity
F_x	vertical flux for aerosol	w	atomic weight
I_{cor}	corrosion current density	x	distance from sea
R_p	polarisation resistance	$\partial S/\partial t$	change in concentration with respect to time
RH	relative humidity		

Appendix D: Paper IV

An optimal condition based maintenance scheduling for metal structures based on a multidisciplinary research approach

Jawwad Latif, Zulfiqar A Khan, Mian H Nazir
Bournemouth University, Department of Design & Engineering, NanoCorr, Energy and Modelling
(NCEM)

Keith Stokes
University of Southampton, National Centre for Advanced Tribology at Southampton (nCATS)
Faculty of Engineering and the Environment, Southampton SO17 1BJ

Richard Smith
Director, The Tank Museum, Linsay Rd, Bovington, Wareham BH20 6JG

Corresponding author name: Zulfiqar A Khan

Corresponding author e-mail: zkhan@bournemouth.ac.uk

An optimal condition based maintenance scheduling for metal structures based on a multidisciplinary research approach

Abstract

Latest research findings show that the deterioration of metal coatings results due to complex combination of material and meteorological parameters. The classical maintenance scheduling do not consider complex interface of materials and meteorological parameters to determine optimal maintenance framework. The cost of recoating can be optimised through appropriate selection of coating specifications and maintenance strategy. This research provides a multidisciplinary algorithmic approach to determine cost-effective solutions for recoating. The specifications of red oxide primer coating and structural steel substrate system are considered for simulation analysis. The results show that the appropriate selection of 10% increase in coating thickness based on coating-substrate system specifications resulted in 20-25% reduction in annual patch failures which reduces 5-6 % cost of recoating. Furthermore, the proposed model also simulated to compare Patch recoating and Part recoating strategy and algorithm show that the Part recoating is cost-effective as compared to Patch recoating if number of annual patch failure is greater than '2' and area of the part is '2x'times larger than the area of the patch. Contrary, the Patch recoating results in low cost if the part area is '10x' times larger than patch area and number of annual patch failures are less than '7'.

Keywords: Structures, Maintenance strategy, Recoating cost, Blistering, Condition based maintenance, Predictive modelling, Corrosion cost

<i>Nomenclature</i>	
$\bar{V}_{p\ k}$	<i>Partial molar volume</i>
c'_k	<i>Concentration gradient</i>
E_i	<i>Elastic modulus of i^{th} coating material</i>
h_i	<i>Thickness of i^{th} layer of coating</i>
ν_i	<i>Poisson's ratio of i^{th} material</i>
σ_{cr}	<i>Critical stress of single layer coating</i>
T_{th}	<i>Total thickness of coating</i>
σ_T	<i>Total unbuckled stress</i>
\cap	<i>De-bonding index</i>
Γ_{IC}	<i>Interface toughness</i>
F_{cr}	<i>Critical de-bonding driving force</i>
F	<i>De-bonding driving force</i>

M_{Th}	<i>Threshold bending moment</i>
M_{ini}	<i>Initiation bending moment</i>
a	<i>Blister diameter</i>
w	<i>Blister amplitude</i>
σ_r	<i>Residual stress</i>
E	<i>Elastic modulus</i>
ϵ	<i>strain</i>
α	<i>coefficient of thermal expansion mismatch</i>
M	<i>bending moment</i>
λ	<i>roughness</i>
N	<i>pre-buckling stress</i>
F_c	<i>future cost</i>
ir	<i>interest rate</i>
Ar_p	<i>Patch area to be recoat</i>
Sp_p	<i>Surface preparation cost</i>
C_p	<i>Patch coating cost</i>
A_e	<i>Total are of vehicle to recoat</i>
Sp_e	<i>Surface preparation cost</i>
C_e	<i>Coating cost</i>
Ar_c	<i>Component area to be recoat</i>
Sp_c	<i>Part surface preparation cost</i>
C_c	<i>Cost of Part coating</i>
t_n	<i>Time duration for patch failure</i>
t_c	<i>Time duration for Part failure</i>
T_e	<i>Time duration for complete failure</i>

1. Introduction

In the past decades, great attention has been given in determining the financial impact of corrosion damage and corresponding maintenance in various industrial organisations. The cost factor includes the cost of corrosion prevention techniques, inspection policies, research and development of finding optimise solutions and various other maintenance related activities. The cost of corrosion computed in recent years is equal to around 3.4% of GDP which is a direct cost. Meanwhile, the addition of indirect cost of corrosion accumulates the financial loss twice (Koch et al., 2016). The drinking water and sewer systems, motor vehicles and defence sector experiences substantial financial loss due to corrosion damages. The military applications cost around 23% of the budget due to corrosion damage

and maintenance. The improvement in reliability by applying effective corrosion detection, control and prevention methods can result in around 15 to 35% in cost savings (Koch et al., 2016).

The LMI government consulting organisation has issued several reports on the cost of corrosion for military vehicles (Hertzberg, 2016; Hertzberg et al., 2006). The method used to determine the annual cost was authorised by the Corrosion Prevention and Control Integrated Team (CPCIPT). The method estimates the direct cost which includes labour and material cost along with indirect cost which includes training and research and development etc.. The primary objective of this study is to determine the sustainment annual cost of corrosion for military vehicles and identify the possible opportunities for cost reduction. Total of 520 types of ground military vehicles containing 446,000 individual parts of vehicle structure are considered to conduct the study for determination of the cost of corrosion and associated maintenance. Other cost elements include labour cost, material cost, coating, Blige cleaning, inspections, disposal, scrap and testing equipment.

The total estimation of the annual cost of corrosion for military vehicles was \$2.019 billion in 2006 report (Hertzberg et al., 2006). According to the latest report published by LMI in 2016, the cost of corrosion estimated for the army equipment was \$3.1 billion which 15.5 % of total maintenance expenditure of equipments (Hertzberg, 2016). The largest corrosion cost has been incurred by preventive measures such as inspections, cleaning, washing, recoating and washing. An effective recoating maintenance strategy can impact in the reduction of maintenance activities such as inspection, recoating, washing and surface treatment. The current work will provide algorithm for cost-effective recoating maintenance strategy which based on multidisciplinary parameters along with the labour, material, coating, inspection and surface preparation factors.

1.1 Research findings at "The Tank Museum",UK

The NCEM research group has been involved in investigation of structural integrity of large military vehicles at The Tank Museum, Bovington, UK. The large military vehicles are operating in diverse and harsh environmental conditions. The outcome of research findings resulted in development of The Vehicle Conservation Centre to provide a suitable environment for high priority structures. The experimental investigations also lead to the development of state-of-the-art prognostic models by incorporating complex parameters to predict the failure mechanism.

The corrosion reaction on metal structures has been observed for several years using sensor suite by embedding Linear Polarisation resistors, temperature and humidity sensors on military vehicles. The primary objective of the research findings at "The Tank Museum" is to provide the solutions for proactive maintenance scheduling in order to prolong the service life at optimal cost without compromising the integrity of structures. The large military vehicles are subjected to various types of structural failures and undergo scheduled recoating maintenance. The Figures 1a and 1b illustrate the flex disc and hull Part of Valentine tank operating in controlled and uncontrolled environmental

conditions for the past several years resulted in significant damage due to coating failure and corrosion phenomena.

The scheduled recoating maintenance is carried out after the appropriate amount of time without considering cost implications. The Figures 1c and 1d illustrate the Parts has been recoated with red oxide primer and top coat. It is obvious that lots of cost implications are associated with the maintenance of complex metal structures including frequency of inspections due to uncertainty in structural failure, cost of surface preparation, cost of coating, labour cost and delay in service/production. The large military vehicles at "The Tank Museum" assembled of numerous parts/components and designed in various geometrical shapes. The deterioration phenomena on parts shown in Figures 1a and 1b started from patch failure leading to Part failure. The solution is required to utilise the research findings in order to estimate the optimal recoating maintenance strategy among Patch recoat, Part recoat and Complete recoat.



Figure 1. The Valentine Tank before and after maintenance

1.2 Prognostic modelling of corrosion and coating failure

The structure experiences various types of failure such as adhesion loss, abrasion, bleaching, blistering, cathodic disbonding, cracking, edge corrosion, erosion etc. The inappropriate coating application process, improper drying, mechanical loading effect combined with electrochemical processes makes it difficult to understand the coating failure phenomena. The other prognostic models related to corrosion can also be embedded in the proposed algorithmic approach to estimate the

rusting and associated cost. In the past decade, the various blistering mathematical relation has been proposed to understand the initiation and propagation of blistering phenomena within the thin coating. The major prognostic models for coating failure in terms of cathodic blistering has been summarised in (Nazir & Khan, 2017) . The mechanical properties were observed through experimentation and mathematical relation has been derived for blister formation as a function of blister height and pressure in relation to the elastic energy release rate (Wan & Liao, 1999).

Later on, the elastic energy release rate was formulated as a function of coating thickness and stiffness, blister height, and pressure (Bressers, Peteves, & Steen, 2000; Galindo, Van Veen, Evans, Schut, & de Hosson, 2005). The mathematical relation for energy release rate as a function of coating stiffness, pressure, height and radius of height was developed in (Kappes, Frankel, & Sridhar, 2010). The fracture mechanics concepts are combined with diffusion concept to better describe the blistering phenomena (Prawoto, 2013; Prawoto & Dillon, 2012).

Research within NanoCorr Energy Modeling and Research group extended the multidisciplinary approach to model cathodic blistering and derived a comprehensive prognostic model to predict the formation and propagation of blister (Latif, Khan, Nazir, Stokes, & Plummer, 2018b; Nazir, Khan, Saeed, & Stokes, 2016a; Prawoto, 2013). The relations for energy release rate based on a multidisciplinary approach has also been derived for straight sided blisters (Khan, Latif, Hammad Nazir, & Stokes, 2018). The algorithm based on multi-disciplinary approach was also extended to blister propagation and the speed at which blister will propagate (Latif et al., 2018b) . However, researchers have investigated the coating failure mechanism through various experimental methodologies and identified various parameters to explain complex coating failure mechanism which resulted in prognostic models but still needs more qualitative improvements in real time environmental conditions. The cathodic blistering is one of the most significant causes of coating degradation which has been considered in current work to determine optimal recoating maintenance strategy.

1.3 Cost factor and maintenance modelling

The maintenance professionals apply preventive and essential recoating maintenance scheduling irrespective of cost-benefit ratio. The Run-to-failure, Preventive and Predictive maintenance strategies are commonly practiced maintenance strategies in industries. The Run-to -failure maintenance strategy is applied to low priority structures but it is considered worst strategy in case of high priority structures. The Preventive maintenance involves timely scheduled maintenance which does not require expertise in inspection but it is inefficient for structures subjected to diverse operating conditions. The Predictive maintenance is condition based recoating strategy which is considered more efficient for high-value structures.

Common stochastic deterioration mathematical models including the Wiener process, Gamma Process, Inverse Gaussian process and general path modes are in practice to manage maintenance

scheduling in various industrial applications (Si, Wang, Hu, & Zhou, 2011; Ye & Xie, 2015). The numerical model for the prediction of corrosion-induced concrete crack is formulated for time-efficient maintenance to prolong the service life of concrete structures (Yang, Xi, Li, & Li, 2018). The optimisation framework has been proposed for seismic protective components used for highway bridges. The performance of seismic protective components based on engineered demand parameters is evaluated to derive repair cost ratio. The proposed methodology considers failure probabilities, the cost associated with replacement of components and damage ratio (Xie & Zhang, 2018). The algorithm for optimal maintenance strategy for pipelines subjected to corrosion is proposed for efficient maintenance decision making (Gong & Zhou, 2018).

The framework based on discrete Bayesian networks has been developed for cost-efficient decisions for Condition based maintenance (Nielsen & Sørensen, 2018). An efficient maintenance framework can reduce the cost through decrease in recoating frequency, excessive inspections and other associated maintenance activities. The conventional maintenance strategy evaluation models do not include the multidisciplinary parameters of real-world scenario which drive the corrosion and coating failure phenomena.

The current work provides algorithmic solution for cost-effective recoating maintenance which is based on a multidisciplinary research approach. Three recoating maintenance strategies are considered such as Patch recoat, Part recoat and Complete recoat. The Patch recoating strategy involves removal of delaminated or rusted area from a specific patch and applying coating on the patch area. The Part recoat involves the surface preparation and recoating of the Part/component. The complete recoating involves preparation of the surface of all the defected areas and applies new coating including anti-rust, primers and top coat.

2. Maintenance Strategy Evaluation Algorithm

The basic architecture of Maintenance Strategy Evaluation Algorithm is shown in the Figure 2. The input parameters of algorithm contain specifications of the structure system, measurements from real-time condition monitoring system and historical maintenance database. The next stage is to apply prognostic models to predict the coating failure. The final stage performs the computation of annual cost associated with a maintenance strategy to determine the cost-effective best fit strategy. Various prognostic models for coating failure and corrosion estimation based on meteorological factors and properties of coating –substrate system have been developed (Khan et al., 2018; Nazir & Khan, 2017; Nazir, Khan, Saeed, & Stokes, 2015; Nazir, Khan, & Stokes, 2015c, 2015d, 2016; Nazir & Khan, 2015). These prognostic models can also be embedded in proposed algorithm to simulate the maintenance strategy for potential structural failures for specific application.

The prognostic models developed by NCEM research group resulted through investigation of structural failures in large military vehicles are highly effected by various modes coating damage.

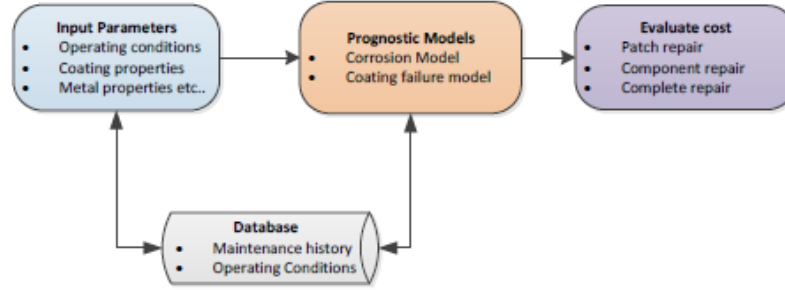


Figure 2. Basic Architecture of Maintenance Strategy Evaluation Algorithm

Therefore, the prognostic model for blistering failure is preferred for current algorithm to evaluate optimal recoating strategy for structures. The combination of complex residual and diffusion-induced stresses play vital role in development of blisters. These blisters propagate by weakening interfacial bonding between the coating and metal structure resulting in removal of coating and exposing metal structure to the surrounding environment (Chuang, Nguyen, & Li, 1997; Irwin, 1957; Nazir, Khan, & Stokes, 2016; Walker, 1970).

The comprehensive description of maintenance strategy evaluation algorithm is shown in the Figure 3. The prognostic model embedded in the current approach is based on latest research findings. It evaluates the performance of coating based on mechanical, chemical and environmental factors to determine the safe, critical and fail conditions of the coating. The propagation of coating failure beginning from a patch of coating failure leading to part coating failure is evaluated in case of part failure. The final stage computes the annual cost based on performance of coating resulted from prognostic model. The annual costs from different recoating strategies are compared to determine the optimal best-fit maintenance strategy. The lack of maintenance database and real-time parameters are the major challenges in evaluation of the proposed algorithm.

2.1 Input Parameters

According to latest research findings, the performance of coating-substrate system depends on numerous factors including the roughness of metal interface, the thickness of the coating, meteorological parameters, mechanical properties of the coating and metal structure as shown in the Figure 4.

2.2 Mechanics and diffusion parameters

The formation and propagation of blistering mechanism are driven by mechanical and diffusion parameters (Nazir, Khan, & Stokes, 2016). The development of residuals stress and diffusion-induced stresses defines the formation and growth rate of the blistering mechanism. The residual stresses exist in the coating-substrate system that is developed during the fabrication of material and application of coating (Totten, 2002).

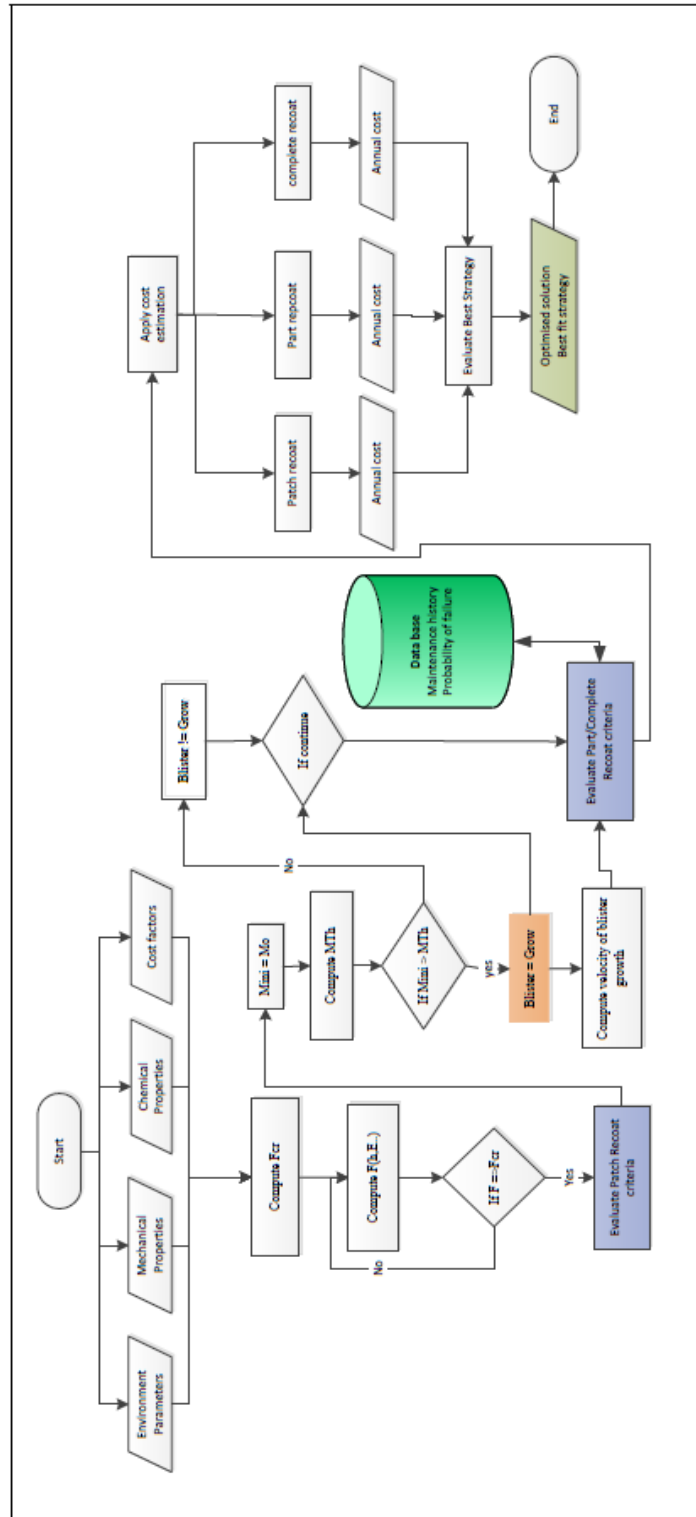


Figure 3. Recoating Maintenance Strategy Evaluation Algorithm

Figure 4. Input parameters

The change in temperature from fabrication temperature accounts for the tensile and compressive stresses within the coating. The tensile stresses are responsible for the opening of cracks in the coating while compressive stresses lead to blister formation (Khan et al., 2018; Nazir, Khan, Saeed, et al., 2015). The inhomogeneity conditions during diffusion process in coating produce diffusion induce stresses (Lim, Yan, Yin, & Zhu, 2012). The relation for residual stress in the coating and substrate is given as (Hsueh, 2002):

$$\sigma_r = E (\varepsilon - \alpha \Delta T) \quad 1$$

where ' E ', ' ΔT ', ' ε ' and ' α ' represents elastic modulus, temperature gradient, strain and coefficient of thermal expansion mismatch, respectively. The intrinsic thermal stresses develops due to change in temperature from application temperature, when coefficient of thermal expansion of coating and substrate are different (Hutchinson, 1996). The uncontrolled and harsh environmental conditions result in the formation of the electrochemical cell due to the reaction of salinity, water, oxygen and metal ions (Chuang, Nguyen, & Lee, 1999). The chemical reaction drives blistering

mechanism through diffusion-induced stress. The following is the expression for diffusion-induced stress in coating and substrate by using the analogy to thermal stress as described in (Zhang, Shyy, & Sastry, 2007).

$$\sigma_d = E \left(\epsilon - \frac{1}{3} c'_k \overline{V_{p k}} \right) \quad 2$$

where ' c'_k ' is concentration gradient of diffusing substance ' k ' analogous to change in temperature and ' $\overline{V_{p k}}$ ' is partial molar volume of substance ' k ' analogous to coefficient of thermal expansion. The residual stresses and diffusion induces stresses accounts for formation and propagation of blistering effect.

2.3 Interfacial Roughness

The adhesion between coating-substrate systems depends on physical parameters including interfacial roughness between coating and substrate, coating thickness and radius of impurity at the interface. According to experimental findings with variable coating-substrate interface roughness, the increase in interfacial roughness results in an increase in the adhesion as it shows maximum resistance against coating failure (Nazir & Khan, 2015).

2.4 Coating thickness

The coating thickness is one of the major bonding strength between the coating-substrate systems. The experimental analysis on steel samples with variable coating thickness has shown an increase in adhesion with respect to increasing in coating thickness (Nazir & Khan, 2015).

2.5 Cost parameters

Several maintenance activities are involved in recoating which needs to be considered in cost evaluation besides the cost of coating applied. These cost factors breakdown into cost of surface treatment, washing, preparing equipment for application of coating, labour hours, washing, drying and other associated activities.

3. Prognostic Model for Coating Failure

There are numerous modes of coating failures including blistering, bleeding, bridging, abrasion, bubbling, cracking and adhesion failure. While blistering is one of the common and complex coating failures that depends on the coating application process, the properties of the coating-substrate system and meteorological parameters. In current work, the formation and propagation of blistering failure have been considered to evaluate the cost-effective recoating maintenance strategy. Previously, the mathematical models for the formation and propagation of circular and straight sided blisters have been modelled and validated through experimental analysis by NCEM research group as discussed comprehensively in (Latif et al., 2018b; Nazir, Khan, et al., 2016a; Nazir, Khan, et al., 2015d; Nazir, Khan, & Stokes, 2016).

The proposed algorithm applies the mathematical prognostic model for the blistering mechanism. The prognostic model provides the value of de-bonding driving force which defines three states of the coating-substrate system as safe, critical and fail. For results analysis in current work, the fail condition calculated from blistering failure prognostic model is considered as patch failure. The blister could be in the form of the circular blister as well as straight-sided blisters. The relation for de-bonding driving force based on fracture mechanics and diffusion parameters for circular blister investigated and validated in previous research finding is given as:

$$F = \left\{ \frac{3}{2} \sum_{i=1}^n \frac{(1 - v_i^2)}{E_i (x_{i+1} - t_p)^3 - (x_i - t_p)^3} M^2 \left[1 + \frac{1}{4} (\sqrt{n-1})^2 \right] \right\} \left\{ 1 + \tan \left(\left(1 - \frac{\Gamma_{IC}}{E_c \lambda} \right) \tan \psi \right)^2 \right\}^{-1} \quad 3$$

The derivation of de-bonding driving force ' F ' for multilayered coating-substrate system as mentioned in above Equation (3) has been compressively discussed in (Latif et al., 2018b). In Equation (3), ' E_i ', ' v_i ', ' Γ_{IC} ', ' λ ' and ' M ' represents elastic modulus, poisson's ratio of i^{th} , interface toughness, interfacial roughness and bending moment, respectively. The top and bottom locations of ' i^{th} ' coating are shown by ' x_{i+1} ' and ' x_i '. The $\tan \psi$ defines the relative mode II to mode I in fracture mechanics (Hutchinson & Suo, 1991). The relation for $\tan \psi$ can be written as following (Faulhaber, Mercer, Moon, Hutchinson, & Evans, 2006):

$$\tan \psi = \frac{K_2}{K_1} = \frac{\sqrt{12} + (T_{th} \Delta N / \Delta M) \tan \omega}{-\sqrt{12} \tan \omega + (T_{th} \Delta N / \Delta M) \tan \omega} \quad 4$$

where ' T_{th} ' and ' N ' represents total coating thickness and pre-buckling stress, respectively. The de-bonding index is represented by ' Ω ' which defines the safe, critical and fail condition of the coating-substrate system. If ' $\Omega < 1$ ' then coating-substrate system is in safe state, If ' $\Omega = 1$ ' then the coating-substrate system is in critical state and. If ' $\Omega > 1$ ' then the coating-substrate system is in fail state. The de-bonding index is the ratio between resultant stress ' σ_r ' and critical stress ' σ_{cr} ' (Nazir, Khan, et al., 2015c). The resultant stress is a summation of diffusion induced stress $\frac{\partial \sigma_{d_{cl}}}{\partial t}$ and residual stress $\frac{\partial \sigma_{r_{cl}}}{\partial x}$.

$$\Omega = \sigma_r / \sigma_{cr} \quad 5(a)$$

$$\sigma_r = \sigma'_d + \sigma'_r = \frac{\partial \sigma_{d_{cl}}}{\partial t} + \frac{\partial \sigma_{r_{cl}}}{\partial x} \quad 5(b)$$

$$\frac{\partial \sigma_{d_{cl}}}{\partial t} + \frac{\partial \sigma_{r_{cl}}}{\partial x} = \frac{\left(D_{k_{cl}} + \frac{D_{k_{cl}} E_{cl} V_{p_{k_{cl}}}^2}{9RT} c_{k_{cl}} \right) \frac{\partial^2 c_{k_{cl}}}{\partial^2 x} + \frac{D_{k_{cl}} E_{cl} V_{p_{k_{cl}}}^2}{9RT} \left(\frac{\delta c_{k_{cl}}}{\delta t} \right)^2}{\frac{D_{k_{cl}} V_{p_{k_{cl}}}^2}{9RT} \frac{\delta c_{k_{cl}}}{\delta t}} \quad 5(c)$$

The relations for resultant stress and critical stress are discussed in detail in (Nazir, Khan, et al., 2015c). When the resultant stress becomes equal to critical stress, the de-bonding index ' $\eta = 1$ ' and value of de-bonding driving force is called as critical debonding driving force ' F_{cr} '.

$$F_{cr} = \left(\frac{3}{2} \sum_{i=1}^n \frac{(1 - v_i^2)}{E_i (x_{i+1} - t_p)^3 - (x_i - t_p)^3} M^2 \right) \left\{ 1 + \tan \left(\left(1 - \frac{\Gamma_{IC}}{E_c \lambda} \right) \frac{1}{\tan \omega} \right)^2 \right\}^{-1} \quad 6$$

If the de-bonding driving force ' F ' is less than critical de-bonding driving force ' F_{cr} ', the coating substrate is in safe condition and when it exceeds the critical de-bonding driving force the coating-substrate system is considered to be in fail state as shown in Table 2.

Table 1. Conditions for patch failure

Condition	State
$F < F_{cr}$	Safe
$F = F_{cr}$	Critical
$F > F_{cr}$	Fail

The initial bending moment and threshold bending moment defines the propagation of blister mechanism (Chuang et al., 1997). The blister will grow if the initial bending moment is greater than the threshold bending moment. The relation for initial bending (M_{ini}) moment and threshold bending moment (M_{Th}) can be given as:

$$M_{ini} = 3 \frac{\sum_{i=1}^n E_i T_{th}^3 w}{a^2} \quad 7$$

$$M_{Th} = 0.73 \sqrt{\sum_{i=1}^n \frac{E_i}{(1 - v_i^2)}} \sqrt{a \sigma_T T_{th}^3} \quad 8$$

where ' w ' and ' a ' represents blister amplitude and blister diameter, respectively. Although the mathematical relation for blister growth rate has been discussed in (Latif et al., 2018b) but the development of number of blisters over the Part area and a number of blisters leading to Part coating failure still needs to be coupled with de-bonding driving force. The profile for de-bonding driving force is show in Figure 5a. The de-bonding driving force approaches critical level as time increases resulting in patch failure. The part failure depends on the geometrical shape, number of blisters per area and growth rate of failure propagation. The component-wise approach is required by incorporating its mechanical and geometrical characteristics for accurate estimation of corrosion

damage and associated maintenance for complex structures (Cavallo, Pagani, Zappino, & Carrera, 2018). The model for failure and propagation proposed in (Latif et al., 2018b) could be further extended for Part failure through incorporating maintenance history, real time monitoring of environmental conditions and experimental investigations.

4. Uniform Database for Maintenance History

The proposed recoating maintenance scheduling is based on complex parameters of real-time scenario which have not been considered in conventional maintenance evaluation techniques. The current solution requires historical data to efficient feedback system to minimise error rate in predictions of failures. Therefore, a uniform database is required to maintain historical maintenance data which should include all possible multidisciplinary parameters as shown in Table 2. The multidisciplinary parameters mentioned in database require various methodologies for measurements. The methods needs be applied on various stages of recoating process. The typical recoating maintenance activities involve several stages such as surface treatment before coating,, application of coating followed by drying stage and then structure is sent for normal operational activities.

The proposed historical database requires recording several parameters at each stage. The several methodologies including optical microscopy, X-ray fluorescence and Scanning electron microscopy to acquire parameters such as interfacial roughness of metal-substrate or thickness of coating have been reported in previous experimental research work of NCEM (Khan et al., 2018; Khan, Latif, Nazir, Stokes, & Plummer, 2017; Latif, Khan, Nazir, Stokes, & Plummer, 2018a; Nazir, Khan, & Stokes, 2015a; Nazir & Khan, 2017; Nazir, Khan, Saeed, et al., 2015; Nazir, Khan, et al., 2016a; Nazir, Khan, Saeed, & Stokes, 2016b; Nazir, Khan, & Stokes, 2015b; Nazir, Khan, et al., 2015c, 2015d; Nazir, Khan, & Stokes, 2016; Nazir, Saeed, & Khan, 2018; Nazir & Khan, 2015; Nazir, Khan, & Saeed, 2018; Nazir, Saeed, & Khan, 2017; Saeed, Khan, Nazir, Hadfield, & Smith, 2017; Saeed, Khan, & Nazir, 2015; Saeed, Khan, & Nazir, 2016). The independent steel sample with same coating and substrate specifications can be used for measurements.

Furthermore, the sensor technology along with wireless communication system can be installed on metal structure to acquire the critical parameters during its operational activities such as corrosion, temperature, humidity and stresses. The corrosion can be monitored using linear polarisation resistor sensors reported comprehensively in (Latif et al., 2018a). The strain gauge sensors can be used to monitor the development of stresses within coating during operational activities reported in (Khan et al., 2017). After acquiring comprehensive historical maintenance data, an efficient neural network technique can be utilised to minimise the error rate between numerically computed predictions and events occurred in real time. The combination of historical data with prognostic calculations will minimise the error rate that will help maintenance professionals to make precise and efficient maintenance decisions.

Table 2. Uniform Database for Maintenance of metal structures

Parameter	Description
Inspection history	The inspection process is time-consuming activity especially in aerospace, museums and automotive industries where a large number of metal structures are operating. The comparison between the frequency of inspection in past and degree of delamination can help to manage the inspection policy accordingly. It can also result in a decrease in the frequency of inspection and any cost associated with the inspection.
Coating thickness	The appropriate selection of coating thickness can result in an increase in adhesion strength between the coating-substrate systems. It can enhance the durability but it will also impact the cost of coating.
Interfacial roughness	The roughness parameter affects the adhesion between coating-substrate systems. The appropriate value of roughness can result in increase in bonding strength.
Salinity	The salinity reacts with water to form an electrochemical cell which results in corrosion damage and coating failure(Latif et al., 2018a). The prediction can be made more efficient based on the accumulation of salinity on structure.
Stress/Strain	The change in temperature results in tensile and compressive stresses within the coating-substrate system (Nazir, Khan, & Stokes, 2016). The behaviour of stress/strain throughout the operating period of metal structure can assist to predict the blisters and cracks propagation in more accurately in real time environment.
Meteorological factors	Different locations on the metal structure may experience different temperature and humidity level e.g. the Parts inside the metal structure of large vehicle may experience a different level of temperature and humidity as compared to Parts outside of the metal structure.
Geometrical shape	According to visual inspection of structures stationed at The Tank Museum, UK, it was observed that more number of coating failures was found on curved surfaces as compared to flat surfaces.

Failure frequency	It is important to maintain the record of frequency of Patch and Part failure for specific Parts of metal structures. The history of cost and frequency of failure will help to better analysis the cost factors for specific Parts and structures.
Time-to- maintenance	The time to complete recoat will differ from strategy to strategy. For example, the time for complete recoat of the metal structure undergoing patch recoat maintenance strategy will come later than the structure undergoing only complete recoat maintenance strategy.
Type of coating applied	The multilayered coating is applied to a metal structure having different characteristics such as corrosion resistant and for decorative purpose.
Operational activities	The decay in the useful life of coating of structures operating in a controlled environment is different from those operating in uncontrolled environmental conditions.
Area recoated (specific to Part)	The area to be recoated can also be classified by using ASTM D610 standard which identify the degree of rusting and area to be coated ("Standard Practice for Evaluating Degree of Rusting on Painted Steel Surfaces," 2012).
Cost factors	The cost factors includes the cost of surface treatment, washing, preparing equipment for application of coating, labour hours, washing, drying and other associated activities..
Prediction error	In predicting the maintenance alerts, there is still a huge gap between real-time scenarios and theoretical calculations. Real-time monitoring along with neural networks can also be applied to past and theoretical data to make more accurate and precise predictions.

5. Cost of Recoating Maintenance

The algorithmic framework for cost-effective maintenance decisions can be developed by fusing the techniques of multidisciplinary prognostic modelling with cost estimation methods. The relation to evaluating the annual cost in the field of economics (Tam & Stierner, 1996) is given as follows:

$$Annual\ cost = F_c \frac{ir}{(1 + ir)^t - 1} \quad 9$$

where ' F_c ' is future cost, ' ir ' is interest rate and exponent ' t ' is annual time. In maintenance, several cost factors are involved which includes the cost of surface preparation, cost of application of coating containing blast abrasives, inspection, maintenance facilities, preparation of coating equipment and containment apparatus. The time ' t ' is the annual time duration of useful coating life. The time ' t ' depends on de-bonding driving force which needs to be forecasted based on properties of individual metal structure and coating materials along with historical maintenance database as described in previous section. In case of Patch recoat, ' t ' is duration when de-bonding driving force remained in safe condition. The coating-substrate system considered for patch recoat when de-bonding driving force exceeds critical level. According to the requirement of recoating application, the modified relation for annual cost ' F_c ' can be given as:

$$Annual\ cost = (Area_Recoat)(Cost_factor)(unit_cost) \left[\frac{ir}{(1+ir)^t - 1} \right] \quad 10$$

In order to find the *Total_Area_Recoat* factor, the area of an individual part to be recoated is determined. The ASTM D610 which evaluates the amount of rusting on coated steel surfaces can be used to classify the corrosion rating and area required to be coated ("Standard Practice for Evaluating Degree of Rusting on Painted Steel Surfaces," 2012).

$$Area_Recoat_i = \left[\frac{Area_to_be_coated\ (\%)}{100} \right] (Surf_area_Part_i) \quad 11$$

The total area to be recoated can be determined by the summation of individual parts as:

$$Total_Area_Recoat = \sum_{i=0}^n Area_Recoat_i \quad 12$$

The metal structures are assembled of multiple parts with various geometrical shapes. The individual Part area and the total area of structure can vary from structure to structure. The area of multiple Parts and total area need to be measured according to a specific metal structure.

The coating maintenance can be divided into three recoating strategies as (Tam & Stiemer, 1996):

Patch recoat

$$Annual\ cost = Area_Recoat * (surf_{prep_{cost}} + coating_{cost}) \left[\frac{ir}{(1+ir)^t - 1} \right] \quad 13$$

Part recoat

$$Annual\ cost = (Area_Recoat * surf_{prep_{cost}}) + (area * coating_{cost}) \left[\frac{ir}{(1+ir)^t - 1} \right] \quad 14$$

Complete recoat

$$Annual\ cost = area * (surf_{prep_{cost}} + coating_{cost}) \left[\frac{ir}{(1 + ir)^t - 1} \right] \quad 15$$

The inflation rate provides the rate of variation in the cost of goods and services. The term $(1 + ir)^t$ can be incorporated in the Equations (13), (14) and (15) as following:

Patch recoat

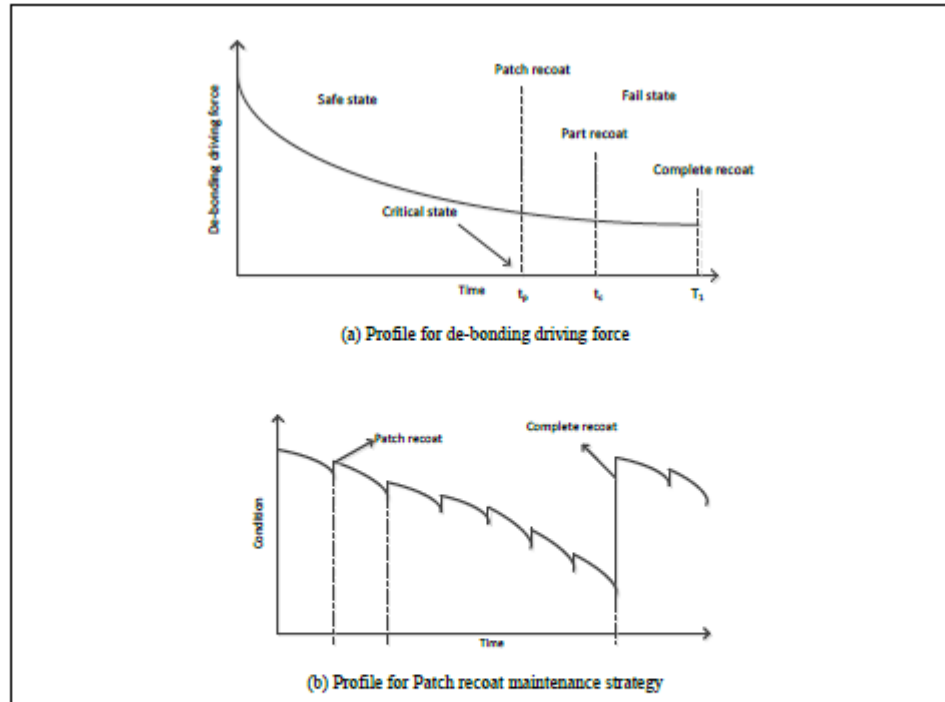
$$Annual\ cost = Area_{Recoat} * (surf_{prep_{cost}} + coating_{cost}) \left[\frac{ir(1 + ir)^t}{(1 + ir)^t - 1} \right] \quad 16$$

Part recoat

$$Annual\ cost = (Area_{Recoat} * surf_{prep_{cost}}) + (area * coating_{cost}) \left[\frac{ir(1 + ir)^t}{(1 + ir)^t - 1} \right] \quad 17$$

Complete recoat

$$Annual\ cost = area * (surf_{prep_{cost}} + coating_{cost}) \left[\frac{ir(1 + ir)^t}{(1 + ir)^t - 1} \right] \quad 18$$



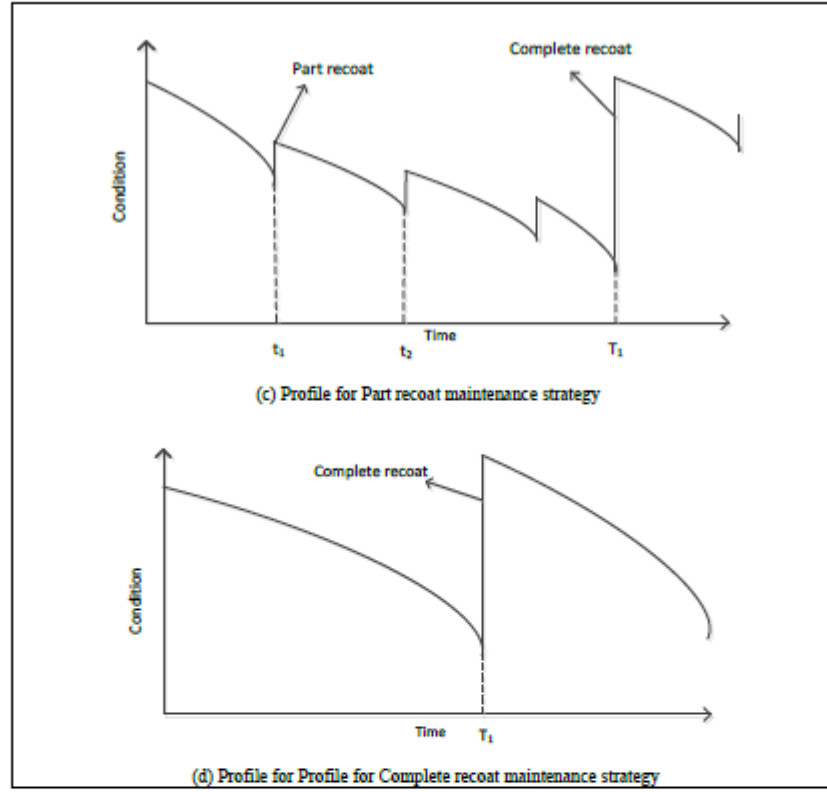


Figure 5. Profiles for de-bonding driving force and maintenance strategies

The maintenance profiles of metal structures associated with maintenance strategies have been shown in the Figures 5b, 5c and 5d. In Patch recoat maintenance strategy, only affected area is recoated that could be the formation of blisters, rusting or cracks. The Patch recoat is effective to stop the damage at the earliest stage but more frequent structural health inspection is required than other maintenance strategies. The history of inspection and associated degree of deterioration of the coating-substrate system can be used to minimise the inspection frequency in future. The structure may require several patch recoats at a different location of a metal structure with time but it will undergo complete recoat after the appropriate time limit. The cost factors can also vary for patch recoats depending on the location of the structure and geometrical shape. The profile for patch recoats is shown in the Figure 5b. The relation for the total annual cost for patch recoat maintenance strategy can be formalised as following:

$$Annual\ cost_{patch\ repair} = \sum_{p=0}^n Ar_p * (Sp_p + C_p) \left[\frac{ir(1+ir)^t}{(1+ir)^{t_n} - 1} \right] + \sum_{e=0}^n A_e * (Sp_e + C_e) \left[\frac{ir(1+ir)^t}{(1+ir)^{t_e} - 1} \right] \quad 19$$

Once coating failure occurs in the form of blisters or cracking, it will propagate with time leading to part failure. The large metal structures are designed in complex geometrical structures and assembled with numerous metallic parts. The parts at different locations may experience diverse factors for the coating and structure damage. Some Part may require frequent recoat than other Parts. The degree of inspection required to identify Part recoat will be less than as compared to patch recoat and it will usually occur later than patch failure. The area of parts and geometrical shapes may differ from each other so does the cost of area preparation and coating application. The profile associated with Part recoat is shown in the Figure 5c. The metal structure receiving Part recoating strategy will also undergo complete recoat after the appropriate time limit. The relation for the total annual cost for Part recoat maintenance strategy can be formalised as following:

$$\begin{aligned} \text{Annual cost}_{\text{Component repair}} &= \sum_{c=0}^n (Ar_c + Sp_c) + (Sp_c + C_c) \left[\frac{ir(1+ir)^t}{(1+ir)^{t_c} - 1} \right] + \sum_{e=0}^n A_e + (Sp_e + C_e) \left[\frac{ir(1+ir)^t}{(1+ir)^{t_e} - 1} \right] \end{aligned} \quad 20$$

In Complete recoat maintenance strategy, the complete structure is recoated once the condition of the metal structure has reached a certain level of deterioration. The frequency of inspection required for complete recoat will be less as compared to other maintenance strategies. The profile for complete recoat is shown in the Figure 5d. The relation for the total annual cost for complete recoat maintenance strategy can be formalised as follows:

$$\text{Annual cost}_{\text{Complete repair}} = \sum_{e=0}^n A_e + (Sp_e + C_e) \left[\frac{ir(1+ir)^t}{(1+ir)^{t_e} - 1} \right] \quad 21$$

The frequency of inspection can vary depending on the complexity of structure and operating conditions. The cost associated with inspection and the movement of a structure for inspection or for the recoating purpose can be written as follows:

$$x_Cost = \sum_{i=0}^n i_Cost_i \left[\frac{ir(1+ir)^t}{(1+ir)^{t_i} - 1} \right] + \sum_{m=0}^n m_Cost_m \left[\frac{ir(1+ir)^t}{(1+ir)^{t_m} - 1} \right] \quad 22$$

where x_Cost is representing the accumulative cost of number of inspections carried out at different time intervals and any cost of moving the structure/military vehicle for inspection or recoating purpose. Above relation can be incorporated in Equation (19), (20) and (21) resulting in relations to find annual cost based on frequency of inspections and cost that could include the movement of an military vehicle for recoating or inspection purpose as follows:

$$\begin{aligned} \text{Annual cost}_{\text{patch repair}} &= \sum_{p=0}^n Ar_p + (Sp_p + C_p) \left[\frac{ir(1+ir)^t}{(1+ir)^{t_p} - 1} \right] \\ &+ \sum_{e=0}^n A_e + (Sp_e + C_e) \left[\frac{ir(1+ir)^t}{(1+ir)^{t_e} - 1} \right] + \sum_{i=0}^n i_Cost_i \left[\frac{ir(1+ir)^t}{(1+ir)^{t_i} - 1} \right] + \sum_{m=0}^n m_Cost_m \left[\frac{ir(1+ir)^t}{(1+ir)^{t_m} - 1} \right] \end{aligned} \quad 23$$

$$\begin{aligned}
 \text{Annual cost}_{\text{component repair}} &= \sum_{i=0}^n (A_{iL} \cdot S_{pL}) + (S_{pL} \cdot C_L) \left[\frac{ir(1+ir)^t}{(1+ir)^{t+1} - 1} \right] \\
 &+ \sum_{s=0}^n A_s \cdot (S_{p_s} + C_s) \left[\frac{ir(1+ir)^t}{(1+ir)^{t+1} - 1} \right] + \sum_{i=0}^n L_{Cost_i} \left[\frac{ir(1+ir)^t}{(1+ir)^{t+1} - 1} \right] + \sum_{m=0}^n m_{Cost_m} \left[\frac{ir(1+ir)^t}{(1+ir)^{t+1} - 1} \right]
 \end{aligned} \quad 24$$

$$\begin{aligned}
 \text{Annual cost}_{\text{complete repair}} &= \sum_{s=0}^n A_s \cdot (S_{p_s} + C_s) \left[\frac{ir(1+ir)^t}{(1+ir)^{t+1} - 1} \right] + \sum_{i=0}^n L_{Cost_i} \left[\frac{ir(1+ir)^t}{(1+ir)^{t+1} - 1} \right] + \sum_{m=0}^n m_{Cost_m} \left[\frac{ir(1+ir)^t}{(1+ir)^{t+1} - 1} \right]
 \end{aligned} \quad 25$$

6. Algorithm Implementation

The algorithm for maintenance strategy evaluation has been simulated and elaborated comprehensively through flow diagram as shown in the Figure 6. The recoating maintenance strategy algorithm contains two primary sections. One section performs prognostic modelling while other computes the annual cost of recoating maintenance. Various scenarios can be simulated for evaluation considering properties of coating materials, different geometrical shapes of metal structures, meteorological parameters etc... In current simulation and analysis, two prepositions have been considered.

Proposition 1: The experimental findings show that the thickness of the coating is proportional to the adhesion of the coating and substrate system. As the thickness of the coating increases the development of blister failure will take more time. The development of blister is taken as patch failure and the algorithm is simulated to evaluate the financial impact of the thickness of the coating on annual cost of patch undergoes Patch recoating maintenance strategy.

Proposition 2: In this scenario, two different recoating maintenance strategies are compared with each other. The impact of Patch recoating and Part recoating strategy on the annual cost of maintenance is evaluated. In Patch recoating the only affected area/patch needs to be treated while in Part recoating requires maintenance treatment of whole component/part of the structure. In order to create all possible conditions, the area of patch to be recoated is taken constant and numbers of patches per year are increased for next ten years. These patches are then compared with various area of parts such as 2x (twice the area of patch area), 3x (thrice the area of patch area) etc...The prognostic model to estimate the de-bonding driving force for blistering failure has already been validated through experimental observations mentioned in publications by NCEM research group (Latif et al., 2018b; Nazir, Khan, Saeed, et al., 2015; Nazir, Khan, et al., 2015c; Nazir, Khan, & Stokes, 2016).

For simulation analysis, the properties of red oxide primer coating and structural steel S275 as substrate are considered as they have been investigated in previous experimental analysis. The red oxide primer coating has Young's modulus 'E' = 6.14 GPa and the coefficient of thermal expansion ' α ' = $21.6 \times 10^{-6}/^\circ\text{C}$. While, the structural steel S275 has Young's modulus 'E' = 210 GPa and the

coefficient of thermal expansion ' α_c' ' = $12 \times 10^{-6}/^\circ\text{C}$ (Latif et al., 2018b). In order to implement the prognostic model for de-bonding driving force, the parameters are converted into dimensionless form.

Initial boundary conditions:

$$c_{k_{c_l}}(x) = c_{k_s} = 0 \quad \text{for time } t = 0 \quad 26(a)$$

$$c_{k_{c_l}}(h) = c_{k_0} \quad \text{for time } t > 0 \quad 26(b)$$

The parameters are converted into a dimensionless form for numerical simulation as following:

$$\tilde{c}_{k_{c_l}} = c_{k_{c_l}}/c_{k_0} \quad 26(c)$$

$$\tilde{E} = \frac{2}{3} \sum_{i=1}^n \frac{E_i}{(1 - v_i^2) E_s} \quad 26(d)$$

$$\tilde{D}_k = D_{k_{c_l}}/D_{k_s} \quad 26(e)$$

$$\tilde{A} = \left(\frac{E_{c_l} V_{p_{k_{c_l}}}^2}{RT} \right) c_{k_0} \quad 26(f)$$

$$\frac{1}{\tilde{\rho}_{d_l}} = \frac{1}{\rho_{d_l} c_{k_0} V_{p_{k_0}}} = 6 \sum_{i=1}^n \frac{E_i t_i (c_{k_l}' V_{p_{k_l}} - c_{k_s}' V_{p_{k_s}})}{E_s s^2 c_{k_0} V_{p_{k_0}}} \quad 26(g)$$

$$\frac{1}{\tilde{\rho}_{r_l}} = \frac{1}{\rho_{r_l} \alpha_{k_0} \Delta T_{k_0}} = 6 \sum_{i=1}^n \frac{E_i t_i (\alpha_i - \alpha_s) \Delta T}{E_s s^2 \alpha_{k_0} \Delta T_{k_0}} \quad 26(h)$$

$$\tilde{x} = ((x_{i+1} - t_p)^3 - (x_i - t_p)^3)/(s + T_{th}) \quad 26(i)$$

The dimensionless form of parameters in Equations (3) and (6) gives following relation for de-bonding driving force:

$$\tilde{F} = \frac{(1/\tilde{E}) \tilde{M} (1/\tilde{x})}{1 + \tan \left((1 - \tilde{B}) \frac{1}{-\tan \omega} \right)^2} \left[1 + \frac{1}{4} \left(\sqrt{n-1} \right)^2 \right] \quad 27$$

$$\tilde{F}_{cr} = \frac{(1/\tilde{E}) \tilde{M} (1/\tilde{\chi})}{1 + \tan \left((1 - \tilde{B}) \frac{1}{-\tan \omega} \right)^2} \quad 28$$

The relation for de-bonding driving is computed through numerical simulation using time-iterative Runge-kutta method. Following steps are involved in solving prognostic modelling section.

- The algorithm takes input parameters which includes various material, chemical, mechanical, and cost parameters.
- The critical de-bonding driving force ' \tilde{F}_{cr} ' is computed using Equation (28).
- As the de-bonding driving force is function of resultant stress, the algorithm updates ' σ_T ' using time iterative method to solve ' \tilde{F} ' in Equation (27).
- The algorithm then compares the de-bonding driving force to find the critical, safe and fail condition according to Table 1.
- The algorithm repeats the 'c' and 'd' unless de-bonding driving force exceeds the critical de-bonding driving force.

The second section contains computation of annual cost for various recoating maintenance strategies. For preposition 1, the algorithm computed the annual cost for Patch recoat with various coating thickness. In preposition 2, the algorithm is computing annual cost for patch recoat and Part recoat strategy including one complete recoat in both cases. The algorithm calculates the annual cost for next e.g., 10 years duration starting from 1 Patch failure per year and similarly calculates the cost for next 10 years by incrementing a number of patch failure per year (from 1 to 10 patches/year).

Once the cost for the patch failure strategy is computed algorithm moves to Part recoat strategy to calculate the annual cost of maintenance by increasing the area of complete Part failure requires recoating. The algorithm calculates the coating cost for next e.g., 10 years considering the area of Part failure is '2x' times than area of patch failure. Similarly, it continues calculating the annual cost by increasing area of Part failure till '10x' which means the area of the Part to be recoated is 10 times greater than the area of patch failure.

7. Results and Discussion

Proposition 1: The simulation results for de-bonding driving force ' \tilde{F} ' for various relative coating thickness (T_{th}/s) as a function of de-bonding index (η) is shown in Fig. 7. As the relative coating thickness increases, the coating and substrate system has high critical de-bonding driving force level (fcr_n). At relative coating thickness = 0.1, the level of critical de-bonding driving force ' fcr_1 ' is lower as compare to critical de-bonding driving force ' fcr_2 '. Similarly, the ' fcr_2 ' with relative coating thickness = 0.2 is lower than the critical de-bonding driving force ' fcr_3 ' with relative coating thickness = 0.3. When the value of debonding index (η) is less than 1, the system is considered in safe condition and no blister failure has occurred which is referenced as patch failure in current simulation.

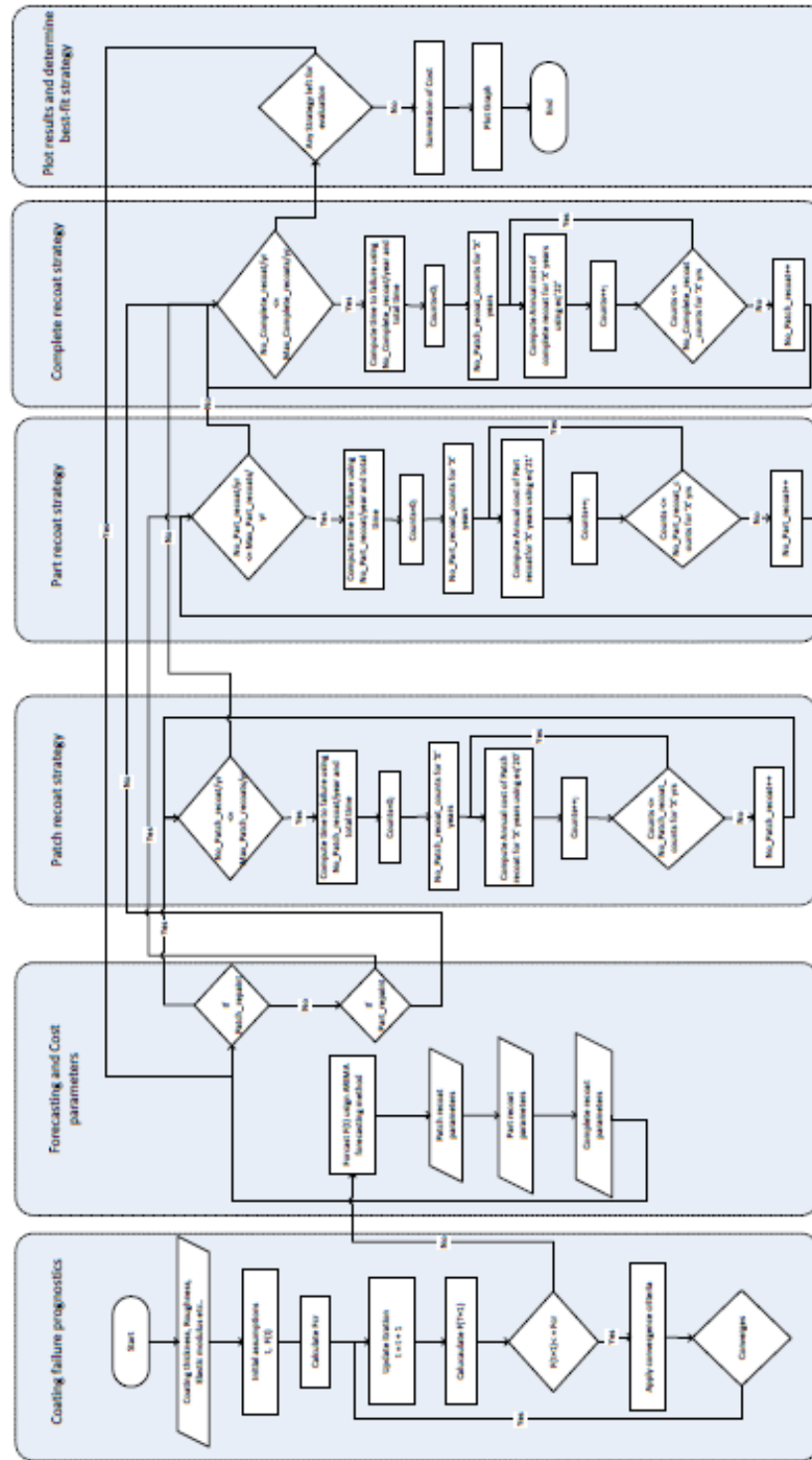


Figure 6. Reconditioning Strategy Evaluation Simulation

When the critical de-bonding driving force exceeds the critical level then patch failure has occurred and patch recoating maintenance is required. The increase in thickness raises the level of adhesion so does critical level for coating and substrate system. The high level of critical de-bonding driving force means that the coating and substrate system will take more time to reach patch failure called as fail condition. The increase in thickness of coating results in less number of patch failures resulting in reduction in recoating maintenance. The comparison of annual cost of different relative coating thickness is shown in Figure 8. Although, increasing the thickness of coating also increases the amount of coating to be applied so does the cost but the reduction in Patch recoating maintenance activities resulted in lower annual cost for high relative coating thickness system. According to current simulations, it can be concluded that the appropriate coating thickness for specific structure can be selected to optimise the cost of recoating maintenance.

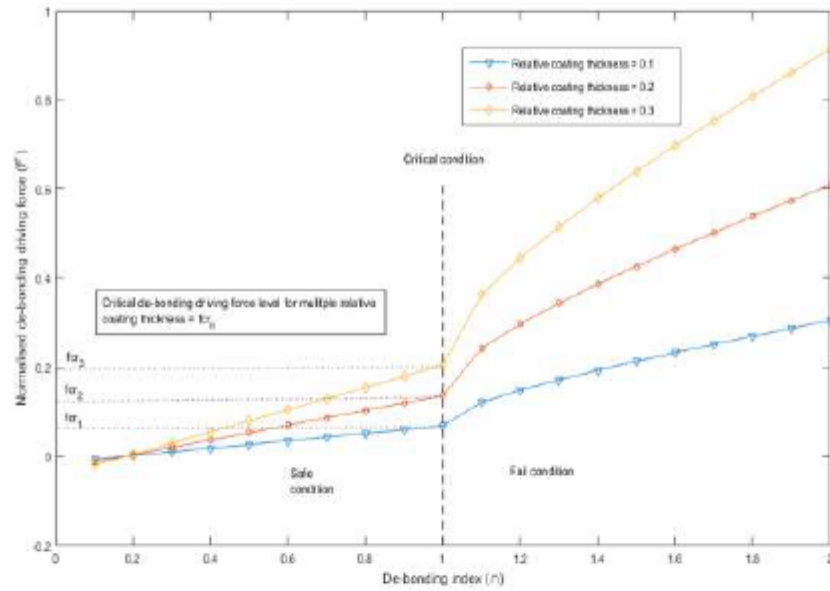


Figure 7. The behaviour of de-bonding driving force as function of de-bonding index

Proposition 2: The simulation results are shown in the Figure 9 explaining the multiple scenarios to make a comparison between Patch recoat strategy and Part recoat strategy. Each value on the graph is presenting the annual cost for 10 years period of time. For simulation, the unit costs of coating and surface preparations for both strategies are considered equal and at least one complete recoat per year is considered for both strategies. The cost for complete recoat is also kept the same in both maintenance strategies. The objective of the current analysis is an evaluation of the best maintenance strategy among Patch recoat and Part recoat for metal structures experiencing patch

failures leading to Part failures. For Patch recoat calculations, the algorithm starts with computing the annual cost for next 10 years considering one patch recoat and one complete recoat.

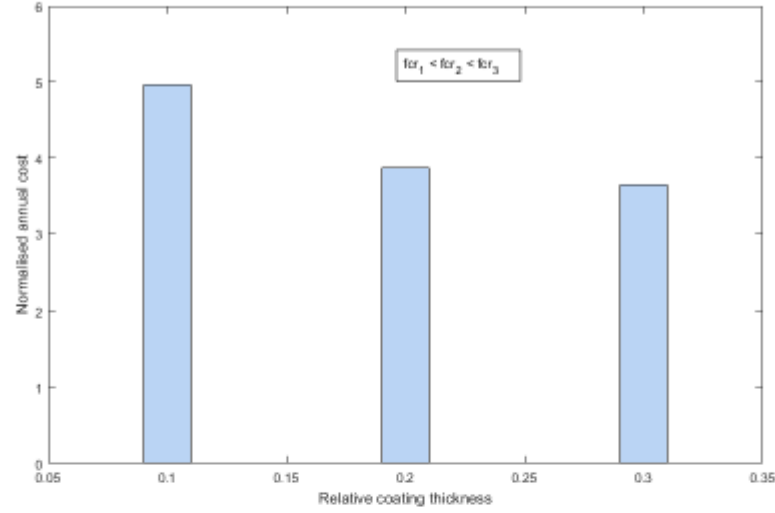


Figure 8. Normalised annual cost as a function of relative coating thickness

Similarly in the next iteration algorithm considers 2 patches recoat per year and computes annual cost for next 10 years. The cost is converted into normalised value by taking ratio with a maximum value of cost. The annual cost of patch recoat is increasing linearly as the number of patches per year increases and its maximum for 10 patches per year as shown in Figure 7. For the Part recoat strategy, the annual cost is computed for variable area of Parts which requires complete Part recoating. The Part recoat area '2x' means the area of a Part selected for complete Part recoat is two times greater than the area of patch failure. Similarly, the cost of Part recoat area '10x' means the area of a Part selected for complete Part recoat is 10 times greater than the area of patch failure.

The algorithm has suggested different best fit maintenance strategies depending on the area of Part failure as compared to patch failure. The point A is marked on the graph to explain the scenario where the cost of both maintenance strategies crossing each other. The point A describes that the Patch recoat strategy is resulting in low cost when a number of patch recoats are less than 4 per year and area of the Part is 5 times greater than the area of Patch failure. The Part recoat strategy is resulting in low cost when patch recoat exceeds 4 per year and Part area is 5 times greater than the area of patch failure requires recoating.

The conclusion from point A can be considered as, if the metal structure is experiencing less than 4 patch recoat and its Part area is 5 times greater than patch failure then Patch recoat maintenance strategy is cost-effective maintenance strategy for corresponding metal structure. However, if the same metal structure is experiencing more than 4 patches failure per year then Part recoat strategy is

more cost effective as compare to Patch recoat strategy. The simulation result shows several crossing for different area of Part and number of patch failures. The conclusion can be made for the specific metal structure based on the frequency of its patch failures per year and area of Parts.

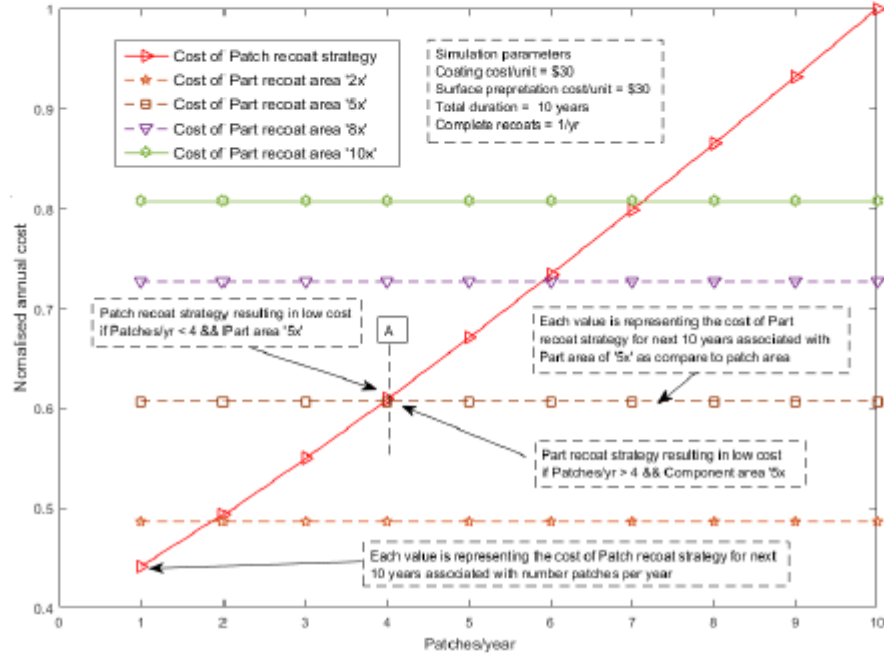


Figure 9. Simulation results for recoating maintenance strategy for metal structures

8. Conclusions

The current work presents very compressive and realistic approach to evaluate optimal recoating maintenance strategy for complex metal structures. The maintenance cost for structures can be evaluated by applying numerous scenarios to the proposed algorithm. The major limitations in the implementation of proposed algorithm are the benchmark for part failure for specific metal structure, historical maintenance data based on model parameters and real time monitoring data of operating locations.

The future work involves development of prognostic models leading to part failure and the collection of the maintenance parameters in real-time to utilise the proposed algorithm more effectively. The NCEM research group is also developing real-time condition monitoring system to acquire various parameters which are required for maintenance model. The fusion of real-time monitoring system, maintenance history database and prognostic models leading to part and complete failure will make the proposed system algorithm more efficient. The collection and management of uniform maintenance history in the form of a database of the individual structure is one of the major

complications to make the maintenance algorithm efficient for real-time scenarios. It is recommended to professionals and researchers to develop a mechanism of maintaining a uniform database of maintenance history associated with specific structures which incorporates all the possible parameters investigated in modern research findings.

Acknowledgements

This research is jointly funded by Defence Science and Technology Laboratory (DSTL), Ministry of Defence (MoD) UK and Bournemouth University. The authors acknowledge their financial support and in-kind contributions.

Disclosure statement

There is no conflict of interest regarding this article.

References

- Bressers, J., Peteves, S., & Steen, M. (2000). Coatings for hot section gas turbine components. *European Structural Integrity Society* (Vol. 26, pp. 115-134): Elsevier. doi: 10.1016/S1566-1369(00)80045-X
- Cavallo, T., Pagani, A., Zappino, E., & Carrera, E. (2018). Effect of Localized Damages on the Free Vibration Analysis of Civil Structures by Component-Wise Approach. *Journal of Structural Engineering*, 144(8). doi: 10.1061/(ASCE)ST.1943-541X.0002128
- Chuang, T.-J., Nguyen, T., & Lee, S. (1999). Micro-mechanic model for cathodic blister growth in painted steel. *Journal of Coatings Technology*, 71(895), 75-85. doi: 10.1007/BF02697925
- Chuang, T., Nguyen, T., & Li, S. (1997). *A non-osmotic blister growth model in coating systems*. Paper presented at the Damage and failure of interfaces. 1st International Conference. Proceedings.
- Faulhaber, S., Mercer, C., Moon, M.-W., Hutchinson, J., & Evans, A. (2006). Buckling delamination in compressed multilayers on curved substrates with accompanying ridge cracks. *Journal of the Mechanics and Physics of Solids*, 54(5), 1004-1028. doi: 10.1016/j.jmps.2005.11.005
- Galindo, R. E., Van Veen, A., Evans, J., Schut, H., & de Hosson, J. T. M. (2005). A modified blister test to study the adhesion of thin coatings based on local helium ion implantation. *Thin Solid Films*, 471(1-2), 170-176. doi: 10.1016/j.tsf.2004.06.129
- Gong, C., & Zhou, W. (2018). Multi-objective maintenance strategy for in-service corroding pipelines using genetic algorithms. *Structure and Infrastructure Engineering*, 14(11), 1561-1571. doi: 10.1080/15732479.2018.1459744
- Hertzberg, E. (2016). Estimated Impact of Corrosion on Cost and Availability of DoD Weapon Systems: FY2016: Report SAL4IT2.
- Herzberg, E. F., Ambrogio, E. D., Barker, C. L., Harleston, E. F., Haver, W. M., O'Meara, N. T., . . . Tran, J. C. (2006). The Annual Cost of Corrosion for Army Ground Vehicles and Navy Ships. *LMI Report SKT50T1*.
- Hsueh, C.-H. (2002). Modeling of elastic deformation of multilayers due to residual stresses and external bending. *Journal of applied physics*, 91(12), 9652-9656. doi: 10.1063/1.1478137
- Hutchinson, J. W. (1996). Stresses and failure modes in thin films and multilayers. *Notes for a Dexam Course. Technical University of Denmark, Lyngby*, 1-45.
- Hutchinson, J. W., & Suo, Z. (1991). Mixed mode cracking in layered materials. *Advances in applied mechanics* (Vol. 29, pp. 63-191): Elsevier.
- Irwin, G. R. (1957). Analysis of stresses and strains near the end of a crack traversing a plate. *Journal of Applied Mechanics*, 24, 351-369.
- Kappes, M., Frankel, G., & Sridhar, N. (2010). Adhesion and adhesion degradation of a pressure sensitive tape on carbon steel. *Progress in Organic Coatings*, 69(1), 57-62. doi: 10.1016/j.porgcoat.2010.05.005

- Khan, Z. A., Latif, J., Hammad Nazir, A. S., & Stokes, K. (2018). Predictive and prognostic modelling and simulation of coatings subject to corrosion and mechanical failures. *Materials Characterisation*, 6(3), 487-498. doi: 10.2495/CMEM-V6-N3-1-13
- Khan, Z. A., Latif, J., Nazir, M. H., Stokes, K., & Plummer, J. (2017). *Sensor based corrosion condition monitoring of coating substrate system informed by fracture mechanics, electrochemistry and heat transfer concepts*. Paper presented at the Department of Defense - Allied Nations Technical Corrosion Conference, Birmingham, AL, USA.
- Koch, G., Varney, J., Thompson, N., Moghissi, O., Gould, M., & Payer, J. (2016). NACE International Impact. In N. I. Gretchen Jacobson, Houston, Texas, USA (Ed.).
- Latif, J., Khan, Z. A., Nazir, M. H., Stokes, K., & Plummer, J. (2018a). Condition monitoring and predictive modelling of coating delamination applied to remote stationary and mobile assets. *Structural Health Monitoring*. doi: 10.1177/1475921718773524
- Latif, J., Khan, Z. A., Nazir, M. H., Stokes, K., & Plummer, J. (2018b). Life assessment prognostic modelling for multi-layered coating systems using a multidisciplinary approach. *Materials Science and Technology*, 34(6), 664-678. doi: 10.1080/02670836.2017.1410358
- Lim, C., Yan, B., Yin, L., & Zhu, L. (2012). Simulation of diffusion-induced stress using reconstructed electrodes particle structures generated by micro/nano-CT. *Electrochimica Acta*, 75, 279-287. doi: 10.1016/j.electacta.2012.04.120
- Nazir, M., Khan, Z., & Stokes, K. (2015a). Modelling of metal-coating delamination incorporating variable environmental parameters. *Journal of Adhesion Science and Technology*, 29(5), 392-423. doi: 10.1080/01694243.2014.990200
- Nazir, M., & Khan, Z. A. (2017). A review of theoretical analysis techniques for cracking and corrosive degradation of film-substrate systems. *Engineering Failure Analysis*, 72, 80-113. doi: 10.1016/j.engfailanal.2016.11.010
- Nazir, M., Khan, Z. A., Saeed, A., & Stokes, K. (2015). Modeling the effect of residual and diffusion-induced stresses on corrosion at the interface of coating and substrate. *Corrosion*, 72(4), 500-517. doi: 10.5006/1804
- Nazir, M., Khan, Z. A., Saeed, A., & Stokes, K. (2016a). A model for cathodic blister growth in coating degradation using mesomechanics approach. *Materials and Corrosion*, 67(5), 495-503. doi: 10.1002/maco.201508562
- Nazir, M., Khan, Z. A., Saeed, A., & Stokes, K. (2016b). A predictive model for life assessment of automotive exhaust mufflers subject to internal corrosion failure due to exhaust gas condensation. *Engineering Failure Analysis*, 63, 43-60. doi: 10.1016/j.engfailanal.2016.02.014
- Nazir, M., Khan, Z. A., & Stokes, K. (2015b). A holistic mathematical modelling and simulation for cathodic delamination mechanism—a novel and an efficient approach. *Journal of Adhesion Science and Technology*, 29(22), 2475-2513. doi: 10.1080/01694243.2015.1071023
- Nazir, M., Khan, Z. A., & Stokes, K. (2015c). Optimisation of interface roughness and coating thickness to maximise coating-substrate adhesion—a failure prediction and reliability assessment modelling. *Journal of Adhesion Science and Technology*, 29(14), 1415-1445. doi: 10.1080/01694243.2015.1026870
- Nazir, M., Khan, Z. A., & Stokes, K. (2015d). A unified mathematical modelling and simulation for cathodic blistering mechanism incorporating diffusion and fracture mechanics concepts. *Journal of Adhesion Science and Technology*, 29(12), 1200-1228. doi: 10.1080/01694243.2015.1022496
- Nazir, M., Khan, Z. A., & Stokes, K. (2016). Analysing the coupled effects of compressive and diffusion induced stresses on the nucleation and propagation of circular coating blisters in the presence of micro-cracks. *Engineering Failure Analysis*, 70, 1-15. doi: 10.1016/j.engfailanal.2016.07.003
- Nazir, M., Saeed, A., & Khan, Z. A. (2018). Electrochemical corrosion failure analysis of large complex engineering structures by using micro-LPR sensors. *Sensors and Actuators B: Chemical*, 268, 232-244. doi: 10.1016/j.snb.2018.02.191
- Nazir, M. H., & Khan, Z. (2015). Maximising the interfacial toughness of thin coatings and substrate through optimisation of defined parameters. *International Journal of Computational Methods and Experimental Measurements*, 3(4), 316-328. doi: 10.2495/CMEM-V3-N4-316-328

- Nazir, M. H., Khan, Z. A., & Saeed, A. (2018). A Novel Non-Destructive Sensing Technology for On-Site Corrosion Failure Evaluation of Coatings. *IEEE Access*, 6, 1042-1054. doi: 10.1109/ACCESS.2017.2777532
- Nazir, M. H., Saeed, A., & Khan, Z. (2017). A comprehensive predictive corrosion model incorporating varying environmental gas pollutants applied to wider steel applications. *Materials Chemistry and Physics*, 193, 19-34. doi: 10.1016/j.matchemphys.2017.01.081
- Nielsen, J. S., & Sørensen, J. D. (2018). Computational framework for risk-based planning of inspections, maintenance and condition monitoring using discrete Bayesian networks. *Structure and Infrastructure Engineering*, 14(8), 1082-1094. doi: 10.1080/15732479.2017.1387155
- Prawoto, Y. (2013). Unified model for blister growth in coating degradation using weight function and diffusion concepts. *Materials and Corrosion*, 64(9), 794-800. doi: 10.1002/maco.201106404
- Prawoto, Y., & Dillon, B. (2012). Failure analysis and life assessment of coating: the use of mixed mode stress intensity factors in coating and other surface engineering life assessment. *Journal of failure analysis and prevention*, 12(2), 190-197. doi: 10.1007/s11668-011-9525-1
- Saeed, A., Khan, Z. A., Nazir, H., Hadfield, M., & Smith, R. (2017). Research impact of conserving large military vehicles through a sustainable methodology. *International Journal of Heritage Architecture*, 1(2), 267-274. doi: 10.2495/HA-V1-N2-267-274
- Saeed, A., Khan, Z. A., & Nazir, M. H. (2015). An optimised approach of protecting and sustaining large vehicle system. *Sustainability*, 7(12), 16451-16464. doi: 10.3390/su71215825
- Saeed, A., Khan, Z. A., & Nazir, M. H. (2016). Time dependent surface corrosion analysis and modelling of automotive steel under a simplistic model of variations in environmental parameters. *Materials Chemistry and Physics*, 178, 65-73. doi: 10.1016/j.matchemphys.2016.04.068
- Si, X.-S., Wang, W., Hu, C.-H., & Zhou, D.-H. (2011). Remaining useful life estimation—a review on the statistical data driven approaches. *European journal of operational research*, 213(1), 1-14. doi: 10.1016/j.ejor.2010.11.018
- Standard Practice for Evaluating Degree of Rusting on Painted Steel Surfaces. (2012). from <https://www.astm.org/Standards/D610.htm>
- Tam, C., & Stierner, S. (1996). Development of bridge corrosion cost model for coating maintenance. *Journal of Performance of Constructed Facilities*, 10(2), 47-56. doi: 10.1061/(ASCE)0887-3828(1996)10:2(47)
- Totten, G. E. (2002). *Handbook of residual stress and deformation of steel*: ASM international.
- Walker, K. (1970). The effect of stress ratio during crack propagation and fatigue for 2024-T3 and 7075-T6 aluminum *Effects of environment and complex load history on fatigue life*: ASTM International.
- Wan, K.-t., & Liao, K. (1999). Measuring mechanical properties of thin flexible films by a shaft-loaded blister test. *Thin Solid Films*, 352(1-2), 167-172. doi: 10.1016/S0040-6090(99)00355-7
- Xie, Y., & Zhang, J. (2018). Design and Optimization of Seismic Isolation and Damping Devices for Highway Bridges Based on Probabilistic Repair Cost Ratio. *Journal of Structural Engineering*, 144(8), 04018125. doi: 10.1061/(ASCE)ST.1943-541X.0002139
- Yang, S., Xi, X., Li, K., & Li, C.-Q. (2018). Numerical Modeling of Nonuniform Corrosion-Induced Concrete Crack Width. *Journal of Structural Engineering*, 144(8), 04018120. doi: 10.1061/(ASCE)ST.1943-541X.0002108
- Ye, Z. S., & Xie, M. (2015). Stochastic modelling and analysis of degradation for highly reliable products. *Applied Stochastic Models in Business and Industry*, 31(1), 16-32. doi: 10.1002/asmb.2063
- Zhang, X., Shyy, W., & Sastry, A. M. (2007). Numerical simulation of intercalation-induced stress in Li-ion battery electrode particles. *Journal of the electrochemical society*, 154(10), A910-A916. doi: 10.1149/1.2759840

Appendix E: Paper V



Paper No. 2017-0000

SENSOR BASED CORROSION CONDITION MONITORING OF COATING SUBSTRATE SYSTEM INFORMED BY FRACTURE MECHANICS, ELECTROCHEMISTRY AND HEAT TRANSFER CONCEPTS

Zulfiqar A Khan, Jawwad Latif, Mian H Nazir

Bournemouth University, Department of Design & Engineering, NanoCorr, Energy and Modelling (NCEM)

Keith Stokes

University of Southampton, National Centre for Advanced Tribology at Southampton (nCATS) Faculty of Engineering and the Environment, Southampton SO17 1BJ

Joseph Plummer

Physical Sciences Division, Defence Science & Technology Laboratory DSTL, Ministry of Defence, Porton Down, Salisbury, SP4 0JQ

Keywords: Corrosion, coating failure, condition monitoring, strain gauge

ABSTRACT

This research investigates delamination and blistering as coating failure mechanisms due to corrosive diffusing species, residual and thermal stresses. Several mathematical models to include environmental variables as temperature, humidity ratio, and atmospheric constituents have been developed and reported. During this study, various coating failures have been analysed through a combination of electrochemistry, fracture mechanics, and heat transfer concepts. This approach enabled the development of comprehensive mathematical models for the prediction and prognoses of coating failures applied to high-value assets. The formation of blister and its propagation due to diffusion of corrosive species was investigated. Fracture mechanics concepts were utilised to study the initiation and propagation of a circular blister as an interfacial crack under the coupling effects of compressive and diffusion-induced stresses along with heat transfer due to pressure gradient at the interface of the coating-substrate system. The direction of blister propagation was defined through a mathematical model with blister radius r and radial angle θ as initial defining parameters. Experimental work was conducted to assess the influence of varying temperatures, humidity ratios, and environmental pollutants as SO_2 and salt particles to

Investigate corrosion failures. Live condition monitoring techniques were developed to assess corrosion rate with respect to large vehicles operation frequencies to study the effects of changing environments. Three years of real time data consisted of 150K data points was acquired for investigating corrosion failures with or without coatings. Both experimental and simulation data was compared to predictive and prognostics models. There is an excellent agreement between experimental and simulation results to be applied for live corrosion condition monitoring of large high-value assets. A sensor based corrosion condition monitoring methodology, informed by experimental and simulation results has been developed and is presented.

INTRODUCTION

Protective coating applied to industrial components, mobile assets and infrastructures are susceptible to mechanical and electrochemical failures. Corrosion and Coating failures within industrial components, infrastructures and large vehicles operating under harsh environmental conditions cause huge financial loss up to 3.1% of GDP for an industrial economy[1]. Live condition monitoring techniques are aimed to reduce the cost through early detection of corrosion and coating failure by changing the scheduled based

maintenance to condition-based maintenance. MEMS sensor provides an adequate way to measure the parameters involved in metal and coating deterioration. The diagnostic and prognostic models can be applied on real-time monitored data to assess the structural health. NanoCorr Energy and Modelling (NCEM) research group analysed the surface corrosion on large vehicles and proposed mathematical models for diagnoses and prognoses of coating life. Variable environmental conditions play a major role in material degradation. The useful life of large vehicles can be extended by enhanced and precision condition monitoring techniques. Corrosion and stresses within coating play a major role in coating delamination process. Sensor technology has a wide range of applications in many areas to monitor, control and diagnose the processes. This research investigates corrosion and stress/strain behavior of coating/substrate system by using micro-electromechanical (MEMS) sensors. Micro-linear polarization Resistors (μ LPR) and strain gauge sensors were used to investigate the effect of corrosion and stresses. Live condition monitoring techniques were utilised to assess corrosion rate with respect to large vehicles operation frequencies to study the effects of changing environmental conditions. Three years of real time data consisted of 150K data points was acquired for investigating corrosion failures with or without coatings. The strain rate was measured by mounting strain gauge sensor on coating/substrate system in an arm of Wheatstone bridge circuit with a protective coating. Live condition monitoring technique can provide data for critical assessment of coating/substrate system to predict the failures.

EXPERIMENTAL PROCEDURE

The application of corrosion sensor and strain gauge sensor for live condition monitoring system is presented. Stress analysis is done through the principle of strain measurement. Strain gauge sensor has been widely adapted to measure stress/strain in foundations, building and other (mechanical and civil) infrastructures. Whilst, the μ LPR concept has been widely utilised to monitor the corrosion problems in aerospace applications, waste water treatment systems, paper manufacturing cooling water systems, civil and mechanical infrastructures where the structure is vulnerable to a corrosive environment. The strain/stress behavior was monitored on coated samples in the accelerated corrosive environment. AISI carbon steel 1010 was used as a substrate with red oxide primer coating [2]. In order to monitor the corrosion rate of vehicles operating under variable environmental conditions, the μ LPRs are mounted

on turret top. Complete insulation process of live condition monitoring mechanism of the strain gauge and μ LPR are discussed in following sections.

Strain Monitoring System

The general purpose strain gage sensors with grid resistance 350.0 ± 0.2 were used to monitor strain on coated samples. Accessories were used to mount strain gauge on the desired area of coated sample as shown in Figure 1. First, the area where the sensor would be installed was conditioned with M-Prep neutralizer by using gauge sponge. The strain gauge was then carefully transferred on a sample by using PCT-2M tape. Strain gauge grid area was wiped by using M-Bond 200 catalyst-C and M-Bond 200 was applied to attach sensor on the coating. The PCT-2M gauge installation tape was removed after two minutes. For bonding, the strain gauge on surface M-Bond 200 was used which does not have any effect on the substrate and coating. After mounting the strain gauge on the sample, solder was used to wire the connections between strain gauge sensor terminals and cable leading to DAC. The mounted strain gauge has shown in Figure 2.

The strain gage sensors were connected to Data Acquisition Conditioner (DAC) which has 8 Hz sampling rate. The DAC has RJ 45 connectors to communicate with strain gauge sensors and powered via USB interface which also connects with base station [3]. It measures the change in strain by measuring the change in resistance through Wheatstone bridge concept which is an electrical circuit used to find unknown electrical resistance by forming a bridge of known resistances. The complete architecture of strain monitoring system is presented in Figure 3. DAC supports quarter, half and full bridge configurations with bridge impedance from 60 to 2000 Ω .



Figure 1: Accessories used for strain gauge installation

The following equation represents the relation between measured unknown resistance and strain.

$$G.F = \frac{\Delta R/R_0}{\epsilon} \quad 1$$

Where $G.F$ is a gauge factor which is defined as relative ratio between mechanical strain and change in electrical resistance, ΔR change in resistance, R_0 is the resistance of the un-deformed gauge and ϵ is strain. Two samples were prepared with strain gauge sensors.



Figure 2: Strain gauge mounted on coating/substrate system



Figure 3: Architecture of strain monitoring system

Corrosion Monitoring System

Large military vehicles exposed to harsh environmental conditions causing concerns for structural health in terms of corrosion and coating failures. Linear polarization resistance (LPR) is the only electrochemical technique being used for real-time monitoring of corrosion rate. The accuracy and precision of LPR in the corrosive environment have been verified using ASTM G85 Annex 5 standard [4]. According to mixed potential theory, the potentials induced at anodic and cathodic sides are equivalent to corrosion potential. The current density between the potential is called corrosion current density [5]. Corrosion current density can be calculated through Stern-Geary equation which can be given as:

$$I_{corr} = \frac{B}{R_p} \quad 2$$

In the above equation I_{corr} represents corrosion current density which is a ratio between proportionality constant (B) and polarization resistance (R_p). For aluminum alloy widely used in aerospace industry has $B = 1000$ and structural

3

carbon steel 1010 has $B = 3000$. Proportionality constant (B) can be determined for any particular material by using anodic and cathodic slopes in Tafel plot [6]. Relation between slopes and proportionality constant can be given as:

$$B = \frac{b_a b_c}{\ln(10)(b_a + b_c)} \quad 3$$

Polarization resistance (R_p) can be determined by using two and three electrode system. The μ LPR sensor is based on the principle of three electrodes system to measure polarization resistance. The rate of corrosion with respect to time at any instant can be computed by modifying Faraday's Law as:

$$CR(t) = I_{corr} \left[\frac{w}{A \cdot e \cdot F} \right] = \frac{B}{R_p} \left[\frac{w}{A \cdot e \cdot F} \right] \quad 4$$

F is Faraday's constant, e is the number electrons exchanged during oxidation reaction, A represents corroding electrode's area and w is the atomic weight of metal.

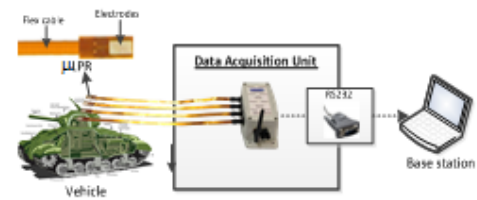


Figure 4: Architecture of corrosion monitoring system

Large military vehicles at the Tank Museum are operating under controlled and uncontrolled environmental conditions. The real-time corrosion monitoring performed on vehicle A operating under controlled and vehicle B operating under uncontrolled environment is presented in this paper. The sensors were mounted on Turret top, which is the most exposed area of the vehicle to environmental changes. The μ LPR has working, reference and counter electrodes as shown in Figure 4. The counter and the reference electrode are made from copper with (ENIG) electroless nickel plating covered with a thin coat of immersion gold to insulate the nickel from oxidation. The working electrode is also fabricated with Electroless nickel immersion gold (ENIG). Electrodes are attached with flex cable which can be installed onto the substrate by using epoxy for corrosion rate measurement. The μ LPR sensors were mounted on Turret top and connected to Data acquisition unit (DAQ) which can store the measured values of linear polarization resistance from the sensor. DAQ has a battery life of

approximately 5-7 years subjected to temperature conditions and duty cycle. The data stored in DAQ can be transferred to the base station by using RS232, RS-484 or wireless ZigBee protocol. The software installed at base station computes corrosion rate based on linear polarization resistance values retrieved from DAQ.

Condition Based Monitoring System

From the past several years, NCEM research group has been making significant contributions in providing engineering solutions for protection of industrial components, large vehicles operating in harsh environmental conditions and valuable assets [2, 7-20]. Several diagnostic and prognostic mathematical models have been proposed and validated based on multidisciplinary research approach.

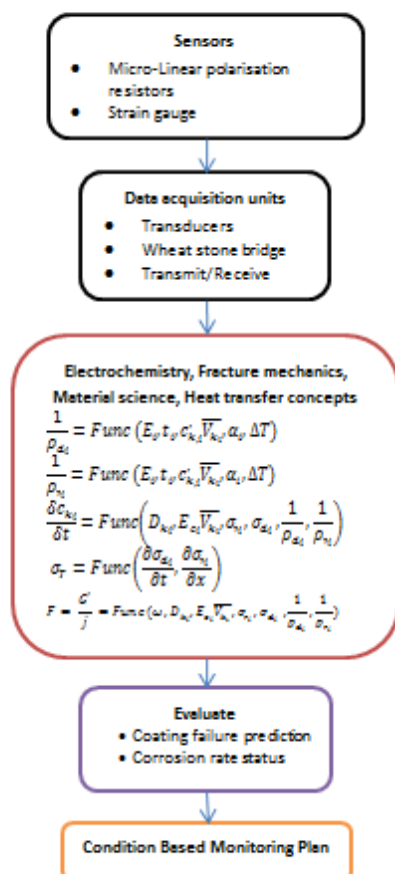


Figure 5: Condition base monitoring system model

Current research is a step advance towards building live condition health monitoring system by incorporating state-of-the-art mathematical model which includes electrochemistry, fracture mechanics, material science and heat transfer concepts. The flow diagram of the proposed condition based monitoring system based on multidisciplinary approach is shown in Figure 5. The application of MEMS sensors presented in this paper and further investigation in more depth using MEMS sensors will be conducted in future to bridge them with mathematical models for accurate future predictions. Khan-Nazir model has been previously reported which is an efficient and novel approach by fusing diffusion and fracture mechanics concepts to explain the behavior of cathodic delamination process [13, 16]. Primary influential parameters like de-bonding driving force have been modeled as a function of mechanical and chemical properties of the coating-substrate system to expound the nucleation and propagation of coating failures including blistering and micro-cracks [10, 12, 14]. The structural steel used in bridges, industrial components, and other high-value assets are greatly affected by acidic rain which contains a solution of water and sulfur dioxide (SO_2). The mathematical relations to simulate the influence of corrosive product (SO_2) on corrosion mechanism of structural steel with respect to time, wind velocity, inclination angle θ was also presented [2]. NCEM research group has also conducted three years of live corrosion monitoring analysis by using μLPR sensors of historical tanks stationed within The Tank Museum at Bovington, United Kingdom. Three years of real time data consisted of 150K data points was acquired for investigating corrosion failures with or without coatings. For accurate condition based monitoring plan, statistical techniques can be applied to the real-time data which was obtained from sensors and mathematical model for reliable detectability of potential risks of structural deterioration.

RESULTS AND DISCUSSION

The performance of strain gauge sensor for coated samples was tested under variable temperature conditions. Stress/strain is a major parameter to drive de-bonding driving force of coating/substrate system. The aim of using strain gauge sensor over the coating is to take real time measurement of stress/strain to monitor current condition of coating and to input real-time stress value into the mathematical models which have been designed for coating failures. The samples with incorporated strain sensor were kept inside the environmental chamber with a wire leading to DAC placed outside the chamber. The experimental results acquired

from DAC are plotted in Figure 6. The experimental results have shown promising results for utilizing this test configuration for live stress measurement. The effect of Thermal stress was observed by increasing temperature when sample 1 was transported into the chamber where the temperature was slightly higher as compared to the surrounding temperature. The change in temperature induces Thermal stress which can be observed at point A in Figure 6. Thermal stress depends on Elastic modulus, the coefficient of Thermal expansion and change in temperature as: $\sigma_{th} = E\alpha\Delta T$ [21]. The Thermal stress due to change in temperature produced compressive strain/stress which can be seen in embedded plot 6.A in Figure 6. The temperature was kept constant for next 24 hours. During constant temperature, Thermal expansion taking place until it reaches maximum level depending on the magnitude of temperature. After 24 hours, the temperature was increased by $\Delta T = 20$. As a result, The Thermal stress induced at this point was large than observed at point A depending on the rate of change in temperature. After point B, the temperature was kept constant again for the next 24 hours. During this period, the Thermal expansion of coating once again started to gain its maximum level corresponding to magnitude of temperature. After 24 hours, temperature was increased further and at this time the $\Delta T = 30$ which resulted in high Thermal stress as compared to point A and point B. The embedded plots of points A, B and C in Figure 6 which shows the behavior of stress when Thermal stress appears due to increase in temperature. It can also be seen that the high change in temperature resulting in high Thermal stress. The experimental work shows promising results to utilize strain gauge sensor for real time values for prognosis models. Similar kind of experiment was also performed on another sample 2 with strain gauge sensor to ensure repeatability of sensor behavior with same sensing equipment. The experimental results can be seen in Figure 7 which shows similar behavior. As temperature increases, the coating material tends to reach its maximum Thermal expansion level corresponding to magnitude of temperature.

The real-time corrosion monitoring of two different vehicles operating (stationary and mobile) in the various environment have been presented. There were two μ LPR sensors mounted on turret top of each large vehicle connected to DAQ. Sensors data were continuously been stored in the memory unit of DAQ and retrieved regularly after few months of time. The vehicle A was remained stationary during the course of this study and was subjected to controlled environment. According to acquired data from vehicle A operating in controlled environmental

conditions, μ LPRs have not shown any data points due to reason that no significant variation in temperature, salinity, and relative humidity had occurred. The results obtained from corrosion monitoring system installed on vehicle A is shown in Figure 8. Whilst, the corrosion was observed in vehicle B, which has been in a dual state of operation i.e. both under the controlled and uncontrolled environmental conditions. The results obtained from sensors mounted on turret top of vehicle B presented in Figure 9. There were two LPR sensors embedded on each large vehicle. LPR1 has not shown any corrosion rate. So its value remained zero in both conditions (Controlled and uncontrolled environment) as shown in Figure 8 and Figure 9. The corrosion rate was observed on several occasions during activity. The area pointed with the caption as activity in Figure 9 represents the existence of corrosion reactions during activity. There are mainly two types of environmental conditions where large vehicles are operated or stationed. One is under the shed, where the environment is controlled and more likely suitable for the structure of large vehicles. The second environment is outside the shed where large vehicles are also operated or stationed for exhibition activity. The Tank Museum is situated near the coast, therefore in the uncontrolled environment the salt particles present in the atmosphere accumulated over uncovered steel parts. These salt particles are a major factor for the initiation of corrosion. The activity of moving vehicle B repeated several times during three years but the corrosion rate is not similar as it kept on decreasing due to the formation of a thin layer of corrosive species over the vehicle surface.

CONCLUSION

The real-time corrosion monitoring and stress/strain measurement techniques have been reported in the current research. The data points obtained from both systems have shown promising results for utilization of MEMS for live and remote structural health monitoring system. The strain gauge sensor has shown the values of thermal compressive stress for minor changes in temperature which will provide useful data for coating life assessment. The μ LPR sensor with wireless technology embedded within high-value assets can send alert/warning about the initiation of corrosion process to the professionals to take necessary actions which will help in prolonging the useful life of these assets. According to the results obtained from experimentation, the strain gauge sensors and μ LPRs will provide an effective way to design state-of-the-art condition based monitoring system.

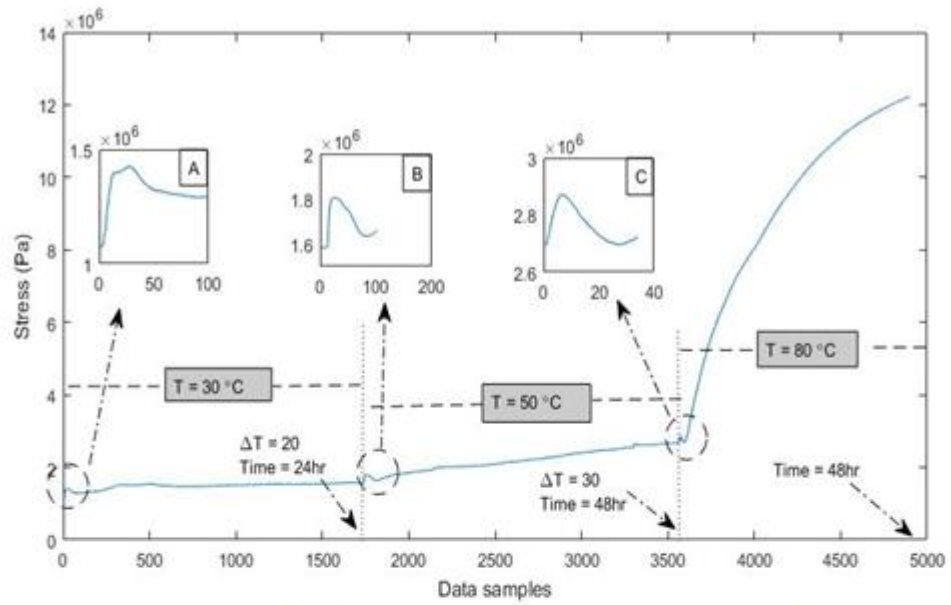


Figure 6: Experimental results acquired from strain gauge monitoring system from sample 1

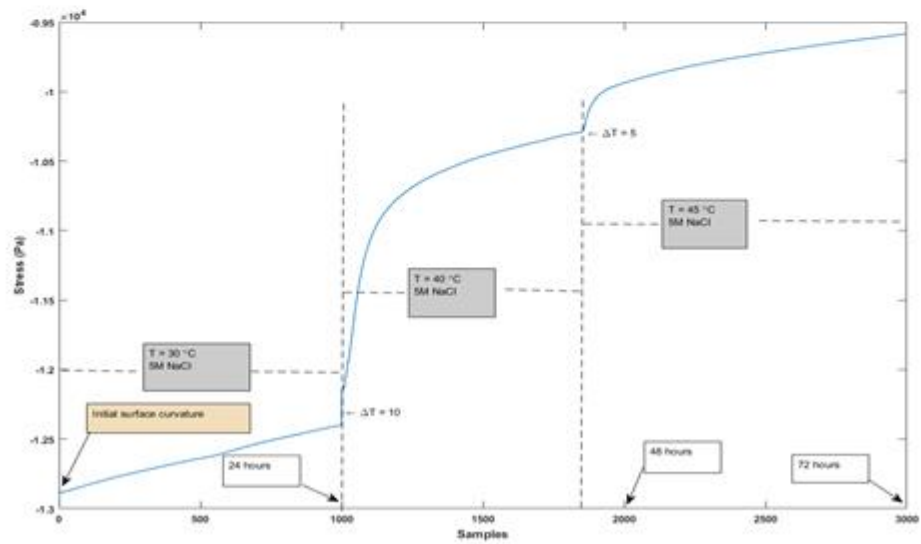


Figure 7: Experimental results acquired from strain gauge monitoring system from sample 2

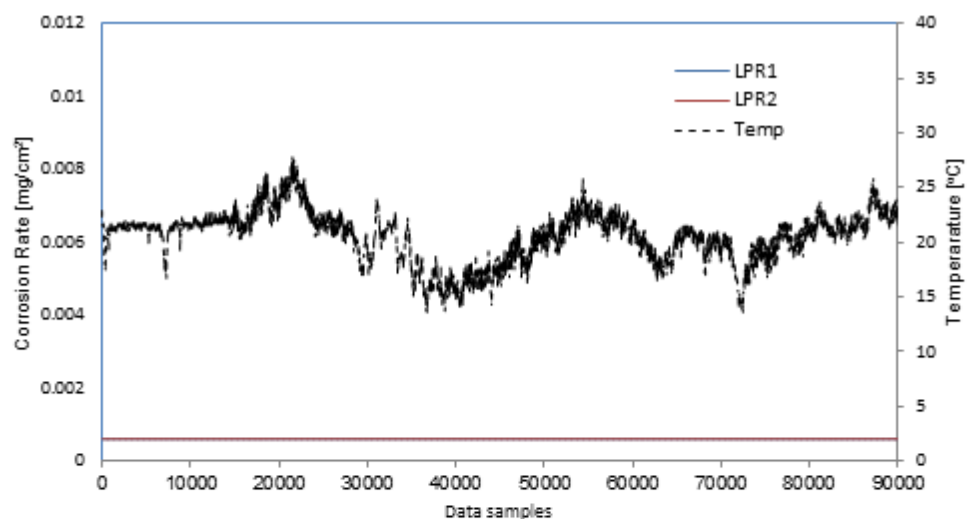


Figure 8: Results obtained from corrosion monitoring system applied on stationary vehicle A

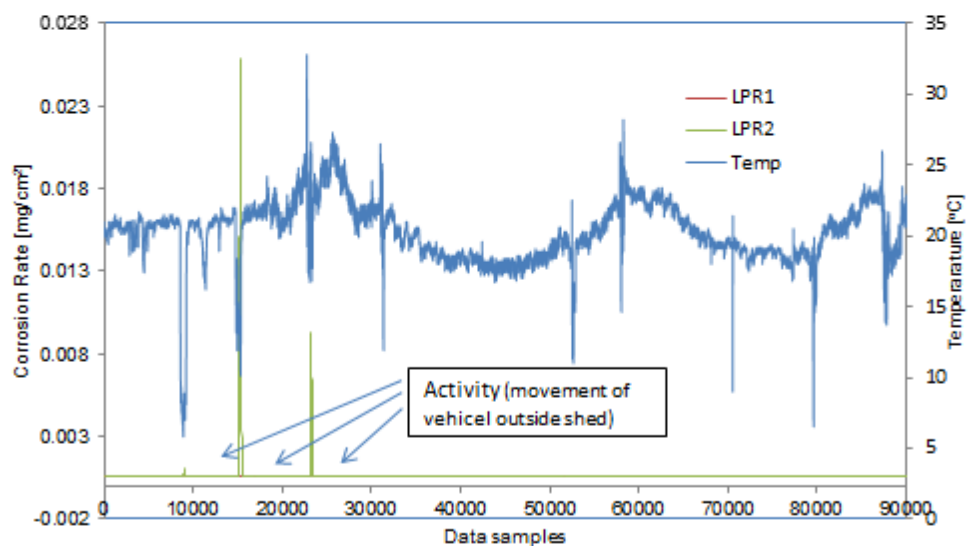


Figure 9: Results obtained from corrosion monitoring system applied on operating vehicle B

ACKNOWLEDGEMENT

This research is jointly funded by Defence Science and Technology Laboratory (DSTL), Ministry of Defence (MoD) and Bournemouth University UK. The authors acknowledge their support and contributions.

REFERENCES

1. NACE study estimates global cost of corrosion at \$2.5 trillion annually. 2016; Available from: <https://inspectioneering.com/news/2016-03-08/5202/nace-study-estimates-global-cost-of-corrosion-at-25-trillion-ann>.
2. Nazir, M.H., A. Saeed, and Z. Khan, A comprehensive predictive corrosion model incorporating varying environmental gas pollutants applied to wider steel applications. *Materials Chemistry and Physics*, 2017. **193**: p. 19-34.
3. *Anatom Structural Health Monitoring Solutions*. 2014; Available from: <https://iee-dataport.org/sites/default/files/analysis/27/IEEE%20Citation%20Guidelines.pdf>.
4. Brown, D.W., et al. Linear Polarization Resistance Sensor Using the Structure as a Working Electrode. in *Proceedings of the Second European Conference of the Prognostics and Health Management Society, Nantes, France*. 2014.
5. Clément, A., et al., Numerical study of the linear polarisation resistance technique applied to reinforced concrete for corrosion assessment. *European Journal of Environmental and Civil Engineering*, 2012. **16**(3-4): p. 491-504.
6. Stern, M. and A.L. Geary, *Electrochemical polarization I. A theoretical analysis of the shape of polarization curves*. *Journal of the electrochemical society*, 1957. **104**(1): p. 56-63.
7. Khan, Z.A., V. Chacko, and H. Nazir, A review of friction models in interacting joints for durability design. *Friction*, 2017.
8. Khan, Z.A., et al., Fabrication and characterisation of electrodeposited and magnetron-sputtered thin films. *International Journal of Computational Methods & Experimental Measurements*, 2015. **3**(2): p. 165-174.
9. Nazir, M. and Z. Khan, A review of theoretical analysis techniques for cracking and corrosive degradation of film-substrate systems. *Engineering Failure Analysis*, 2016.
10. Nazir, M., et al., A model for cathodic blister growth in coating degradation using mesomechanics approach. *Materials and Corrosion*, 2015.
11. Nazir, M., et al., A predictive model for life assessment of automotive exhaust mufflers subject to internal corrosion failure due to exhaust gas condensation. *Engineering Failure Analysis*, 2016. **63**: p. 43-60.
12. Nazir, M., et al., Modeling the Effect of Residual and Diffusion-Induced Stresses on Corrosion at the Interface of Coating and Substrate. *Corrosion*, 2015. **72**(4): p. 500-517.
13. Nazir, M., Z.A. Khan, and K. Stokes, A holistic mathematical modelling and simulation for cathodic delamination mechanism—a novel and an efficient approach. *Journal of Adhesion Science and Technology*, 2015. **29**(22): p. 2475-2513.
14. Nazir, M., Z.A. Khan, and K. Stokes, Analysing the coupled effects of compressive and diffusion induced stresses on the nucleation and propagation of circular coating blisters in the presence of micro-cracks. *Engineering Failure Analysis*, 2016. **70**: p. 1-15.
15. Nazir, M., Z.A. Khan, and K. Stokes, Optimisation of interface roughness and coating thickness to maximise coating-substrate adhesion—a failure prediction and reliability assessment modelling. *Journal of Adhesion Science and Technology*, 2015. **29**(14): p. 1415-1445.
16. Nazir, M., Z.A. Khan, and K. Stokes, A unified mathematical modelling and simulation for cathodic blistering mechanism incorporating diffusion and fracture mechanics concepts. *Journal of Adhesion Science and Technology*, 2015. **29**(12): p. 1200-1228.
17. Nazir, M.H. and Z. Khan, Maximising the interfacial toughness of thin coatings and substrate through optimisation of defined parameters. *International Journal of Computational Methods and Experimental Measurements*, 2015. **3**(4): p. 316-328.
18. Saeed, A., et al., Research Impact Of Conserving Large Military Vehicles Through A Sustainable Methodology. *International Journal of Heritage Architecture*, 2017. **1**(2): p. 267-274.
19. Saeed, A., Z.A. Khan, and M.H. Nazir, Time dependent surface corrosion analysis and modelling of automotive steel under a simplistic model of variations in environmental parameters. *Materials Chemistry and Physics*, 2016. **178**: p. 65-73.

20. Saeed, A., Z.A. Khan, and M.H. Nazir, *An optimised approach of protecting and sustaining large vehicle system*. Sustainability, 2015. 7(12): p. 16451-16464.
21. Carneiro, J., et al., *A real time scale measurement of residual stress evolution during coating deposition using electric extensometry*. Rev. Adv. Mater. Sci, 2004. 7: p. 32-40.

Appendix F: Simulation code

Simulation code for Optimal maintenance strategy

```
% Parameters for patch repair

Patch_A = zeros(500,1) ;
Patch_Sp_cost = zeros(500,1);
Patch_Cting_Cost = zeros(500,1) ;

Patch_A(1:500)= Patch_Area ;
Patch_Sp_cost(1:500) = Patch_Surfprep_cost;
Patch_Cting_Cost(1:500) = Patch_Coating_Cost ;

% Parameters for component repair
Comp_A = zeros(500,1) ;
Comp_A_recoat = zeros(500,1);
Comp_Sp_cost = zeros(500,1);
Comp_Cting_Cost = zeros(500,1) ;

Comp_A(1:500) = Comp_Area;
Comp_A_recoat(1:500) = Comp_Area_recoat;
Comp_Sp_cost(1:500) = Comp_Surfprep_cost;
Comp_Cting_Cost(1:500) = Comp_Coating_Cost;

% Parameters for complete repair
Complt_A = zeros(500,1) ;
Complt_A_struct = zeros(500,1) ;
Complt_Sp_cost = zeros(500,1);
Complt_Cting_Cost = zeros(500,1) ;

Complt_A(1:500) = Complt_Area ;
Complt_A_struct(1:500) = Complt_Area_struct;
Complt_Sp_cost(1:500) = Complt_Surfprep_cost;
Complt_Cting_Cost(1:500) = Complt_Coating_Cost ;

Annual_patch_cost = zeros(500,1);
Annual_Comp_cost = zeros(500,1);
Annual_Complt_cost = zeros(500,1);

ttp = 0;
ttc = 0;
```

Appendix F: Simulation code

```
ttcs = 0;

    if Maintenance_Strategy == 1
        Total_cost = zeros(Max_No_patch_repair,1);
        Patch = zeros(Max_No_patch_repair,1);
        XXX = No_Patch_repair;
        YYY = Max_No_patch_repair;
    end

    if Maintenance_Strategy == 2
        Total_cost = zeros(Max_No_comp_repair,1);
        No_Path_Component = zeros(Max_No_comp_repair,1);
        XXX = No_Component_repair;
        YYY = Max_No_comp_repair;
    end

    if Maintenance_Strategy == 3
        Total_cost = zeros(Max_No_complt_repair,1);
        No_Path_Component = zeros(Max_No_complt_repair,1);
        XXX = No_Complete_repair;
        YYY = Max_No_complt_repair;
    end

j=1;

Total_Time_months = 0;%%% tried./....
Time_Patch_repair_months = 0;
Time_Comp_repair_months = 0;

while XXX <= YYY      %%%% No_Patch_repair <= Max_No_patch_repair

    XXX
    YYY

    %% Calculations for time for all strategies

    Total_Time_months = Total_Time_years * 12;
    Time_Patch_repair_months = 12/No_Patch_repair;
    Time_Comp_repair_months = 12/No_Component_repair;
    %   No_Component_repair
    %   Time_Comp_repair_months

    Time_Complt_repair_months = 12/No_Complete_repair;

    Time_Patch_repair_year = Time_Patch_repair_months / 12;
    tp = Time_Patch_repair_year;

    Time_Comp_repair_year = Time_Comp_repair_months / 12;
    tc = Time_Comp_repair_year;

    Time_Complt_repair_year = Time_Complt_repair_months / 12;
    tcs = Time_Complt_repair_year;
```

Appendix F: Simulation code

```

        No_Patch_repair_counts      =      Total_Time_months      /
Time_Patch_repair_months;
        No_Comp_repair_counts      =      Total_Time_months      /
Time_Comp_repair_months;

        No_Complt_repair_counts      =      Total_Time_months      /
Time_Complt_repair_months;

if Maintenance_Strategy == 1

    for i = 1:No_Patch_repair_counts

        ttp = tp + ttp;
        cp = Patch_Sp_cost(i) + Patch_Cting_Cost(i);

        Annual_patch_cost(i) = ((Patch_A(i)) * cp * (ir*(1+ir)^ttp))/
((1+ir)^ttp-1);

        Patch_A(i)

        Annual_patch_cost(i)
    end
    ttp = 0;

end

if Maintenance_Strategy == 2
    for i = 1:No_Comp_repair_counts
        %i
        %No_Comp_repair_counts
        cc = (Comp_Sp_cost(i))*(Comp_A_recoat(i));
        ca = (Comp_A(i)* Comp_Cting_Cost(i) );

        ttc = tc + ttc;

        Annual_Comp_cost(i)      =      ((cc+ca)*(ir*(1+ir)^ttc))
/(((1+ir)^ttc)-1);
        % Annual_Comp_cost(i)
        % ttc
    end
    ttc = 0;

end

    for i = 1:No_Complt_repair_counts
```

Appendix F: Simulation code

```
        cs      =      (Complt_A_struct(i)*(Complt_Cting_Cost(i)      +
Complt_Sp_cost(i)));

        ttcs = tcs + ttcs;

        Annual_Complt_cost(i)= (cs *(ir*(1+ir)^ttcs))/(((1+ir)^ttcs)-
1);
        Annual_Complt_cost(i)
    end
    ttcs = 0;

    Total_Cost(j) = sum(Annual_patch_cost) + sum(Annual_Comp_cost) +
sum(Annual_Complt_cost);
    No_Path_Component(j) = XXX ;      %% Patch(j) = No_Patch_repair ;

    j = j+1;

    Annual_patch_cost(500:1) = 0;
    Annual_Comp_cost(500:1) = 0;
    Annual_Complt_cost(500:1) = 0;

    if Maintenance_Strategy == 1
        No_Patch_repair = No_Patch_repair + incr_patches;
        XXX = No_Patch_repair;
    end

    if Maintenance_Strategy == 2
        No_Component_repair = No_Component_repair + incr_comp;
        XXX = No_Component_repair;
    end

    if Maintenance_Strategy == 3
        No_Complete_repair = No_Complete_repair + incr_complt;
        XXX = No_Complete_repair;
    end

end

%Patch

%j

Save_Patch_Values = zeros(10:1);

Save_Component_Values = zeros(10:1);

%Annual_patch_cost

if Maintenance_Strategy == 1
    Max_Value = max(Total_Cost(1:j-1));
```

Appendix F: Simulation code

```
Save_Patch_Values(1:10) = Total_Cost(1:j-1)/MAx_Value;
Save_Patch_Values

plot(Total_Cost(1:j-1)/MAx_Value);
%plot(No_Path_Component(1:j-1),Total_Cost(1:j-1));
end

if Maintenance_Strategy == 2
Total_Cost(1:10) =sum(Total_Cost());

Save_Component_Values(1:10) = Total_Cost(1:10)/MAx_Value;
plot(Total_Cost(1:10)/MAx_Value);
%plot(No_Path_Component(1:j-1),Total_Cost(1:j-1));
end

if Maintenance_Strategy == 3
plot(Total_Cost(1:j-1));
%plot(No_Path_Component(1:j-1),Total_Cost(1:j-1));
end

hold on

Total_Cost(1:10) = 0;
end
hold on
```

Appendix G: Data sheet

SPECIFICATIONS

NI cRIO-9063

Embedded Real-Time Controller with Reconfigurable FPGA for C Series Modules

This document lists the specifications for the NI cRIO-9063. The following specifications are typical for the -20 °C to 55 °C operating temperature range unless otherwise noted.



Caution Do not operate the cRIO-9063 in a manner not specified in this document. Product misuse can result in a hazard. You can compromise the safety protection built into the product if the product is damaged in any way. If the product is damaged, return it to NI for repair.

Processor

Type	Xilinx Zynq-7000, XC7Z020 All Programmable SoC
Architecture	ARM Cortex-A9
Speed	667 MHz
Cores	2
Flash reboot endurance ¹	100,000 cycles

Operating System



Note For minimum software support information, visit ni.com/info and enter the Info Code `swsupport`.

Supported operating system	NI Linux Real-Time (32-bit)
----------------------------	-----------------------------

¹ You can increase the flash reboot endurance value by performing field maintenance on the device. If you expect that your application may exceed the maximum cycle count listed in this document, contact NI support for information about how to increase the reboot endurance value.

Software requirements

Application software	
LabVIEW	LabVIEW 2014 SP1 or later, LabVIEW Real-Time Module 2014 SP1 or later, LabVIEW FPGA Module 2014 SP1 or later ²
Driver software	NI-RIO Device Drivers 14.5 or later

Memory

Nonvolatile memory ³	512 MB
Volatile memory (DRAM)	256 MB

Network

Network interface	10Base-T, 100Base-T, 1000Base-T Ethernet
Compatibility	IEEE 802.3
Communication rates	10 Mbps, 100 Mbps, 1,000 Mbps auto-negotiated, half/full-duplex
Maximum cabling distance	100 m/segment

Internal Real-Time Clock

Accuracy	5 ppm
----------	-------

USB Ports

USB device port	
Type	USB 2.0 Hi-Speed, with standard B connector
Maximum data rate	480 Mbps
USB host port	
Type	USB 2.0 Hi-Speed, with standard A connector
Maximum data rate	480 Mbps

² LabVIEW FPGA Module is not required when using Scan Interface mode. To program the user-accessible FPGA on the cRIO-9063, LabVIEW FPGA Module is required.

³ Formatted capacity of nonvolatile memory may be slightly less than this value.

Reconfigurable FPGA

Type	Xilinx Zynq-7000, XC7Z020 All Programmable SoC
Number of logic cells	85,000
Number of flip-flops	106,400
Number of 6-input LUTs	53,200
Number of DSP slices (18 × 25 multipliers)	220
Available block RAM	4480 kbits
Number of DMA channels	16
Number of logical interrupts	32

Battery



Note The battery is not user-replaceable. Refer to the [Battery Replacement and Disposal](#) section for information about replacing the battery.



Note Battery life may drop dramatically in extreme temperatures.

Typical battery life with power applied to power connector	10 years
Typical battery life in storage at 55 °C	5 years

Power Requirements

Voltage input range	9 VDC to 30 VDC
Reverse-voltage protection	30 VDC maximum
Maximum power input, with four C Series modules	18 W
Maximum power input, without C Series modules	14 W

Physical Characteristics

If you need to clean the cRIO-9063, wipe it with a dry towel.



Tip For two-dimensional drawings and three-dimensional models of the cRIO-9063, visit ni.com/dimensions and search by module number.

Weight (unloaded)	683 g (24.10 oz)
Dimensions (unloaded)	178.1 mm × 87.3 mm × 64.3 mm (7.01 in. × 3.44 in. × 2.63 in.)
Screw-terminal wiring	
Gauge	0.2 mm ² to 2.1 mm ² (24 AWG to 14 AWG) copper conductor wire
Wire strip length	6 mm (0.24 in.) of insulation stripped from the end
Temperature rating	85 °C
Torque for screw terminals	0.20 N · m to 0.25 N · m (1.8 lb · in. to 2.2 lb · in.)
Wires per screw terminal	One wire per screw terminal
Connector securement	
Securement type	Screw flanges provided
Torque for screw flanges	0.3 N · m to 0.4 N · m (2.7 lb · in. to 3.5 lb · in.)

Safety Voltages

Connect only voltages that are within the following limits:

V terminal to C terminal	30 VDC max, Measurement Category I
--------------------------	------------------------------------

Measurement Category I is for measurements performed on circuits not directly connected to the electrical distribution system referred to as *MAINS* voltage. MAINS is a hazardous live electrical supply system that powers equipment. This category is for measurements of voltages from specially protected secondary circuits. Such voltage measurements include signal levels, special equipment, limited-energy parts of equipment, circuits powered by regulated low-voltage sources, and electronics.



Caution Do not connect the cRIO-9063 to signals or use for measurements within Measurement Categories II, III, or IV.



Note Measurement Categories CAT I and CAT O are equivalent. These test and measurement circuits are not intended for direct connection to the MAINS building installations of Measurement Categories CAT II, CAT III, or CAT IV.

Safety and Hazardous Locations Standards

This product is designed to meet the requirements of the following electrical equipment safety standards for measurement, control, and laboratory use:

- IEC 61010-1, EN 61010-1
- UL 61010-1, CSA 61010-1
- EN 60079-0:2012, EN 60079-15:2010
- IEC 60079-0: Ed 6, IEC 60079-15: Ed 4
- UL 60079-0: Ed 5, UL 60079-15: Ed 3
- CSA 60079-0:2011, CSA 60079-15:2012



Note For UL and other safety certifications, refer to the product label or the [Online Product Certification](#) section.

Electromagnetic Compatibility

This product meets the requirements of the following EMC standards for electrical equipment for measurement, control, and laboratory use:

- EN 61326-1 (IEC 61326-1): Class A emissions; Industrial immunity
- EN 55011 (CISPR 11): Group 1, Class A emissions
- EN 55022 (CISPR 22): Class A emissions
- EN 55024 (CISPR 24): Immunity
- AS/NZS CISPR 11: Group 1, Class A emissions
- AS/NZS CISPR 22: Class A emissions
- FCC 47 CFR Part 15B: Class A emissions
- ICES-001: Class A emissions



Note In the United States (per FCC 47 CFR), Class A equipment is intended for use in commercial, light-industrial, and heavy-industrial locations. In Europe, Canada, Australia and New Zealand (per CISPR 11) Class A equipment is intended for use only in heavy-industrial locations.



Note Group 1 equipment (per CISPR 11) is any industrial, scientific, or medical equipment that does not intentionally generate radio frequency energy for the treatment of material or inspection/analysis purposes.



Note For EMC declarations and certifications, and additional information, refer to the [Online Product Certification](#) section.

CE Compliance

This product meets the essential requirements of applicable European Directives, as follows:

- 2014/35/EU; Low-Voltage Directive (safety)
- 2014/30/EU; Electromagnetic Compatibility Directive (EMC)
- 94/9/EC; Potentially Explosive Atmospheres (ATEX)

Online Product Certification

Refer to the product Declaration of Conformity (DoC) for additional regulatory compliance information. To obtain product certifications and the DoC for this product, visit ni.com/certification, search by model number or product line, and click the appropriate link in the Certification column.

Hazardous Locations

U.S. (UL)	Class I, Division 2, Groups A, B, C, D, T4; Class I, Zone 2, AEx nA IIC T4
Canada (C-UL)	Class I, Division 2, Groups A, B, C, D, T4; Class I, Zone 2, Ex nA IIC T4
Europe (ATEX) and International (IECEx)	Ex nA IIC T4 Gc

Environmental

Temperature (IEC 60068-2-1 and IEC 60068-2-2)

Operating	-20 °C to 55 °C
Storage	-40 °C to 85 °C



Caution Failure to follow the mounting instructions in the user manual can cause temperature derating. Visit ni.com/info and enter Info Code `criomounting` for more information about mounting configurations and temperature derating.

Ingress protection	IP40
Operating humidity (IEC 60068-2-56)	10% RH to 90% RH, noncondensing
Storage humidity (IEC 60068-2-56)	5% RH to 95% RH, noncondensing
Pollution Degree (IEC 60664)	2
Maximum altitude	5,000

Indoor use only.⁴

Shock and Vibration

To meet these specifications, you must mount the cRIO-9063 system directly on a flat, rigid surface as described in the user manual, affix ferrules to the ends of the terminal wires, install an SD card cover (SD Door Kit, 783660-01), and use retention accessories for the USB host ports (NI Industrial USB Extender Cable, 152166-xx), USB device port (NI Locking USB Cable, 157788-01), and mini DisplayPort connector (NI Retention Accessory for Mini DisplayPort, 156866-01). All cabling should be strain-relieved near input connectors. Take care to not directionally bias cable connectors within input connectors when applying strain relief.

Operating vibration

Random (IEC 60068-2-64)	5 g _{rms} , 10 Hz to 500 Hz
Sinusoidal (IEC 60068-2-6)	5 g, 10 Hz to 500 Hz
Operating shock (IEC 60068-2-27)	30 g, 11 ms half sine; 50 g, 3 ms half sine; 18 shocks at 6 orientations

Environmental Management

NI is committed to designing and manufacturing products in an environmentally responsible manner. NI recognizes that eliminating certain hazardous substances from our products is beneficial to the environment and to NI customers.

For additional environmental information, refer to the *Minimize Our Environmental Impact* web page at ni.com/environment. This page contains the environmental regulations and directives with which NI complies, as well as other environmental information not included in this document.

Waste Electrical and Electronic Equipment (WEEE)



EU Customers At the end of the product life cycle, all NI products must be disposed of according to local laws and regulations. For more information about how to recycle NI products in your region, visit ni.com/environment/weee.

Battery Replacement and Disposal



Battery Directive This device contains a long-life coin cell battery. If you need to replace it, use the Return Material Authorization (RMA) process or contact an authorized National Instruments service representative. For more information about compliance with the EU Battery Directive 2006/66/EC about Batteries and

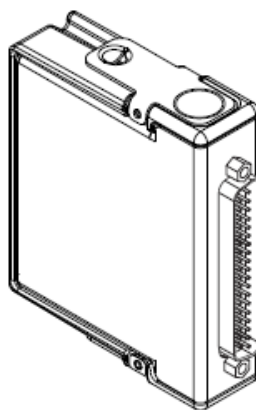
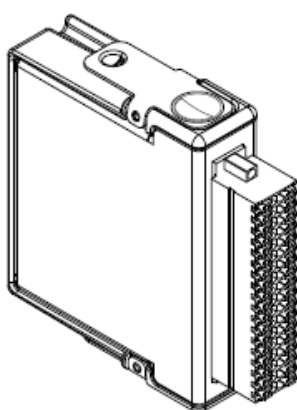
⁴ Use NI 9917 and NI 9918 industrial enclosures to protect the device in harsh, dirty, or wet environments.

Appendix H: Data sheet

DATASHEET

NI 9207

16 AI, ± 20 mA/ ± 10 V, 24 Bit, 500 S/s Aggregate



- 8 current and 8 voltage inputs, 500 S/s
- ± 20 mA current inputs, ± 10 V voltage inputs, 24-bit resolution
- High-Resolution Mode with 50/60 Hz rejection
- 250 Vrms, CAT II, channel-to-earth isolation (spring terminal); 60 VDC, CAT I, channel-to-earth isolation (DSUB)
- DSUB or spring-terminal connectivity
- -40 °C to 70 °C operating range, 5 g vibration, 50 g shock

The NI 9207 combination voltage and current input C Series module has eight channels of ± 20 mA input and eight channels of ± 10 V input with built-in 50/60 Hz rejection for noise rejection.

Designed with industrial systems in mind, the NI 9207 combines the two most common inputs to reduce the overall number of modules you need. A system that uses fewer modules has the benefit of leaving slots open for other measurement types or reducing the overall cost and size of the system. The NI 9207 has a standard 37-pin DSUB and 36-pin spring terminal connections for use with cables and connector blocks.

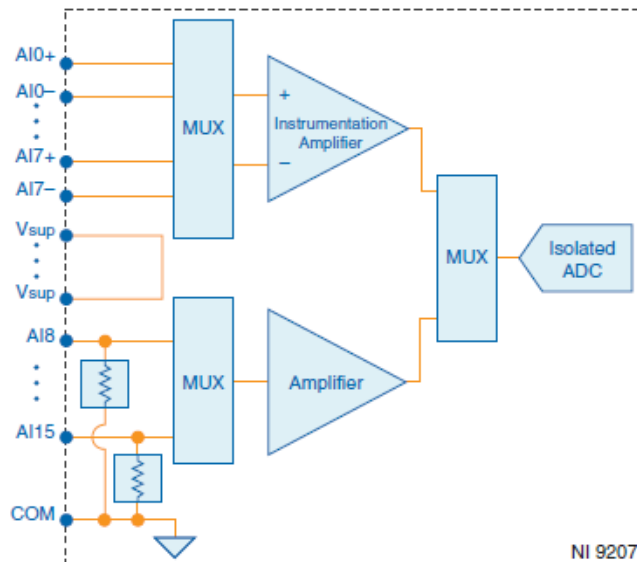




NI LabVIEW Real-Time Module

- Design deterministic real-time applications with LabVIEW graphical programming
- Download to dedicated NI or third-party hardware for reliable execution and a wide selection of I/O
- Take advantage of built-in PID control, signal processing, and analysis functions
- Automatically take advantage of multicore CPUs or set processor affinity manually
- Take advantage of real-time OS, development and debugging support, and board support
- Purchase individually or as part of a LabVIEW suite

Circuitry



The input signals are scanned, amplified, conditioned, and then sampled by a single 24-bit ADC.

NI 9207 Specifications

The following specifications are typical for the range -40 °C to 70 °C unless otherwise noted. All voltages are relative to COM unless otherwise noted.



Caution Do not operate the NI 9207 in a manner not specified in this document. Product misuse can result in a hazard. You can compromise the safety protection built into the product if the product is damaged in any way. If the product is damaged, return it to NI for repair.

Input Characteristics

Number of channels	16 analog input channels: 8 voltage and 8 current
ADC resolution	24 bits
Type of ADC	Delta-Sigma
Sampling mode	Scanned
Input range	
Voltage channels	
Minimum	± 10.2 V
Typical	± 10.4 V
Current channels	
Minimum	± 21.5 mA
Typical	± 22.0 mA
Maximum working voltage for analog inputs (signal voltage + common mode voltage), voltage channels only	Each channel must remain within ± 10.2 V of common
Conversion time (per channel)	
High-Resolution Mode	52 ms
High-Speed Mode	2 ms
Overvoltage protection, channel-to-COM, all channels	± 30 V maximum on one channel at a time
Vsup pins, current channels only	
Current	2 A maximum
Voltage	0 to 30 V maximum
Input impedance	
Voltage channels	>1 G Ω
Current channels	85 Ω

Table 1. Accuracy

Calibrated Measurement Conditions	Channels	Percent of Reading (Gain Error)	Percent of Range ¹ (Offset Error)
Maximum (-40 °C to 70 °C)	Voltage channels	±0.52%	±0.04%
	Current channels	±0.87%	±0.05%

Input noise

Voltage channels

High-Resolution Mode	16 μ Vrms
----------------------	---------------

High-Speed Mode	80 μ Vrms
-----------------	---------------

Current channels

High-Resolution Mode	50 nArms
----------------------	----------

High-Speed Mode	200 nArms
-----------------	-----------

Stability

Voltage channels

Gain drift	±21 ppm/°C
------------	------------

Offset drift	±14 μ V/°C
--------------	----------------

Current channels

Gain drift	±43 ppm/°C
------------	------------

Offset drift	±30 nA/°C
--------------	-----------

CMRR (f_{in} = 0 Hz to 60 Hz), voltage channels only	86 dB
---	-------

CMRR, channel-to-earth ground (50/60 Hz)²

High-Resolution Mode	160 dB
----------------------	--------

High-Speed Mode	120 dB
-----------------	--------

NMRR (High-Resolution Mode only)

50 Hz	66 dB
-------	-------

60 Hz	68 dB
-------	-------

¹ Range equals 10.4 V for voltage channels and 22.0 mA for current channels.

² Voltage channel of NI 9207 with spring terminal only.

Power Requirements

Power consumption from chassis	
Active mode	295 mW maximum
Sleep mode	25 μ W maximum
Thermal dissipation (at -40 °C)	
Active mode	0.75 W maximum
Sleep mode	0.59 W maximum

Physical Characteristics

If you need to clean the module, wipe it with a dry towel.



Tip For two-dimensional drawings and three-dimensional models of the C Series module and connectors, visit ni.com/dimensions and search by module number.

Push-in spring-terminal wiring	
Gauge	0.14 mm ² to 1.5 mm ² (26 AWG to 16 AWG) copper conductor wire
Wire strip length	10 mm (0.394 in.) of insulation stripped from the end
Temperature rating	90 °C minimum
Wires per spring terminal	One wire per spring terminal; two wires per spring terminal using a 2-wire ferrule
Ferrules	0.14 mm ² to 1.5 mm ²
Connector securement	
Securement type	Screw flanges provided
Torque for screw flanges	0.2 N · m (1.80 lb · in.)
Weight	
NI 9207 with spring terminal	161 g (5.7 oz)
NI 9207 with DSUB	144 g (5.1 oz)

NI 9207 with Spring Terminal Safety Voltages

Connect only voltages that are within the following limits:

Isolation	
Channel-to-channel	None

Appendix I: Data sheet

DATASHEET



NI 9217

4 RTD, 0 Ω to 400 Ω , 24 Bit, 400 S/s Aggregate, PT100



- Screw-terminal connectivity
- 50 Hz/60 Hz noise rejection
- 250 Vrms, CAT II, channel-to-earth isolation

The NI 9217 is an RTD analog input module for NI CompactDAQ and CompactRIO systems. The NI 9217 features four channels and 24 bits of resolution for PT100 RTD measurements. The NI 9217, compatible with 3- and 4-wire RTD measurements, automatically detects the type of RTD (3- or 4-wire) connected to the channel and configures each channel for the appropriate mode. The module provides 1 mA of current excitation per channel and has less than a 1 $^{\circ}\text{C}$ accuracy error over its entire operating temperature range. NI provides calibration services for the NI 9217.

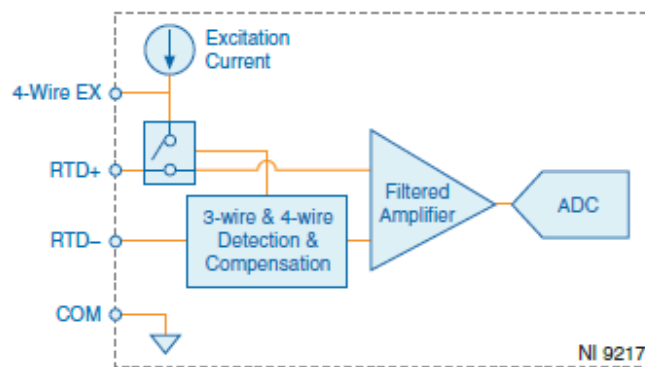
	Kit Contents <ul style="list-style-type: none">• NI 9217• NI 9217 Getting Started Guide
	Accessories <ul style="list-style-type: none">• NI 9939 Backshell Connector Kit• NI 9975 Screw-Terminal Block



NI LabVIEW Real-Time Module

- Design deterministic real-time applications with LabVIEW graphical programming
- Download to dedicated NI or third-party hardware for reliable execution and a wide selection of I/O
- Take advantage of built-in PID control, signal processing, and analysis functions
- Automatically take advantage of multicore CPUs or set processor affinity manually
- Take advantage of real-time OS, development and debugging support, and board support
- Purchase individually or as part of a LabVIEW suite

Input Circuitry



- RTD channels share a common ground that is isolated from other modules in the system.
- Each RTD channel is filtered and then sampled by a 24-bit analog-to-digital converter (ADC).

NI 9217 Specifications

The following specifications are typical for the range -40 °C to 70 °C unless otherwise noted.

All specifications given in °C are specific to 100 Ω platinum RTDs.



Caution Do not operate the NI 9217 in a manner not specified in this document. Product misuse can result in a hazard. You can compromise the safety protection built into the product if the product is damaged in any way. If the product is damaged, return it to NI for repair.

Input Characteristics

Number of channels	4 analog input channels
ADC resolution	24 bits
Type of ADC	Delta-sigma
Sampling mode	Scanned
Measurement range	
Temperature	-200 °C to 850 °C
Resistance	0 Ω to 400 Ω
Common-mode range	
COM-to-earth ground	± 250 Vrms
Channel-to-COM	50 mV
Conversion time	
High-resolution mode	200 ms per channel, 800 ms total for all channels
High-speed mode	2.5 ms per channel, 10 ms total for all channels

Temperature accuracy (including noise)¹, 4-wire mode

Measured Value	Typical (25 °C)	Maximum (-40 to 70 °C)
-200 °C to 150 °C	0.15 °C	0.35 °C
150 °C to 850 °C	0.20 °C	1.0 °C

Temperature accuracy (including noise)¹, 3-wire mode

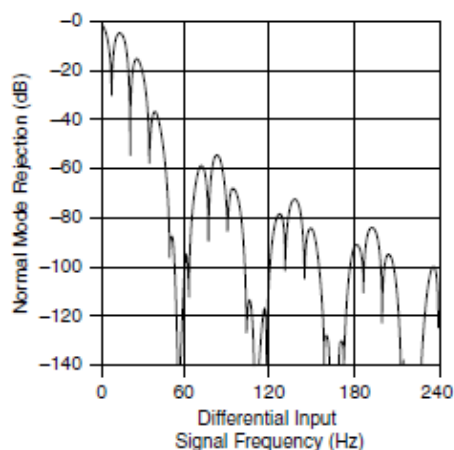
Measured Value	Typical (25 °C)	Maximum (-40 to 70 °C)
-200 °C to 150 °C	0.20 °C	0.50 °C
150 °C to 850 °C	0.30 °C	1.0 °C

Noise

High-resolution mode	0.003 °C
High-speed mode	0.02 °C

¹ For high-speed mode, add a 0.1 °C error.

Excitation current	1 mA per channel
Noise rejection	
Normal mode (50/60 Hz)	
High-resolution mode	85 dB minimum
High-speed mode	None
Common-mode rejection, channel to earth ground (50/60 Hz)	
High-resolution mode	170 dB minimum
High-speed mode	155 dB
Input bandwidth (high-resolution mode)	3.3 Hz
High-resolution filter response ^{2, 3}	



Overvoltage protection	± 30 V between inputs
MTBF	891,597 hours at 25 °C; Bellcore Issue 2, Method 1, Case 3, Limited Part Stress Method

Power Requirements

Power consumption from chassis	
Active mode	350 mW maximum
Sleep mode	1 mW maximum

² This image is provided courtesy of Linear Technology Corp.

³ High-speed filter response has the same characteristics as the high-resolution filter response except that the first notch is at 14 kHz.

Thermal dissipation (at 70 °C)

Active mode	350 mW maximum
Sleep mode	1 mW maximum

Physical Characteristics

Screw-terminal wiring

Gauge	0.05 mm ² to 1.5 mm ² (30 AWG to 14 AWG) copper conductor wire
Wire strip length	6 mm (0.24 in.) of insulation stripped from the end
Temperature rating	90 °C minimum
Torque for screw terminals	0.22 N · m to 0.25 N · m (1.95 lb · in. to 2.21 lb · in.)
Wires per screw terminal	One wire per screw terminal; two wires per screw terminal using a 2-wire ferrule
Ferrules	0.25 mm ² to 1.5 mm ²

Connector securement

Securement type	Screw flanges provided
Torque for screw flanges	0.2 N · m (1.80 lb · in.)

Safety

Safety Voltages

Connect only voltages that are within the following limits.

Maximum Voltage

Connect only voltages that are within the following limits.⁴

All terminals-to-COM	±30 V
----------------------	-------

Isolation Voltages

Channel-to-channel	None
--------------------	------

⁴ The maximum voltage that can be applied between any channel or Vsup terminal and a COM terminal without damaging the module or other devices.

Channel-to-earth ground

Continuous	
up to 2,000 m	250 Vrms, Measurement Category II
up to 5,000 m	60 VDC, Measurement Category I
Withstand	
up to 2,000 m	2,300 Vrms, verified by a 5 s dielectric withstand test
up to 5,000 m	1,000 Vrms, verified by a 5 s dielectric withstand test

Measurement Category II is for measurements performed on circuits directly connected to the electrical distribution system. This category refers to local-level electrical distribution, such as that provided by a standard wall outlet, for example, 115 V for U.S. or 230 V for Europe.



Note Measurement Categories CAT I and CAT O are equivalent. These test and measurement circuits are not intended for direct connection to the MAINS building installations of Measurement Categories CAT II, CAT III, or CAT IV.



Caution Do not connect the NI 9217 to signals or use for measurements within Measurement Categories III or IV.

Hazardous Locations

U.S. (UL)	Class I, Division 2, Groups A, B, C, D, T4; Class I, Zone 2, AEx nA IIC T4
Canada (C-UL)	Class I, Division 2, Groups A, B, C, D, T4; Class I, Zone 2, Ex nA IIC T4
Europe (ATEX) and International (IECEx)	Ex nA IIC T4 Gc

Safety and Hazardous Locations Standards

This product is designed to meet the requirements of the following electrical equipment safety standards for measurement, control, and laboratory use:

- IEC 61010-1, EN 61010-1
- UL 61010-1, CSA 61010-1
- EN 60079-0:2012, EN 60079-15:2010
- IEC 60079-0: Ed 6, IEC 60079-15; Ed 4
- UL 60079-0; Ed 5, UL 60079-15; Ed 3
- CSA 60079-0:2011, CSA 60079-15:2012



Note For UL and other safety certifications, refer to the product label or the [Online Product Certification](#) section.

Electromagnetic Compatibility

This product meets the requirements of the following EMC standards for electrical equipment for measurement, control, and laboratory use:

- EN 61326-1 (IEC 61326-1): Class A emissions; Industrial immunity
- EN 55011 (CISPR 11): Group 1, Class A emissions
- CE, C-Tick, ICES, and FCC Part 15; Class A emissions



Note For EMC declarations and certifications, and additional information, refer to the [Online Product Certification](#) section.

CE Compliance

This product meets the essential requirements of applicable European Directives, as follows:

- 2014/35/EU; Low-Voltage Directive (safety)
- 2014/30/EU; Electromagnetic Compatibility Directive (EMC)
- 94/9/EC; Potentially Explosive Atmospheres (ATEX)

Online Product Certification

Refer to the product Declaration of Conformity (DoC) for additional regulatory compliance information. To obtain product certifications and the DoC for this product, visit ni.com/certification, search by model number or product line, and click the appropriate link in the Certification column.

Shock and Vibration

To meet these specifications, you must panel mount the system.

Operating vibration

Random (IEC 60068-2-64)	5 g _{rms} , 10 Hz to 500 Hz
Sinusoidal (IEC 60068-2-6)	5 g, 10 Hz to 500 Hz
Operating shock (IEC 60068-2-27)	30 g, 11 ms half sine; 50 g, 3 ms half sine; 18 shocks at 6 orientations

Environmental

Refer to the manual for the chassis you are using for more information about meeting these specifications.

Operating temperature (IEC 60068-2-1, IEC 60068-2-2)	-40 °C to 70 °C
Storage temperature (IEC 60068-2-1, IEC 60068-2-2)	-40 °C to 85 °C

Ingress protection (with power plug attached)	IP 40
Operating humidity (IEC 60068-2-78)	10% RH to 90% RH, noncondensing
Storage humidity (IEC 60068-2-78)	5% RH to 95% RH, noncondensing
Pollution Degree	2
Maximum altitude	5,000 m

Indoor use only.

Environmental Management

NI is committed to designing and manufacturing products in an environmentally responsible manner. NI recognizes that eliminating certain hazardous substances from our products is beneficial to the environment and to NI customers.

For additional environmental information, refer to the *Minimize Our Environmental Impact* web page at ni.com/environment. This page contains the environmental regulations and directives with which NI complies, as well as other environmental information not included in this document.

Waste Electrical and Electronic Equipment (WEEE)



EU Customers At the end of the product life cycle, all NI products must be disposed of according to local laws and regulations. For more information about how to recycle NI products in your region, visit ni.com/environment/weee.

电子信息产品污染控制管理办法（中国 RoHS）



中国客户 National Instruments 符合中国电子信息产品中限制使用某些有害物质指令 (RoHS)。关于 National Instruments 中国 RoHS 合规性信息, 请登录 ni.com/environment/rohs_china。(For information about China RoHS compliance, go to ni.com/environment/rohs_china.)

Calibration

You can obtain the calibration certificate and information about calibration services for the NI 9217 at ni.com/calibration.

Calibration interval	1 year
----------------------	--------

Appendix J: Data sheet

Hardware Manual – Operation Instructions, Safety Guidelines and Specifications

SEA 9741

3G/GPS Communication Module for CompactRIO™



Part No.: 60000066



Doc. No.:
HB/SEA 9741 Hardware Manual/2.0/Nov-2016

Prerequisites

The SEA 9741 module is shipped with the following accessory:

- Printed 'Hardware Manual - Operation Instructions, Safety Guidelines and Specifications'

In order to operate the module further components are required (not shipped with the module):

- Power cable for external power supply, order no.: 61000011, mandatory for operation
- Ethernet bridge cable, order no.: 61000051, mandatory for operation
- Software driver
Can be downloaded from the support area on <http://www.sea-gmbh.com>.
- CompactRIO system from National Instruments
- Power supply with 7 to 30VDC and 2 A
- GSM antenna
Is required to use the GSM related features. Matching GSM antennas can be purchased separately from S.E.A. Please refer to our web shop.

Connecting SEA 9741

The SEA 9741 module provides sockets for one GPS (3) and one GSM antenna (5), one Ethernet port (7), a reset switch (6), a connector for an external GPS receiver (4) and a connector for an external power supply (2). Four LEDs (1) show the current state of the module, refer to Fig. *Front side* on the right.

On the back side of the module there is a SIM card slot and a micro SD card slot, refer to Fig. *Insert SIM* on page 17. The micro SD card slot is designated for special purposes and shall not be used for regular operation.

Finally, on the side with the imprint a set of DIP switches is available. With these switches the behaviour of the module can be controlled, refer to Fig. *DIP Switches* on page 18.


 Only one SEA 9741 module can be operated within a single CompactRIO system. It is not possible to operate more than one SEA 9741 module inside a single CompactRIO system.



Fig. 1: Front side



Power Requirements ²		
Operating Voltage Typical	VDC	7 to 30 12
Operating Current Typical Peak Sleep Mode	mA	173 245 2
Physical Characteristics		
Weight	g	ca. 200
Dimensions	mm	80 x 23 x 88
Environmental Conditions		
Operating Temperature	°C	-30 to +70
Storage Temperature	°C	-40 to +85
Ingress Protection ¹		IP 30
Operating humidity	% ²	10 to 90

² The exact power consumption is dependant on the active communication standard as well as the antenna and reception quality.

¹ with connected power cable

² RH, noncondensing



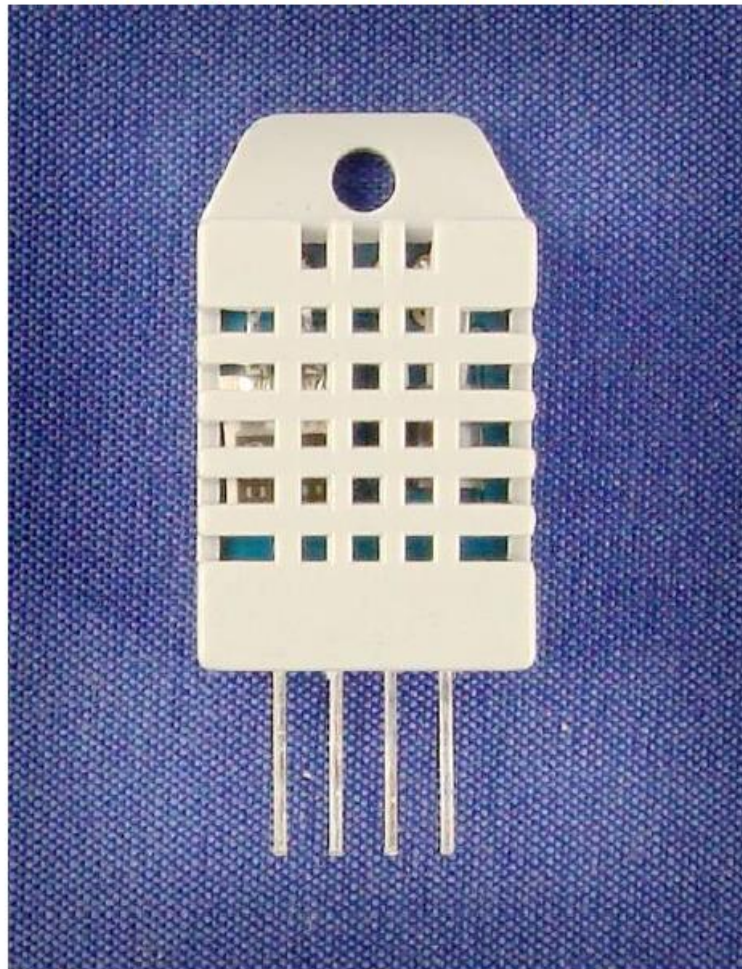
Appendix K: Data sheet

Aosong Electronics Co.,Ltd

Your specialist in innovating humidity & temperature sensor

Digital-output relative humidity & temperature sensor/module

DHT22 (DHT22 also named as AM2302)



Capacitive-type humidity and temperature module/sensor

1

Thomas Liu (Business Manager)

Email: thomasliu198518@yahoo.com.cn

Aosong Electronics Co.,Ltd

Your specialist in innovating humidity & temperature sensors

1. Feature & Application:

- * Full range temperature compensated
- * Relative humidity and temperature measurement
- * Calibrated digital signal
- * Outstanding long-term stability
- * Extra components not needed
- * Long transmission distance
- * Low power consumption
- * 4 pins packaged and fully interchangeable

2. Description:

DHT22 output calibrated digital signal. It utilizes exclusive digital-signal-collecting-technique and humidity sensing technology, assuring its reliability and stability. Its sensing elements is connected with 8-bit single-chip computer.

Every sensor of this model is temperature compensated and calibrated in accurate calibration chamber and the calibration-coefficient is saved in type of programme in OTP memory, when the sensor is detecting, it will cite coefficient from memory.

Small size & low consumption & long transmission distance(20m) enable DHT22 to be suited in all kinds of harsh application occasions.

Single-row packaged with four pins, making the connection very convenient.

3. Technical Specification:

Model	DHT22
Power supply	3.3-6V DC
Output signal	digital signal via single-bus
Sensing element	Polymer capacitor
Operating range	humidity 0-100%RH; temperature -40~80Celsius
Accuracy	humidity +2%RH(Max +5%RH); temperature <+-0.5Celsius
Resolution or sensitivity	humidity 0.1%RH; temperature 0.1Celsius
Repeatability	humidity +1%RH; temperature +0.2Celsius
Humidity hysteresis	+0.3%RH
Long-term Stability	+0.5%RH/year
Sensing period	Average: 2s
Interchangeability	fully interchangeable
Dimensions	small size 14*18*5.5mm; big size 22*28*5mm

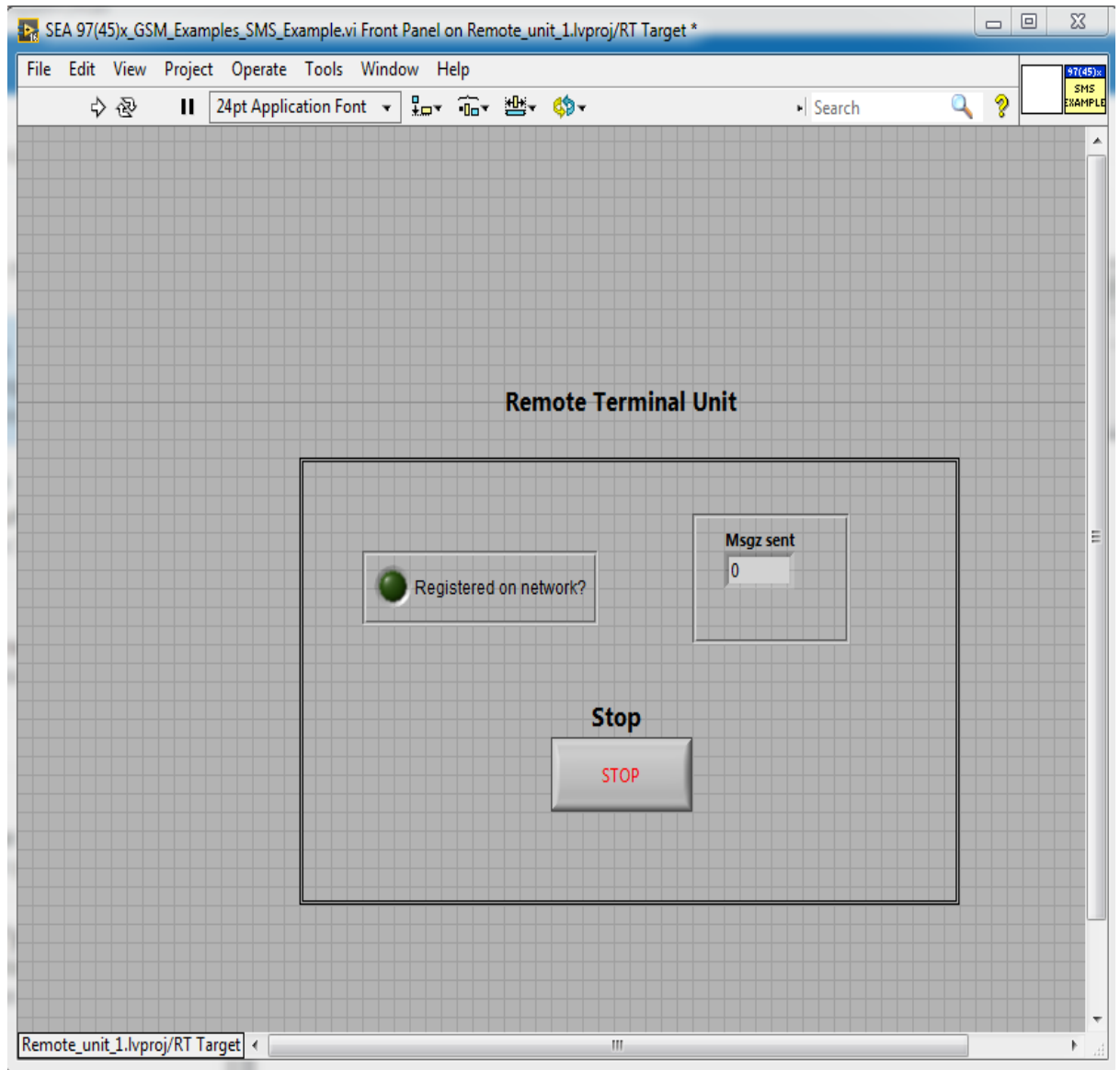
4. Dimensions: (unit---mm)

1) Small size dimensions: (unit---mm)

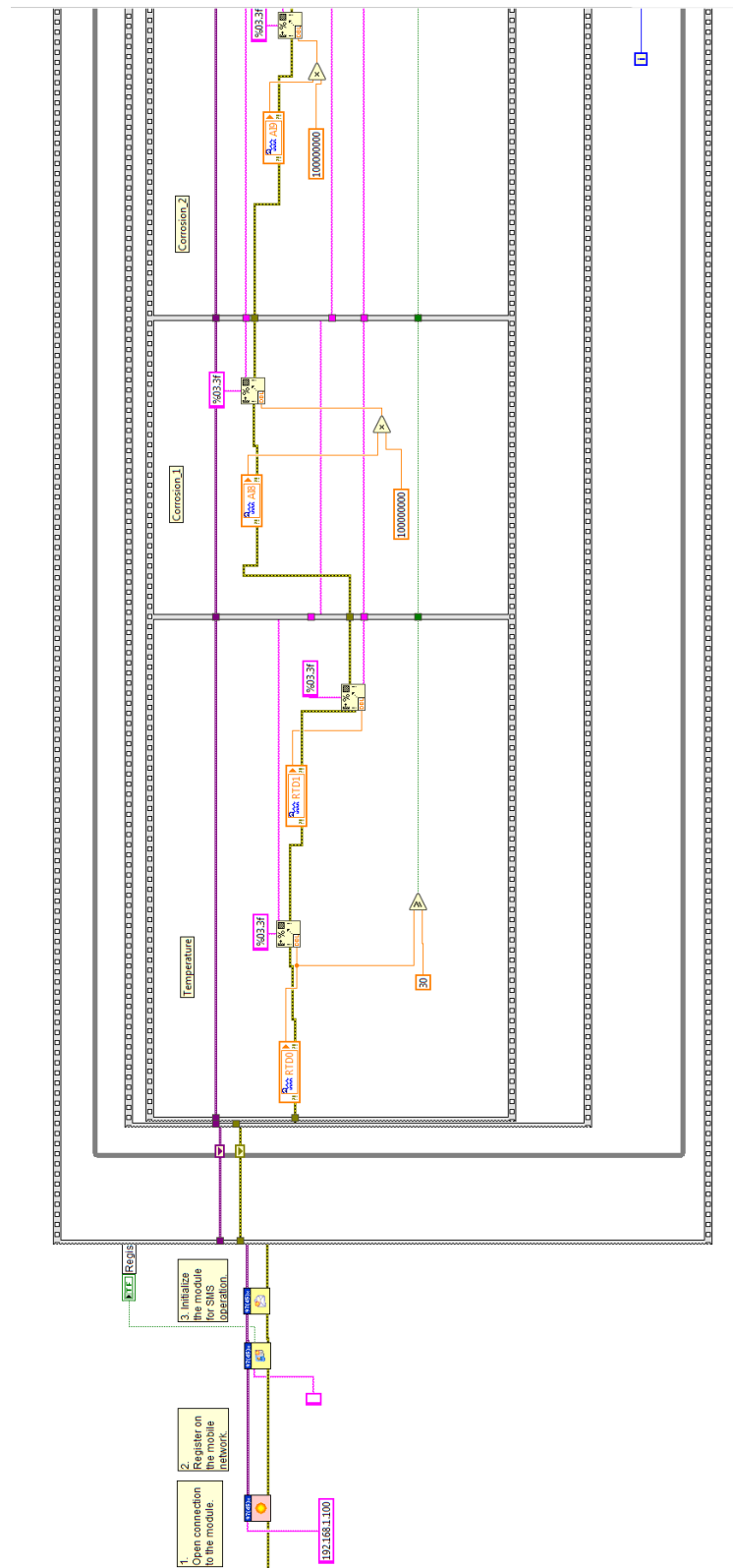
Appendix L: LabVIEW Program

HP Remote Terminal Unit

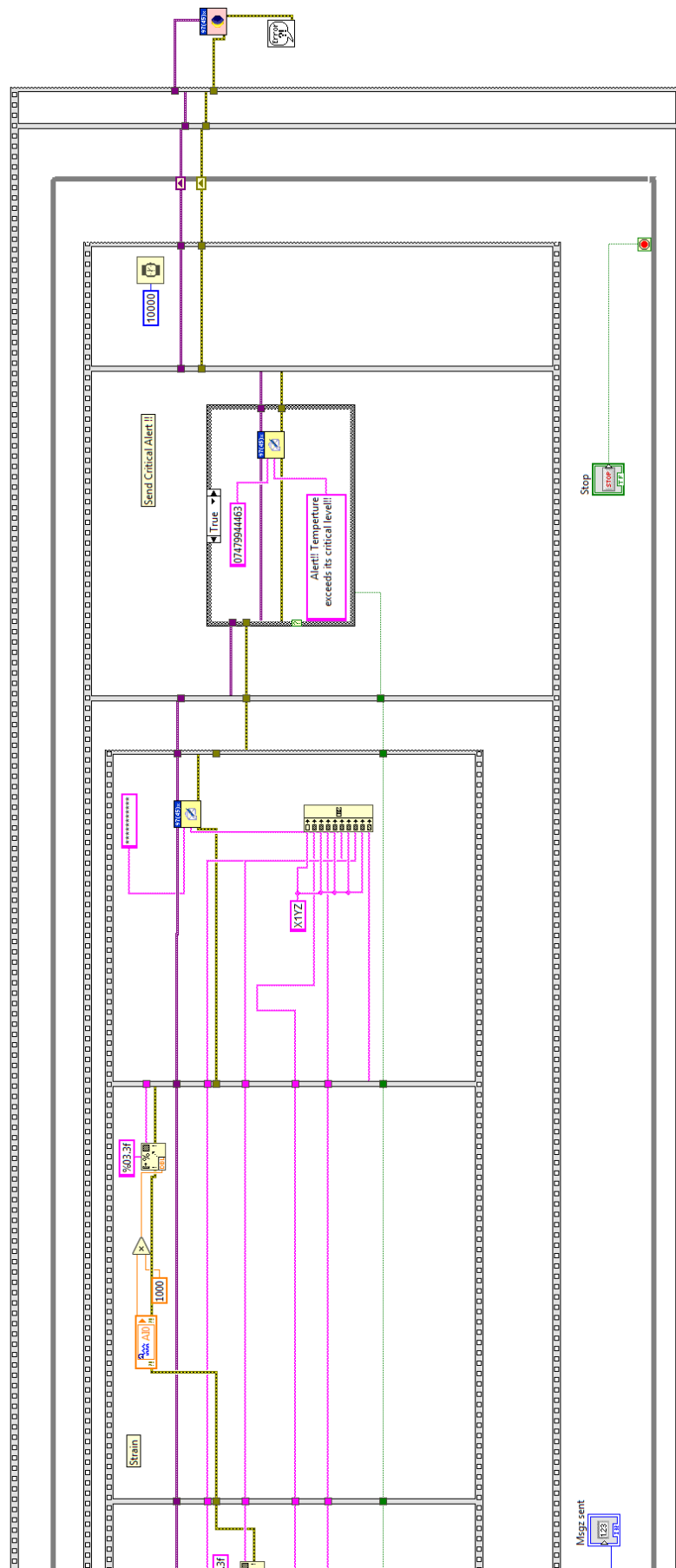
Front Panel



Block Diagram



Appendix L: LabVIEW Program



Appendix M: Data sheet

NCEM_Smart ver1.0 Data sheet



NCEM_SMART

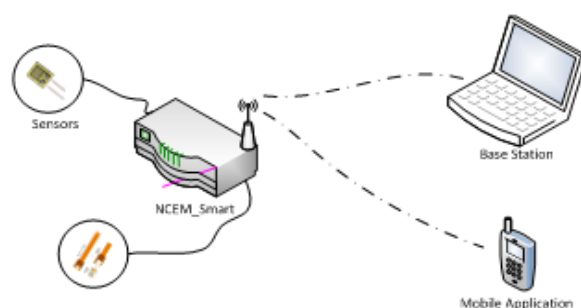
Version 1.0 Data Sheet

Description:

The remote unit (NCEM_Smart ver1.0) for structural health monitoring system has been developed to acquire real time measurements of critical parameters of structures operating at remote locations. It has multiple channels of Temperature, Humidity, Corrosion and Strain sensors, to monitor the variation in mechanical and chemical properties of metal structures subjected to meteorological factors. The data can be observed at base station for further analysis. The duration for the reception of data packets can be adjusted according to requirements. It has status LED's to indicate the proper functioning of device and battery life. The SIM card with sms package and batteries (9V) are required to operate the device.

Specifications:

Sr. No	Sensor Type	Channels	Technical detail
1.	Strain	4	Grid Resistance = $350.0 \pm 0.2\%$, Gage factor = $(+1.2 \pm 0.2)$
2.	Humidity	4	Accuracy = $\pm 2\%RH$ (Max $\pm 5\%RH$), Sensitivity = $0.1\%RH$
3.	Temperature	4	Accuracy = $\pm 0.5^\circ C$, Sensitivity = $0.1^\circ C$
4.	Linear Polarisation Resistor	4	Available on (http://www.analatom.com/products-LPR.html)

System Model:

Developed by: NanoCorr Energy Modelling Research Center | Bournemouth University

Appendix N: Arduino code

Arduino Code for NCEM_Smartv1.0

```
/* NCEM_Smart version 1.0
 *
 * Structural Health Monitoring system
 * Features...
 *   TMP and Humidity sensor
 *   LPR sensors
 *   Strain sensors
 *   battery check
 *   status leds
 *   rtc alarm
 */

// Data packet {humid temp lpr time date}
// code word {X2YZ}and {TD}
// With RTC..

//Librarie
#include <Wire.h>
#include <RTClibExtended.h>
#include <LowPower.h>
#include <dht.h>

dht DHT;

RTC_DS3231 RTC;      //we are using the DS3231 RTC

//----- Input Parameters-----
-----

//char Code_Word[4] = "X2YZ"; // TD for Time

#define Code_Word "X2YZ"
// #define BS_Number "07459444370"
// #define BS_Number "07404940521" // myRen
#define BS_Number "07466533214" // MyRio
// #define BS_Number "07404673762" // myRich
// #define BS_Number "07479944463"

unsigned int No_LPR_Snsr = 2;
unsigned int No_Strain_Snsr = 1;
unsigned int No_humid_Snsr = 2;
unsigned int No_temp_Snsr = 2;
```


Appendix N: Arduino code

```
unsigned int Min_Interval = 1;   /// Enter packet Rx duration

unsigned int Crnt_Sec = 0;       // Enter the current time
unsigned int Crnt_Min = 55;
unsigned int Crnt_Hr = 23;

unsigned int Crnt_yr = 18;
unsigned int Crnt_Mth = 02;
unsigned int Crnt_Day = 14;

//-----Status LED's-----
-----
#define wakePin 2
#define Green_LED 23 // Module working fine
#define Red_LED 24 // Something Might be faulty
#define Yellow_LED 25 // Transmission in progress

//-----Temperature and Humdidity sensors-----
-----

#define Temp_Humid_1 3 // DHT 22 (AM2302) -
#define Temp_Humid_2 4 // DHT 22 (AM2302) -
#define Temp_Humid_3 5 // DHT 22 (AM2302) -
#define Temp_Humid_4 6 // DHT 22 (AM2302) -

float humid[6]; //Stores humidity value
float temp[6]; //Stores temperature value

//-----Linear Polarisation resistors-----
-----

#define LPR_1 A0
#define LPR_2 A1
#define LPR_3 A2
#define LPR_4 A3
#define LPR_5 A4

float volt_LPR[6];

//-----Strain sensors-----

#define Strain_1 A6
#define Strain_2 A7
#define Strain_3 A8
#define Strain_4 A9
#define Strain_5 A10
```

Appendix N: Arduino code

```
float volt_Strain[6];

//-----Battery Check-----

#define Battery_1 A12
#define Battery_2 A13
#define Battery_3 A14
#define Battery_4 A15

//-----Relay-----

#define Relay_1 31
#define Relay_2 32

//-----Global variables
int rp = 0;    // remove when rtc
int byt_cnt = 0;
bool Valid_Resp;
bool startup = true;

//uint16_t y_now, m_now , d_now , hh_now , mm_now , ss_now;
DateTime Time_now;

unsigned int Alarm_Min = 0;
byte AlarmFlag = 0;
byte ledStatus = 1;
bool state = 1;
unsigned long lastInterrupt;

char Ok_Resp[6] = { 0x0D , 0x0A, 0x4F , 0x4B , 0x0D , 0x0A};    //
..OK..

void wakeUp()           // here the interrupt is handled after wakeup
{
    if (millis() - lastInterrupt > 40) // we set a 40ms no-interrupts
    window for any glitch
    {
        Serial.write("Enter wakeupp");
        lastInterrupt = millis();
    }
}

void setup() {
    // initialize both serial ports:
    Serial.begin(9600); // for debugging
```

Appendix N: Arduino code

```
Serial1.begin(9600); // for GSM

pinMode(Relay_1, OUTPUT); //Set Pin12 as output
pinMode(Relay_2, OUTPUT); //Set Pin12 as output

// Initialize pins for battery check
pinMode(Battery_1, INPUT);
pinMode(Battery_2, INPUT);
pinMode(Battery_3, INPUT);
pinMode(Battery_4, INPUT);

digitalWrite(Relay_1, LOW); //Turn on relay
digitalWrite(Relay_2, LOW); //Turn on relay

init_LED_Pins();
init_LPR__Strain_BtryChck_Pins();
delay(100); // Imp
Ping_GSM();
Init_RTC_Clock();

digitalWrite(Relay_1, HIGH); //Turn off relay
digitalWrite(Relay_2, HIGH); //Turn off relay
}

void loop() {

    //while(rp <= 3) // remove when rtc...
    //{
    //rp = rp + 1;
    //attachInterrupt(0, wakeUp, LOW); remove once program tested

    if (AlarmFlag == 0 ) {
        // while(AlarmFlag == 0 ) {
        attachInterrupt(0, wakeUp, LOW); //use
interrupt 0 (pin 2) and run function wakeUp when pin 2 gets LOW
        // digitalWrite(RedLed, LOW);
        //switch-off the led for indicating that we enter the sleep mode
        ledStatus = 0; //set
the led status accordingly
        Serial.write("---Enter Sleep Mode :");
        delay(200);
        LowPower.powerDown(SLEEP_FOREVER, ADC_OFF, BOD_OFF);
        //arduino enters sleep mode here
        detachInterrupt(0);
        //execution resumes from here after wake-up

        digitalWrite(Relay_1, LOW); //Turn on relay
        digitalWrite(Relay_2, LOW); //Turn on relay
        Read_Temp_Humid();
        Read_LPR_pins();
        Read_Strain_pins();
        Send_DatPacket();
        digitalWrite(Relay_1, HIGH); //Turn off relay
        digitalWrite(Relay_2, HIGH); //Turn off relay
        RTC.clearAlarm(1);
```

Appendix N: Arduino code

```
    Alarm_Min = Alarm_Min + Min_Interval ;
    if ( Alarm_Min >= 60 ) // adjust next hour.. // if ( Alarm_Min
> 60 )
    {
        Alarm_Min = Alarm_Min - 60;
    }
    RTC.setAlarm(ALM1_MATCH_MINUTES, 0, Alarm_Min, 0, 0);
    RTC.alarmInterrupt(1, true);
}

}

void init_LED_Pins()
{
    // initialize digital pin LED_BUILTIN as an output
    pinMode(Green_LED, OUTPUT);
    pinMode(Red_LED, OUTPUT);
    pinMode(Yellow_LED, OUTPUT);
}

void init_LPR__Strain_BtryChck_Pins()
{
    // Initialize pins for LPR sensors
    pinMode(LPR_1, INPUT);
    pinMode(LPR_2, INPUT);
    pinMode(LPR_3, INPUT);
    pinMode(LPR_4, INPUT);
    pinMode(LPR_5, INPUT);

    pinMode(Strain_1, INPUT);
    pinMode(Strain_2, INPUT);
    pinMode(Strain_3, INPUT);
    pinMode(Strain_4, INPUT);
    pinMode(Strain_5, INPUT);

    pinMode(Battery_1, INPUT);
    pinMode(Battery_2, INPUT);
    pinMode(Battery_3, INPUT);
    pinMode(Battery_4, INPUT);

}

void Ping_GSM()
{
    Serial.write("Flush Buffer"); // remove any prior data on port
    while (Serial1.available())
    {
        Serial.write(Serial1.read());
    }

    // delay(1000);
    Serial.write("Sending ATE0 Command");
    Serial1.write("ATE0\r\n");
    Valid_Resp = Rx_Check_Response();
}
```

Appendix N: Arduino code

```
Print_Validation();

Serial.write("Sending AT Command");
Serial1.write("AT\r\n");

Valid_Resp = Rx_Check_Response();
Print_Validation();

Serial.write("Sending AT+CMGS Command");
Serial1.write("AT+CMGF=1\r\n");

Valid_Resp = Rx_Check_Response();
Print_Validation();

// Starup Succesfull Signal
if ( startup == true) {
    digitalWrite(Green_LED, HIGH); // Turn Green LED
}
else {
    digitalWrite(Red_LED, HIGH);
}
}

void Init_RTC_Clock()
{
    //Initialize communication with the clock
    Wire.begin();
    RTC.begin();
    RTC.adjust(DateTime(Crnt_yr, Crnt_Mth, Crnt_Day , Crnt_Hr,
Crnt_Min, Crnt_Sec)); //set RTC date and time to COMPILE time
(uint16_t year, uint8_t month, uint8_t day, uint8_t hour, uint8_t
min, uint8_t sec)

    //clear any pending alarms
    RTC.armAlarm(1, false);
    RTC.clearAlarm(1);
    RTC.alarmInterrupt(1, false);
    RTC.armAlarm(2, false);
    RTC.clearAlarm(2);
    RTC.alarmInterrupt(2, false);

    //Set SQW pin to OFF (in my case it was set by default to 1Hz)
    //The output of the DS3231 INT pin is connected to this pin
    //It must be connected to arduino D2 pin for wake-up
    RTC.writeSqwPinMode(DS3231_OFF);
    Alarm_Min = Crnt_Min + Min_Interval;

    if ( Alarm_Min >= 60) // adjust next hour
    {
        Alarm_Min = Crnt_Min + Min_Interval - 60;
    }

    RTC.setAlarm(ALM1_MATCH_MINUTES, 0, Alarm_Min, 0, 0);
    // RTC.setAlarm(ALM2_MATCH_MINUTES,0,49, 12, 30);
}
```

Appendix N: Arduino code

```
RTC.alarmInterrupt(1, true);

}

void Read_Temp_Humid()
{
    Serial.write("Reading temp");
    //----- Temperature and Huumidty Sensors
    DHT.read22(Temp_Humid_1);
    humid[0] = DHT.humidity;
    temp[0] = DHT.temperature;

    DHT.read22(Temp_Humid_2);
    humid[1] = DHT.humidity;
    temp[1] = DHT.temperature;

    DHT.read22(Temp_Humid_3);
    humid[2] = DHT.humidity;
    temp[2] = DHT.temperature;

    DHT.read22(Temp_Humid_4);
    humid[3] = DHT.humidity;
    temp[3] = DHT.temperature;

    // DHT.read22(Temp_Humid_5);
    // humid[4] = DHT.humidity;
    // temp[4] = DHT.temperature;

}

void Read_LPR_pins()
{
    //----- Linear Polarisation
    resistance
    int sensorValue_1 = analogRead(LPR_1);
    volt_LPR[0] = sensorValue_1 * (5 / 1023.0); // Convert the analog
    reading (which goes from 0 - 1023) to a voltage (0 - 5V)

    int sensorValue_2 = analogRead(LPR_2);
    volt_LPR[1] = sensorValue_2 * (5 / 1023.0);

    int sensorValue_3 = analogRead(LPR_3);
    volt_LPR[2] = sensorValue_3 * (5 / 1023.0);

    int sensorValue_4 = analogRead(LPR_4);
    volt_LPR[3] = sensorValue_4 * (5 / 1023.0);

    int sensorValue_5 = analogRead(LPR_5);
```

Appendix N: Arduino code

```
volt_LPR[4] = sensorValue_5 * (5 / 1023.0);

}

void Read_Strain_pins()
{
    //----- Strain sensor measurments

    int sensor_S_Value_1 = analogRead(Strain_1);
    volt_Strain[0] = sensor_S_Value_1 * (5 / 1023.0); // Convert the
    analog reading (which goes from 0 - 1023) to a voltage (0 - 5V)

    int sensor_S_Value_2 = analogRead(Strain_2);
    volt_Strain[1] = sensor_S_Value_2 * (5 / 1023.0);

    int sensor_S_Value_3 = analogRead(Strain_3);
    volt_Strain[2] = sensor_S_Value_3 * (5 / 1023.0);

    int sensor_S_Value_4 = analogRead(Strain_4);
    volt_Strain[3] = sensor_S_Value_4 * (5 / 1023.0);

    int sensor_S_Value_5 = analogRead(Strain_5);
    volt_Strain[4] = sensor_S_Value_5 * (5 / 1023.0);

}

void Send_DatPacket()
{
    //----- Send Data packet
    Serial.write("Check");
    Serial.write("Sending SMS Command");
    Serial1.write("AT+CMGS=\"");
    Serial1.write(BS_Number);
    Serial1.write("\"\\r\\n");
    delay(3000); // imp may vary...

    //
    while(Serial1.available())
    {
        int inByte = Serial1.read();
        Serial.write(inByte);
        delay(100);
    }

    for (int s = 0; s < No_temp_Snsr ; s++)
```


Appendix N: Arduino code

```
{
    Serial1.write(Code_Word);
    Serial1.print(temp[s]);
}

for (int c = 0; c < No_LPR_Snsr ; c++)
{
    Serial1.write(Code_Word);
    Serial1.print(volt_LPR[c]);
}

for (int s = 0; s < No_humid_Snsr ; s++)
{
    Serial1.write(Code_Word);
    Serial1.print(humid[s]);
}

for (int s = 0; s < No_Strain_Snsr ; s++)
{
    Serial1.write(Code_Word);
    Serial1.print(volt_Strain[s]);
}

    Serial1.write(Code_Word);
    Time_now = RTC.now();

    Serial1.write("TD");

    Serial1.print(Time_now.hour());
    Serial1.write(":");
    Serial1.print(Time_now.minute());
    Serial1.write(":");
    Serial1.print(Time_now.second());

    Serial1.write("GG");
    Serial1.print(Time_now.day());
    Serial1.write("/");
    Serial1.print(Time_now.month());
    Serial1.write("/");
    Serial1.print(Time_now.year());
    Serial1.write("TD");

    Serial1.write(Code_Word); //End of packet

    delay(1000); // imp
    Serial1.write("\x1A");

    Serial.write("SMS Sent-----");
    delay(4000); // very important delay

    Valid_Resp = Rx_Check_Response();
    //byt_cnt = 0;
```

Appendix N: Arduino code

```
Print_Validation();

}

// Functions starts from here.....

bool Rx_Check_Response()
{
    delay(2000);
    char Rx_Resp[30];

    while (Serial1.available())
    {
        int inByte = Serial1.read();
        Serial.write(inByte);
        // Serial.print(inByte);
        Rx_Resp[byt_cnt] = inByte;
        byt_cnt++;
        delay(100);
    }

    int max_byt_cnt = byt_cnt - 1;

    Serial.write("----byt_cnt_rcvd---");
    Serial.print(max_byt_cnt);
    Serial.print(byt_cnt - 1);

    bool Check = true;

    for (int j = 5 , i = 0 ; j >= 0, i <= 5 ; j--, i++ )
    {

        if (Rx_Resp[max_byt_cnt - i] == Ok_Resp[j]) //invert....
        {
            // Serial.write("____Matched____");
        }
        else
        {
            Serial.write("----Not Matched---");
            Serial.write(Rx_Resp[max_byt_cnt - i]);
            Serial.write(Ok_Resp[j]);
            Check = false;
        }
    }

    byt_cnt = 0;
    max_byt_cnt = 0;
    //Rx_Resp[] = NULL;

    if (Check == true) return true;
    else return false;
}
```

Appendix N: Arduino code

```
}

void Print_Validation()
{
    if (Valid_Resp == true) {
        Serial.write("__/Valid Response/_");
        digitalWrite(26, HIGH);    // turn the LED on (HIGH is the
        voltage level)
        delay(1000);                // wait for a second
        digitalWrite(26, LOW);    // turn the LED off by making the
        voltage LOW
    }
    else {
        startup = false; Serial.write("__-NOT Valid Response-__");
        digitalWrite(Red_LED, HIGH);    // turn the LED on (HIGH is the
        voltage level)
    }
}

void Check_Batteries()
{
    // read the input on analog pin 0:

    int sensorValue = analogRead(A15);
    // Convert the analog reading (which goes from 0 - 1023) to a
    voltage (0 - 50V):
    float voltage = sensorValue * (5.0 / 1024.0) * 10;

    if(voltage < 6 )
    {
        digitalWrite(Red_LED, HIGH);    // turn the LED on (HIGH is the
        voltage level)
        delay(500);
        digitalWrite(Red_LED, LOW);
        delay(500);
        digitalWrite(Red_LED, HIGH);
    }

    sensorValue = analogRead(A14);
    // Convert the analog reading (which goes from 0 - 1023) to a
    voltage (0 - 50V):
    voltage = sensorValue * (5.0 / 1024.0) * 10;

    if(voltage < 6 )
    {
        digitalWrite(Red_LED, HIGH);    // turn the LED on (HIGH is the
        voltage level)
        delay(500);
        digitalWrite(Red_LED, LOW);
        delay(500);
        digitalWrite(Red_LED, HIGH);
    }
}
```

Appendix N: Arduino code

```
    }

    sensorValue = analogRead(A13);
    // Convert the analog reading (which goes from 0 - 1023) to a
    voltage (0 - 50V):
    voltage = sensorValue * (5.0 / 1024.0) * 10;

    if(voltage < 6 )
    {
        digitalWrite(Red_LED, HIGH);    // turn the LED on (HIGH is the
        voltage level)
        delay(500);
        digitalWrite(Red_LED, LOW);
        delay(500);
        digitalWrite(Red_LED, HIGH);
    }

    sensorValue = analogRead(A12);
    // Convert the analog reading (which goes from 0 - 1023) to a
    voltage (0 - 50V):
    voltage = sensorValue * (5.0 / 1024.0) * 10;

    if(voltage < 6 )
    {
        digitalWrite(Red_LED, HIGH);    // turn the LED on (HIGH is the
        voltage level)
        delay(500);
        digitalWrite(Red_LED, LOW);
        delay(500);
        digitalWrite(Red_LED, HIGH);
    }

}
```

DHT_22 Library

```
//
//   FILE: dht.cpp
//   AUTHOR: Rob Tillaart
//   VERSION: 0.1.18
//   PURPOSE: DHT Temperature & Humidity Sensor library for Arduino
//   URL: http://arduino.cc/playground/Main/DHTLib
//

// inspired by DHT11 library
//
// Released to the public domain
//

#include "dht.h"

////////////////////////////////////////
//
```

Appendix N: Arduino code

```
// PUBLIC
//

int dht::read11(uint8_t pin)
{
    // READ VALUES
    int result = _readSensor(pin, DHTLIB_DHT11_WAKEUP,
DHTLIB_DHT11_LEADING_ZEROS);

    // these bits are always zero, masking them reduces errors.
    bits[0] &= 0x3F;
    bits[2] &= 0x3F;

    // CONVERT AND STORE
    humidity = bits[0]; // bits[1] == 0;
    temperature = bits[2]; // bits[3] == 0;

    // TEST CHECKSUM
    // bits[1] && bits[3] both 0
    uint8_t sum = bits[0] + bits[2];
    if (bits[4] != sum)
    {
        return DHTLIB_ERROR_CHECKSUM;
    }
    return result;
}

int dht::read(uint8_t pin)
{
    // READ VALUES
    int result = _readSensor(pin, DHTLIB_DHT_WAKEUP, DHTLIB_DHT_LEADING_ZEROS);

    // these bits are always zero, masking them reduces errors.
    bits[0] &= 0x03;
    bits[2] &= 0x83;

    // CONVERT AND STORE
    humidity = word(bits[0], bits[1]) * 0.1;
    temperature = word(bits[2] & 0x7F, bits[3]) * 0.1;
    if (bits[2] & 0x80) // negative temperature
    {
        temperature = -temperature;
    }

    // TEST CHECKSUM
    uint8_t sum = bits[0] + bits[1] + bits[2] + bits[3];
    if (bits[4] != sum)
    {
        return DHTLIB_ERROR_CHECKSUM;
    }
    return result;
}

////////////////////////////////////
//
// PRIVATE
//

int dht::_readSensor(uint8_t pin, uint8_t wakeupDelay, uint8_t leadingZeroBits)
{
    // INIT BUFFERVAR TO RECEIVE DATA
```

Appendix N: Arduino code

```
uint8_t mask = 128;
uint8_t idx = 0;

uint8_t data = 0;
uint8_t state = LOW;
uint8_t pstate = LOW;
uint16_t zeroLoop = DHTLIB_TIMEOUT;
uint16_t delta = 0;

leadingZeroBits = 40 - leadingZeroBits; // reverse counting...

// replace digitalRead() with Direct Port Reads.
// reduces footprint ~100 bytes => portability issue?
// direct port read is about 3x faster
uint8_t bit = digitalPinToBitMask(pin);
uint8_t port = digitalPinToPort(pin);
volatile uint8_t *PIR = portInputRegister(port);

// REQUEST SAMPLE
pinMode(pin, OUTPUT);
digitalWrite(pin, LOW); // T-be
delay(wakeupDelay);
digitalWrite(pin, HIGH); // T-go
pinMode(pin, INPUT);

uint16_t loopCount = DHTLIB_TIMEOUT * 2; // 200uSec max
// while(digitalRead(pin) == HIGH)
while ((*PIR & bit) != LOW )
{
    if (--loopCount == 0) return DHTLIB_ERROR_CONNECT;
}

// GET ACKNOWLEDGE or TIMEOUT
loopCount = DHTLIB_TIMEOUT;
// while(digitalRead(pin) == LOW)
while ((*PIR & bit) == LOW ) // T-rel
{
    if (--loopCount == 0) return DHTLIB_ERROR_ACK_L;
}

loopCount = DHTLIB_TIMEOUT;
// while(digitalRead(pin) == HIGH)
while ((*PIR & bit) != LOW ) // T-reh
{
    if (--loopCount == 0) return DHTLIB_ERROR_ACK_H;
}

loopCount = DHTLIB_TIMEOUT;

// READ THE OUTPUT - 40 BITS => 5 BYTES
for (uint8_t i = 40; i != 0; )
{
    // WAIT FOR FALLING EDGE
    state = (*PIR & bit);
    if (state == LOW && pstate != LOW)
    {
        if (i > leadingZeroBits) // DHT22 first 6 bits are all zero !!
DHT11 only 1
        {
            zeroLoop = min(zeroLoop, loopCount);
            delta = (DHTLIB_TIMEOUT - zeroLoop)/4;
        }
    }
}
```

Appendix N: Arduino code

```
    }
    else if ( loopCount <= (zeroLoop - delta) ) // long -> one
    {
        data |= mask;
    }
    mask >>= 1;
    if (mask == 0)    // next byte
    {
        mask = 128;
        bits[idx] = data;
        idx++;
        data = 0;
    }
    // next bit
    --i;

    // reset timeout flag
    loopCount = DHTLIB_TIMEOUT;
}
pstate = state;
// Check timeout
if (--loopCount == 0)
{
    return DHTLIB_ERROR_TIMEOUT;
}

}
pinMode(pin, OUTPUT);
digitalWrite(pin, HIGH);

return DHTLIB_OK;
}
//
// END OF FILE
//
```

Real Time Clock Library

```
// Code by JeeLabs http://news.jeelabs.org/code/
// Released to the public domain! Enjoy!

#include <Wire.h>
#include "RTCLibExtended.h"
#ifdef __AVR__
    #include <avr/pgmspace.h>
#elif defined(ESP8266)
    #include <pgmspace.h>
#elif defined(ARDUINO_ARCH_SAMD)
    // nothing special needed
#elif defined(ARDUINO_SAM_DUE)
    #define PROGMEM
    #define pgm_read_byte(addr) (*(const unsigned char *)(addr))
    #define Wire Wire1
#endif
```

Appendix N: Arduino code

```
#if (ARDUINO >= 100)
#include <Arduino.h> // capital A so it is error prone on case-sensitive
filesystems
// Macro to deal with the difference in I2C write functions from old and new
Arduino versions.
#define _I2C_WRITE write
#define _I2C_READ read
#else
#include <WProgram.h>
#define _I2C_WRITE send
#define _I2C_READ receive
#endif

static uint8_t read_i2c_register(uint8_t addr, uint8_t reg) {
    Wire.beginTransmission(addr);
    Wire._I2C_WRITE((byte)reg);
    Wire.endTransmission();

    Wire.requestFrom(addr, (byte)1);
    return Wire._I2C_READ();
}

static void write_i2c_register(uint8_t addr, uint8_t reg, uint8_t val) {
    Wire.beginTransmission(addr);
    Wire._I2C_WRITE((byte)reg);
    Wire._I2C_WRITE((byte)val);
    Wire.endTransmission();
}

////////////////////////////////////
// utility code, some of this could be exposed in the DateTime API if needed

const uint8_t daysInMonth [] PROGMEM = { 31,28,31,30,31,30,31,31,30,31,30,31 };

// number of days since 2000/01/01, valid for 2001..2099
static uint16_t date2days(uint16_t y, uint8_t m, uint8_t d) {
    if (y >= 2000)
        y -= 2000;
    uint16_t days = d;
    for (uint8_t i = 1; i < m; ++i)
        days += pgm_read_byte(daysInMonth + i - 1);
    if (m > 2 && y % 4 == 0)
        ++days;
    return days + 365 * y + (y + 3) / 4 - 1;
}

static long time2long(uint16_t days, uint8_t h, uint8_t m, uint8_t s) {
    return ((days * 24L + h) * 60 + m) * 60 + s;
}

////////////////////////////////////
// DateTime implementation - ignores time zones and DST changes
// NOTE: also ignores leap seconds, see http://en.wikipedia.org/wiki/Leap_second

DateTime::DateTime (uint32_t t) {
    t -= SECONDS_FROM_1970_TO_2000;    // bring to 2000 timestamp from 1970

    ss = t % 60;
    t /= 60;
    mm = t % 60;
    t /= 60;
```


Appendix N: Arduino code

```
    hh = t % 24;
    uint16_t days = t / 24;
    uint8_t leap;
    for (yOff = 0; ; ++yOff) {
        leap = yOff % 4 == 0;
        if (days < 365 + leap)
            break;
        days -= 365 + leap;
    }
    for (m = 1; ; ++m) {
        uint8_t daysPerMonth = pgm_read_byte(daysInMonth + m - 1);
        if (leap && m == 2)
            ++daysPerMonth;
        if (days < daysPerMonth)
            break;
        days -= daysPerMonth;
    }
    d = days + 1;
}

DateTime::DateTime (uint16_t year, uint8_t month, uint8_t day, uint8_t hour,
uint8_t min, uint8_t sec) {
    if (year >= 2000)
        year -= 2000;
    yOff = year;
    m = month;
    d = day;
    hh = hour;
    mm = min;
    ss = sec;
}

DateTime::DateTime (const DateTime& copy):
    yOff(copy.yOff),
    m(copy.m),
    d(copy.d),
    hh(copy.hh),
    mm(copy.mm),
    ss(copy.ss)
{}

static uint8_t conv2d(const char* p) {
    uint8_t v = 0;
    if ('0' <= *p && *p <= '9')
        v = *p - '0';
    return 10 * v + *++p - '0';
}

// A convenient constructor for using "the compiler's time":
//   DateTime now (__DATE__, __TIME__);
// NOTE: using F() would further reduce the RAM footprint, see below.
DateTime::DateTime (const char* date, const char* time) {
    // sample input: date = "Dec 26 2009", time = "12:34:56"
    yOff = conv2d(date + 9);
    // Jan Feb Mar Apr May Jun Jul Aug Sep Oct Nov Dec
    switch (date[0]) {
        case 'J': m = date[1] == 'a' ? 1 : m = date[2] == 'n' ? 6 : 7; break;
        case 'F': m = 2; break;
        case 'A': m = date[2] == 'r' ? 4 : 8; break;
        case 'M': m = date[2] == 'r' ? 3 : 5; break;
        case 'S': m = 9; break;
    }
```

Appendix N: Arduino code

```
        case 'O': m = 10; break;
        case 'N': m = 11; break;
        case 'D': m = 12; break;
    }
    d = conv2d(date + 4);
    hh = conv2d(time);
    mm = conv2d(time + 3);
    ss = conv2d(time + 6);
}

// A convenient constructor for using "the compiler's time":
// This version will save RAM by using PROGMEM to store it by using the F macro.
//   DateTime now (F(__DATE__), F(__TIME__));
DateTime::DateTime (const __FlashStringHelper* date, const __FlashStringHelper*
time) {
    // sample input: date = "Dec 26 2009", time = "12:34:56"
    char buff[11];
    memcpy_P(buff, date, 11);
    yOff = conv2d(buff + 9);
    // Jan Feb Mar Apr May Jun Jul Aug Sep Oct Nov Dec
    switch (buff[0]) {
        case 'J': m = buff[1] == 'a' ? 1 : m = buff[2] == 'n' ? 6 : 7; break;
        case 'F': m = 2; break;
        case 'A': m = buff[2] == 'r' ? 4 : 8; break;
        case 'M': m = buff[2] == 'r' ? 3 : 5; break;
        case 'S': m = 9; break;
        case 'O': m = 10; break;
        case 'N': m = 11; break;
        case 'D': m = 12; break;
    }
    d = conv2d(buff + 4);
    memcpy_P(buff, time, 8);
    hh = conv2d(buff);
    mm = conv2d(buff + 3);
    ss = conv2d(buff + 6);
}

uint8_t DateTime::dayOfTheWeek() const {
    uint16_t day = date2days(yOff, m, d);
    return (day + 6) % 7; // Jan 1, 2000 is a Saturday, i.e. returns 6
}

uint32_t DateTime::unixtime(void) const {
    uint32_t t;
    uint16_t days = date2days(yOff, m, d);
    t = time2long(days, hh, mm, ss);
    t += SECONDS_FROM_1970_TO_2000; // seconds from 1970 to 2000

    return t;
}

long DateTime::secondstime(void) const {
    long t;
    uint16_t days = date2days(yOff, m, d);
    t = time2long(days, hh, mm, ss);
    return t;
}

DateTime DateTime::operator+(const TimeSpan& span) {
    return DateTime(unixtime()+span.totalseconds());
}
```

Appendix N: Arduino code

```
DateTime DateTime::operator-(const TimeSpan& span) {
    return DateTime(unixtime()-span.totalseconds());
}

TimeSpan DateTime::operator-(const DateTime& right) {
    return TimeSpan(unixtime()-right.unixtime());
}

////////////////////////////////////
// TimeSpan implementation

TimeSpan::TimeSpan (int32_t seconds):
    _seconds(seconds)
{}

TimeSpan::TimeSpan (int16_t days, int8_t hours, int8_t minutes, int8_t seconds):
    _seconds((int32_t)days*86400L + (int32_t)hours*3600 + (int32_t)minutes*60 +
seconds)
{}

TimeSpan::TimeSpan (const TimeSpan& copy):
    _seconds(copy._seconds)
{}

TimeSpan TimeSpan::operator+(const TimeSpan& right) {
    return TimeSpan(_seconds+right._seconds);
}

TimeSpan TimeSpan::operator-(const TimeSpan& right) {
    return TimeSpan(_seconds-right._seconds);
}

////////////////////////////////////
// RTC_DS1307 implementation

static uint8_t bcd2bin (uint8_t val) { return val - 6 * (val >> 4); }
static uint8_t bin2bcd (uint8_t val) { return val + 6 * (val / 10); }

boolean RTC_DS1307::begin(void) {
    Wire.begin();
    return true;
}

uint8_t RTC_DS1307::isrunning(void) {
    Wire.beginTransmission(DS1307_ADDRESS);
    Wire._I2C_WRITE((byte)0);
    Wire.endTransmission();

    Wire.requestFrom(DS1307_ADDRESS, 1);
    uint8_t ss = Wire._I2C_READ();
    return !(ss>>7);
}

void RTC_DS1307::adjust(const DateTime& dt) {
    Wire.beginTransmission(DS1307_ADDRESS);
    Wire._I2C_WRITE((byte)0); // start at location 0
    Wire._I2C_WRITE(bin2bcd(dt.second()));
    Wire._I2C_WRITE(bin2bcd(dt.minute()));
    Wire._I2C_WRITE(bin2bcd(dt.hour()));
    Wire._I2C_WRITE(bin2bcd(0));
}
```

Appendix N: Arduino code

```
Wire._I2C_WRITE(bin2bcd(dt.day()));
Wire._I2C_WRITE(bin2bcd(dt.month()));
Wire._I2C_WRITE(bin2bcd(dt.year() - 2000));
Wire.endTransmission();
}

DateTime RTC_DS1307::now() {
    Wire.beginTransaction(DS1307_ADDRESS);
    Wire._I2C_WRITE((byte)0);
    Wire.endTransmission();

    Wire.requestFrom(DS1307_ADDRESS, 7);
    uint8_t ss = bcd2bin(Wire._I2C_READ() & 0x7F);
    uint8_t mm = bcd2bin(Wire._I2C_READ());
    uint8_t hh = bcd2bin(Wire._I2C_READ());
    Wire._I2C_READ();
    uint8_t d = bcd2bin(Wire._I2C_READ());
    uint8_t m = bcd2bin(Wire._I2C_READ());
    uint16_t y = bcd2bin(Wire._I2C_READ()) + 2000;

    return DateTime (y, m, d, hh, mm, ss);
}

Ds1307SqwPinMode RTC_DS1307::readSqwPinMode() {
    int mode;

    Wire.beginTransaction(DS1307_ADDRESS);
    Wire._I2C_WRITE(DS1307_CONTROL);
    Wire.endTransmission();

    Wire.requestFrom((uint8_t)DS1307_ADDRESS, (uint8_t)1);
    mode = Wire._I2C_READ();

    mode &= 0x93;
    return static_cast<Ds1307SqwPinMode>(mode);
}

void RTC_DS1307::writeSqwPinMode(Ds1307SqwPinMode mode) {
    Wire.beginTransaction(DS1307_ADDRESS);
    Wire._I2C_WRITE(DS1307_CONTROL);
    Wire._I2C_WRITE(mode);
    Wire.endTransmission();
}

void RTC_DS1307::readnvram(uint8_t* buf, uint8_t size, uint8_t address) {
    int addrByte = DS1307_NVRAM + address;
    Wire.beginTransaction(DS1307_ADDRESS);
    Wire._I2C_WRITE(addrByte);
    Wire.endTransmission();

    Wire.requestFrom((uint8_t) DS1307_ADDRESS, size);
    for (uint8_t pos = 0; pos < size; ++pos) {
        buf[pos] = Wire._I2C_READ();
    }
}

void RTC_DS1307::writenvram(uint8_t address, uint8_t* buf, uint8_t size) {
    int addrByte = DS1307_NVRAM + address;
    Wire.beginTransaction(DS1307_ADDRESS);
    Wire._I2C_WRITE(addrByte);
    for (uint8_t pos = 0; pos < size; ++pos) {
```

Appendix N: Arduino code

```
        Wire._I2C_WRITE(buf[pos]);
    }
    Wire.endTransmission();
}

uint8_t RTC_DS1307::readnvram(uint8_t address) {
    uint8_t data;
    readnvram(&data, 1, address);
    return data;
}

void RTC_DS1307::writenvram(uint8_t address, uint8_t data) {
    writenvram(address, &data, 1);
}

////////////////////////////////////
// RTC_Millis implementation

long RTC_Millis::offset = 0;

void RTC_Millis::adjust(const DateTime& dt) {
    offset = dt.unixtime() - millis() / 1000;
}

DateTime RTC_Millis::now() {
    return (uint32_t)(offset + millis() / 1000);
}

////////////////////////////////////
// RTC_PCF8563 implementation

boolean RTC_PCF8523::begin(void) {
    Wire.begin();
    return true;
}

boolean RTC_PCF8523::initialized(void) {
    Wire.beginTransaction(PCF8523_ADDRESS);
    Wire._I2C_WRITE((byte)PCF8523_CONTROL_3);
    Wire.endTransmission();

    Wire.requestFrom(PCF8523_ADDRESS, 1);
    uint8_t ss = Wire._I2C_READ();
    return ((ss & 0xE0) != 0xE0);
}

void RTC_PCF8523::adjust(const DateTime& dt) {
    Wire.beginTransaction(PCF8523_ADDRESS);
    Wire._I2C_WRITE((byte)3); // start at location 3
    Wire._I2C_WRITE(bin2bcd(dt.second()));
    Wire._I2C_WRITE(bin2bcd(dt.minute()));
    Wire._I2C_WRITE(bin2bcd(dt.hour()));
    Wire._I2C_WRITE(bin2bcd(dt.day()));
    Wire._I2C_WRITE(bin2bcd(0)); // skip weekdays
    Wire._I2C_WRITE(bin2bcd(dt.month()));
    Wire._I2C_WRITE(bin2bcd(dt.year() - 2000));
    Wire.endTransmission();

    // set to battery switchover mode
}
```

Appendix N: Arduino code

```
Wire.beginTransaction(PCF8523_ADDRESS);
Wire._I2C_WRITE((byte)PCF8523_CONTROL_3);
Wire._I2C_WRITE((byte)0x00);
Wire.endTransmission();
}

DateTime RTC_PCF8523::now() {
    Wire.beginTransaction(PCF8523_ADDRESS);
    Wire._I2C_WRITE((byte)3);
    Wire.endTransmission();

    Wire.requestFrom(PCF8523_ADDRESS, 7);
    uint8_t ss = bcd2bin(Wire._I2C_READ() & 0x7F);
    uint8_t mm = bcd2bin(Wire._I2C_READ());
    uint8_t hh = bcd2bin(Wire._I2C_READ());
    uint8_t d = bcd2bin(Wire._I2C_READ());
    Wire._I2C_READ(); // skip 'weekdays'
    uint8_t m = bcd2bin(Wire._I2C_READ());
    uint16_t y = bcd2bin(Wire._I2C_READ()) + 2000;

    return DateTime (y, m, d, hh, mm, ss);
}

Pcf8523SqwPinMode RTC_PCF8523::readSqwPinMode() {
    int mode;

    Wire.beginTransaction(PCF8523_ADDRESS);
    Wire._I2C_WRITE(PCF8523_CLKOUTCONTROL);
    Wire.endTransmission();

    Wire.requestFrom((uint8_t)PCF8523_ADDRESS, (uint8_t)1);
    mode = Wire._I2C_READ();

    mode >>= 3;
    mode &= 0x7;
    return static_cast<Pcf8523SqwPinMode>(mode);
}

void RTC_PCF8523::writeSqwPinMode(Pcf8523SqwPinMode mode) {
    Wire.beginTransaction(PCF8523_ADDRESS);
    Wire._I2C_WRITE(PCF8523_CLKOUTCONTROL);
    Wire._I2C_WRITE(mode << 3);
    Wire.endTransmission();
}

////////////////////////////////////
// RTC_DS3231 implementation

boolean RTC_DS3231::begin(void) {
    Wire.begin();
    return true;
}

bool RTC_DS3231::lostPower(void) {
    return (read_i2c_register(DS3231_ADDRESS, DS3231_STATUSREG) >> 7);
}

void RTC_DS3231::adjust(const DateTime& dt) {
    Wire.beginTransaction(DS3231_ADDRESS);
    Wire._I2C_WRITE((byte)0); // start at location 0
    Wire._I2C_WRITE(bin2bcd(dt.second()));
}
```

Appendix N: Arduino code

```
Wire._I2C_WRITE(bin2bcd(dt.minute()));
Wire._I2C_WRITE(bin2bcd(dt.hour()));
Wire._I2C_WRITE(bin2bcd(0));
Wire._I2C_WRITE(bin2bcd(dt.day()));
Wire._I2C_WRITE(bin2bcd(dt.month()));
Wire._I2C_WRITE(bin2bcd(dt.year() - 2000));
Wire.endTransmission();

uint8_t statreg = read_i2c_register(DS3231_ADDRESS, DS3231_STATUSREG);
statreg &= ~0x80; // flip OSF bit
write_i2c_register(DS3231_ADDRESS, DS3231_STATUSREG, statreg);
}

DateTime RTC_DS3231::now() {
    Wire.beginTransaction(DS3231_ADDRESS);
    Wire._I2C_WRITE((byte)0);
    Wire.endTransmission();

    Wire.requestFrom(DS3231_ADDRESS, 7);
    uint8_t ss = bcd2bin(Wire._I2C_READ() & 0x7F);
    uint8_t mm = bcd2bin(Wire._I2C_READ());
    uint8_t hh = bcd2bin(Wire._I2C_READ());
    Wire._I2C_READ();
    uint8_t d = bcd2bin(Wire._I2C_READ());
    uint8_t m = bcd2bin(Wire._I2C_READ());
    uint16_t y = bcd2bin(Wire._I2C_READ()) + 2000;

    return DateTime (y, m, d, hh, mm, ss);
}

Ds3231SqwPinMode RTC_DS3231::readSqwPinMode() {
    int mode;

    Wire.beginTransaction(DS3231_ADDRESS);
    Wire._I2C_WRITE(DS3231_CONTROL);
    Wire.endTransmission();

    Wire.requestFrom((uint8_t)DS3231_ADDRESS, (uint8_t)1);
    mode = Wire._I2C_READ();

    mode &= 0x93;
    return static_cast<Ds3231SqwPinMode>(mode);
}

void RTC_DS3231::writeSqwPinMode(Ds3231SqwPinMode mode) {
    uint8_t ctrl;
    ctrl = read_i2c_register(DS3231_ADDRESS, DS3231_CONTROL);

    ctrl &= ~0x04; // turn off INTCON
    ctrl &= ~0x18; // set freq bits to 0

    if (mode == DS3231_OFF) {
        ctrl |= 0x04; // turn on INTCN
    } else {
        ctrl |= mode;
    }
    write_i2c_register(DS3231_ADDRESS, DS3231_CONTROL, ctrl);

    //Serial.println( read_i2c_register(DS3231_ADDRESS, DS3231_CONTROL), HEX);
}
```

Appendix N: Arduino code

```
/*-----*/

float RTC_DS3231::getTemp() {
    int8_t temp_msb, temp_lsb;

    Wire.beginTransaction(DS3231_ADDRESS);
    Wire.write(DS3231_TEMP);
    Wire.endTransmission();

    Wire.requestFrom((uint8_t)DS3231_ADDRESS, (uint8_t)2);
    temp_msb = Wire._I2C_READ();
    temp_lsb = (Wire._I2C_READ() >> 6) & 0x03;
    Wire.endTransmission();

    if(temp_msb & 0b10000000) {        //check if negative number
        temp_msb ^= 0b11111111;
        temp_msb += 0x1;
        return (-1.0 * ((float)temp_msb) + ((float)temp_lsb * 0.25));
    }
    else {
        return ((float)temp_msb + ((float)temp_lsb * 0.25));
    }
}

/*-----*
 * Enable or disable an alarm "interrupt" which asserts the INT pin      *
 * on the RTC.                                                            *
 *-----*/
void RTC_DS3231::alarmInterrupt(byte alarmNumber, bool interruptEnabled)
{
    uint8_t controlReg, mask;

    Wire.beginTransaction(DS3231_ADDRESS);
    Wire.write(DS3231_CONTROL);
    controlReg = Wire.endTransmission();
    if (!controlReg) {
        Wire.requestFrom((uint8_t)DS3231_ADDRESS, (uint8_t)1);
        controlReg = Wire._I2C_READ();
        Wire.endTransmission();
    }

    mask = _BV(A1IE) << (alarmNumber - 1);
    if (interruptEnabled)
        controlReg |= mask;
    else
        controlReg &= ~mask;

    Wire.beginTransaction(DS3231_ADDRESS);
    Wire.write(DS3231_CONTROL);
    Wire.write(controlReg);
    Wire.endTransmission();
}

/*-----*
 * Set an alarm time. Sets the alarm registers only. To cause the      *
 * INT pin to be asserted on alarm match, use alarmInterrupt().          *
 * This method can set either Alarm 1 or Alarm 2, depending on the      *
 * value of alarmType (use a value from the ALARM_TYPES_t enumeration). *
 * When setting Alarm 2, the seconds value must be supplied but is      *
 * ignored, recommend using zero. (Alarm 2 has no seconds register.)    *
 *-----*/
```


Appendix N: Arduino code

```
void RTC_DS3231::setAlarm(Ds3231_ALARM_TYPES_t alarmType, byte seconds, byte
minutes, byte hours, byte daydate){

    uint8_t addr;
    byte alarmNumber;

    seconds = bin2bcd(seconds);
    minutes = bin2bcd(minutes);
    hours = bin2bcd(hours);
    daydate = bin2bcd(daydate);
    if (alarmType & 0x01) seconds |= _BV(A1M1);
    if (alarmType & 0x02) minutes |= _BV(A1M2);
    if (alarmType & 0x04) hours |= _BV(A1M3);
    if (alarmType & 0x10) hours |= _BV(DYDT);
    if (alarmType & 0x08) daydate |= _BV(A1M4);

    if ( !(alarmType & 0x80) ) {    //alarm 1
        alarmNumber = 1;
        addr = ALM1_SECONDS;
        Wire.beginTransaction(DS3231_ADDRESS);
        Wire.write(addr++);
        Wire.write(seconds);
        Wire.endTransmission();
    }
    else {
        alarmNumber = 2;
        addr = ALM2_MINUTES;    //alarm 2
    }

    Wire.beginTransaction(DS3231_ADDRESS);
    Wire.write(addr++);
    Wire.write(minutes);
    Wire.endTransmission();

    Wire.beginTransaction(DS3231_ADDRESS);
    Wire.write(addr++);
    Wire.write(hours);
    Wire.endTransmission();

    Wire.beginTransaction(DS3231_ADDRESS);
    Wire.write(addr++);
    Wire.write(daydate);
    Wire.endTransmission();

    armAlarm(alarmNumber, true);
    clearAlarm(alarmNumber);
}

/*-----*
 * Set an alarm time. Sets the alarm registers only. To cause the      *
 * INT pin to be asserted on alarm match, use alarmInterrupt().        *
 * This method can set either Alarm 1 or Alarm 2, depending on the     *
 * value of alarmType (use a value from the ALARM_TYPES_t enumeration). *
 * However, when using this method to set Alarm 1, the seconds value    *
 * is set to zero. (Alarm 2 has no seconds register.)                  *
 *-----*/
void RTC_DS3231::setAlarm(Ds3231_ALARM_TYPES_t alarmType, byte minutes, byte
hours, byte daydate) {
    setAlarm(alarmType, 0, minutes, hours, daydate);
}
```

Appendix N: Arduino code

```
/*-----*
 * This method arms or disarms Alarm 1 or Alarm 2, depending on the *
 * value of alarmNumber (1 or 2) and arm (true or false).           *
 *-----*/
void RTC_DS3231::armAlarm(byte alarmNumber, bool armed) {
    uint8_t value, mask;

    Wire.beginTransaction(DS3231_ADDRESS);
    Wire.write(DS3231_CONTROL);
    Wire.endTransmission();

    Wire.requestFrom((uint8_t)DS3231_ADDRESS, (uint8_t)1);
    value = Wire._I2C_READ();
    Wire.endTransmission();

    mask = _BV(alarmNumber - 1);
    if (armed) {
        value |= mask;
    }
    else {
        value &= ~mask;
    }

    Wire.beginTransaction(DS3231_ADDRESS);
    Wire.write(DS3231_CONTROL);
    Wire.write(value);
    Wire.endTransmission();
}

/*-----*
 * This method clears the status register of Alarm 1 or Alarm 2,   *
 * depending on the value of alarmNumber (1 or 2).                 *
 *-----*/
void RTC_DS3231::clearAlarm(byte alarmNumber) {
    uint8_t value, mask;

    Wire.beginTransaction(DS3231_ADDRESS);
    Wire.write(DS3231_STATUSREG);
    Wire.endTransmission();

    Wire.requestFrom((uint8_t)DS3231_ADDRESS, (uint8_t)1);
    value = Wire._I2C_READ();
    Wire.endTransmission();

    mask = _BV(alarmNumber - 1);
    value &= ~mask;

    Wire.beginTransaction(DS3231_ADDRESS);
    Wire.write(DS3231_STATUSREG);
    Wire.write(value);
    Wire.endTransmission();
}

/*-----*
 * This method can check either Alarm 1 or Alarm 2, depending on the *
 * value of alarmNumber (1 or 2).                                     *
 *-----*/
bool RTC_DS3231::isArmed(byte alarmNumber) {
    uint8_t value;

    Wire.beginTransaction(DS3231_ADDRESS);
```

Appendix N: Arduino code

```
Wire.write(DS3231_CONTROL);
Wire.endTransmission();

Wire.requestFrom((uint8_t)DS3231_ADDRESS, (uint8_t)1);
value = Wire._I2C_READ();
Wire.endTransmission();

if (alarmNumber == 1) {
    value &= 0b00000001;
}
else {
    value &= 0b00000010;
    value >>= 1;
}
return value;
}

/*-----*
 * This method writes a single byte in RTC memory *
 * Valid address range is 0x00 - 0x12, no checking. *
 *-----*/
void RTC_DS3231::write(byte addr, byte value) {

    Wire.beginTransaction(DS3231_ADDRESS);
    Wire.write(addr);
    Wire.write(value);
    Wire.endTransmission();
}

/*-----*
 * This method reads a single byte from RTC memory *
 * Valid address range is 0x00 - 0x12, no checking. *
 *-----*/
byte RTC_DS3231::read(byte addr) {
    uint8_t value;

    Wire.beginTransaction(DS3231_ADDRESS);
    Wire.write(addr);
    Wire.endTransmission();

    Wire.requestFrom((uint8_t)DS3231_ADDRESS, (uint8_t)1);
    value = Wire._I2C_READ();
    Wire.endTransmission();

    return value;
}

/*-----*
 * The temperature registers are updated after every 64-second *
 * conversion. If you want force temperature conversion call this *
 * function. *
 *-----*/
void RTC_DS3231::forceConversion(void) {
    uint8_t value;

    Wire.beginTransaction(DS3231_ADDRESS);
    Wire.write(DS3231_CONTROL);
    Wire.endTransmission();

    Wire.requestFrom((uint8_t)DS3231_ADDRESS, (uint8_t)1);
    value = Wire._I2C_READ();
}
```

Appendix N: Arduino code

```
Wire.endTransmission();

value |= 0b00100000;

Wire.beginTransaction(DS3231_ADDRESS);
Wire.write(DS3231_CONTROL);
Wire.write(value);
Wire.endTransmission();

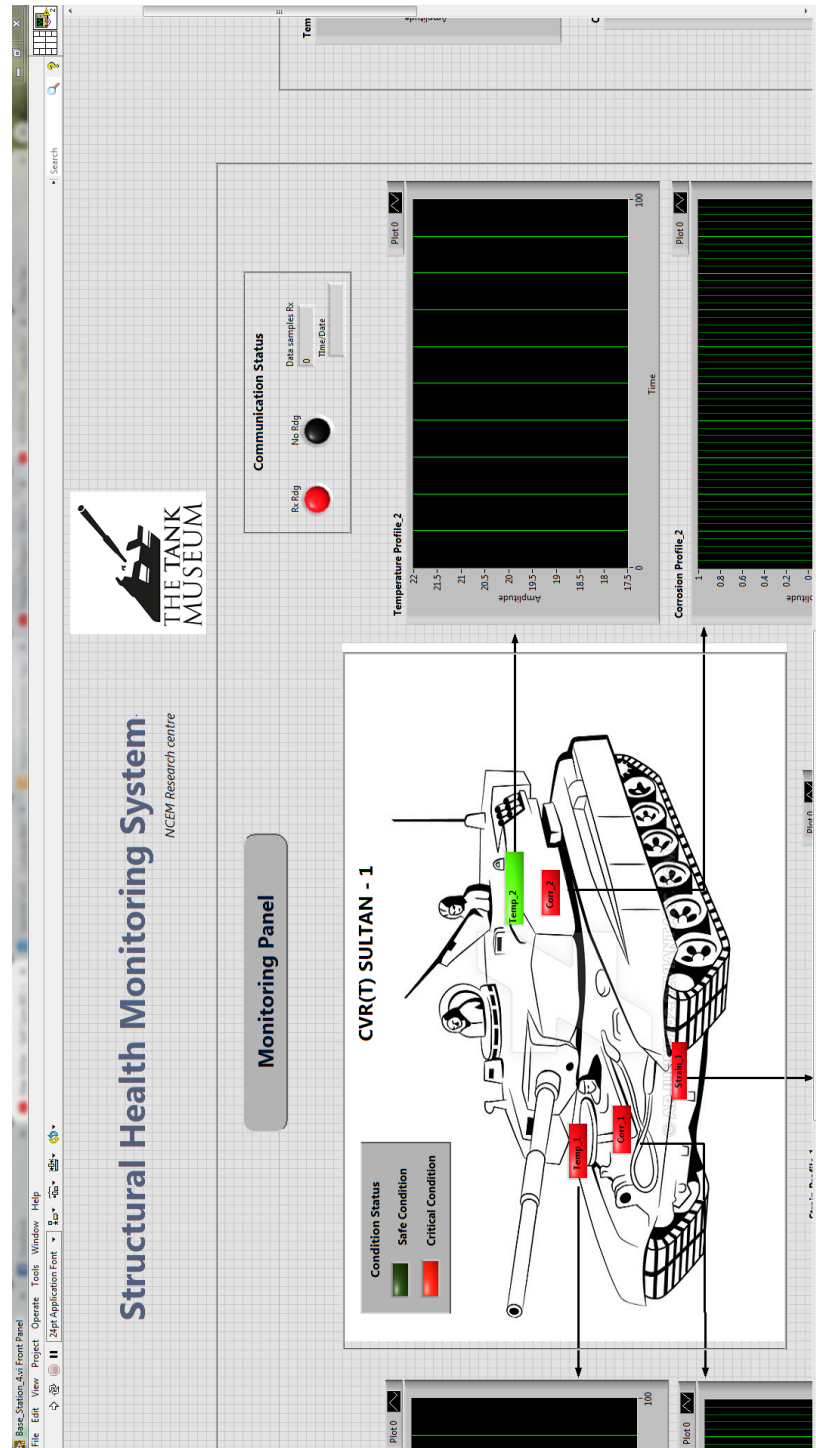
do {
    Wire.beginTransaction(DS3231_ADDRESS);
    Wire.write(DS3231_CONTROL);
    Wire.endTransmission();

    Wire.requestFrom((uint8_t)DS3231_ADDRESS, (uint8_t)1);
    value = Wire._I2C_READ();
    Wire.endTransmission();
} while ((value & 0b00100000) != 0);
}
```

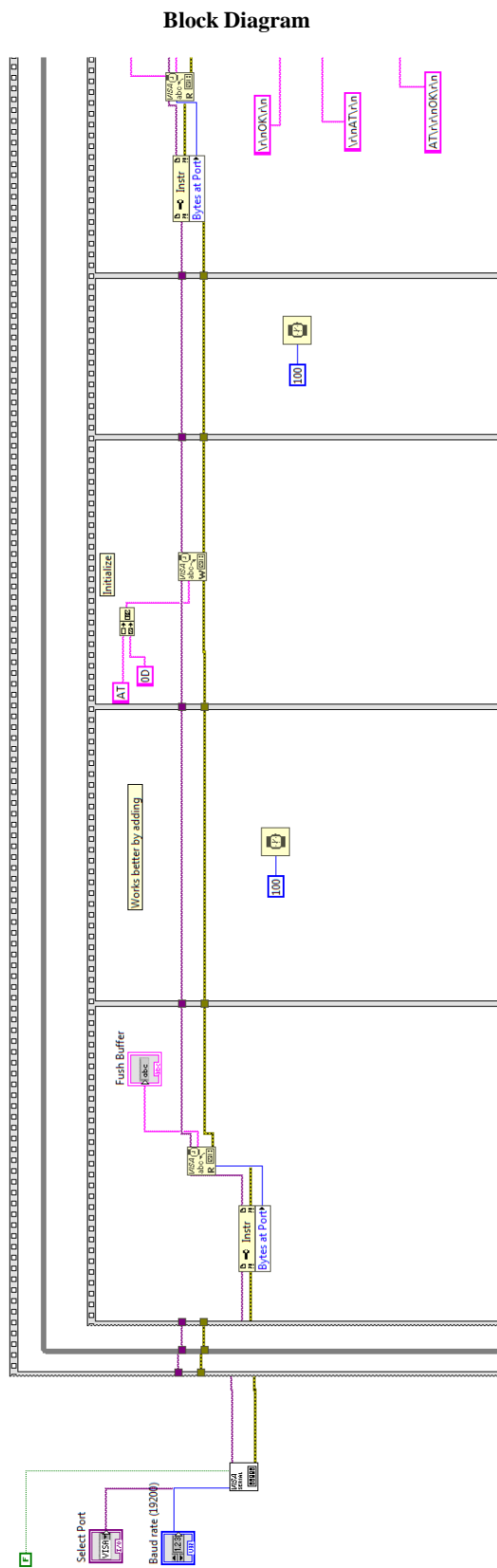
Appendix O: LabVIEW Program

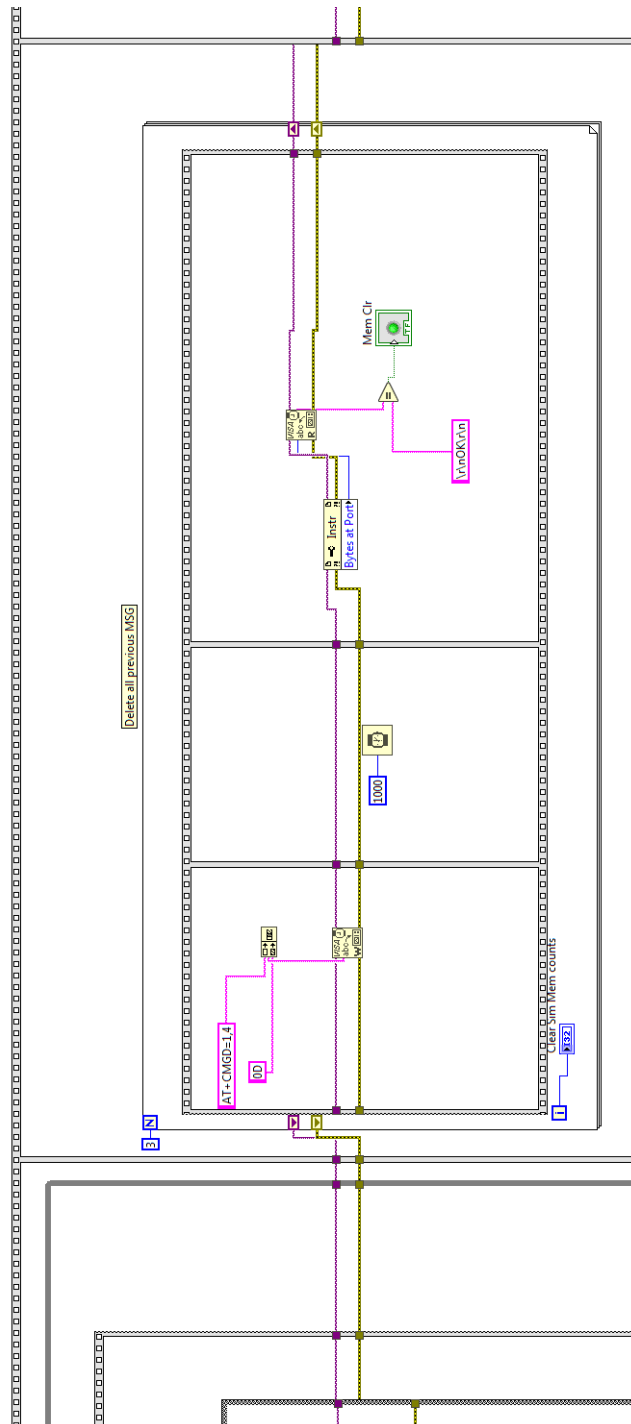
Base Station

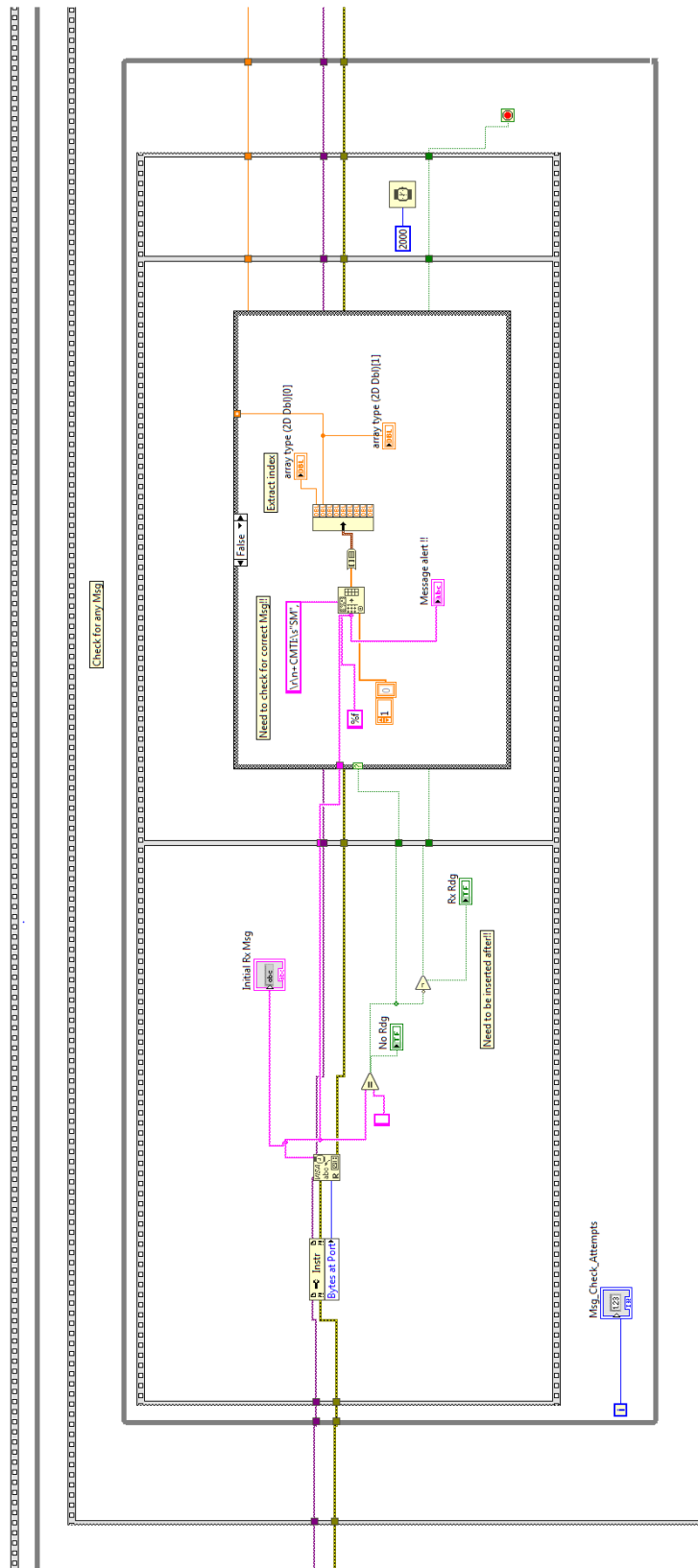
Front Panel



Appendix O: LabVIEW Program







Appendix O: LabVIEW Program

